SEISMIC VULNERABILITY ASSESSMENT OF WHARF STRUCTURES

A Dissertation
Presented to
The Academic Faculty

by

Abdollah Shafieezadeh

In Partial Fulfillment
Of the Requirements for the Degree
Doctor of Philosophy in the
School of Civil and Environmental Engineering

Georgia Institute of Technology

August, 2011

SEISMIC VULNERABILITY ASSESSMENT OF WHARF STRUCTURES

Approved by:

Dr. Reginald DesRoches, Advisor
School of Civil and Environmental Engineering
Georgia Institute of Technology

Dr. Glenn J. Rix
School of Civil and Environmental Engineering
Georgia Institute of Technology

Dr. Dominic Assimaki
School of Civil and Environmental Engineering
Georgia Institute of Technology

Dr. Roberto T. Leon
School of Civil and Environmental Engineering
Georgia Institute of Technology

Dr. Alan Erera
School of Industrial and Systems Engineering
Georgia Institute of Technology

Date Approved: 7/7/2011

ACKNOWLEDGEMENTS

My Ph.D. study at Georgia Tech was truly a journey of learning and inspiration. I owe this great opportunity foremost to my advisor, Professor Reginald DesRoches, who granted me the privilege to work in his research group. With his guidance, I could pass through all the ups and downs of my doctoral work. In short, I am proud to be his student and I wish that my three years at Georgia Tech are only the beginning of a life-long friendship with him.

My special thanks go to Professor Glenn Rix, the PI of the Grand Challenge Project and the instructor of Geotechnical Earthquake Engineering. I admire his modest personality, patience, and true scholarship that made working on this project a great pleasure for me. I would also like to acknowledge Professors Assimaki and Leon for the valuable technical discussions I had with them, and to thank them for sharing their knowledge of soil-structure interaction and pile connection modeling with me. I acknowledge Professor Erera for showing interest in my work and serving on thesis defense committee.

I have been very fortunate to be surrounded by very talented and friendly fellow graduate students. I would like to give my special thanks to my colleagues and best friends, Karthik and Tim for the memorable times we had together. Thanks to my former and current officemates at 522A Mason and my research fellows: Mathew, Laura, Jazalyn, Niki, Chris, Nathan, Stephani, Jong-Su, Sarah, Dapeng, and Towhid. I would also like to thank Ben for sharing his crane models and Varun for helping me integrate his macroelement into OpenSEES.

I owe a debt of gratitude to the project sponsor. The material presented in this research is based upon work supported by the NEESR program of the National Science Foundation under Grants No. CMS-0530478 and CMS-0402490, Project Title "NEESR-GC: Seismic Risk Mitigation for Port Systems." Any opinions, findings, and conclusions or recommendations expressed in this material are those of the author(s) and do not necessarily reflect the views of NSF.

Finally, I would like to thank my fiancé, Jieun Hur, for her unimaginable support, encouragement, and unwavering love. It is not possible to appreciate everything that she has done for me. I would also like to extend my sincere appreciation to my parents Hassan Shafieezadeh and Havva Fotoukian and my brother and sister, Mahdi and Tayebeh Shafieezadeh for their unconditional love and endless support.

TABLE OF CONTENTS

ACKNOWLEDGEMENTS iii
LIST OF TABLES viii
LIST OF FIGURES ix
SUMMARY xvi
CHAPTER 1: INTRODUCTION 1
1.1 Problem Description 1
1.2 Objectives and Scope of Research 7
1.3 Outline of Thesis 8
CHAPTER 2: REVIEW AND ASSESSMENT OF THE STATE OF THE ART 10
2.1 Introduction 10
2.2 Wharf Configurations 11
2.2.1 Closed Wharves 11
2.2.2 Open Wharves 13
2.3 Wharf Numerical Modeling and Analysis 16
2.3.1 Simplified Analysis 16
2.3.2 Nonlinear Pushover Analysis 18
2.3.3 Nonlinear Dynamic Analysis 20
2.3.4 Selection of the analysis procedure 23
2.4 Wharf-Crane Interaction 26
2.5 Fragility Analysis 30
2.5.1 Fragility Curves 32
CHAPTER 3: TWO DIMENSIONAL PLAIN STRAIN MODELING AND ANALYSIS OF THE PILE SUPPORTED CONTAINER WHARVES 36
3.1 Introduction 36
3.2 Wharf Configuration and Model 38
3.2.1 Deck 40
3.2.2 Piles 41
3.2.3 Batter piles 46
3.2.4 Pile-to-deck connections 50
3.2.5 Soil Properties 53
3.2.6 Soil Springs 54
3.2.7 Damping 56
3.3 Numerical Results 57
3.3.1 Modal Analysis 57
3.3.2 Pushover Analysis 63
3.3.3. Time-History Analysis 67
3.4. Closure 86
CHAPTER 4: DYNAMIC INTERACTION BEHAVIOR OF PILE-SUPPORTED WHARVES AND CONTAINER CRANES 89
4.1 Introduction 89
4.2 Container Cranes 91

4.3 Simplified Crane Models 95
4.3.1 Pinned Based Portal Frame Crane Models 95
4.3.2 Wharf without Crane and Wharf with 5% Additional Mass 95
4.3.3 Wharf with Constant Gravity Loads of the Crane 96
4.4 Time-History Analysis 96
4.4.1 Ground Deformation History 97
4.4.2 Detailed Time-History Response Study of the Wharf with Crane and without Crane 99
4.4.3 Simplified Analytical Study of the Foundation-Wharf-Crane Interaction 104
4.4.4 Detailed Numerical Evaluation of the Effect of Crane's Gravity and lateral Wharf-Crane Interaction on the Lateral Response of the Wharf 110
4.4.5 Response of Wharf-Crane Models to the Bin of Ground Motions 115
4.5. Simplified Relations for Prediction of Cranes' Behavior 121
4.5.1 Yielding of the Portal Frame 122
4.5.2 Uplift 123
4.5.3 Sliding 123
4.5.4 Evaluating Analytical Relations against Numerical Results 124
4.6 Closure 127
CHAPTER 5: THREE DIMENSIONAL MODELING AND ANALYSIS OF THE PILE SUPPORTED CONTAINER WHARF 130
5.1 Introduction 130
5.2 Analytical Modeling 131
5.2.1 Modal Analysis 133
5.2.2 Out-of-Plane Ground Motion Generation 136
5.2.3 Three-Dimensional Response of the Wharf 142
5.3 Simplified Wharf Model 152
5.3.1 Simplifying One Wharf Segment 153
5.3.2 Modeling Lateral Resistance 154
5.3.3 Modeling Torsional Resistance 155
5.3.4 Equivalent Mass 159
5.3.5 Equivalent Damping 160
5.3.6 Validation of the Simplified Model 160
5.4 Boundary Conditions of Wharf Segments 165
5.4.1 Pounding Elements 166
5.4.2. Shear Key 168
5.5 Response Evaluation of the Full Wharf Model Using Simplified Model of the Wharf 172
5.6 Closure 177
CHAPTER 6: PROBABILISTIC SEISMIC DEMAND MODELING AND FRAGILITY ANALYSIS OF THE PILE SUPPORTED CONTAINER WHARF 180
6.1 Introduction 180
6.2 Fragility Analysis Framework 182
6.3 Ground Motion Selection 183
6.4 Probabilistic Seismic Demand Models 186
6.5 Optimal Intensity Measures 189

6.5.1 Criteria for Optimality of Intensity Measures 190
6.5.2 Considered Intensity Measures 193
6.5.3 Efficiency, Proficiency and Practicality Comparisons 195
6.5.4 Sufficiency Comparisons 197
6.6 PSDMs of Wharf Components Using PGV as IM 201
6.6.1 PSDMs from Two-Dimensional Wharf Model 201
6.6.2 PSDMs from Three-Dimensional Wharf Model 204
6.7 Component Limit States 207
6.7.1 Pile-Deck Connections 208
6.7.2 Pile Sections 209
6.7.3 Relative Displacement of the Wharf with Respect to the Landside Rail 211
6.7.4 Shear Keys 211
6.7.5 Collector Trench 212
6.8. Component Fragility Curves 213
6.9 Closure 218
CHAPTER 7: SUMMARY AND CONCLUSIONS, IMPACT, AND FUTURE WORK 221
7.1 Summery and Conclusions 221
7.2 Impact 225
7.3 Future Work 227
REFERENCES 228

LIST OF TABLES

Table 2.1 Acceptable level of damage in performance-based design[a] 24
Table 2.2 Performance grades S, A, B, and C 24
Table 2.3 Performance grade based on the importance category of port structures 25
Table 2.4 Types of analysis related to performance grades 25
Table 3.1 Soil layer properties 54
Table 4.1 Characteristics of the selected ground motions 98
Table 5.1 Natural periods of the first eighteen modes of the wharf and corresponding mass participation factors 136
Table 6.1 Wharf component demand measures 189
Table 6.2 Intensity measures used in the study 195
Table 6.3 Statistics of the estimated parameters of demand models. 202
Table 6.4 Statistics of the estimated parameters of demand models. 206
Table 6.5 Strain limits associated with defined limit states for constitutive materials of pre-stress pile sections 210
Table 6.6 The deformation limits of critical wharf components corresponding to the chosen limit states. 213

LIST OF FIGURES

Figure 1.1Damaged port in Port-au-Prince following the January 12, 2010 earthquake (Photo courtesy of Glenn Rix)..... 4

Figure 1.2 Constitutive structural and geotechnical components of a port..... 6

Figure 2.1 Schematic configuration of (a) sheet pile wall, (b) stiff pile wall, and (c) sheet pile with platform (from PIANC 2001). 12

Figure 2.2 Typical configuration of (a) caisson quay-walls, (b) massive quay-walls, (c) cantilever quay-walls, (d) block quay walls, and (e) cellular block quay-walls (PIANC 2001, OCDI 2002) 13

Figure 2.3 The schematic view of the configuration of (a) large diameter pile-supported wharves and (b) small diameter pile-supported wharves (PIANC 2001, OCDI 2002). 15

Figure 2.4 The configuration of a column supported wharf (PIANC 2001, OCDI 2002) 16

Figure 2.5 Failure modes of a typical pile-supported wharf due to (a) inertial response of the wharf deck, (b) horizontal force from lateral movement of the retaining wall, and (c) the differential horizontal deformation of the loose sand with respect to the firm layer of soil. 19

Figure 2.6 Container crane boundary condition with wheel/rail interaction in (a) side view and (b) front view. 26

Figure 2.7 The coupled elastic and nonlinear uplift response of a typical container crane (Kosbab 2010). 27

Figure 2.8 The damage to the crane under (a) relative horizontal displacement of the crane rails and (b) differential settlement of the crane rails (PIANC 2001). 29

Figure 3.1 Configuration of the wharf and landside crane rail. 40

Figure 3.2 Section geometry and reinforcement details for 18” and 16” square piles. 42

Figure 3.3 Discretization of pile sections in radial and circumferential directions to be used as fiber cross-sections in the FE analysis..... 43

Figure 3.4 Configuration the batter piles (a) geometry and reinforcing detail and (b) numerical FE model..... 50

Figure 3.5 Typical configurations of common pile-deck connections: (a) embedded dowel with outward bent bars, (b) embedded dowel with T-headed bars, (c) extended pile, and (d) extended strand. 51

Figure 3.6 Section geometry and reinforcement details of the tested pre-stressed pile (based on Lehman et al. 2009). 52

Figure 3.7 The calibration results of the pile-deck connection: (a) shear force versus drift response and (b) moment versus drift response. 53

Figure 3.8 Schematic showing components of the nonlinear macroelement (modified from Varun 2010)..... 55

Figure 3.9 The first five mode-shapes of the wharf and landside crane rail with associated natural periods and damping ratios..... 61

Figure 3.10 Force-deformation response of (a) wharf and landside rail and (b) individual piles..... 64

Figure 3.11 Profile of curvature demand with the location of the yielded pile sections and pile-deck connections. 66

Figure 3.12 Final deformed shape of the wharf with the location of plastic hinges.66

Figure 3.13 Characteristics of the selected ground motions NGA0753 and NGA1057 at bedrock: (a) accelerograms NGA0753, (b) accelerograms NGA1057, and (c) PSD of NGA0753 and NGA1057..... 69

Figure 3.14 Contours of free field site soil response in the vicinity of the wharf deck: (a) maximum PWP ratio for NGA0753, (b) final soil displacement for NGA0753, (c) maximum PWP ratio for NGA1057, and (d) final soil displacement for NGA1057. 70

Figure 3.15 Horizontal soil displacement at node C1 (Figure 3.1) for NGA0753 and NGA1057. 71

Figure 3.16 Displacement time-histories of node C2 and C3: (a) horizontal displacement for NGA0753, (b) horizontal displacement for NGA1057, (c) vertical displacement for NGA0753, and (d) vertical displacement for NGA1057. 74

Figure 3.17 Acceleration time-histories of node C2 and C3: (a) horizontal acceleration for NGA0753, (b) vertical acceleration for NGA0753, (c) horizontal acceleration for NGA1057, and (d) vertical acceleration for NGA1057. 75

Figure 3.18 Pile H connection response to NGA0753: (a) time-history of connection rotation, (b) time-history of connection moment, and (c) moment-rotation behavior of the connection. 76

Figure 3.19 Pile H connection response to NGA1057: (a) time-history of connection rotation, (b) time-history of connection moment, and (c) moment-rotation behavior of the connection. 77

Figure 3.20 Wharf and crane rail response during NGA0753: (a) profile of the maximum curvature ductility demand and (b) final deformed shape of the wharf with the location of plastic hinges. 80

Figure 3.21 Wharf and crane rail response during NGA1057: (a) profile of the maximum curvature ductility demand and (b) final deformed shape of the wharf with the location of plastic hinges. 81

Figure 3.22 Force-deformation response of the macroelement in four depths along pile D (Figure 3.1) together with the time-histories of excess pore water pressure ratio and deformation of the macroelement during NGA0753. 84

Figure 3.23 Force-deformation response of the macroelement in four depths along pile D (Figure 3.1) together with the time-histories of excess pore water pressure ratio and deformation of the macroelement during NGA1057. 85

Figure 4.1 Typical container crane, Swanston dock container crane, Melbourne, Australia (photo courtesy of http://marineshiping.blogspot.com). 91

Figure 4.2 Configuration of J100 container crane. 92

Figure 4.3 Container crane boundary condition with wheel/rail interaction 93

Figure 4.4 Idealized portal frame crane model, illustrating removal of constraint during uplift achieved by use of frictional contact elements 94

Figure 4.5 Combined model of the wharf and container crane..... 97

Figure 4.6 Lateral displacement of the wharf with and without crane for a) landside crane rail and b) seaside crane rail 100

Figure 4.7 Differential settlement of the crane rails 101

Figure 4.8 The uplift response of a) landside crane leg and b) seaside crane leg.. 102

Figure 4.9 Sliding response of a) landside crane leg and b) seaside crane leg 103

Figure 4.10 The lateral drift response of a) landside crane leg and b) seaside crane leg..... 104

Figure 4.11 Simplified lumped mass representation of foundation-wharf-crane system. 105

Figure 4.12 The ratio of dynamic amplification factors γ as a function of α (natural frequency ratio) and β (ground frequency ratio) a) three dimensional view and b) two dimensional contour view 108

Figure 4.13 Response of the soil along pile G for NGA1086, a) the lateral displacement response of the nodes, b-g) the oscillating component of the horizontal displacement of the nodes, and h) the frequency content of the oscillating displacement response of the nodes. 110

Figure 4.14 Vertical displacement response of different wharf-crane representations at (a) landside crane rail and (b) seaside crane rail 112

Figure 4.15 Lateral displacement response of different wharf-crane representations (a) total displacement response at landside crane rail, (b) total displacement response at seaside crane rail, (c) average displacement response at landside crane rail, (d) average displacement response at seaside crane rail, (e) oscillating displacement response at landside crane rail, (f) oscillating displacement response at seaside crane rail 115

Figure 4.16 The ratio of the maximum horizontal displacement of the wharf with simplified crane models to the maximum horizontal displacement of the wharf with full crane model for a) horizontal displacement of the seaside rail and b) relative horizontal displacement of the crane rails 117

Figure 4.17 The ratio of the maximum vertical displacement of the wharf with simplified crane models to the maximum vertical displacement of the wharf with

full crane model for a) vertical displacement of the seaside rail and b) relative vertical displacement of the crane rails..... 118

Figure 4.18 The ratio of the maximum curvature response of the wharf with simplified crane models to the maximum curvature response of the wharf with full crane model for a) pile sections and b) pile-deck connections. 120

Figure 4.19 The maximum drift response of a) landside crane rail and b) seaside crane rail..... 121

Figure 4.20 The spectral acceleration response of the motion at a) landside and b) seaside crane rails 125

Figure 4.21 The drift response of the portal frame versus a) PSA of the landside rail and b) PSA of seaside rail..... 127

Figure 5.1 The process of generating the three-dimensional model of the wharf segment from the two-dimensional model of the wharf. 133

Figure 5.2 Mode shapes of the three-dimensional wharf model for a) first, b) second, c) third, d) forth, e) fifth, and f) sixth mode..... 134

Figure 5.3 Mode shapes of the three-dimensional wharf model for a) ninth, b) eleventh and c) thirteenth mode. 135

Figure 5.4 The acceleration time-history of NGA0810 in a) transverse and b) longitudinal directions. 137

Figure 5.5 Acceleration response spectrum of NGA0810 in a) transverse and b) longitudinal directions. 138

Figure 5.6 Transfer function from X to Z. 138

Figure 5.7 Components of the transverse soil response on top of pile K: a) total and permanent displacements, b) oscillating displacement, and c) PSD of permanent and oscillating responses. 140

Figure 5.8 Spectral acceleration of a) oscillating component of the soil displacement at top of pile K during NGA0810 and b) the corresponding response in the longitudinal direction. 141

Figure 5.9 The longitudinal displacement of the embankment soil at top of pile K during NGA0810. 141

Figure 5.10 Schematic view of the wharf 143

Figure 5.11 Displacement responses of the three-dimensional and two-dimensional wharf models: a) transverse displacement at the seaside rail, b) transverse displacement at the landside rail, c) longitudinal displacement at the seaside rail, and d) longitudinal displacement at the landside rail..... 144

Figure 5.12 Longitudinal displacement response of the landside and seaside rails. 145

Figure 5.13 Acceleration responses of the three-dimensional and two-dimensional wharf models: a) transverse acceleration at the seaside rail, b) transverse

acceleration at the landside rail, c) longitudinal acceleration at the seaside rail, and d) longitudinal acceleration at the landside rail. 146

Figure 5.14 Longitudinal acceleration response of the landside and seaside rails. 147

Figure 5.15 Pile H connection response to NGA0810 in the transverse direction: (a) time-history of connection rotation, (b) time-history of connection moment, and (c) moment-rotation behavior of the connection. 148

Figure 5.16 Pile H connection response to NGA0810 in the longitudinal direction: (a) time-history of connection rotation, (b) time-history of connection moment, and (c) moment-rotation behavior of the connection. 149

Figure 5.17 Profile of the maximum curvature ductility demand of the wharf and landside crane rail during NGA0810. 150

Figure 5.18 Final deformed shape of the wharf and landside crane rail during NGA0810. 151

Figure 5.19 The configuration of the simplified model 154

Figure 5.20 Pushover model configuration (left) and pushover results for different piles 156

Figure 5.21 The plan view of a typical wharf segment with piles replaced with nonlinear springs (assuming that *n* in an odd number) 157

Figure 5.22 Fitted lateral force-deformation curve for piles in row C (Figure 5.21) 158

Figure 5.23 (a) Individual moment-rotation curves of the piles in row C and (b) equivalent rotational spring moment-rotation curve for the corresponding row of piles. 159

Figure 5.24 Mode shapes of the three-dimensional simplified wharf model for a) first, b) second, c) third, d) forth, and e) fifth mode. 162

Figure 5.25 Displacement response of the full and simplified wharf models at Node C in a) transverse, b) vertical, and c) longitudinal directions during NGA0451 and the displacement response of the full and simplified wharf models at Node C in d) transverse, e) vertical, and f) longitudinal directions during NGA0810..... 164

Figure 5.26 Displacement response of the full and simplified wharf models at Node D in a) transverse, b) vertical, and c) longitudinal directions during NGA0451 and the displacement response of the full and simplified wharf models at Node D in d) transverse, e) vertical, and f) longitudinal directions during NGA0810..... 165

Figure 5.27 Schematic view of two wharf segments and the boundary conditions between the segments. 166

Figure 5.28 Model of the impact element 167

Figure 5.29 Schematic configuration of a shear key..... 168

Figure 5.30 Applied and resisting force mechanism in a typical shear key (Priestley et al., 1996) 169

Figure 5.31 Nonlinear model of the shear key. 172

Figure 5.32 Simplified response evaluation procedure 174

Figure 5.33 Curvature response of the pile section with the largest maximum curvature in a) full wharf mode and b) simplified model of the wharf during NGA0451. 176

Figure 5.34 Curvature response of the pile section with the largest maximum curvature in a) full wharf mode and b) simplified model of the wharf during NGA0810. 176

Figure 6.1 Median spectral acceleration response of the bins in the horizontal direction from a) earthquake records and b) attenuation law. 185

Figure 6.2 Median spectral acceleration response of the bins in the vertical direction from a) earthquake records and b) attenuation law. 185

Figure 6.3 Bilinear model for PSDA. 188

Figure 6.4 Appropriateness of different IMs in terms of a) practicality, b) efficiency, c) proficiency, and d) R^2. 196

Figure 6.5 Sufficiency of different IMs with respect to a) moment magnitude and b) closest distance to rupture. 199

Figure 6.6 Sufficiency of PGV with respect to M for a) pile sections, b) pile-deck connections, and c) relative movement of the wharf with respect to the landside crane rail 200

Figure 6.7 Sufficiency of PGV with respect to R for a) pile sections, b) pile-deck connections, and c) relative movement of the wharf with respect to the landside crane rail 201

Figure 6.8 Probabilistic seismic demand models for (a) pile-deck connections, (b) pile sections, and (c) relative movement of the wharf with respect to the landside crane rail 203

Figure 6.9. Distribution of the error ln(ε) for (a) individual zones of IM and (b) the entire range of IM. 204

Figure 6.10 Probabilistic seismic demand models for (a) pile-deck connections, (b) pile sections, (c) relative movement of the wharf with respect to the landside crane rail, (d) shear keys, and (e) collector trenches. 207

Figure 6.11 Damage to pile-deck connections at a) slight, b) moderate, and c) severe damage states (Lehman et al., 2009) 209

Figure 6.12 Moment curvature curves of different sections of the piles and the median limit states. 211

Figure 6.13 Crane Rail and Collector Trench (Photographs courtesy of Bill Cooke of Manson Construction Co., Richmond CA.) 213

Figure 6.14 Seismic fragility curves for (a) pile sections, (b) pile-deck connections, and (c) relative movement of the wharf with respect to the landside crane rail (solid

lines are the fragility estimates and the dashed lines are the corresponding 90% confidence bounds). 216

Figure 6.15 Seismic fragility curves for (a) pile sections, (b) pile-deck connections, (c) relative movement of the wharf with respect to the landside crane rail, (d) shear keys, and (e) collector trenches (solid lines are the fragility estimates and the dashed lines are the corresponding 90% confidence bounds)..... 218

SUMMARY

Serving as critical gateways for international trade, seaports are pivotal elements in transportation networks. Any disruption in the activities of port infrastructures may lead to significant losses from secondary economic effects, and can hamper the response and recovery efforts following a natural disaster. Particularly poignant examples which revealed the significance of port operations were the 1995 Kobe earthquake and 2010 Haiti earthquake in which liquefaction and lateral spreading of embankments imposed severe damage to both structural and non-structural components of ports systems.

Since container wharf structures are responsible for loading and unloading of cargo, it is essential to understand the performance of these structures during earthquakes. Although previous studies have provided insight into some aspects of the seismic response of wharves, limitations in the modeling of wharf structures and the surrounding soil media have constrained the understanding of various features of the wharf response. This research provides new insights into the seismic behavior of wharves by using new and advanced structure and soil modeling procedures to carry out two and three-dimensional seismic analyses of a pile-supported marginal wharf structures in liquefiable soils. Furthermore, this research investigates the interactions between cranes and wharves and closely assesses the role of wharf-crane interaction on the response of each of these systems. For this purpose, the specific effect of wharf-crane interaction is studied by incorporating advanced models of the crane with sliding/uplift base conditions. To reduce the computational time required for three-dimensional nonlinear dynamic analysis of the wharf in

order to be applicable for probabilistic seismic demand analysis, a simplified wharf model and an analysis technique are introduced and verified. In the next step probabilistic seismic demand models (PSDMs) are generated by imposing the wharf models to a suit of ground deformations of the soil embankment and pore water pressure generated for this study through free-field analysis. Convolving PSDMs and the limit states, a set of fragility curves are developed for critical wharf components whose damage induces a disruption in the normal operation of ports. The developed fragility curves provide decision makers with essential tools for maximizing investment in wharf retrofit and fill a major gap in seismic risk assessment of seaports which can be used to assess the regional impact of the damage to wharves during a natural hazard event.

CHAPTER 1

INTRODUCTION

1.1 Problem Description

Water transport has come a long way since ancient civilizations used it as a mean for traveling and acquiring food. Although with the emergence of commercial aviation, the significance of sea travel has decreased in modern times, water transportation still remains the largest carrier of freight in the world. The large demand for water transport is partially due to the continuously increasing rate of international trade. With the introduction of containerization in the 1960s, cargo is handled in a standard form in all stages of transportation enabling the flow of cargo to increase and the cost of shipping to decrease (Stopford 2003). One of the immediate consequences of containerization was the deployment of huge containerships which consequently required large ports and port facilities. The continuous increase in the size and number of seaports, particularly in industrialized countries whose economies rely on the export and import of merchandise, has led to an increasing dependence on seaports as a means for global trade.

Seaports have an important role in the development of regional and global economies. Statistical data provided by the Bureau of Economic Analysis (BEA) has shown that in 2006, the top 13 port metropolitan areas were responsible for 32% of United States Gross Domestic Product (GDP) (BEA, 2008). Also from a national perspective, the effect of seaports has been shown to be considerable on the US economy. In 2007, seaport activities contributed 3.2 trillion dollars and created more than 212 billion dollars in tax revenues (Nagle, 2009 a,b). Waterborne trades

(foreign and domestic) amounted to 2.3 billion metric tons among which more than 99% of overseas cargoes were handled by seaports. Furthermore, seaport activities are responsible for approximately 13.3 million domestic jobs – 9% of all jobs in the United States (Nagle, 2009 a,b). Because of their important role, seaport stakeholders in the US have invested more than 2.5 billion dollars annually to maintain and enhance their infrastructure in recent years (Nagle, 2009 b). Other economical aspects of seaport activities are highlighted below (U.S. Maritime Administration, 2009).

- In 2007, water transportation ranked second among modes of transportation in energy efficiency (energy costs per dollar of gross output).

- For the period 2002-2007, the value of water transportation fixed assets increased by 35 percent, the highest 5-year growth in 25 years.

- For the period 2002-2007, value-added (gross output less the cost of intermediate inputs) for water transportation increased by 53 percent despite a 145 percent increase in the cost of energy inputs.

- Over the last 5 years, 25,800 jobs were added in water transportation and related industries.

Serving as critical gateways for international trade, seaports are pivotal elements in transportation networks. Any disruption in the activities of port infrastructures may lead to significant losses from secondary economic effects in addition to direct losses associated with physical port damage. The cost of closure of a major port for

a month is estimated to incur a loss of 4.5 billion dollars based on the estimation provided by Congressional budget office (Kruse, 2009); and 60 billion dollars according to an estimate provided by the US Coast Guard (Kruse, 2009).

A recent example of economic impacts of seaport activities interruption is the port of Kobe after 1995 Great Hanshin (Kobe) earthquake. During the seismic event, liquefaction and lateral ground displacement occurred which resulted in the damage of all container berths. The total damage to the port was estimated to be 10 billion dollars and it took over two years to repair (Japan Ministry of Transportation, 1996). Accounting for the impact of port operations and related industries on the regional economy, the secondary loss as a consequence of the Kobe earthquake was estimated to be $4 billion for the 9 months following the earthquake, primarily from the loss of income of 40,000 people and increased transportation costs (Chang, 2000). In addition to direct economical losses, the interruption in port operations forced container ship owners to redirect their transportation flow to other available ports. This had a dramatic impact on the rank of the port of Kobe wherein its rank fell from 6 in 1995 before the earthquake to 38 in the aftermath (Rix et al., 2009).

The January 12, 2010 earthquake in Haiti highlighted the importance of seaports in the immediate response following a natural disaster. During the earthquake, three large wharves, two in the port of Port-au-Prince and one in Carrefour suffered considerable damages. The wharf frontage of the main wharf in Port-au-Prince completely collapsed throwing one crane into the water. The second long finger pier of Port-au-Prince lost 40 percent to 50 percent of its total length. In Carrefour, an earth spit connecting a large dock to the shore disappeared after the earthquake.

One of the major causes of failures in Haitian port facilities was assessed to be liquefaction, however structural damages contributing to the failure are hard to assess due to the disappearance of the wharf into the water. As a result of these damages, the delivery of international aid services was severely limited by the inability to transport aid supplies including medical supplies and food, through the port. Although the Haitian airport was operational in the aftermath of the earthquake, it could not serve as efficiently as a seaport in transporting large, massive volumes of goods and supplies and consequently it was overwhelmed quickly. This signifies the sea transport as the most efficient transportation mode especially when large amount of materials are to be transported.

Figure 1.1Damaged port in Port-au-Prince following the January 12, 2010 earthquake (Photo courtesy of Glenn Rix).

A large number of US seaports including ports of Los Angeles, Long Beach, Seattle, Oakland, Charleston, and Savannah are located in moderate to high seismic

hazard zones. Considering the importance of seaports on the economy of the US, it is necessary to provide a better insight on the performance of these structures during seismic events. In a general view, ports are complex systems which are composed of interactive subsystems, as shown in Figure 1.2. The normal operation of ports relies on the proper performance of each of the constitutive components. Following the general trend in any system, disruption in the normal operation of port components may cause the system to cease operating or to diminish the operating capabilities. In port infrastructure systems, wharves are one of the most critical elements to which the operation of the system and its constitutive components such as cranes are highly dependent. In addition, the excessive response of wharves in a number of response measures including relative lateral displacement of crane rails, spectral acceleration response of the deck, and differential settlement of the wharf may cause severe damage in cranes such as derailment and/or overturning of the crane.

The dynamic response of wharves during seismic events is quite complex, particularly when liquefaction and lateral spreading of the surrounding embankment soil further complicate the sophisticated soil-foundation interaction phenomenon. Furthermore, the nonlinear wharf-foundation interaction through pile-deck connections and the interaction of the wharf with sliding/uplift capable huge container cranes mounted on top of the deck are a quite complex phenomena. The schematic view of a typical pile supported wharf with a container crane mounted on top is shown in Figure 1.2.

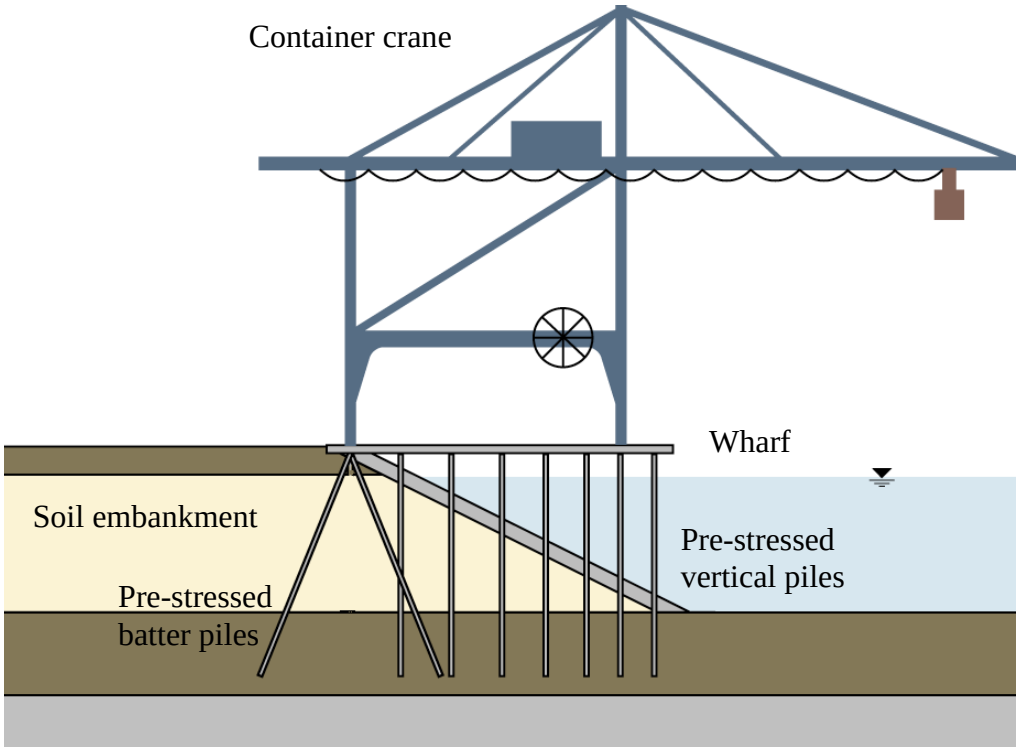

Figure 1.2 Constitutive structural and geotechnical components of a port.

Considering the important role of wharves in port systems and the extent of damage they suffered in historical cases of wharf damage, it is quite necessary to thoroughly understand the behavior of wharves during seismic events and assess their seismic vulnerability in a general reliable framework. This can provide engineers and decision makers with reliable tools to decide whether the vulnerability of a wharf in its current configuration is acceptable and what constitutive components of the wharf are the most critical ones in terms of their importance to wharf performance and the level of damage they are expected to face during an expected seismic hazard scenario.

Evaluation of the seismic risk at a port requires a thorough assessment of the vulnerability of a wharf, which can be most effectively done through the use of fragility curves. Using the information on the demand and capacity of the systems,

fragility curves provide the probability that the structure under consideration will fail to satisfy a performance limit or a set of limits at a given intensity measure of earthquake disturbance. In this study, analytical fragility curves for typical pile supported wharves on the west coast of the United States are developed using nonlinear time-history analysis on detailed foundation-wharf models for various seismic hazard scenarios.

1.2 Objectives and Scope of Research

This study aims to provide detailed understanding of the overall seismic performance of pile supported wharves for various seismic hazard scenarios by incorporating realistic representation of the constitutive components. The final objective of this research is to develop a systematic approach for seismic vulnerability assessment of wharf structures in liquefiable soil embankments and provide the first set of fragility curves for the typical class of pile supported wharves located on the west coast of the United States. The outcome of this research supports risk mitigation efforts for port systems for which insights on the seismic vulnerability of wharves is essential. In order to achieve these goals, enhanced numerical wharf models are generated followed by the generation of fragility curves.

The associated research tasks that will be accomplished as part of this research are as follows:

1. Generating two and three dimensional nonlinear finite element models of wharves using realistic representation of various wharf components.

2. Characterizing the dynamic interaction between wharves and container cranes and providing analytical relations to predict the nonlinear stages of the crane response.
3. Generating probabilistic seismic demand models (PSDMs) for the wharf components.
4. Exploring the impact of using various earthquake intensity measures on the PSDMs.
5. Identifying appropriate capacities and limit states for the components of the wharf.
6. Producing a set of fragility curves of the wharf using two and three-dimensional wharf models.

1.3 Outline of Thesis

This thesis is composed of seven chapters with the following content:

Chapter II provides a literature review in various fields pertinent to modeling and seismic response assessment of wharves.

Chapter III presents detailed two-dimensional analytical modeling of a typical pile-supported wharf located on the west coast of the United States.

Chapter IV studies the interaction of the wharf and various representations of a jumbo container crane in liquefiable embankment soils.

Chapter V presents detailed and simplified three-dimensional numerical modeling of wharves.

Chapter VI evaluates the seismic demand of two and three-dimensional wharf models and presents the results of fragility analyses.

Chapter VII summarizes the research, provides a set of general conclusions drawn from the outcomes of the research, and outlines future research needs.

CHAPTER 2

REVIEW AND ASSESSMENT OF THE STATE OF THE ART

2.1 Introduction

Following recent earthquake events in coastal areas, it was found that both direct and secondary economic losses in the affected region are largely dependant on the damage to seaports. This is in large part due to the significant role of seaports as gates for a large transfer of a variety of merchandise both on the national and international level. However the experience form past earthquakes revealed the high vulnerability of port infrastructures to damage during moderate to large seismic hazard events. This, together with the high seismicity of the location of many seaports in the west and east coast of the United States motivated a number of investigators to better understand the complex nonlinear dynamic nature of port infrastructure systems and its constitutive subsystems during seismic events. In a general framework, the outcome of these studies will help to quantify the potential social and economic losses of communities across the nation. Wharf fragility curves thus have gained attention as they are an essential component to the risk assessment methodology of seaport infrastructure systems.

This chapter first reviews different wharf configurations built in practice and provides a brief understanding of their seismic response. Then, the analysis procedures commonly used for response evaluation of wharves are presented and their merits and shortcomings are discussed. The chapter continues with an introduction to container cranes and their interaction with the wharf which is followed by reviewing the limited literature available on that subject.

2.2 Wharf Configurations

Due to geographical, economical, and functional considerations, different types of wharf configurations have been designed and constructed. One of the important factors that affects the choice of the most economical wharf structure type is the sub-surface soil conditions. Considering this factor, wharf structures are classified into two major categories: *open type* in which the wharf allows water to run below the deck and otherwise *closed type* (Gaythwaite 2005). Closed type wharves are the common construction type where the depth to firm soil is shallow as well as the depth of water which results in a limited wave action against the wharf. These conditions can be found in rivers, and shallow depth shorelines.

2.2.1 Closed Wharves

In closed type wharves, a vertical and commonly concrete wall separates the seawater or river from the shore. Behind the wall is filled with soil and covered with concrete on top forming the deck for required port operations. Based on the configuration of the wall, closed wharves are categorized into pile walls and gravity walls.

2.2.1.1 Pile Walls

Pile walls refers to a type of closed wharves in which a row of large diameter stiff piles driven into the soil provides lateral and vertical resistance against the horizontal soil pressure from the backfill and the vertical and horizontal loads from the deck as a result of gravity, seismic, or operational loads. The redundancy in these types of structural systems is low (Werner, 1998) and the stability of the system to a large degree relies on the performance of the anchorages that ties the

pile walls deep in the soil on the shore. In practice, pile walls have been constructed in three main types including sheet pile wall, stiff pile wall, and sheet pile with platform. These three variations are shown in Figure 2.1.

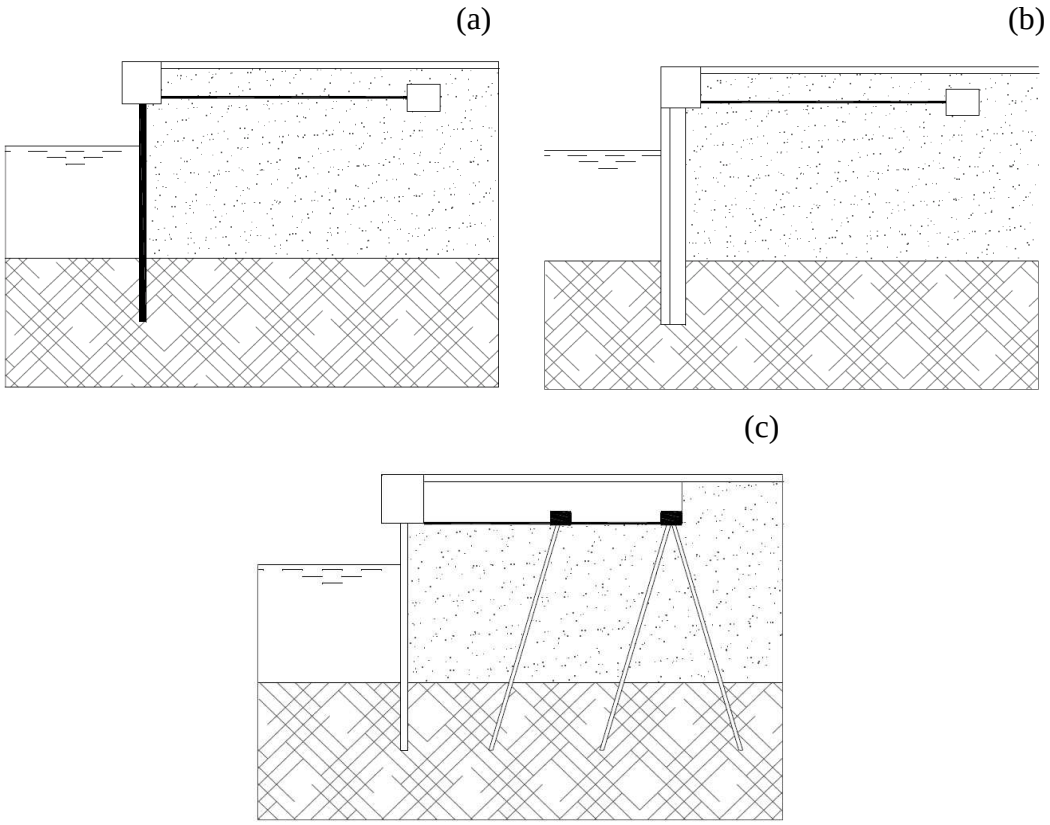

Figure 2.1 Schematic configuration of (a) sheet pile wall, (b) stiff pile wall, and (c) sheet pile with platform (from PIANC 2001).

2.2.1.2 Gravity Walls

Compared to pile walls, gravity walls are massive resisting systems that withstand the lateral induced loads from the backfill and the deck and consequently the resulting overturning moments in the horizontal in-plane direction by stabilizing moments from their huge weight. In large seismic events, the large pressure of the embankment may result in excessive seaward displacement of the wharf but on the other hand loosening of the underneath soil may cause tilting or large vertical settlement of the wharf. OCDI (2002), PIANC (2001), and Werner (1998) classify

gravity walls into Caisson Quay-wall, Massive Quay-Wall, Cantilever Quay-wall, Block Quay-wall, and Cellular Block Quay-wall. Schematic configurations of these wharves are shown in Figure 2.2.

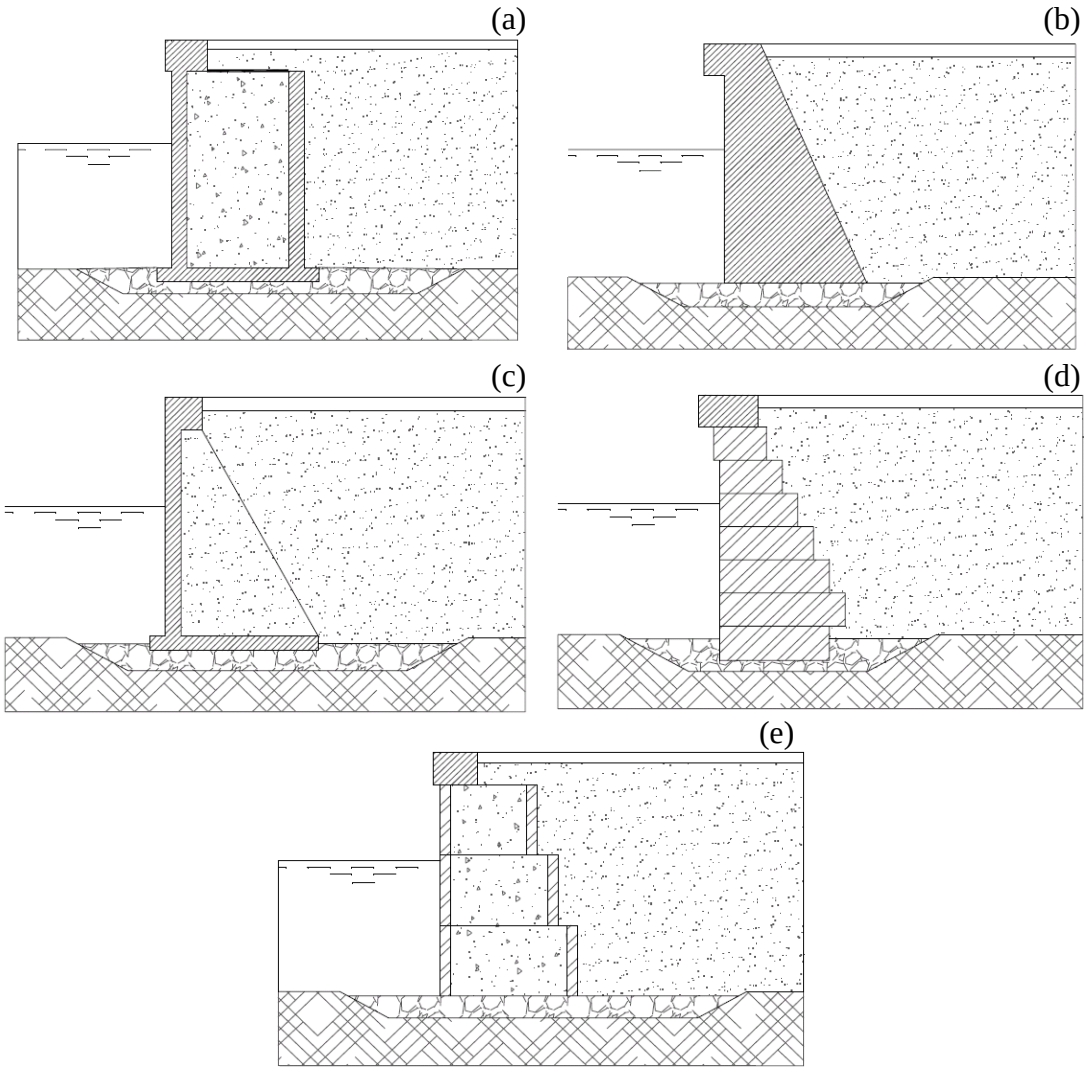

Figure 2.2 Typical configuration of (a) caisson quay-walls, (b) massive quay-walls, (c) cantilever quay-walls, (d) block quay walls, and (e) cellular block quay-walls (PIANC 2001, OCDI 2002)

2.2.2 Open Wharves

As mentioned before, the open type wharves allow the sea or river water to run below the deck. Open type wharves are mainly classified into large diameter pile

supported wharves, small diameter pile supported wharves, and column supported wharves.

A typical configuration of a large diameter pile supported wharf is shown in Figure 2.3a. These structures consist of a reinforced or pre-stress concrete deck supported by a group of large diameter – 1 to 2 m. The group of piles in the land-sea direction called transverse direction is repeated in the perpendicular direction in the plane of the deck which is called the lateral direction. The free length of the piles in the transverse direction differs by going from the landside to the seaside and consequently the center of rigidity does not coincide with the center of mass in the lateral direction. This introduces a torsional mode to the three dimensional response of the wharf. The lateral resistance provided by each pile depends on the structural properties of the piles, embedded length of the piles, and soil-pile interaction properties. Different types of piles are used for pile supported wharves including pre-stressed concrete cylinder piles, cast in-drilled holes concrete piles, steel H-shaped piles, and steel pipe piles. The deck in pile-supported wharves is usually cast-in-place reinforced concrete; however cast-in-place concrete beam and slab structure, long span concrete box girder deck system, pre-stressed pre-cast concrete panel, and pre-cast reinforced concrete panel are also used in practice.

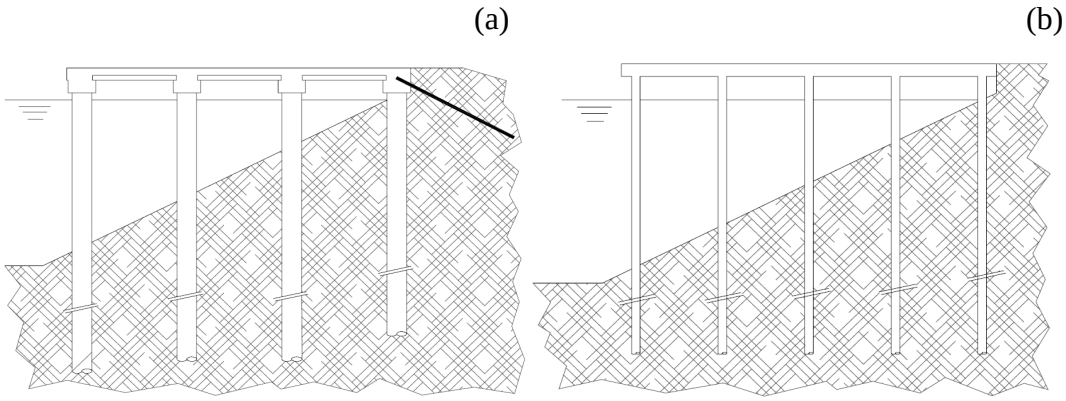

Figure 2.3 The schematic view of the configuration of (a) large diameter pile-supported wharves and (b) small diameter pile-supported wharves (PIANC 2001, OCDI 2002).

The other type of open wharves is the small diameter pile supported wharf shown in Figure 2.3b. These structures are similar to large diameter pile supported wharves but as can be inferred from their name, the diameter of the piles is smaller. The same concept for the structural and geotechnical behavior of the large diameter pile supported wharves are valid for this class of wharves. These types of wharves are one of the most popular configurations for wharves which are being used for various applications as container wharves to cruise liners.

In case the sea or river bed at the location of the piles is rock or stiff granular material, the open type wharf is called a column supported wharf which is shown in Figure 2.4.

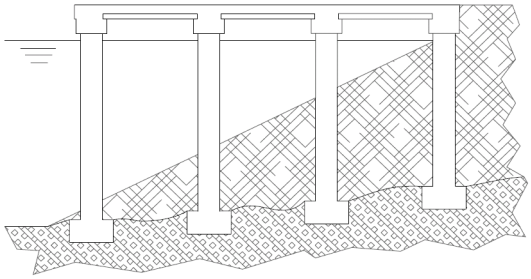

Figure 2.4 The configuration of a column supported wharf (PIANC 2001, OCDI 2002)

2.3 Wharf Numerical Modeling and Analysis

Wharves are quite complex geotechnical and structural systems and as a consequence their performance evaluation is a challenging task. There have been a number of methods to assess the seismic performance of wharves during earthquakes; each one is based on some simplifying assumptions. The choice of the method to analyze the behavior of the wharves depends on the level of detail and accuracy required for the performance assessment and the extent of available information as well as the capability of the numerical tools. These methods range from simplified analysis, to nonlinear static pushover method and nonlinear time-history analysis.

2.3.1 Simplified Analysis

In this approach simplified procedures are adopted to represent both the structural/geotechnical system and the input disturbance on the system. Due to the difference in the configuration of closed and open type wharves, the physics of their response and consequently the appropriate simplification procedures are different.

Closed type wharves such as gravity and sheet pile quay-walls are modeled by rigid blocks. In case the site is susceptible to liquefy, the effect of liquefaction needs to

be considered. The potential earthquake is represented in terms of the peak ground acceleration with local site effects included. Having the rigid model of the wharf, the driving inertial force, the resisting gravity load, and the soil pressure, the simplified analysis can estimate the limit of the threshold level, the limit of the elastic response and very approximate deformation response of the wharf using the conventional force-balance approach.

Due to the flexibility of the open type wharves in the lateral direction and the concentration of the mass at the deck level, open wharves can be approximately represented by a single degree of freedom (SDF) system. The natural frequency and the damping ratio of the SDF system is found for the system of the wharf and surrounding soil for the dominant lateral mode. The mass of the SDF system is the mass of the deck with a portion of the live load. Consequently the effective stiffness of the system in the lateral direction is found form the effective mass and the dominant period. The post-yield behavior of the wharf frame can be represented in this model by introducing the ductility factor. Having the simplified model of the wharf, the response of the system is approximately calculated using the response spectrum method. The shape of the spectrum can be found using either site response quantities provided in hazard maps or spectral analysis of empirical or simulated ground motions for the region under study. Since the procedure only accounts for the inertial response of the wharf, the kinematic response of the wharf to embankment deformations is neglected.

Smith-Padro and Firat (2008) studied the implications of representing the lateral stiffness of the embankment soil by means of constant points of fixity for the piles.

This was done by comparing the result of the nonlinear pushover analysis of the wharf with soil effects represented by soil springs and the model of the wharf in which the effect of soil stiffness on the lateral response of wharves has been taken into account by estimating the locations at which the piles are assumed to be fully restrained against rotation. The results of the pushover analysis of the two wharf models showed that the simplified method overestimates the lateral displacement demand by only 20 percent. In another study, Thach and Yang (2009) investigated the application of the multi-mode spectral method (MSM) for estimating the target displacement of pile-supported wharves under seismic loading. Performing a statistical analysis on the response of the wharf found from MSM, simplified relations are derived for the displacement amplification factor as a function of eccentricity to the longitudinal length of wharf segment.

2.3.2 Nonlinear Pushover Analysis

Although the simplified analysis can roughly account for the nonlinear behavior of wharves by introducing the ductility parameter, the efficiency of response modification factors is under question. A more appropriate understanding of the initial elastic and post-yield response behavior of wharves can be derived using nonlinear pushover analysis. The degree of the accuracy of the results relies on the proper representation of the wharf components. For open type wharves where the mass and consequently the induced seismic inertial force is concentrated in the deck, the pushover load is simply a horizontal load applied at the center of the wharf mass at the deck level. Increasing the pushover load stepwise, the deformation response as well as the induced element forces of the constitutive wharf components are

found in each step. Comparing the deformation/force response of the critical wharf components with the corresponding capacities, the vulnerability of wharf components are identified in the path to failure. In pile-supported wharves, the failure occurs when the successive formation of plastic hinges on the top of the piles and in a close distance from the surface of the embankment slope leads to the occurrence of a collapse mechanism. The failure modes of a typical pile supported wharf are shown in Figure 2.5a-c.

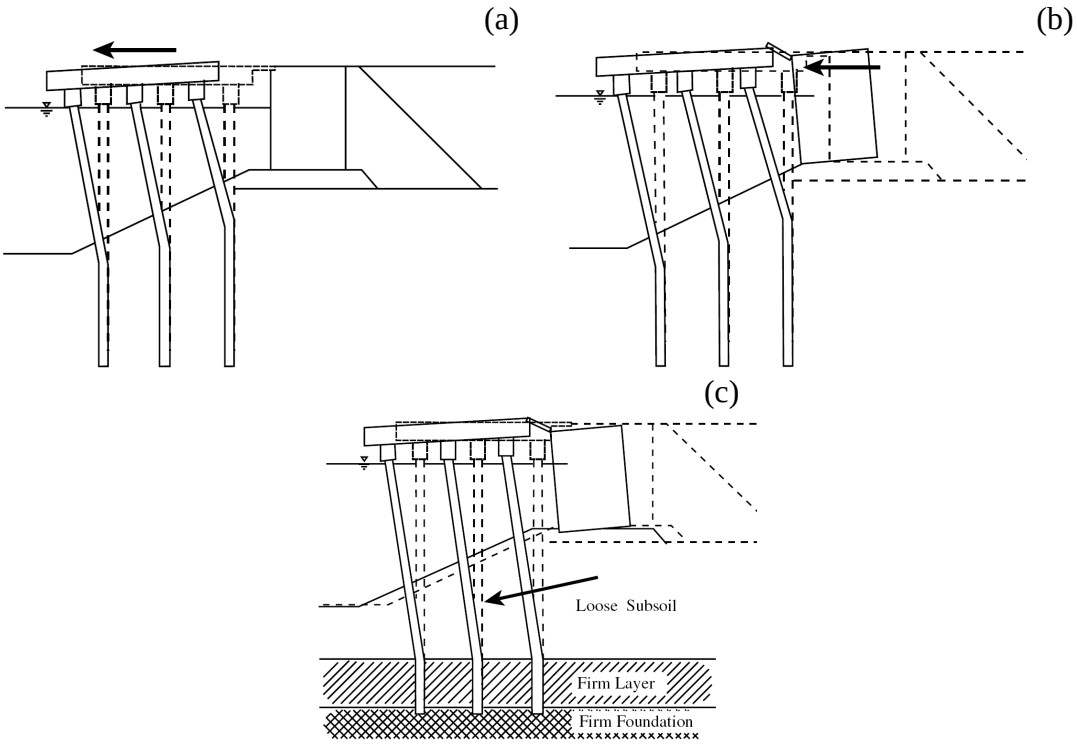

Figure 2.5 Failure modes of a typical pile-supported wharf due to (a) inertial response of the wharf deck, (b) horizontal force from lateral movement of the retaining wall, and (c) the differential horizontal deformation of the loose sand with respect to the firm layer of soil.

One of the drawbacks of this procedure is its inability to consider the effect of the permanent soil deformation on the total response of the wharf. In addition, although the pushover technique can properly account for the nonlinear force-deformation characteristics of different wharf components including piles and pile-deck

connections, it cannot include the dynamic effects of soil-structure interaction and permanent soil deformations. Moreover, the standard pushover technique studies the performance of the wharf under the first mode of the structure in the initial elastic state. However, as the wharf enters the nonlinear realm, the mode shape of the structure associated with the dominant mode changes; a factor which is not accounted for in the pushover method. The level of the introduced approximation for using the initial dominant load pattern increases as the nonlinearity in the structure increases.

2.3.3 Nonlinear Dynamic Analysis

The most advanced and accurate method for seismic response evaluation of wharf systems is nonlinear dynamic analysis. In contrary to the pushover technique, time-history analysis has the capability to consider the effect of soil-structure interaction on the response of the wharf properly. In addition, the dynamic analysis considers the contribution of all modes in the total response of the wharf. This can have a significant effect on the wharf response especially for three dimensional models where the torsional models may have a major contribution in the total response of the system. This type of analysis is common for both closed type wharves and open type wharves with difference stemming from the difference in soil-structure interaction surfaces. Two common numerical simulation techniques for dynamic response evaluation of wharves are Finite Element (FE) and Finite Difference (FD) methods both of them are being used in available software packages. The level of detail in numerical modeling of the wharf (e.g. linear versus nonlinear) depends on the extent of the available information, and the required level of accuracy for

seismic performance evaluation. The earthquake loading can be represented by acceleration time-histories of the ground motion at the location of the wharf or the displacement time-histories of the ground. In case the fully coupled soil-structure model is considered in the numerical model of the wharf, dynamic analysis to both types of input motions account for the inertial as well as kinematic response of the wharf. However, when the effect of the surrounding embankment soil is lumped into the model of soil spring elements, applying the ground acceleration as a uniform acceleration at the boundaries of the wharf cannot properly account for the effect of the kinematic interaction of the soil-foundation and the permanent soil deformation of the embankment soil on the response of the wharf. Wharves in the gravity wall class including massive quay-walls, caisson quay-walls, and block quay-walls behave almost rigidly during an earthquake and the source of nonlinearity in their response comes primarily from the inelastic behavior of the surrounding soil and its interaction with the rigid wharf structure. Therefore, it is sufficient to model gravity quay-walls linearly if the nonlinear soil-structure interaction is captured properly. On the other hand, for other types of closed wharves and open type wharves, the wharf structure may undergo nonlinear deformations even under moderate levels of ground shaking. To capture the response of these structures, the nonlinear force-deformation characteristics of structural elements including piles and pile-deck connections needs to be properly modeled. Obtaining the required information for the wharf model including structural and geotechnical properties is challenging since this type of data are not readily available and requires field investigation and to some degree engineering judgment to properly select the properties. This type of analysis can capture failure

modes of the wharf as well as evaluate the response of the system and its constitutive components in terms of displacement, stress, ductility, and strain.

Most of the research in seismic performance evaluation of wharves implemented nonlinear dynamic analysis. Dodds et al. (2004) used elastic-perfectly plastic models of site soil materials and piles at the Kings Wharf in Suva, Fiji in order to evaluate the seismic stability of the wharf structure. A similar modeling approach was used by Smith et al. (2004) in order to evaluate a new design of a wharf at the Port of Vancouver, British Columbia. In another example, Roth et al. (2003) modeled a number of wharves located on the west coast of the United States. This model incorporated elastic-perfectly plastic soil models and elasto-plastic beam elements with the capability of forming plastic hinges at predetermined locations. The goal of their research was to show the importance of soil-structure interaction models on the total response of wharves. Na et al. (2009) used a similar modeling procedure to develop fragility curves for characterizing the response of a typical pile-supported marginal wharf structure to ground motions generated under the SAC project (Federal Emergency Management Agency 2000). Because of the incapability of 2D models in capturing 3D effects, they were not able to account for torsional-horizontal coupling, shear key effects in transverse direction and pounding in the longitudinal direction. Donahue et al. (2004) studied the seismic performance of the wharf structure at Berth 24/25 of the Port of Oakland during the 1989 Loma Prieta earthquake. This study carried out seismic analysis of the response of this structure to ground motions from the Loma Prieta Earthquake, and then compared these analytical predictions to motions recorded at the structure during this

earthquake. Reasonable agreement was observed between the recorded data and the predicted response of the wharf. However, because the level of shaking of the structure during the earthquake was small, the response of the soil and structure were essentially linear. Therefore, the structure was modeled by using the initial uncracked stiffnesses of the piles and elastic-perfectly plastic spring models of the soils, in which effects of pore water pressure and soil liquefaction were neglected.

2.3.4 Selection of the analysis procedure

In order to have a systematic procedure for selecting the appropriate method of analysis, PIANC (2001) has suggested to relate the choice of the analysis method to the performance grade. For this, two levels of earthquake motions typically used for performance based design are considered as follows.

Level I: The level of earthquake motion that is likely to occur during the life span of the structure.

Level II: The level of earthquake motion associated with infrequent rare events that typically involve very strong ground shaking.

Next, the possible damage to wharves are classifies into four degrees of damage and the associated acceptable level of damage for each group for the expected operational level is defined as shown in Table (2.1). The operational level is defined based on the amount of work required to recover the serviceability of the wharf.

Table 2.1 Acceptable level of damage in performance-based design[a]

Level of Damage	Structural	Operational
Degree I: Servicable	Minor or no damage	Little or no loss of serviceability
Degree II: Repairable	Controlled damage[b]	Short-term loss of serviceability[c]
Degree III: Near Collapse	Extensive damage in near collapse	Long-term or complete loss of serviceability
Degree IV: Collapse[d]	Complete loss of structure	Complete loss of serviceability

[a] Considerations: Protection of human life and property, functions as an emergency base for transportation, and protection from spilling hazardous materials, if applicable, should be considered in defining the damage criteria in addition to those shown in this table.
[b] With limited inelastic response and residual deformation.
[c] Structure out of service for short to moderate time of repairs.
[d] Without significant effects.

Associating the level of acceptable damage to the level of earthquake, PIANC (2001) suggested four performance grades from which the required performance of the wharf may be specified (Table 2.2).

Table 2.2 Performance grades S, A, B, and C

	Design Earthquake	
Performance Grade	Level I (L1)	Level II (L2)
Grade S	Degree I: Servicable	Degree I: Servicable
Grade A	Degree I: Servicable	Degree II: Repairable
Grade B	Degree I: Servicable	Degree III: Near Collapse
Grade C	Degree II: Repairable	Degree IV: Collapse

The appropriate performance grade for structural systems reflects the balance between the economy aspect of the project and the proper and safe performance of the systems. One way to select the performance grade is characterizing the importance of the structure under consideration. The importance categories are mainly defined based on the primary and secondary effects of the damage to the system on the economy, human life, and environment. Table (2.3) relates the

performance grades in Table (2.2) to the importance of the structure defined in terms of the effect of the seismic damage.

Table 2.3 Performance grade based on the importance category of port structures

Performance Grade	Definition based on seismic effects on structures
Grade S	1. Critical structures with potential for extensive loss of human life and property upon seismic damage 2. Key structures that are required to be serviceable for recovery from earthquake disaster 3. Critical structures that handle hazardous materials 4. Critical structures that, if disrupted, devastate economic and social activities in the earthquake damage area.
Grade A	Primary structures having less serious effects for 1-4 than Grade S structures, or 5, structures that, if damages, are difficult to restore.
Grade B	Ordinary structures other than those of Grades S, A, and C
Grade C	Small, easily restorable structures

The appropriate type of analysis procedure required for performance assessment of the wharf can be logically related to the performance grade e.g. the better the performance grade, the more accurate and detailed analysis method is required. Table (2.4) shows the relation between the type of analysis and the performance grades.

Table 2.4 Types of analysis related to performance grades

	Performance Grade			
Type of Analysis	Grade C	Grade B	Grade A	Grade S
Simplified analysis	■	▒	▒	▒
Pushover analysis		■	▒	▒
Dynamic Analysis			■	■

Note: Black area is standard/final design and gray area is preliminary design or low level of excitation

2.4 Wharf-Crane Interaction

Depending on the required functionality, different types of cranes are constructed and implemented in seaports. One of the most common configurations of cranes are container cranes used to load and unload containers from the deck of wharves to the deck of vessels and vice versa. Container cranes are most often composed of two segments: the bottom steel frame and the upper part which is responsible for carrying and handling cargo. The upper segment of cranes is supported and moved by the lower steel frame called portal frame. The legs of the portal frame rest on the crane rails through the wheels. The wheels provide unique boundary conditions for the crane legs; they cannot transfer tension forces and as a consequence cranes can uplift. The restraint against the lateral movement of the whole crane is provided by the flanges of the wheels. The details of the boundary condition between the crane legs and crane rails are shown in Figure 2.6a,b.

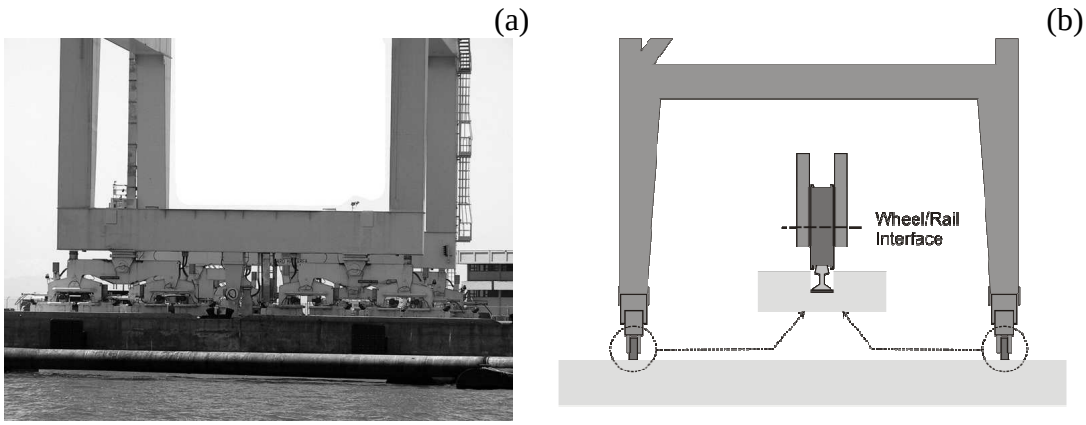

Figure 2.6 Container crane boundary condition with wheel/rail interaction in (a) side view and (b) front view.

In normal conditions, a crane remains still under the effect of the gravity of the crane. In case the crane is not operating, the legs of the crane are fixed to the rails by anchors or clamps. Under lateral loads on the crane induced by the seismic

response of the wharf or strong winds, the crane tends to sway. The overturning moments as a result of the lateral loads on the crane is resisted by the restoring moment from the gravity of the crane. If the lateral loads are large enough to overcome the restoring action of the gravity loads, the crane uplifts and in this case the lateral restraint at the uplifted leg will not be effective anymore. As the crane returns to the rest position due to the change in the direction or magnitude of the applied load, the uplifted leg sits on the wharf deck but highly likely not in the initial rest location i.e. the crane rail. From this time forward, the base shear of the uplifted leg is not provided by the lateral restraint of the wheels' flanges but from the friction of the crane leg with the deck of the wharf. The stages of the coupled elastic uplift response of the crane are shown in Figure 2.7a-d.

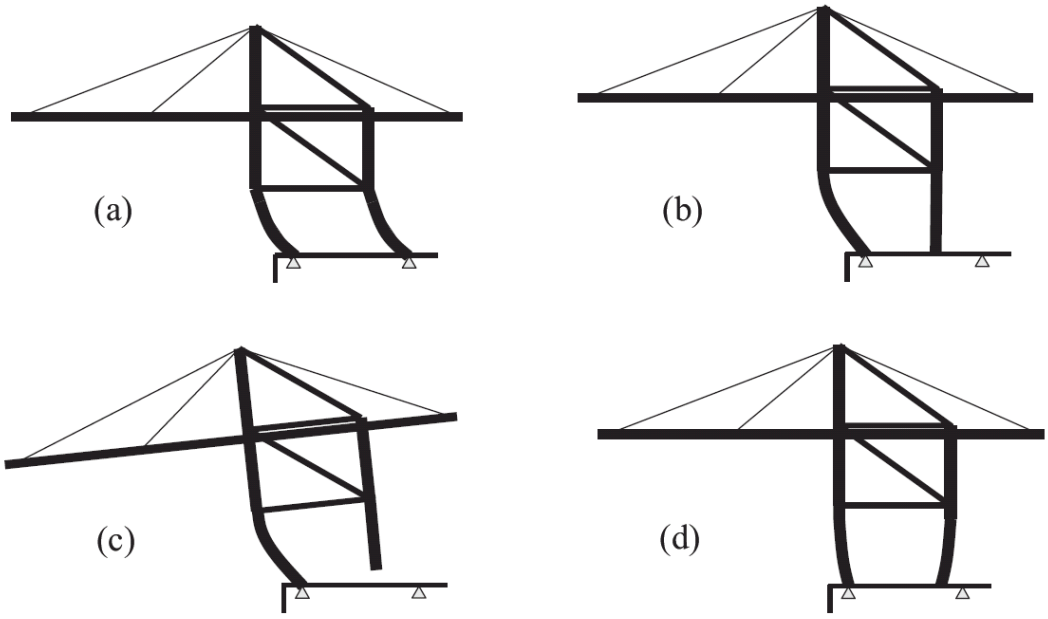

Figure 2.7 The coupled elastic and nonlinear uplift response of a typical container crane (Kosbab 2010).

The uplift response of the cranes was considered as a favorable response for early container cranes. This was mainly due to the common belief that the uplift of the

crane provides a form of isolation for the dynamic response of cranes and decreases force demands on the crane to the forces required to uplift the crane (Werner 1998, Soderberg 2009). As a consequence based on this assumption, tie downs were only implemented for areas with low seismicity and strong winds to mitigate the risk of overturning of the crane (McCarthy et al. 2009). However the performance of cranes during Kobe earthquake demonstrated that the uplift response of cranes may lead to excessive deformations of the portal frame followed by crane's failure (Kanayama et al. 1998). Typical failure modes of container cranes during earthquakes are derailment of wheels, yielding of tie downs, buckling in the portal frame, and overturning. In addition to the portal sway deformation and sliding/uplift response of the crane in response to the acceleration response of the deck transferred to the crane through the boundary conditions at the interface of crane rails and crane legs, the relative deformation of the crane rails in the horizontal and vertical directions may also result in the damage to the crane. In case the horizontal distance between the seaside and landside crane rails increases which may occur under large lateral deformations of the liquefied embankment, the crane legs are susceptible to derail or undergo buckling (Figure 2.8a). On the other hand if the differential settlement of the crane rails is considerable, tilting or overturning of the crane may occur (Figure 2.8b).

(a) (b)

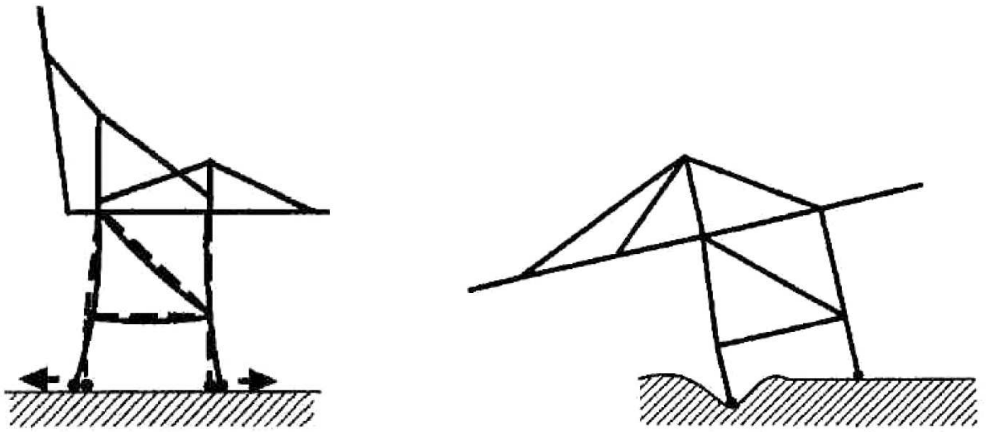

Figure 2.8 The damage to the crane under (a) relative horizontal displacement of the crane rails and (b) differential settlement of the crane rails (PIANC 2001).

Several investigators have studied the seismic response behavior of container cranes using numerical simulations and shake table tests. Kanayama and Kashiwazaki (1998) and Kanayama et al. (1998) conducted a series of shake table tests on container crane models of different scales. Using the time-history records of the Kobe earthquake, it was found that the landside legs of the container crane models derail and uplifts during the simulated earthquake. Kobayashi et al. (2004) numerically modeled large container cranes using the finite segment approach and included the kinematic constraints between the crane rails and the crane legs. In another attempt, Kosbab et al. (2009) developed several models of typical container cranes common in the United States. The models were able to capture the complex sliding and uplift behavior of the cranes by implementing contact elements at the base of the crane legs. Jacobs et al. (2010) performed a series of 1:20 scale shake table tests of the model container cranes under increasing levels of acceleration. Nonlinear time-history analysis of the crane models developed by Kosbab et al. (2010) was carried out for the earthquake motions recorded at the shake table. It

was found that the nonlinear finite element model of the crane can capture the coupled response of sliding/uplift and the lateral response of the portal frame of the crane accurately (Jacobs et al., 2010).

Despite the significant body of research on the seismic performance of wharves and cranes – a number of them are cited above; very limited research studies have been conducted to characterize the dynamic interaction behavior of wharves and container cranes. This is especially due to the common belief that the container cranes act as tuned mass dampers for the underlying wharf structures during seismic events and therefore it is conservative to neglect the effect of the crane's presence on the response of the wharf (POLA, 2007). Chaudhuri et al. (2009) studied the seismic performance of a container crane supported by a gravity-type quay wall. In their approach, the interaction problem between wharf and crane is treated in two stages. First, the seismic response of the wharf excluding crane is evaluated for a number of bedrock motions. In the second step, the response of the wharf at the deck level is used as the input excitation at the base of the crane model. Although this method considers the interactive nature of the problem more realistically compared to other investigations, the effect of the crane dynamics on the behavior of the wharf is ignored.

2.5 Fragility Analysis

Several studies have been conducted in order to gain more knowledge of the behavior of structural systems subjected to earthquake events. However, improving system performance from a structural and/or geotechnical point of view is not the only critical factor and economic considerations including cost and time also play a

major role in decision-making for natural hazards. Seismic Risk Analysis provides a framework through which both economical issues and system performance can be taken into account. Using numerical models representing the system, this approach takes seismic hazard information as the input and estimates probabilities that social and/or economical consequences exceed certain values. Using the seismic risk framework, one will be able to find the vulnerability of existing structures and explore different retrofit strategies in order to enhance the overall system performance.

Economic loss at a port due to earthquake loading was studied by Na and Shinozuka (2009) by considering the container throughputs as the indicator of seismic loss. For the retrofitting scenario, they generated fragility curves by simply shifting median values of lognormal distributions of original fragility curves. The restoration time for each of the structural limit states were assumed to be a uniform distribution between a lower and upper limit. Considering a port operation model, system fragilities for a set of pre-defined limit states were calculated. In another attempt, Pachakis and Kiremidjian (2004) estimated downtime related revenue losses in ports under seismic events. Their study focused on nonstructural losses which are mainly due to the disruption in ship traffic streams resulting from the incapability of port facilities to serve arriving ships. An operation model of a port was developed and used to simulate the operation of a terminal under a seismic event. Based on the probability of failure and downtimes of rail mounted cranes provided in HAZUS, generated ship streams were used as an input to the operation port model with and without an earthquake event and the difference in revenues was considered as the loss.

A number of uncertainty sources contribute to the overall uncertainty involved in seismic risk assessment of a system. Focusing on structural and geotechnical aspects, uncertainties in capacities and demands impact the overall seismic risk and need to be characterized. Uncertainties in capacity are due to the differences between the real behavior and the captured behavior of materials, sections, and elements using numerical models, while uncertainties in demands are largely due to the stochastic nature of input earthquake ground motions. Since a large number of factors are involved in the evaluation of capacities and demands of a system, it is extremely important to the influence of uncertainties on the overall performance of the system which can be done using fragility analysis.

2.5.1 Fragility Curves

The goal of modern seismic risk assessment methods is to provide the probability of loss at different levels of hazard by decomposing loss into its components using the law of total probability. The elementary components which contribute to the total loss includes: seismic ground motion hazard, structural response of the system to input ground motions, induced damages to structural and nonstructural components, and the resulting consequences of the damages. Using the law of total probability, one can combine these probabilities to find the probability of total loss exceeding a predefined value *c* as in Equation (2.1).

$$P[Loss > c] = \sum_{s} \sum_{LS} \sum_{d} P[Loss > c \mid DS = dm]\ P[DS = dm \mid LS]\ P[LS \mid IM = s]\ P[IM = s] \quad (2.1)$$

In this relation, *IM* denotes the intensity measure representing the intensity of earthquake ground motions usually in terms of PGA, PGV, S_a, etc and *s* is the realization of the intensity measure. Giovenale et al. (2004) pointed out that sufficiency, efficiency, and hazard computability are the essential properties of a good IM. In addition, practicality (Luco and Cornell 2007) and proficiency (Padgett et al. 2008) are properties that need to be considered, the latter one being a composite measure of efficiency and practicality. Efficiency criterion implies that the intensity measure should have small dispersion around the estimated structure response, while by practicality, the IM requires having a direct correlation to known engineering measurements. Hazard compatibility requires that the data needed to evaluate the probability of the chosen intensity measure be readily accessible through hazard maps or other sources. The next term in Equation (2.1) which is conditional on the IM is the probability of exceeding a limit state, LS. This component is determined by comparing the EDP from structural response with predefined values of EDP representing the capacity of the structure in different limit states. The procedure to evaluate P[LS|IM=s] is called “Fragility Analysis” of the structure. Based on defined structural limit states, one can quantify the probability of associated damage states which are commonly evaluated in qualitative terms to represent the level of functionality of the structure. The last component in Equation (2.1) gives the probability of loss exceeding a predefined value *c* given the damage state *DS=dm*.

Previous studies have shown that the conditional probability representing the fragility of a structure can be modeled by a two parameter lognormal probability distribution (Cornell et al. 2002, Ellingwood et al. 2007) as follows.

$$P[EDP \geq d \mid IM] = \Phi\left(\ln\left(\frac{EDP}{d} \right) \Big/ \beta_R \right) \tag{2.2}$$

In which d and β_R are median capacity and logarithmic standard deviation respectively and Φ is the standard normal probability integral. Although β_R represents uncertainties inherent in seismic capacity, other sources of uncertainty also contribute to the capacity assessment. These uncertainties stem from assumptions made in system analysis and limitations in supporting databases (Ellingwood et al. 2007). To account for these uncertainties, d is replaced by a lognormal random variable M_R with median m_R and logarithmic standard deviation β_{RU} called epistemic uncertainty. The total uncertainty of the model is then replaced by

$$\beta_R = \sqrt{\beta_{RR}{}^2 + \beta_{RU}{}^2} \tag{2.3}$$

where β_{RR} represents aleatoric uncertainty.

In order to simplify the demand model, Cornell et al. (2002) proposed a power model to estimate the median demand for a given IM.

$$EDP = a.IM^{\,b}.\varepsilon \tag{2.4}$$

where ε is a lognormal random variable with median 1 and logarithmic standard deviation $\sigma_{ln\varepsilon}$. Taking natural logarithm from both sides of Equation (2.4), the relation between ln(*EDP*) and ln(*IM*) appears to be linear and parameters *a*, *b*, and ε can be determined by regression analysis. Considering that the median of parameter ε is 1, the estimated median of *EDP* is

$$\hat{EDP} = a.IM^{\,b} \tag{2.5}$$

To evaluate aleatoric uncertainty β_{RR}, Ellingwood et al. (2007) suggested the following relationship.

$$\beta_{RR} = \sqrt{\beta_{D|IM}{}^2 + \beta_C{}^2} \tag{2.6}$$

in which $\beta_{D|IM}$ is the logarithmic standard deviation of the demand and β_C represents the aleatoric uncertainty inherent in capacity.

The above methodology is implemented in this research for the fragility analysis of wharf components. The fragility of all vulnerable structural and nonstructural components which their damage imposes direct or indirect loss is needed to be identified.

CHAPTER 3

TWO DIMENSIONAL PLAIN STRAIN MODELING AND ANALYSIS OF THE PILE SUPPORTED CONTAINER WHARVES

3.1 Introduction

Many existing pile-supported marginal wharf structures within ports along the west coast of the United States were designed in the late 1960s and early 1970s using then available seismic design criteria. These criteria are much less robust than current criteria at these seaports and, as a result, many structures designed using these criteria are vulnerable to damage from moderate-to-large earthquakes.

The dynamic response of this group of wharves during seismic events is complex, particularly when the soils are susceptible to liquefaction. Because container wharf structures are essential to a port's cargo throughput, it is important to understand the performance of these structures during earthquakes. Seismic performance of wharves has been the subject of a number of studies using numerical simulations (Roth et al. 2003, Dodds et al. 2004, Smith et al. 2004, Donahue et al. 2004, Na et al. 2009). The seismic performance of pile-supported wharves has also been investigated experimentally. For example, centrifuge testing has been used for this purpose by several investigators (e.g., Takahashi et al. 1998, Iai and Sugano 1999, McCullough et al. 2001). Although previous studies such as those cited above have provided valuable insight into some aspects of the seismic response of wharves, limitations in the modeling of wharf structures and the surrounding soil media have constrained the understanding of various features of the wharf response, particularly

those features pertaining to pile and pile-deck connection failure mechanisms and permanent deformations of potentially liquefiable soil embankments.

This chapter provides new insights into these features by using new and advanced structure and soil modeling procedures to carry out two-dimensional, plane-strain seismic analyses of a pile-supported marginal wharf structure in liquefiable soils. Also, the wharf structure that is analyzed represents a typical configuration that was designed in the 1960s and early 1970s using criteria that are much less robust than current seismic design criteria. Because such structures are common within west coast seaports, an additional benefit of the analysis results from this chapter is the insights that they provide regarding potential seismic vulnerabilities of wharf structures of this vintage.

The remainder of this chapter describes the marginal wharf configuration that has been analyzed, and how this structure and its surrounding soil materials have been modeled in order to account for the effects of nonlinear behavior of pile elements and their connections to the wharf deck, and effects of nonlinear dynamic pile-soil interaction for situations where the soils undergo liquefaction. Then, the chapter presents results of the analyses carried out using these modeling procedures, including the soil-structure system's mode shapes, modal periods, and modal damping ratios as obtained from a complex eigenvalue analysis, as well as results from nonlinear static pushover analysis. Detailed nonlinear dynamic analyses are performed in order to characterize the seismic behavior of the wharf structure-soil system in response to time histories of ground motions and pore pressures within the surrounding soil medium. Predicted wharf damage patterns based on these

analysis results are compared to damage patterns in such structures that were observed during past earthquakes.

3.2 Wharf Configuration and Model

Wharves are marine structures constructed on the shoreline for berthing vessels to load and unload cargo and passengers. Due to geographical, economical, and functional considerations, different types of wharf configurations have been designed and constructed, as discussed in chapter 2. One of the important factors that largely affect the choice of wharf structure type is the sub-surface soil conditions. Considering this factor, wharf structures are classified into two major categories: open type in which the wharf structure allows water to run below the deck and otherwise closed type. One of the common configurations of open type wharves are pile supported container wharves which are commonly used in the west coast of the United States. A pile-supported wharf is composed of a platform called a deck supported by a substructure consisting of piles and a dike. The lateral resistance of the wharf structure is provided by a number of vertical and/or batter piles which are connected to the deck by moment resisting connections. The vertical loads induced by gravity, wind, and earthquake are simply transferred by the axial constraint in connections from deck to the piles. Depending on the location of the piles, seaward, landward, or in the middle, the overall and embedded lengths of piles differ. The deck is usually made of either reinforced concrete or pre-stressed concrete with thickness ranging from 0.3 m to 1.0 m. Since the wharf deck is very rigid in the plane of the deck, the movement of the top of the piles is constrained

with the rigid diaphragm action of the deck. Accordingly, shorter piles face larger curvature demands during seismic events compared to longer piles.

The wharf structure configuration that is analyzed in this research is typical of wharves in seaports along the west coast of the United States that have been designed during the late 1960s and early 1970s. The configuration of the wharf together with the embankment soil profile is shown in Figure 3.1. The structure consists of a wharf deck with the length of 30.2 m in the landside-seaside (transverse) direction supported by seven rows of vertical piles and a single row of batter piles, and a structurally separate landside crane rail that is supported by a single row of batter piles (Figure 3.1). It was seismically designed according to criteria that were commonly used during the late 1960s and early 1970s, which represents the vintage of many wharf structures within seaports along the west coast.

The finite element (FE) model of this wharf has been developed in OpenSEES, an object-oriented FE analysis framework (McKenna et al. 2010). In the following, properties of different components of the wharf are explained and the modeling issues are discussed.

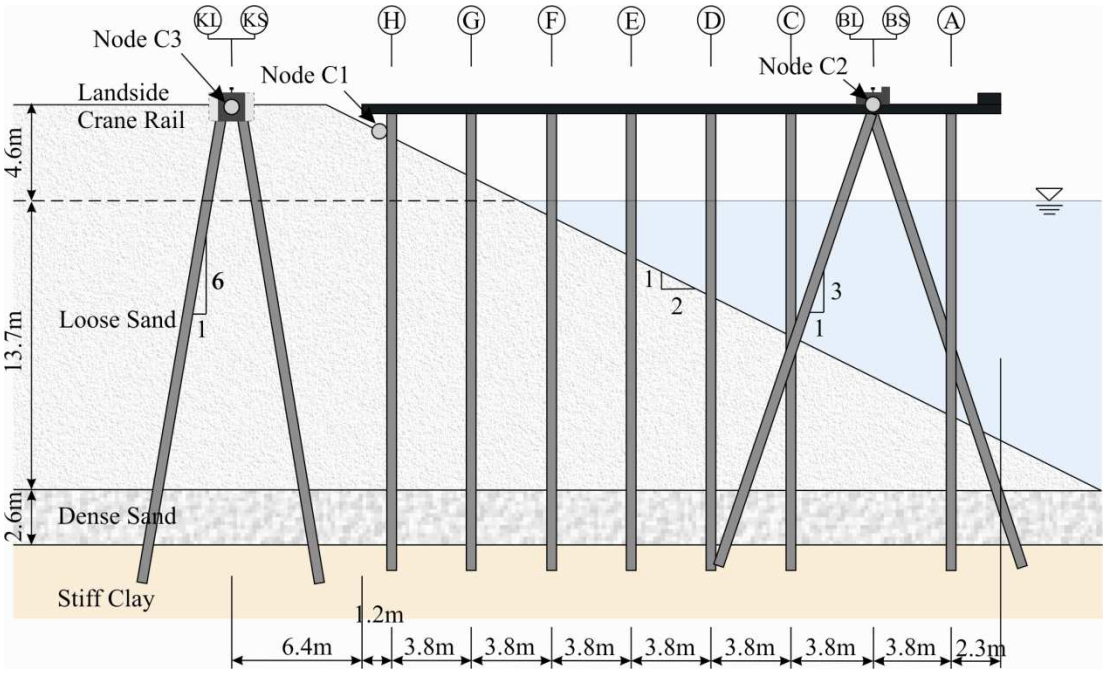

Figure 3.1 Configuration of the wharf and landside crane rail.

3.2.1 Deck

The deck is responsible for carrying the dead and live loads from the self-weight, container cranes, containers, and vehicles and transfers the loads to the underlying foundation through the piles.. Several types of deck have been constructed in ports including cast-in-place concrete flat slabs, cast-in-place concrete beam and slab structures, long-span concrete box girder deck system, precast pre-stressed concrete panels, precast normally-reinforced concrete panels, and ballasted deck pavement system (Werner 1998).

The deck of the wharf of this study is a cast-in-place concrete flat slab with a thickness of 46 cm, constructed of reinforced concrete with the concrete strength of 41.4 MPa. Because of its large thickness and corresponding substantial rigidity in the horizontal plane, flexural deformations of the deck will be negligibly small. Therefore, the deck is modeled with rigid beam elements.

3.2.2 Piles

Generally, piles serve as foundations for wharves and other components of port systems including cargo handling and temporary storage structures. The foundation support of the piles is provided by the transfer of the induced loads from the superstructure to underlying soil layers through the friction mechanism at the face of the piles or end bearing. Depending on the vertical orientation of the piles, pile systems are classified as vertical or batter piles. In vertical piles, the lateral loads are resisted by the bending action of the piles, while in the batter piles, the lateral loads are carried by the simultaneous action of the bending and axial resistance of the piles.

The most common types of piles used in waterfront structures are square and octagonal precast pre-stressed concrete piles with the size varying from 0.3 m to 0.6 m. The limited corrosion in these types of piles and the benefit of controlled, offsite fabrication are the poignant desirable features of precast pre-stressed concrete piles compared to other types of piles.

The wharf structure of this study is supported by vertical and battered pre-stressed concrete piles with a square cross section. Figure 3.2 shows the cross-section configuration of the pre-stressed concrete piles together with the reinforcing details. The piles that support the wharf deck along rows C, D, and E and the landside crane rail along rows KS, and KL have a side dimension of 40.6 cm reinforced by circular layers of 16 #32 mild steel vertical bars and 10 #13 pre-stress tendons. The piles along the remaining rows have a side dimension of 45.7 cm with circular layers of 16 #32 mild steel vertical bars and 10 #13 pre-stress tendons. The transverse

confinement of the piles is provided by #13 spirals whose pitch varies along the length of the piles and ranges from 5.1 cm in the vicinity of the pile-to-deck connection to 7.6 cm along the remainder of the pile. The concrete compressive strength at 28 days is 41.4 MPa and all reinforcing bars are ASTM A706, Grade 60. The pre-stress strands for all piles conform to ASTM A416, Grade 270 and impose an effective pre-stress of 5.5 MPa.

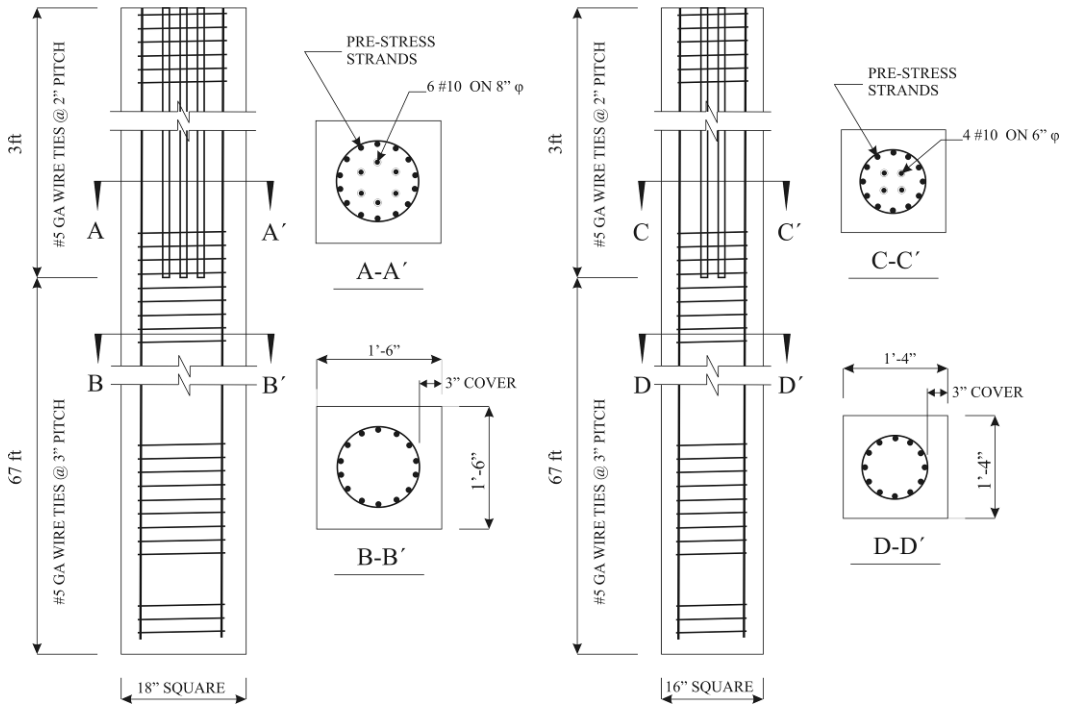

Figure 3.2 Section geometry and reinforcement details for 18" and 16" square piles.

The pre-stressed piles are modeled by force-based *nonlinearBeamColumn* elements (Spacone et al. 1996 and De Sousa 2000) with fiber cross-sections with the ability to consider the spread of plasticity along the length of the elements. Five integration points are used along the length of the *nonlinearBeamColumn* elements. Fiber cross-sections for these elements are defined by the pile's cross-sectional geometry, longitudinal reinforcement bars, pre-stressing strands, and concrete material properties.

The fiber cross-section of the piles contains four discretized sub-regions: the cover layer of unconfined concrete, the inner core region containing confined concrete, the circular layer of longitudinal reinforcing steel, and the circular layer of pre-stressing strand. The number of subdivisions chosen for the core and cover sub-regions are as follows.

- Number of subdivisions in the circumferential direction for the core: 16
- Number of subdivisions in the radial direction for the core: 18
- Number of subdivisions in the circumferential direction for the cover: 16
- Number of subdivisions in the radial direction for the cover: 6

The details of the discretization of the cross-sections of the piles in Figure 3.2 are shown in Figure 3.3.

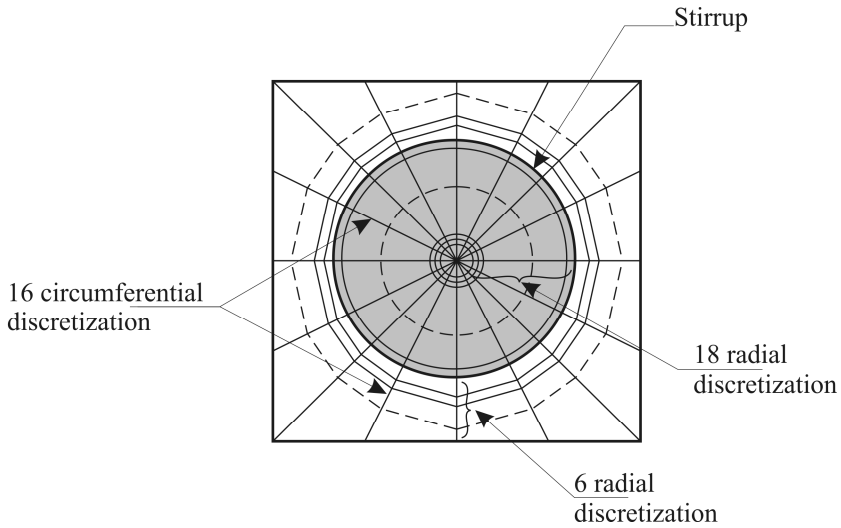

Figure 3.3 Discretization of pile sections in radial and circumferential directions to be used as fiber cross-sections in the FE analysis.

The stress-strain relationship of the unconfined cover concrete and confined core concrete is modeled by “concrete 02” material model in OpenSees which is the model proposed by Mohd Yassin (1994). In this model, the monotonic envelope form in the modified Kent-Park model (Park et al. 1982) is enhanced to incorporate the cyclic loading effects. The compressive portion of the relationship was adopted from the model proposed by Kent and Park (1971) which consists of a parabolic curve up to the concrete compressive strength followed by a downward sloping line to the concrete crushing strength. Piecewise linear unloading stress-strain characteristics in the model are adopted from the model proposed by Karsan and Jirsa (1969). The following material properties are used to model the unconfined cover concrete:

- Concrete compressive strength, f'_c: 6.0 ksi
- Concrete elastic modulus, E_c: 57. $f'^{0.5}_c$ *(E_c in ksi and f'_c in psi)*
- Ratio of maximum to nominal concrete strength, K_{fc}: 1.0
- Ratio of ultimate to maximum concrete strength, K_{res}: 0.1
- Strain at compressive strength, ε_{c0}: 0.002
- Strain at ultimate concrete compressive strength, εcu: 0.005
- Maximum concrete compressive strength, $f'cc$: K_{fc}. f'_c
- Ultimate concrete compressive strength, $f'cu$: K_{res}. $f'cc$
- Ratio between unloading slope at εcu and the initial slope, λ: 0.5

- Concrete tensile strength (MacGregor 1997), f_t : $0.1f'cc$

- Tension softening stiffness, E_{ts}: $0.1E_c$

The material properties used to model the core concrete are given below.

- Concrete compressive strength, f'_c: 6.0 ksi

- Concrete elastic modulus, E_c: $57.\ f'^{0.5}_c$ *(E_c in ksi and f'_c in psi)*

- Ratio of maximum to nominal concrete strength, K_{fc}: 1.54

- Ratio of ultimate to maximum concrete strength, K_{res}: 1.16

- Strain at compressive strength, ε_{c0}: 0.0074

- Strain at ultimate concrete compressive strength, εcu: 4.42 ε_{c0}

- Maximum concrete compressive strength, $f'cc$: $K_{fc}.\ f'_c$

- Ultimate concrete compressive strength, $f'cu$: $K_{res}.\ f'cc$

- Ratio between unloading slope at εcu and the initial slope, λ: 0.5

- Concrete tensile strength (MacGregor 1997), f_t : $0.1f'cc$

- Tension softening stiffness, E_{ts}: $0.1E_c$

The quantities for K_{fc}, K_{res}, ε_{c0}, and ε_{cu} are found from the equations provided by Mander et al. (1988) and Priestley et al (1996).

The stress-strain relationship of steel reinforcement is modeled by "steel 02" material model in OpenSees which represents the constitutive model by Menegotto and Pinto (1973). This model can capture the Bauschinger effect, under which the nonlinear response in the unloading branch develops at strains significantly lower than the yield strain (Paulay and Priestley 1992). The following material properties are used to model the reinforcing steel:

- Yield strength of steel, f_y: 60 ksi
- Modulus of elasticity of steel, E_s: 29,000 ksi
- Strain at yield strength of steel, ε_y: f_y/E_s
- Ultimate strength of steel, f_u : 90 ksi
- Strain at ultimate strength of steel, ε_u: 0.12
- Stain hardening ratio, SHR: $(f_u - f_y)/(\varepsilon_u - \varepsilon_y)/E_s$

The pre-stressing steel is modeled with an elastic-perfectly plastic material model with a nonzero initial strain. In order to induce pre-stress in strands, the initial strain is found such that the final stress in strands under zero external loads equals the working stress.

3.2.3 Batter piles

The contribution of the lateral resistance of the batter piles in the horizontal deformation of wharves is large compared to the contribution of vertical piles. The lateral displacement of the wharf deck is accommodated by axial deformations in

batter piles which can induce tension or compression in the piles, depending on the orientation of the batter pile with respect to the direction of deck displacement. The large axial rigidities of batter piles are the main contributor to the lateral resisting mechanism of the wharf; hence attracting a larger portion of the lateral loads. At first glance, it seems very economic to have batter piles to limit the lateral movement of the wharves, however the large axial forces in batter piles is accompanied by a number of damage mechanisms including pile pullout from soil in tension batter piles, failure of pile sections due to excessive axial deformations, and shearing of the batter pile-to-deck connections.

The configuration of batter piles along rows BL and BS within the wharf deck with their associated FE models are shown in Figure 3.4a,b. Similar to vertical piles, a portion of the batter piles is embedded in the wharf deck as shown in Figure 3.4a which is used to model the pile-deck connection in the FE model. Although the force-deformation characteristics of batter piles is mainly governed by the behavior of the pile in the axial direction, the moment-rotation behavior of the batter piles is modeled in a similar fashion as the vertical piles with assigning calibrated material properties to the sections in the plastic hinge zone. The load transfer mechanism between the batter piles and the wharf deck is similar to the load transfer in eccentric bracing systems where the axial force in the brace induces shear forces in the connection. During moderate to large seismic events, batter pile connections face large shear forces that may lead to considerable shearing damages in the connections. A number of studies investigated shear behavior of reinforced concrete connections among which the model by Teraoka and Fujii (2000) performed well in

predicting shear behavior of beam-column connections. In lieu of experimental studies for shear behavior of batter pile-deck connections, a simple elastic-perfectly plastic model is implemented at the end of the batter piles with shear capacity calculated from the relations by Teraoka and Fujii (2000) (Figure 3.4b). Nominal joint shear strength in this approach is defined in the following form.

$$V_j = k\varphi F_j b_j D_j \tag{3.1}$$

where k is in-plane geometry factor (1.0 for interior joints, 0.7 for exterior joints, and 0.4 for knee joints), φ is the out-of-plane geometry factor (1.15 for joints with two transverse beams and 1.0 for other types), and F_j is the standard value of joint shear strength calculated from

$$F_j = 0.8 f_c'^{0.7} \text{ (MPa)} \tag{3.2}$$

The effective joint shear area of the connection is defined by the effective joint width b_j and the effective joint shear depth D_j.

Based on ACI 352R-02, the nominal joint shear strength is calculated by

$$V_j = \gamma \sqrt{f_c'} b_j h_c \tag{3.3}$$

where γ is the joint shear strength factor (1.25 $\text{MPa}^{0.5}$ for joints with a discontinuous column and effectively confined on all four vertical faces), b_j is the effective joint shear width, and h_c is the column depth.

As noted previously, the lateral movement of the wharf is limited by the flexural and axial-flexural resistance of vertical and batter piles respectively. The significant

contribution of axial forces in the overall lateral resistance of batter piles accompanies with larger axial section deformations compared to the deformations in the batter piles which especially in tension may lead to section failure. The effect of axial deformation of batter piles in damage evaluation is accounted for by finding the strain limits of section components for the associated yield and plastic moment curvatures and comparing with the axial strains of section components from nonlinear time-history analysis.

The other type of damage associated with batter piles is the pile pullout from soil. Under lateral displacements of the wharf, a number of batter piles experience tension forces accompanied by axial pile deformations as well as deformations in the soil close to the pile surface. During large seismic events, the deformation of the surrounding soil in the direction of the pile shaft may exceed the corresponding yield deformations after which point the soil is not able to provide considerable resistance to additional axial displacement of the pile and consequently, the pile is susceptible to “pullout” from the soil. Exceedance of force/deformation response of t-z springs at the end of the batter piles simply implies that all the above t-z springs have passed their corresponding yield limits and therefore is an appropriate measure to check for the pullout of the batter piles.

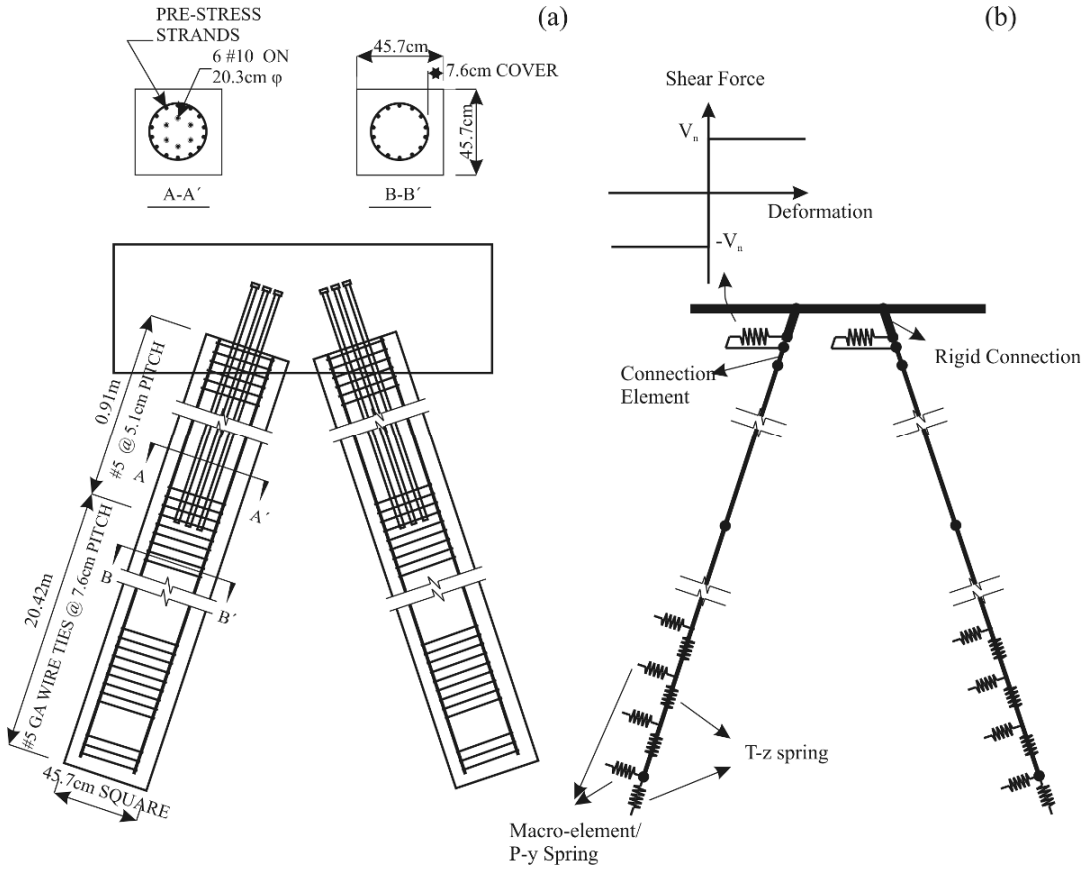

Figure 3.4 Configuration the batter piles (a) geometry and reinforcing detail and (b) numerical FE model

3.2.4 Pile-to-deck connections

Pile-deck connections are structural elements or more accurately structural detailing through which piles are connected to the deck. Several types of pile-deck connections are common in port facilities including embedded dowels, extended piles, embedded piles, and extended strand (Brackmann 2009). The typical configuration of these connections is shown in Figure 3.5a-d. Within each of these types, the size, number, and type of bars and strands and the embedment of piles and reinforcing bars in the deck may vary.

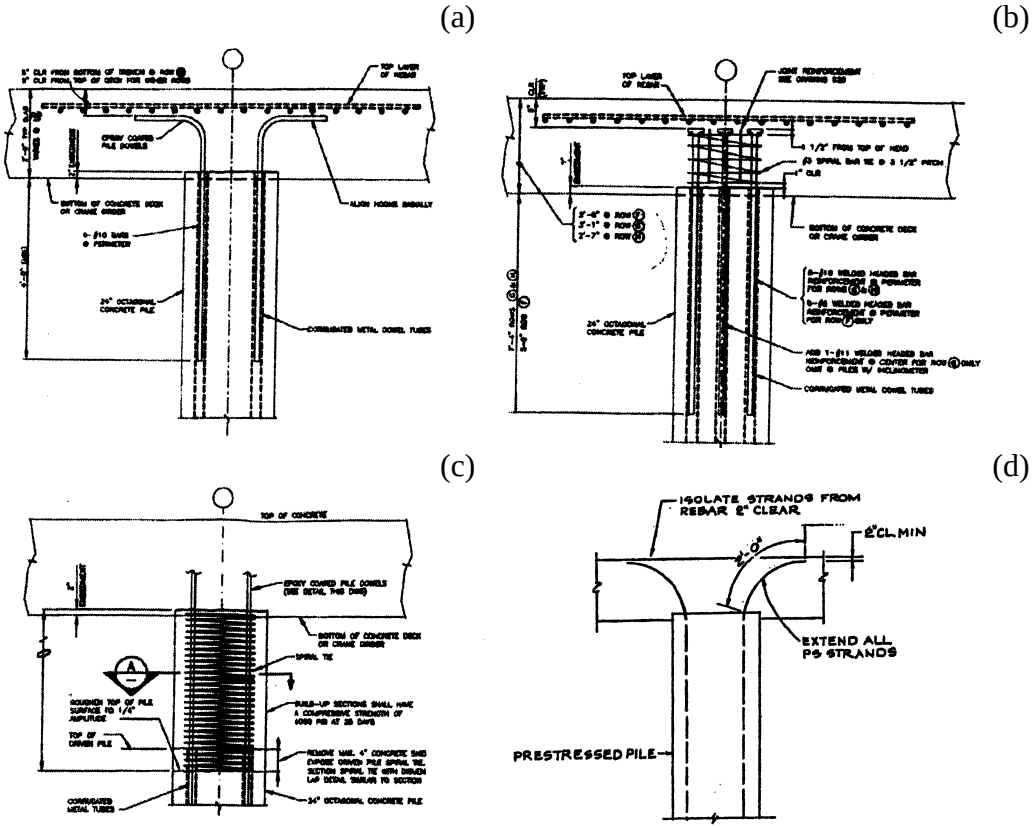

Figure 3.5 Typical configurations of common pile-deck connections: (a) embedded dowel with outward bent bars, (b) embedded dowel with T-headed bars, (c) extended pile, and (d) extended strand.

The piles and the deck in the wharf of this study are connected by T-headed dowel bars which is a common connection for wharf structures of this vintage (Roeder et al. 2005, Brackmann 2009). Modeling of the nonlinear behavior of this connection has been calibrated against a full-scale test conducted by Lehman et al. (2009). The details of the specimen are shown in Figure 3.6. In this test, lateral cyclic loads were applied at a distance of 2.54 m from the face of the reinforced concrete base with a constant axial load on the pile simulating the gravity load.

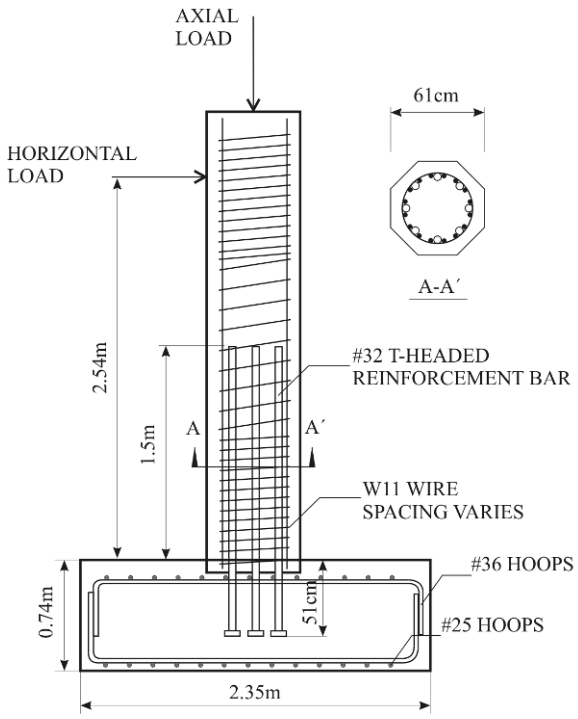

Figure 3.6 Section geometry and reinforcement details of the tested pre-stressed pile (based on Lehman et al. 2009).

The pile-deck connection is modeled by a nonlinear connection element with fiber sections that represents a 3.8 cm embedment of the pile into the wharf deck (Figure 3.6). This connection element extends into the anchorage length of the steel wire strands; therefore, the effects of pre-stress strands within this embedment length are not included in the fiber section representation of the connection element. The reinforced concrete that surrounds the embedded portion of the pile provides lateral confinement for the concrete and, therefore, the confined concrete material model is applied for all of the concrete in the section. The degradation behavior of the connection is assumed to be concentrated within the plastic hinge length. Material properties of pre-stress strands and longitudinal reinforcement are assumed to be identical to those of the pile; but concrete properties are changed to calibrate the force-deformation response of the numerical model with the corresponding response from the experiment. These changes in the concrete properties are limited

to the concrete crushing strain, based on which the parameters required to define the confined concrete stress-strain model are based on relationships adopted from Priestley et al. (1996).

The resulting lateral-force and base-moment versus drift responses from the experiment by Lehman et al. (2009) and the numerical simulations using this pile-deck connection model are shown in Figure 3.7. This figure shows that the numerical model captures the experimental nonlinear force-deformation behavior of the connection very well. Thus, this calibrated numerical model has been used to represent the material properties of all of the pile-deck connections in the FE model.

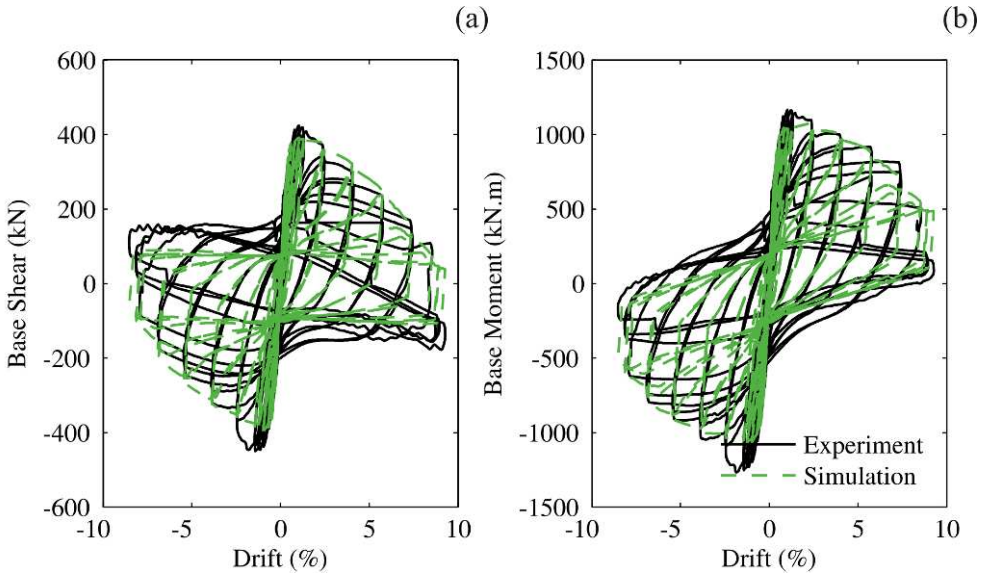

Figure 3.7 The calibration results of the pile-deck connection: (a) shear force versus drift response and (b) moment versus drift response.

3.2.5 Soil Properties

The assumed soil profile for the wharf (Figure 3.1) consists of three layers whose properties are listed in Table 3.1. The first layer within the top 18.3 m of the soil profile consists of a hydraulically placed loose sand fill that is susceptible to

liquefaction. The loose sand layer is underlain by a layer of dense sand with a thickness of 2.6 m on top of a stiff-to-hard clay. The water table level is located 4.6 m beneath the ground surface.

Table 3.1 Soil layer properties

Layer	Mass density (gr/cm3)	Initial tangent shear modulus G_{max} (MPa)	Drained Poisson's ratio ν	Effective friction angle φ (deg)	Undrained shear strength c_u (kPa)
Loose sand	1.85	80	0.2	34	-
Dense sand	2.05	120	0.2	38	-
Stiff clay	1.75	100	0.4	-	48

3.2.6 Soil Springs

Pile-soil interaction in the horizontal direction is modeled by a series of nonlinear soil springs that consists of macroelements within the loose sand layer (Varun and Assimaki 2010) and conventional p-y springs within the underlying dense sand and clay layers (Boulanger et al. 1999). The interaction between the pile and the soil in the vertical direction is modeled by t-z and q-z springs for side and tip resistance, respectively.

The macroelement is composed of a modified Bouc-Wen type hysteresis model, a coupled viscous damper and a nonlinear closure gap spring. The configuration of different components of the macroelement is shown in Figure 3.8. The coupled viscous damper simulates changes in radiation damping with increasing material nonlinearity. To ensure that the total response of the macroelement never exceeds the ultimate soil strength, the damping coefficient of the macroelement is inversely related to the hysteretic dimensionless control parameter of the Bouc-Wen model.

The effect of liquefaction on the pile-soil interaction is considered by evaluating the average effective stress in the vicinity of the pile using the "liquefaction front" concept developed by Iai et al. (1992). In this approach, pore pressure generation is directly proportional to the total amount of plastic shear work done per unit volume of soil (Towhata and Ishihara 1985). The model also accounts for pore pressure dissipation by allowing drainage between near-field and far-field controlled by hydraulic conductivity of soil. The performance of the macroelement has been checked by simulating a number of centrifuge tests. Predicted results showed a close agreement with the experimental results (Varun et al. 2010). Other types of soil springs including conventional p-y, t-z, and q-z springs are well documented and thorough description of their formulation is available in Boulanger et al. (2007).

The embedded length of the piles is discretized into a number of segments with approximate length of 1m with each node on pile connected to a horizontal and vertical soil spring. The other end of the spring is connected to free-field node through which free-field pore pressures for the macroelement and corresponding free-field displacements for all soil springs can be input into the model. For batter piles, macroelements and p-y springs are applied perpendicular to the pile axis, and t-z and q-z springs are applied parallel to the pile axis.

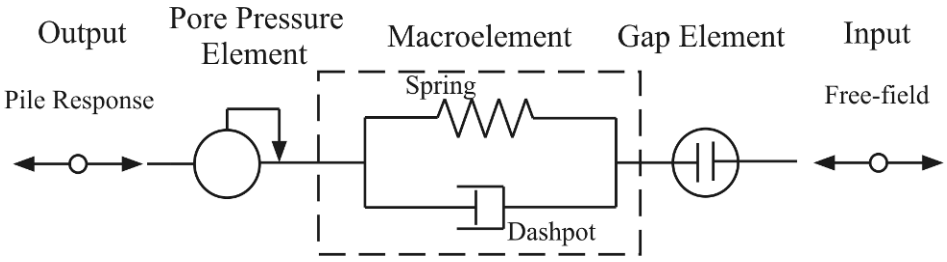

Figure 3.8 Schematic showing components of the nonlinear macroelement (modified from Varun 2010)

3.2.7 Damping

Primary sources of inherent energy dissipation in a structure come from material damping and damping at bearings and joints for which 5% damping in the form of Rayleigh proportional is assigned to the deck, joints, and piles.

Soil damping mechanisms have a different nature from the damping in structures. Energy dissipation of seismic waves in soil media is composed of the contribution of several mechanisms including small-strain material damping, radiation damping, and hysteretic damping due to large nonlinear soil deformations. At very small strain levels, the material damping of soil is generally less than about 10% and is usually considered to be independent of frequency (Aki and Richards 1980, Ishihara 1996, Lai and Rix, 1998). In this study, a material damping ratio of 5% is assigned for small strain levels. The energy dissipation from radiation damping is modeled using the method proposed by Gazetas and Makris (1991) for the vertical direction and by Makris and Gazetas (1992) for the lateral horizontal direction. In these models, the radiation damping is accounted for by using a linear dashpot in parallel with the soil spring. The damping coefficient for the unit length of the pile is given by

$$c = \rho_s V_s a_0^{-1/4} Qd \tag{3.4}$$

where ρ_s is the density of soil, V_s is the shear wave velocity in soil, d is the pile diameter, $a_0=\omega B/V_s$ is the normalized frequency of loading, and Q is a shape factor. For the lateral direction, the value of Q is assigned to be 3 (Badoni and Makris 1996, Varun 2010) and for the vertical direction Q is set to π (Makris and Gazetas

1992). Using the relation in Equation (5), contributions of radiation to soil damping are calculated for each soil layer at the location of soil springs and are assigned accordingly in parallel to macroelements and p-y and t-z springs. Finally, the hysteretic damping of the soil, which is the direct consequence of the nonlinear soil deformations, is automatically captured by the nonlinear hysteretic force-deformation behavior of soil springs in the horizontal and vertical directions.

3.3 Numerical Results

As explained previously, the FE model of the wharf structure and landside crane rail together with the soil springs is modeled in OpenSEES. Modal and nonlinear time-history analyses are performed on the wharf and the methodology and results are discussed in the following sections.

3.3.1 Modal Analysis

In this study, modal analysis of the nonlinear soil-structure wharf system has been carried out to provide basic insights into the system's seismic response characteristics. Soil-structure interaction (SSI) is among a class of engineering problems where damping is no longer of the classical type and finding modal properties requires performing a complex eigenvalue analysis. Assuming that the soil-structure system is in the linear state, the governing equation of motion in the free vibration mode is as follows

$$\mathbf{M}\ddot{u} + \mathbf{C}\dot{u} + \mathbf{K}u = 0 \tag{3.5}$$

where M, C, and K are the nominal mass, damping, and stiffness matrices and u is the vector of system response. The eigenvalue problem associated with this equation can be represented by the $\lambda-$matrix problem (Lancaster, 1966)

$$s_j^2\mathbf{M}\boldsymbol{\varphi}_j + s_j\mathbf{C}\boldsymbol{\varphi}_j + \mathbf{K}\boldsymbol{\varphi}_j = 0 \tag{3.6}$$

where the complex number s_j is the jth eigenvalue and the complex vector φ_j is the jth eigenvector of the system. The eigenvalues, s_j, are the roots of the characteristic polynomial

$$\det[s^2\mathbf{M} + s\mathbf{C} + \mathbf{K}] = 0 \tag{3.7}$$

The roots of the above equation appear in complex conjugate pairs s_k and s^*_k (k=1,2,…,N). The relation between s_k and s^*_k with modal frequencies, ω_k, and modal damping ratios, ξ_k is determined from the associated equation of a single degree of freedom oscillator (Fenves and DesRoches 1994),

$$s_k, s_k^* = -\xi_k\omega_k \pm i\omega_k\sqrt{1-\xi_k^2} \tag{3.8}$$

from which the modal frequencies and damping ratios can be computed as

$$\omega_k = \sqrt{s_k.s_k^*}, \quad \xi_k = -\frac{\mathrm{Re}(s_k)}{\omega_k} \tag{3.9}$$

This analysis is performed in MATLAB for which the mass, stiffness, and damping matrices are required. The mass matrix, M, is found by assembling the lumped nodal masses at the deck level, and the stiffness matrix, K, is found by assembling element stiffness matrices in the global coordinate system. In order to find local

element stiffness matrices, axial and bending rigidities are obtained by section analysis (moment-curvature and axial force-axial strain analyses) for each of the 10 sections defined for the piles. Under normal conditions, the wharf-foundation system is under permanent loads including the weight of the wharf and a portion of the live load. The axial load in structural members induced by permanent loads reduces the local element stiffness under P-Delta effects and consequently elongates modal periods of the structure. A gravity analysis is performed in OpenSEES and the recorded element level forces are used to form the geometric stiffness for each element. The non-classical damping matrix, C, is constructed by superposition of two components: 1) Rayleigh damping for the structural parts of the wharf, e.g., deck, piles, and pile-deck connections and small strain damping in soil and 2) lumped dashpots at the locations where piles interact with surrounding soils through p-y and/or macroelements in the direction perpendicular to the axis of the piles and t-z springs parallel to the pile axis. For the first component, a modal damping ratio of 5% is assigned to the first and second modes of the undamped model. The second component is formed by assembling the damping constants of the lumped dashpots, c_{ij}, found by Equation (3.4) in the same global coordinate system used for constructing the stiffness matrix K.

$$\mathbf{C} = \alpha\mathbf{M} + \beta\mathbf{K} + [c_{ij}] \tag{3.10}$$

where α and β are frequency dependent Rayleigh coefficients.

Constructing the mass, stiffness, and damping matrices in the way explained above, static condensation is performed on stiffness and damping matrices in order to

achieve a reduced-order model. The use of static condensation reduces the size of the model from 1353 degrees-of-freedom in the original model to 22 in the reduced-order model. In order to check the numerical accuracy of the above procedure, a classical modal analysis is performed on the undamped system in MATLAB and OpenSEES. The first five natural periods of the undamped wharf found in MATLAB are 0.264, 0.172, 0.107, 0.060, and 0.036 sec, while the corresponding natural periods from OpenSEES model are 0.264, 0.176, 0.103, 0.047, and 0.033 sec. Good agreement is observed in the natural periods of the wharf derived by MATLAB and OpenSEES. The reduced-order matrices are then substituted into Equation (3.8) and the resulting polynomial equation is solved using MATLAB. The first five mode shapes and the corresponding modal properties computed with the complex eigenvalue analysis are shown in Figure 3.9. Based on these results, a number of observations can be made about the free vibration characteristics of this two-dimensional plane strain wharf model.

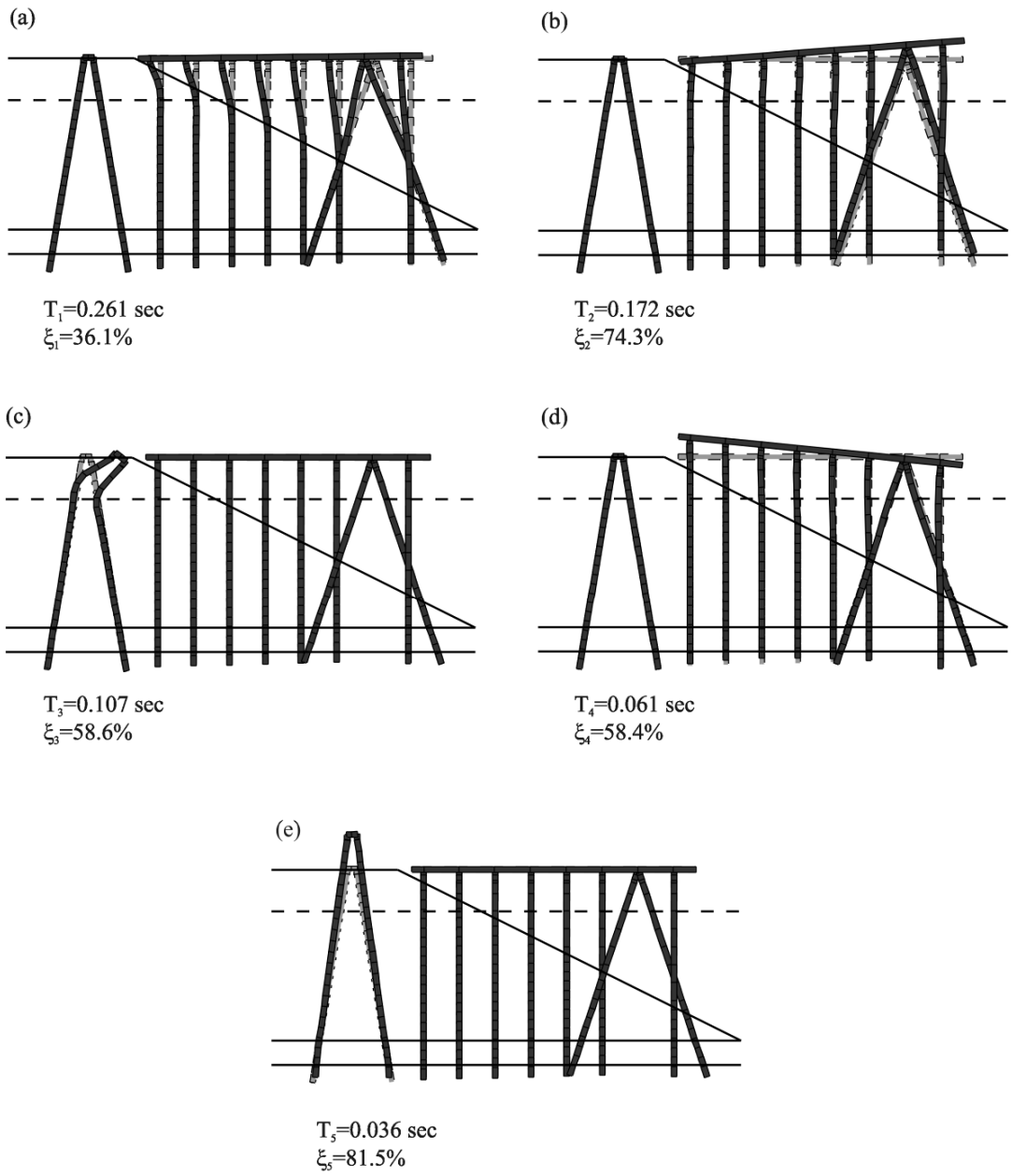

Figure 3.9 The first five mode-shapes of the wharf and landside crane rail with associated natural periods and damping ratios.

The first and the third modes of the wharf are transverse modes with the deck and landside crane rail bending away from the at-rest configuration, respectively. In the second, fourth, and fifth modes, the seaside and landside of the wharf and the landside crane rail move in the vertical direction.

The transverse mode in each of the segments – wharf deck and landside crane rail – is a lower mode compared to the vertical modes in the same segment. The transverse modes engage the bending stiffness of the piles, the axial resistance of batter piles, and the soil resistance within a shallow depth of soil near the surface, while the vertical modes involve the axial stiffness of piles and vertical soil resistance along the entire length of the piles. Therefore, the magnitude of resistance for a unit deck displacement from both piles and soil layers is very large in the vertical direction compared with the transverse direction.

The transverse and vertical modes of the landside crane rail are higher modes of the system compared to their corresponding modes of the wharf segment. This can be attributed to the following factors: (1) the mass per pile ratio in the crane rail is on average about 40% of the ratio in the wharf, and (2) batter piles along the landside crane rail are fully embedded into the soil and therefore the effective length of the piles is short whereas, within the wharf deck, the embedded length of the piles decreases and the free length of the piles increases from landside to seaside.

The natural frequency of the third mode (the transverse mode of the landside crane rail) is higher than the natural frequency of the second mode (the first vertical mode of the wharf deck). Since the embedded length of the seaside piles along the wharf deck is short, a small volume of soil is engaged with the vertical movement of the seaside tip of the deck. This fact together with the two factors explained in the previous paragraph explain why the transverse mode of the landside crane rail corresponds to a higher mode than the seaside vertical mode of the wharf deck.

The modal damping ratios found in this study are very large compared to the modal damping ratios assumed in prior studies for the linear elastic range (Benzoni and Priestley 2003). This can affect the procedures for simplification of the wharf models using equivalent linear elastic models.

Modal damping values associated with the vertical modes are found to be larger than the modal damping values for the transverse modes. This is because a relatively small volume of soil participates in the wharf's transverse modes of vibration, whereas a much larger volume of soil is mobilized when the vertical modes of the wharf are excited.

3.3.2 Pushover Analysis

Force-deformation characteristics of the wharf are studied by performing a nonlinear static pushover analysis on the two segments of the wharf simultaneously. For this purpose, permanent loads are applied vertically at the location of each pile on the deck level. Each vertical point load represents the gravity load of the tributary mass of the deck associated with the corresponding pile and a portion of live loads which are assumed to be 25% of the applied gravity loads. Subsequently, horizontal point loads are imposed at the deck level at each pile location proportional to their tributary mass. The horizontal load pattern represents inertial loads in the first and third modes of the wharf where the wharf deck and landside crane rail move horizontally from the at-rest configuration. In the absence of ground displacements imposed on the free end of soil springs, pushover analysis only accounts for inertial loads induced by acceleration in the superstructure and therefore kinematic loads will be ignored.

The total force versus deck displacement for the wharf and landside crane rail is shown in Figure 3.10a. The total capacity of the wharf and the crane rail are found to be 1051 kN and 706 kN with the yield displacement of 4 cm and 1.5 cm. The yield displacement corresponds to the displacement where 80% of the capacity is reached.

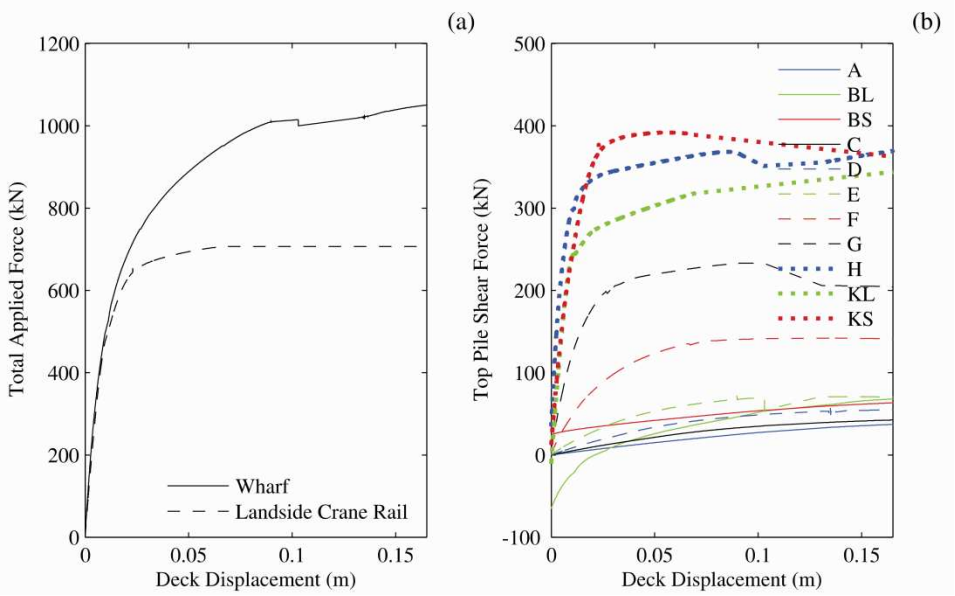

Figure 3.10 Force-deformation response of (a) wharf and landside rail and (b) individual piles.

The force-displacement relation of each pile which is the contribution of the pile in the total force-displacement behavior of the wharf and landside crane rail is shown in Figure 3.10b. The application of vertical permanent loads prior to the horizontal pushover loads, induces shear forces in the landside batter piles in the opposite direction of the pushover loads which induces negative initial forces in these piles.

Moving from landside to seaside of the wharf, the total length of the piles and the ratio of the free length to the embedded length increases. The inflection point in each pile deformation profile under monotonically increasing pushover loads on the

deck level is close to the soil surface. An approximate substitute for soil flexibility effects on piles is the equivalent depth to fixity (Priestley, 1996) approach in which the system is modeled as an equivalent, fixed base, with the fixity point at approximately four to five pile diameters below ground surface. Based on force-deformation relations for a beam with fixed ends, the yield displacement is proportional to the square of the effective length of the pile, while the yield force of the piles is inversely proportional to the effective length. This trend is observed in the results shown in Figure 3.10b. For the batter piles, the axial stiffness of the pile and t-z soil springs contributes to the lateral resistance of the piles against pushover loads.

The ductility demand of the sections is evaluated by simply finding the maximum curvature for each section during pushover analysis and normalizing it by the corresponding yield curvature. The profile of the ductility demand on the piles is shown in Figure 3.11. The definition of the yield curvature is adopted from the study by Park and Falconer (1983) on partially pre-stressed concrete sections where the yield curvature is defined as the curvature at the intersection of the nominal moment Mn and a line passing through the origin representing the moment-curvature response of a pile with a constant flexural rigidity equal to that computed at 0.75 M_n. The nominal moment resistance M_n is defined as the section moment when the extreme fiber concrete compressive strain is 0.003. Similarly, the curvature at the onset of plastic hinge formation, plastic curvature, is defined as the curvature when the section reaches the nominal moment resistance M_n. The successive yielding of piles is also indicated in Figure 3.11 with solid dots. The

yielding of piles and pile-deck connections starts with the yielding of the connection of pile H to the deck followed by the yielding of the in-ground section of the pile H close to the soil surface. As pushover loads increase, the pile-deck connections and in-ground sections of piles G, F, E, KL, KS, and D successively yield.

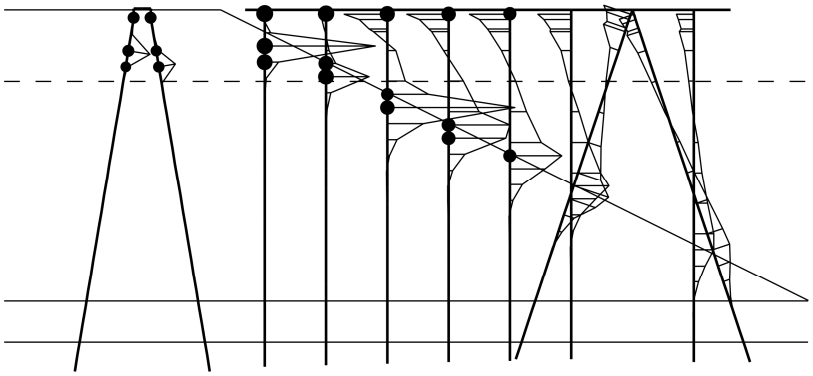

Figure 3.11 Profile of curvature demand with the location of the yielded pile sections and pile-deck connections.

The deformed shape of the wharf at the end of the pushover analysis is shown in Figure 3.12. The white dots in the figure indicate the location of the plastic hinges.

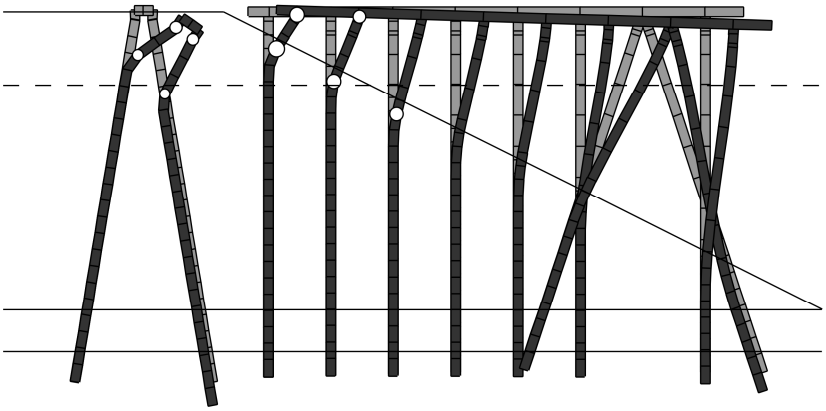

Figure 3.12 Final deformed shape of the wharf with the location of plastic hinges.

3.3.3. Time-History Analysis

Nonlinear time-history analyses of the response of the wharf-soil system for both high and moderate levels of ground shaking have been carried out. This section presents the results from these analyses.

3.3.3.1. Analysis Procedure

This analysis has been carried out according to the following three step approach (Idriss et al. 1979).

1. Firm-site input motions are applied to a model of the soil embankment and subsurface soil materials (excluding the presence of the wharf) in order to compute the site-specific free field ground motion and pore water pressure time histories.

2. To represent effects of soil-structure interaction, soil materials are modeled as a series of nonlinear soil springs that are distributed along the length of each of the piles that supports the wharf deck and landside crane rail. Properties of the soil springs including force-deformation characteristics and visco-elasticity are found based on the associated soil layer properties.

3. The plane strain model of the pile-supported wharf deck and landside crane rail from Step 2 are subjected to the site-specific free field ground motion and pore pressure time histories from Step 1, which are applied to the end of each soil spring along the length of the piles. This enables the analysis of the nonlinear dynamic response of the wharf at each node point in the model, including effects of liquefaction of the surrounding soil materials.

Each of these steps is further discussed in the paragraphs that follow.

3.3.3.2. Firm-Site Input Motions

Firm-site input motions for the free field site response analyses conducted under Step 1 consist of two sets of accelerograms selected from the database used to develop the Next Generation Attenuation of Ground Motions (NGA) project (Chiou et al. 2008). One set represents strong levels of ground shaking and corresponds to the horizontal and vertical accelerograms NGA0753 from the NGA strong motion record database. The peak ground accelerations (PGA) of this ground motion are 0.64 g and 0.48 g in the horizontal and vertical directions respectively. These motions were recorded during the 1989 Loma Prieta earthquake (M_w of 6.9) at the Corralitos station whose closest distance to the fault rupture was 3.9 km. The second set of accelerograms represents a more moderate level of ground shaking and corresponds to horizontal and vertical accelerograms NGA1057 from the NGA database with PGA of 0.14 g and 0.08 g in the horizontal and vertical directions respectively. These motions were recorded during the 1994 Northridge Earthquake (M_w of 6.4) at the Playa Del Ray station whose closest distance to the fault rupture was 31.7 km. Time-histories of these two sets of horizontal and vertical accelerograms and the power spectral densities (PSD) of the motions in the horizontal direction are shown in Figure 3.13.

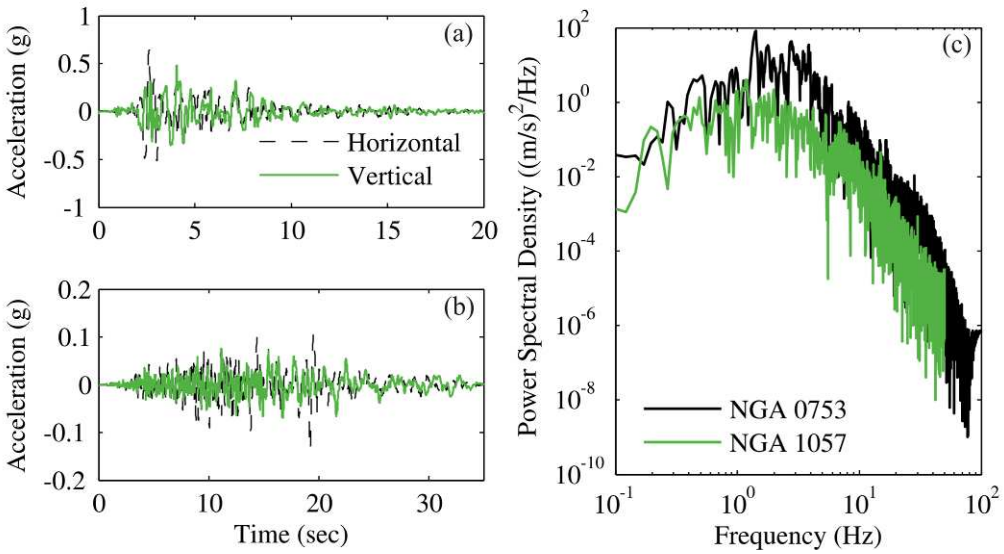

Figure 3.13 Characteristics of the selected ground motions NGA0753 and NGA1057 at bedrock: (a) accelerograms NGA0753, (b) accelerograms NGA1057, and (c) PSD of NGA0753 and NGA1057.

3.3.3.3. Free-Field Site Response Analysis

The free-field analysis of the soil embankment conducted under Step 1 of the analysis procedure was carried out by Vytiniotis et al. (2010). This analysis used a critical elasto-plastic constitutive soil model proposed by Dafalias and Manzari (2004) that has been implemented in OpenSEES. The model is able to realistically capture the stress-strain behavior of potentially liquefiable sands. More details about the soil model and free-field simulation procedure and results can be found in Vytiniotis et al. (2010). In order to have a better understanding of the seismic behavior of the wharf during two aforementioned ground motions, some of the important features of the embankment response are explained here.

Contours of maximum soil displacement and maximum excess pore water pressure ratio in the wharf embankment during the NGA0753 and NGA1057 earthquakes are shown in Figures 3.14a-d. The distribution of excess pore pressure for NGA0753

(Figure 3.14a) shows three zones with excess pore pressure ratios greater than 0.9. These regions are located 1) at the location of the landside crane rail from the free water level to the interface of the loose and dense sand layers, 2) in the middle of the embankment slope close to surface, and 3) at the toe of the embankment. The same regions of high excess pore pressure ratios are observed for NGA1057 (Figure 3.14c) but with magnitudes lower than 0.8. Contours of maximum soil displacement are shown in Figures 3.14b,d for NGA0753 and NGA1057, respectively. Noticeable in these figures is the difference in the magnitude of soil displacement response for the two motions where the slope moves as much as 1.06 m during NGA0753, while the maximum response of the embankment is limited to 0.19 m during NGA1057. However, the isolines of the maximum displacement response for the two ground motions follow the same pattern and are parallel to potential failure surfaces within the slope.

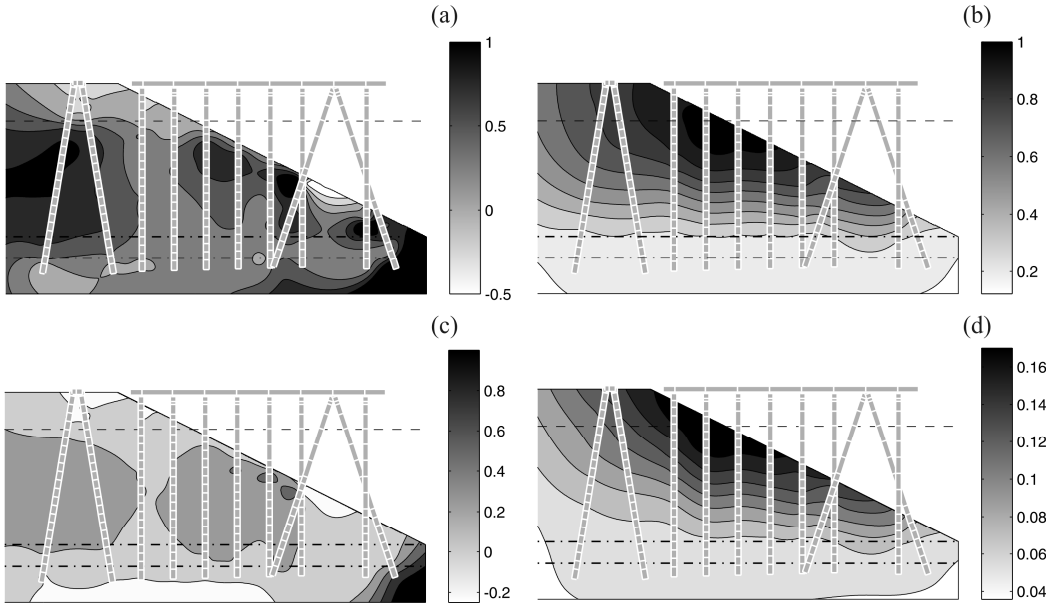

Figure 3.14 Contours of free field site soil response in the vicinity of the wharf deck: (a) maximum PWP ratio for NGA0753, (b) final soil displacement for NGA0753, (c) maximum PWP ratio for NGA1057, and (d) final soil displacement for NGA1057.

Displacement time-histories of node C1 near the landside edge of the embankment (Figure 3.1) during NGA0753 and NGA1057 are shown in Figure 3.15. Compared to the 10-second duration of the strong ground motion of NGA0753, the slope continues to deform until 40 seconds, where it reaches almost a steady state. When excess pore pressures in the soil embankment are large enough to cause liquefaction, a significant strength loss occurs in the soil. In sloping embankments, this will be followed by lateral deformations due to static shear stresses induced by the sloping grounds which are referred to as lateral spreading. After strong ground shaking ceases, if the post-liquefaction shear strength remains less than the static shear stress, deformations continue until equilibrium is achieved. This type of damage is called flow failure and is one of the eight types of failures associated with liquefaction during earthquakes (National Research Council 1985). For NGA1057, lateral soil deformations stop increasing after 25 seconds, which is the duration of the input motion.

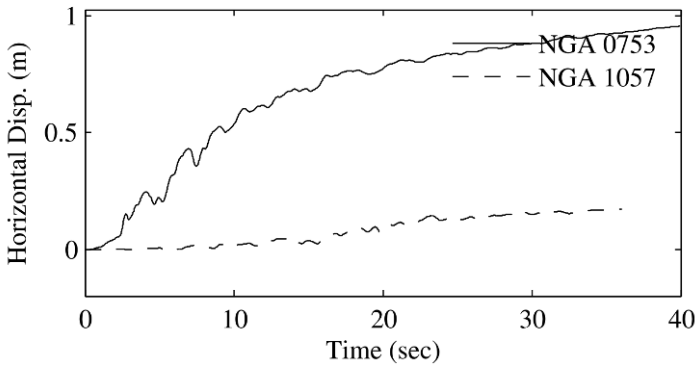

Figure 3.15 Horizontal soil displacement at node C1 (Figure 3.1) for NGA0753 and NGA1057.

3.3.3.4. Soil-Structure Interaction

In the analysis of soil-structure interaction effects under Step 2 of the analysis procedure, effects of the structure on surrounding soil are categorized into local and global effects. Excess pore pressures around the piles are the result of pore pressure generation in the far-field and the localized pore pressure due to soil-pile interaction in the near-field. Results of centrifuge tests in a number of studies indicated the formation of a zone around the piles with a different pattern of excess pore pressure from those in the far-field (Gonzalez et al. 2009 and Wilson et al. 2000). These near-field local effects are accounted for in the formulation of the macroelement used in these analyses by updating the total excess pore pressure close to the face of the piles based on the amount of shear work done as a consequence of the drained response in the macroelement (Varun 2010). The global effect of the piles on the surrounding soil is triggered when liquefaction in the soil embankment leads to the lateral movement of the slope. During the lateral movement of the embankment, the piles develop reaction forces called pinning forces either due to superstructure constraints or embedment in non-liquefiable soil layers (Boulanger et al. 2003). These pinning effects can be considerable when the volume of the moving soil is small compared to the available pinning forces, e.g. bridge embankments. However in cases where a large volume of soil is susceptible to the lateral movement, e.g. in wharf embankments, pinning forces of the piles cannot prevent the lateral movement of the embankment. This has been reported by Takahashi et al. (1998) where embankment soils in centrifuge tests with and without piles moved laterally and their time-history displacement response closely matched, showing the negligible effect of pile pinning forces in such cases.

3.3.3.5. Time-history responses of wharf components

Deck

Horizontal and vertical displacement time-histories of the wharf at the location of the crane rails – nodes C2 and C3 (Figure 3.1) – are shown in Figure 3.16a-d. During NGA0753 which corresponds to a large level of ground shaking, a large difference in the maximum displacement response of the seaside and landside crane rail is observed for both horizontal and vertical directions. This was suggested by the pattern of isolines in the soil deformation contour in Figure 3.16b where the flow failure of the dyke slope induces large deformations in the slope while other zones of the embankment undergo less deformation; thereby a considerable difference is observed in the displacement response of the wharf and landside crane rail. The large relative displacement of the two segments, 29 cm in the horizontal direction and 8 cm in the vertical direction, may cause derailment of the crane legs which would result in disruption to crane operations at the port. Although the same pattern is observed for NGA1057 which corresponds to moderate levels of ground shaking, the smaller differences of the displacement response of the two segments in both horizontal and vertical directions 7 cm and 4 cm respectively can be attributed to the smaller level of deformations of the embankment soil.

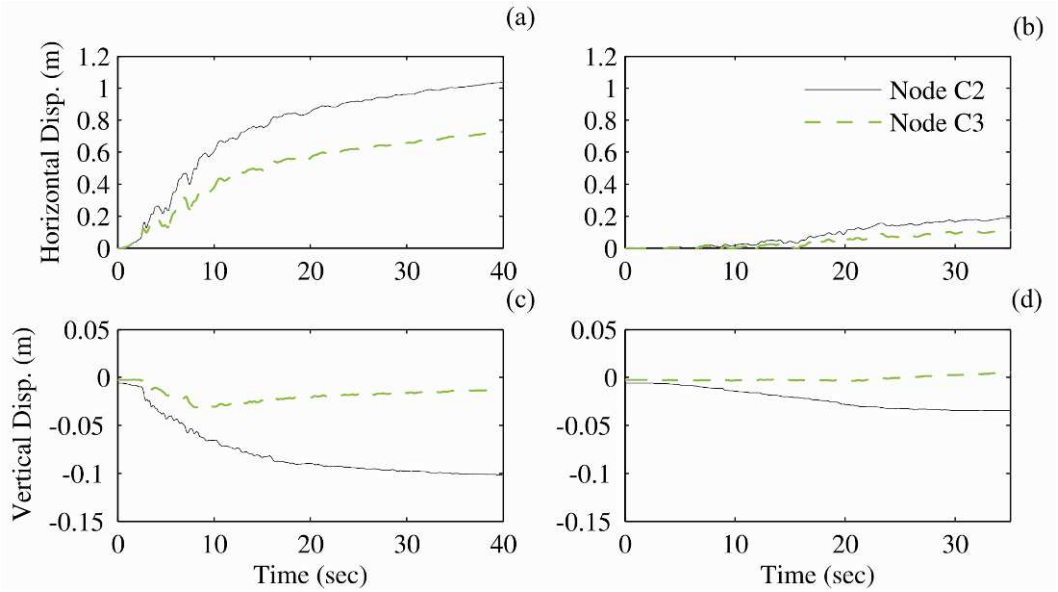

Figure 3.16 Displacement time-histories of node C2 and C3: (a) horizontal displacement for NGA0753, (b) horizontal displacement for NGA1057, (c) vertical displacement for NGA0753, and (d) vertical displacement for NGA1057.

Acceleration time-histories of nodes C1 and C2 are presented in Figures 3.17a-d. For NGA0753, acceleration of the landside crane rail almost matches the acceleration response of the seaside crane rail in the horizontal direction but with smaller magnitude (Figure 3.17a). The maximum horizontal acceleration of the crane rails in the seaside and landside of the wharf are 0.40g and 0.37g respectively which when compared to the PGA of 0.64g at bedrock are reduced. Contrary to the horizontal direction, the maximum vertical acceleration of the landside crane rail, 0.10g, is small compared to the corresponding response of the seaside crane rail, 0.16g. Comparing these values with the PGA of bedrock in the vertical direction, 0.48g, indicates a considerable reduction. Similar observations are made for acceleration responses of the crane rails for NGA1057. In the horizontal direction, the maximum acceleration of seaside and landside crane rails are 0.14g and 0.09g respectively. In the vertical direction, the maximum acceleration of crane rails in

the seaside and landside crane rails are 0.02g and 0.01g respectively which are very small compared to the corresponding PGA of 0.08g at bedrock.

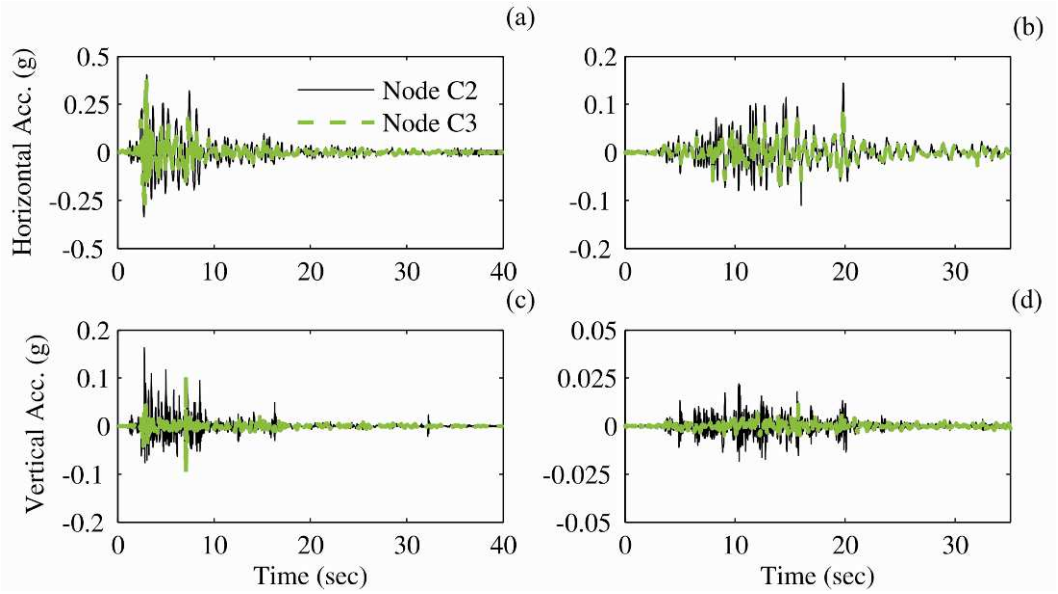

Figure 3.17 Acceleration time-histories of node C2 and C3: (a) horizontal acceleration for NGA0753, (b) vertical acceleration for NGA0753, (c) horizontal acceleration for NGA1057, and (d) vertical acceleration for NGA1057.

Pile-deck connections

Figures 3.18a-c and 3.19a-c show the response of the pile-deck connection in pile H – the most landside pile of the wharf (Figure 3.1) – during NGA0753 and NGA1057 respectively. The time-history rotation response of the connection in Figure 3.18a and 3.19a indicate an almost monotonic increase in the connection rotation response that occurs during the monotonic movement of the wharf toward the sea (Figure 3.16a,b). However, the maximum rotation of the connection during NGA1057 is 0.0016 rad which is about three times smaller than the maximum rotation response of 0.0042 rad during NGA0753. Time-histories of the moment response of the connection during NGA0753 and NGA1057 are shown in Figures 3.18b and 3.19b respectively. It is observed that the moment in the connection

increases consistently with the connection rotation in both earthquakes, however the connection moment during NGA0753 reaches the plastic moment limit of the connection while the rotational deformation of the connection during NGA1057 is not large enough to push the connection to pass the plastic limit. Moment-rotation responses of the connection are shown in Figures 3.18c and 3.19c in which the residual state of the connection are indicated by a white dot.

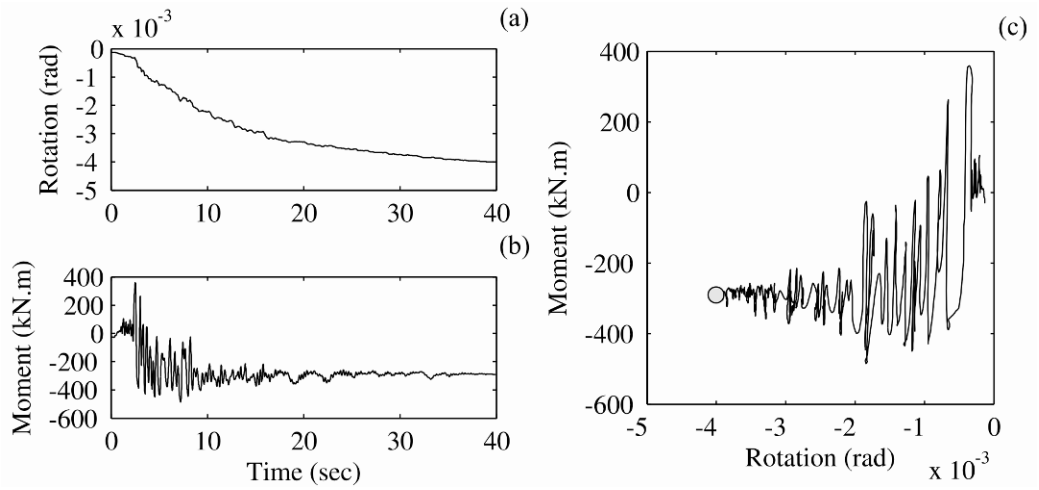

Figure 3.18 Pile H connection response to NGA0753: (a) time-history of connection rotation, (b) time-history of connection moment, and (c) moment-rotation behavior of the connection.

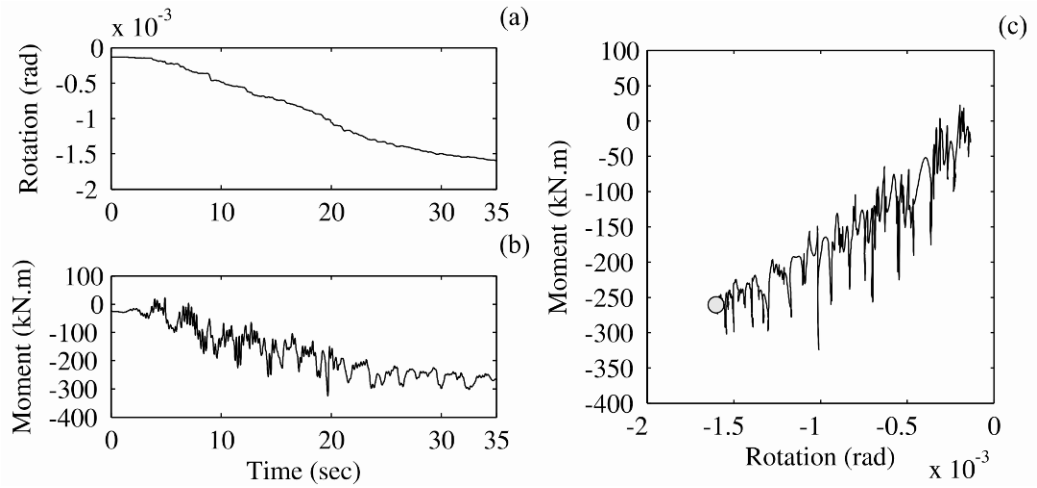

Figure 3.19 Pile H connection response to NGA1057: (a) time-history of connection rotation, (b) time-history of connection moment, and (c) moment-rotation behavior of the connection.

Piles under assumed severe level of ground shaking

The profile of curvature ductility demand of the pile section together with the location of the yielded sections and yielded pile-deck connections for NGA0753 are shown in Figure 3.20a. Ductility demands are evaluated by simply finding the maximum curvature of each section during nonlinear time-history analysis and normalizing it by the corresponding yield curvature of the section.

From the curvature ductility demand profile, piles BS, C, D, and E experience large deformations during the earthquake with maximum responses occuring near the boundary between loose and dense sand layers. This was suggested by the contour of free-field soil displacements in Figure 3.14b which shows differing levels of soil deformation immediately above and below the interface of sand layers. Liquefaction in the top loose sand layer imposes large curvature demands (and corresponding large bending moments) on the piles through kinematic constraints

of soil-pile interaction. These large curvature demands are resisted by the embedment of the pile in the underlying dense sand and stiff clay layers.

The other components that are susceptible to large deformations are pile-deck connections. The resisting soil pressures in the underlying dense sand and clay layers provide an almost clamped condition in piles near the interface of sand layers. As a consequence, the lateral movement of the wharf within these dense layers is constrained and the moment resisting pile-deck connections undergo large deformations to accommodate soil displacements of the liquefied sand. Finally, moving from seaside to landside piles, soil pressures on the face of the piles increase consistently with soil deformation for each depth which together with the lateral deck resistance provided by seaside piles especially batter piles BL and BS provide a nearly fixed-fixed end conditions with distributed member loads for landside piles. This results in the formation of the third zone of yielding components in the middle of landside piles below the embankment surface (Figure 3.20a).

The successive yielding of piles sections and pile-deck connections are also shown with dots in Figure 3.20a where the larger size of a dot indicates earlier occurrence of the yielding in the connection or section. The first yielding occurs in the piles sections close to the interface of the loose and dense sand layers in piles BL, C, and D followed by yielding of the connection of the batter piles in the landside crane rail. The next part of the wharf that undergoes yielding is the pile-deck connection of pile H. The deformation of the wharf continues by yielding of the piles sections

in the bottom of the loose sand and the rest of the pile-deck connections followed by yielding of the landside piles section near the embankment surface.

The final deformed shape of the wharf at the end of NGA0753 with the location of plastic hinges indicated by white dots is shown in Figure 3.20b (wharf deformations are magnified by a factor of 2). As previously explained, the kinematic constraints in soil-pile interactions force the wharf to deform in a consistent manner with the soil. The landside crane rail and the wharf move horizontally in response to the horizontal displacement of the soil induced by the flow failure of the slope. Locations of plastic hinges in the wharf are also shown in Figure 3.20b. The first plastic hinge occurs in pile H connection to the deck followed by the formation of plastic hinges near the interface between the liquefied and non-liquefied sand layers. This agrees well with the damage observed in the wharf at the Port of Kobe during Hyogo-ken Nambu (Kobe) earthquake where large deformations occurred in piles close to the wharf deck and at the interface of liquefied and non-liquefied sand layers (Matsui and Oda 1996, Tokimatsu and Asaka 1998). As the wharf continues to deform, other pile-deck connections including the connection of the batter piles to deck undergo plastic deformations which are followed by the formation of the third zone of plastic hinging in the middle of the landside piles below the embankment surface (Figure 3.20b).

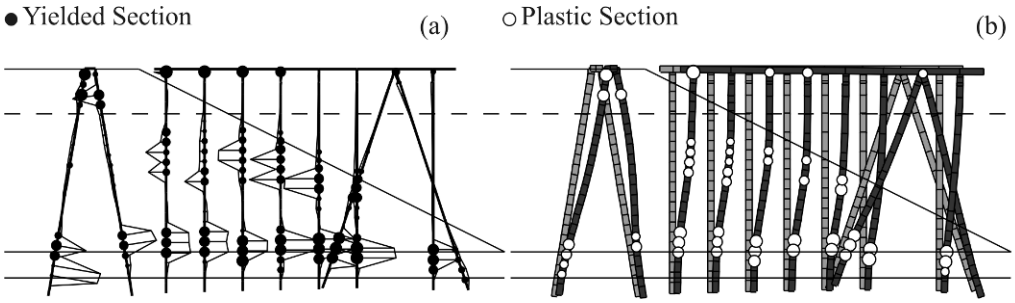

Figure 3.20 Wharf and crane rail response during NGA0753: (a) profile of the maximum curvature ductility demand and (b) final deformed shape of the wharf with the location of plastic hinges.

Piles under assumed moderate level of ground shaking

The profile of the maximum curvature ductility demand of the piles sections in the wharf and landside crane rails during NGA1057 is shown in Figure 3.21a. Curvature ductility ratios are magnified 20 times compared to the ratios of curvature ductility for NGA0753. It is observed that only the pile-deck connection of the batter pile KL of the landside crane rail and the connection of pile H yield. However, the pattern of the curvature ductility demand distribution shows the three zones with relatively large deformed components observed in NGA0753. The deformed shape of the wharf at the end of NGA1057 is shown in Figure 3.21b. Similar to Figure 3.20b, wharf deformations are magnified by a factor of 2. It is seen that during NGA1057, the wharf slightly deforms compared to the wharf deformations during NGA0753 and no plastic hinge is formed in the wharf and landside crane rail.

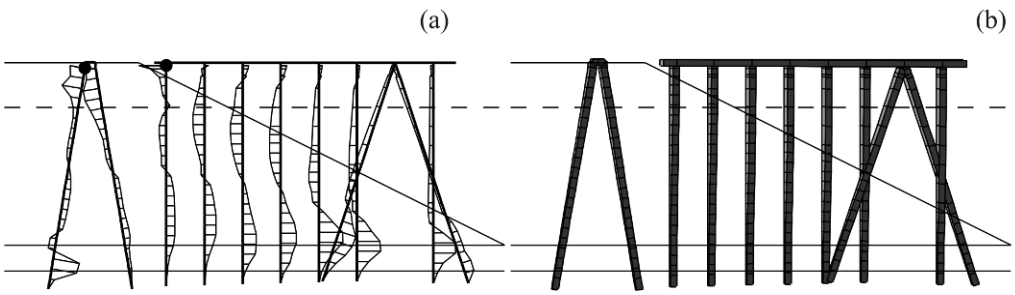

Figure 3.21 Wharf and crane rail response during NGA1057: (a) profile of the maximum curvature ductility demand and (b) final deformed shape of the wharf with the location of plastic hinges.

Batter piles

As noted previously, the lateral movement of the wharf is resisted by the flexural and axial-flexural resistance of vertical and batter piles respectively. In these wharf analyses, effects of axial deformations on the seismic performance of the batter piles are accounted for by finding the limiting strains that correspond to the onset of the pile yield and plastic moment curvatures and comparing them with the demand axial strains of the pile cross section as computed from the nonlinear time-history analysis.

The other type of failure associated with batter piles is pile “pullout” from the soil. Under lateral displacements of the wharf, a number of batter piles experience tension forces accompanied by axial pile deformations as well as deformations in the soil close to the surface of the pile. During large seismic events, surrounding soil deformations parallel to the pile shaft may become large enough to “soften” the soil and substantially reduce its ability to resist additional axial displacement of the pile. This will increase the susceptibility of the pile to pullout from the soil. In this wharf seismic analysis, the occurrence of batter pile pullout is checked by

comparing the axial tension forces in batter piles to the sum of the ultimate capacities of t-z springs attached to the pile.

From the configuration of the wharf in the embankment, it is expected that Pile BL (Figure 3.1) experiences large axial tension forces during seismic events. During NGA0753, the axial tension forces in Pile BL reached 234 kN which approaches the ultimate pullout capacity of the surrounding soil, which is 236 kN.

Macroelements

The force-deformation response of the macroelement at four depths along pile D (Figure 3.1) together with the time-histories of excess pore water pressure ratio and deformation of the macroelement for NGA0753 and NGA1057 are shown in Figures 3.22 and 3.23, respectively. The deformation of the macroelement is defined as the soil displacement at the free-field end of the element subtracted from the corresponding displacement at the end attached to the pile with the positive direction toward the sea. Comparing the force-deformation of the macroelements during two earthquakes at each depth, it is observed that macroelements undergo large deformations and consequently impose larger forces to the piles in NGA0753 compared to NGA1057. This observation is consistent with the levels of deformation that the wharf experiences during both earthquakes.

The other noticeable phenomenon in the force-deformation response of the macroelements at depths 4.64 m and 7.64 m is the force relaxation at the end of both earthquakes (Figures 3.22, 3.23). When a pile moves relative to the surrounding soil, the lack of tension resisting forces between the pile surface and

the soil causes the formation of gap in the back of the piles. In cohesionless soils, the gap will be filled in with collapsing soil and therefore the reloading stiffness will be smaller than the unloading stiffness which in small cyclic loops results in force relaxation. This phenomenon is captured through the Bouc-Wen hysteresis model in the formulation of the macroelement (Varun 2010).

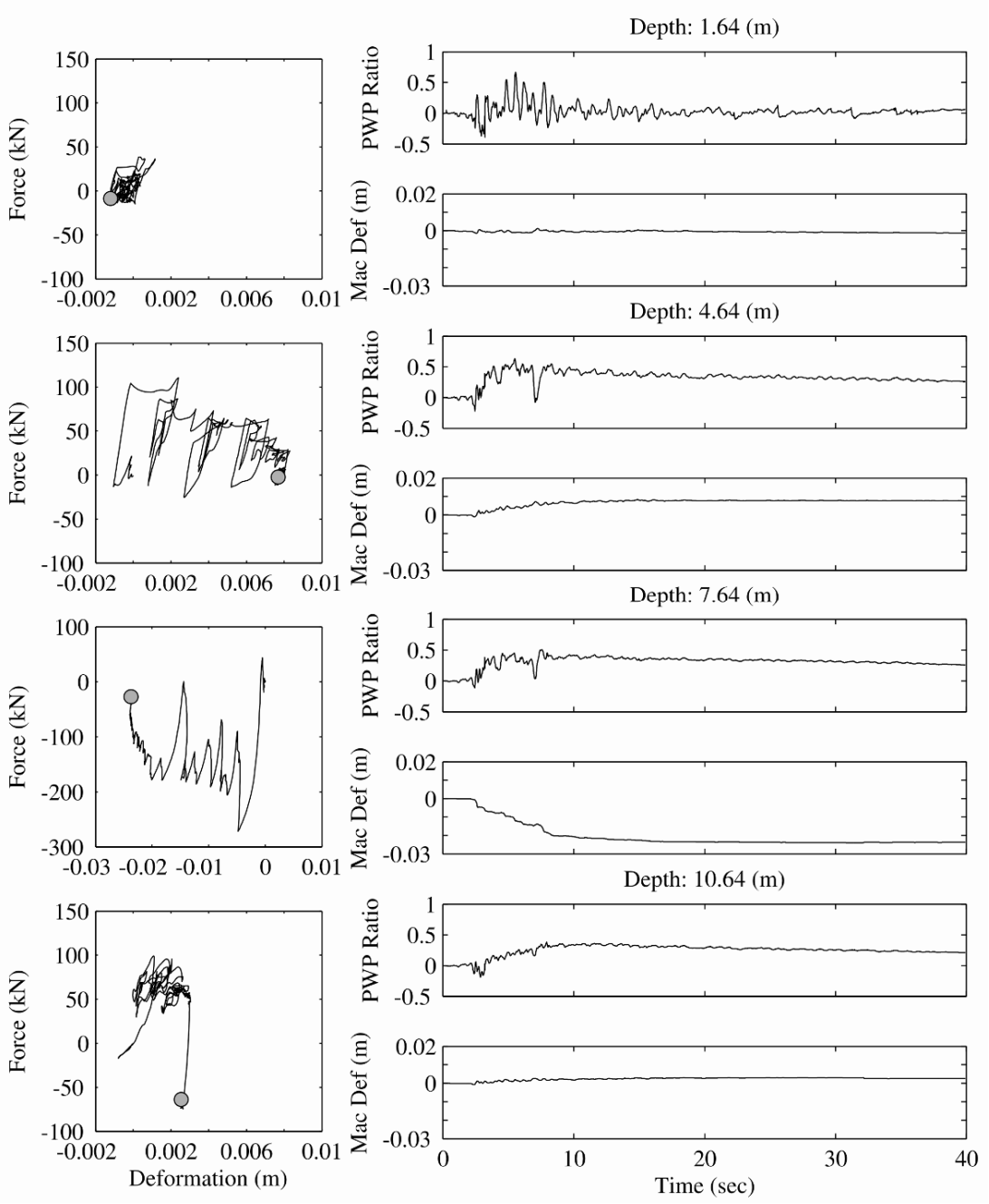

Figure 3.22 Force-deformation response of the macroelement in four depths along pile D (Figure 3.1) together with the time-histories of excess pore water pressure ratio and deformation of the macroelement during NGA0753.

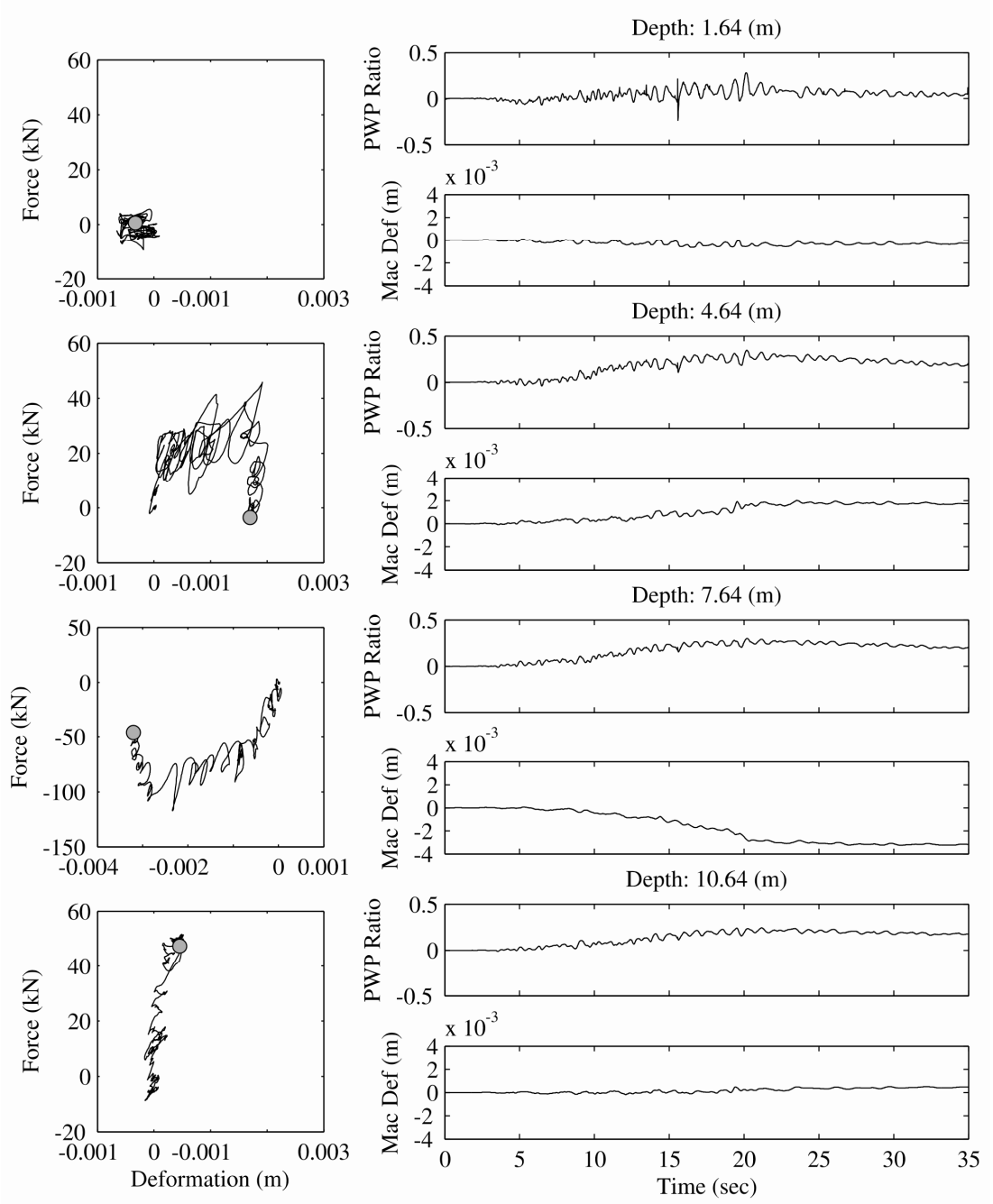

Figure 3.23 Force-deformation response of the macroelement in four depths along pile D (Figure 3.1) together with the time-histories of excess pore water pressure ratio and deformation of the macroelement during NGA1057.

3.4. Closure

Dynamic characteristics and seismic performance of a typical marginal wharf in potentially liquefiable soils has been studied using numerical simulations of the 2D plane strain structure model that incorporates new and advanced structural and soil-structure interaction modeling procedures. The configuration, material properties, and structural detailing of this wharf correspond to seismic designs carried out during the late 1960s and early 1970s using design procedures that are much less robust than current procedures. Because such wharf structures are commonly encountered in seaports located in earthquake-prone areas along the west coast, it is important to develop an understanding of the seismic performance and vulnerability of these structures. The analyses described in this research provide important insights along these lines.

The overall 2D model used in these analyses features advanced models of the piles, the pile-deck connections, and interaction of the wharf with potentially liquefiable soils. Modal properties of the wharf including mode shapes, modal periods, and modal damping ratios were studied by performing a complex eigenvalue analysis on the wharf. The main conclusions of the modal analysis are:

1. The first and third modes are transverse modes of the wharf landside crane rail respectively. The second, forth, and fifth modes are vertical modes where seaside and landside of the wharf and the landside crane rail move vertically.

2. Modal damping ratios of the wharf are very large compared to the 5% modal damping ratio has traditionally been used in most earthquake analysis

problems. The complex eigenvalue analysis indicates that the damping ratios range from 36.1% to 81.5%.

3. Since large volumes of soil are involved in the movement of the wharf in the vertical direction, vertical modes have larger damping ratios compared to transverse modes.

The nonlinear seismic analysis of the wharf subjected to the strong level of ground shaking showed the occurrence of significant liquefaction of the surrounding soil materials and the following effects on the wharf structure;

1. The liquefaction-induced movements of the embankment soil under the effect of gravity and seismic loads imposes large deformations in the piles and the pile-deck connections that are sufficient to severely damage the wharf structure when it is subjected to strong levels of ground shaking. Therefore, it is important to consider the liquefaction potential of the embankment and any underlying fills during the seismic performance evaluation of wharves of this vintage.

2. The analysis results also showed large liquefaction-induced values of relative horizontal displacements between the structurally separated landside crane rail and the wharf deck (which supports the waterside crane rail). This is particularly important since even small relative displacement between the landside and waterside crane rails can cause crane derailment and damage.

3. The wharf structure was severely damaged. This damage was located within: (a) pile sections near the boundary between loose and dense sand

layers, (b) pile sections close to the surface of the embankments, and (c) pile-deck connections.

4. Batter piles experience large axial forces in the liquefied case where tension forces may cause pullout of batter piles from soil.

5. Liquefaction was an important source of damage to piles. Therefore, improvement of the surrounding soils to reduce their potential for liquefaction during future earthquakes should be an important element of seismic retrofit programs for wharf structures of this vintage. Another seismic retrofit element that should be considered for these wharf structures is the construction of grade beams to connect the landside crane rail and the wharf deck that will eliminate relative displacement of these elements.

Analysis of the nonlinear response of the wharf to the moderate level of ground shaking considered in this study showed the following results.

1. This level of ground shaking did not cause liquefaction of the surrounding soil materials.

2. Damage to the wharf structure was minor.

CHAPTER 4

DYNAMIC INTERACTION BEHAVIOR OF PILE-SUPPORTED WHARVES AND CONTAINER CRANES

4.1 Introduction

Seismic performance of wharf-crane systems is one of the key factors in the functionality of the ports in the aftermath of earthquake events. From the structural and geotechnical engineering perspective, any seismic performance evaluation of seaports requires an understanding of the behavior of each of the constitutive components including foundation, wharf, and crane and their interaction within the system. As mentioned in previous chapters, the seismic response of wharves has been investigated in a number of research studies using numerical simulations as well as centrifuge tests. However none of these studies included the crane model in their numerical or experimental investigations. The reason for this is that researchers believe that cranes act as tuned mass dampers, thereby reducing the response of the underlying wharf. (POLA 2007). Based on the argument in the latter case, excluding the crane model leads to conservative estimates of the wharf response. As a consequence, despite the significant body of research on the seismic performance of wharves, very limited research studies have been conducted to characterize the dynamic interaction behavior of wharves and container cranes. Chaudhuri et al. (2009) studied the seismic performance of a container crane supported by a gravity-type quay wall. In their approach, the interaction problem between the wharf and the crane is treated in two stages. First, the seismic response of the wharf excluding the crane is evaluated for a number of bedrock motions. In the second step, the response of the wharf at the deck level is used as the input

excitation at the base of the crane model. Although this method considers the interactive nature of the problem more realistically compared to other investigations, the feedback of the crane dynamics on the behavior of the wharf is ignored.

Chapter III studied the dynamic characteristics and seismic performance of a typical marginal wharf in potentially liquefiable soils by using numerical simulations of the 2D plane strain structure model. This chapter focuses on characterizing the dynamic interaction of the pile-supported wharf model of chapter III and a typical container crane and the contribution of this interaction on the response of the wharf. To achieve this goal, a systematic procedure is developed to model the crane by incorporating a realistic representation of a sliding/uplift capable model of a container crane. Subjecting the wharf to time histories of ground displacement and excess pore water pressures within the underlying soil embankment and performing nonlinear time-history analyses, it is found that unlike the conclusion of former studies, the interaction between the wharf and crane may amplify the response of the wharf considerably. These results suggest that wharf–crane interaction should be given more careful consideration than is currently required when evaluating the seismic response of a wharf system. After presenting the numerical modeling procedure, the chapter studies the dynamic interaction of the wharf and crane in two orthogonal horizontal and vertical directions followed by a numerical investigation of the wharf-crane response for several simplified crane models including rigidly attaching 5% of the wharf mass, the wharf with crane gravity loads, and a pinned base portal frame crane idealization. The chapter concludes by presenting analytical bounds on the spectral acceleration response of the wharf to predict the occurrence

of nonlinear crane response features including sliding, uplift, and yielding of the portal frame. The accuracy of these bounds in response prediction of container cranes is evaluated by a series of nonlinear time-history analyses on the sliding/uplift crane model mounted on top of the wharf.

4.2 Container Cranes

Container cranes are an important component of container ports which are responsible for loading and unloading of intermodal containers from containerships. The configuration of a typical container crane is shown in Figure 4.1.

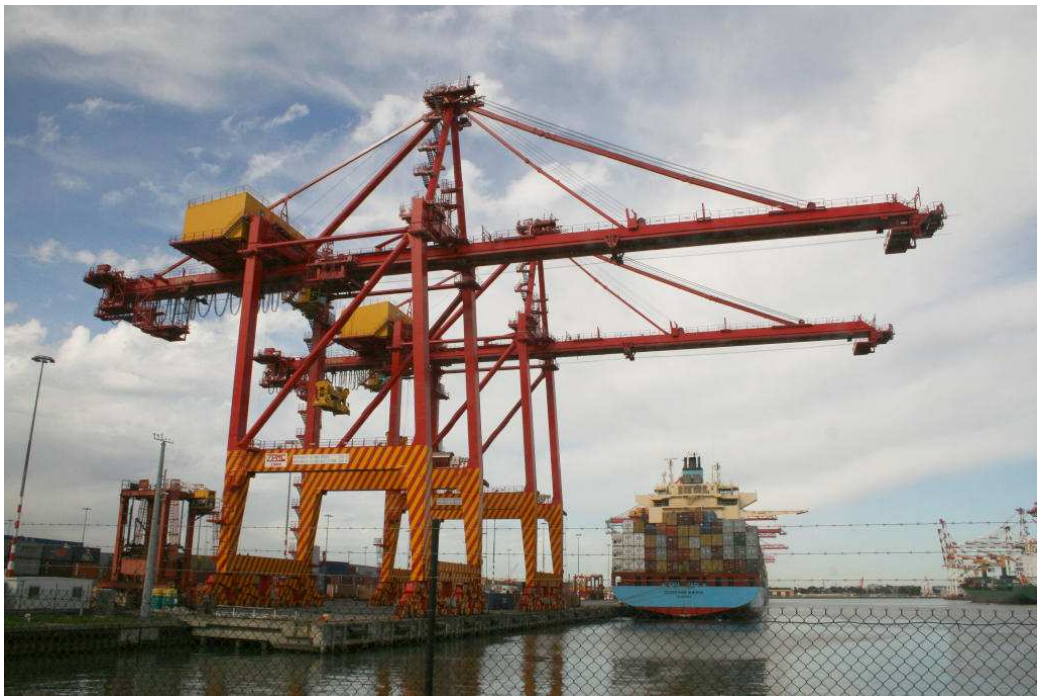

Figure 4.1 Typical container crane, Swanston dock container crane, Melbourne, Australia (photo courtesy of http://marineshiping.blogspot.com).

Container cranes are constructed in similar configurations which consequently results in them having similar dynamic response characteristics. This feature of construction is used in a number of studies to classify container cranes into a number of representative groups within which cranes will respond similarly. This

study considers a modern jumbo crane (J100) which is representative of the class of cranes ranging from *Large Post-Panamax* up to moderate *Super Post-Panamax* cranes (Kosbab 2010). The configuration of the J100 crane along with its dimensions is shown in Figure 4.2.

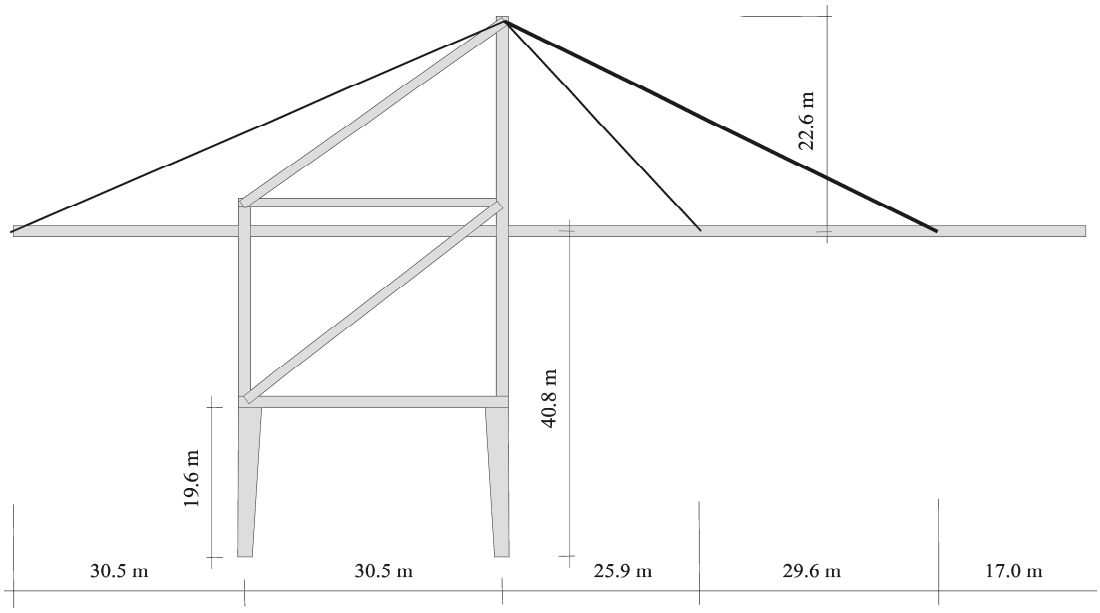

Figure 4.2 Configuration of J100 container crane.

The critical dynamic response characteristics of a typical container crane subjected to seismic accelerations are its portal sway deformation and a sliding/uplift response (Kosbab et al. 2010a). The portal sway deformation is an intuitive response where large transverse deformations of the crane are strongly concentrated at the portal beam level due to inherent flexibility of the portal frame lower section relative to the rest of the structure (Kanayama et. al 1998). The sliding/uplift response is a more complicated and less intuitive response, but also in the transverse direction. It is a result of the interface between the crane wheels and crane rails, depicted in Figure 4.3. this boundary condition acts as a pin under normal loading, but since it does not provide positive vertical restraint, the wheels are free to uplift and displace

laterally under sufficient portal sway response. Kosbab (2010) completed a rigorous analysis of this sliding/uplift response.

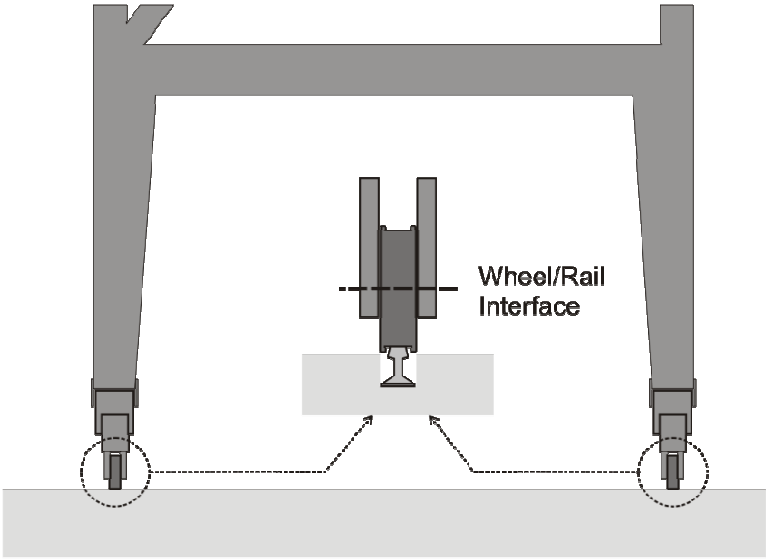

Figure 4.3 Container crane boundary condition with wheel/rail interaction

Simplified 2D finite element crane models have been shown to capture these two fundamental responses well (Jacobs et. al 2010). In fact, it has been shown that a simple portal frame model, consisting of two flexible columns with a rigid and heavy portal beam, can capture the critical responses with surprising accuracy, given an appropriate boundary condition (Kosbab et al. 2010b, Sugano 2008). Here a frictional contact element is used, with a friction coefficient of 0.8, which acts essentially pinned until it uplifts, at which point it behaves freely. A generalized form of this idealized portal frame model is shown in Figure 4.4. All elements of the crane are elastic, however,nonlinear hinges are implemented in the connections of the crane legs to the portal beam. The yield rotation of the hinges is found such that the portal frame yields when the lateral drift is 2%. The ratio of the post-yield to initial stiffness of the portal frame is 0.15 as suggested by Kosbab (2010) (for

simplicity here, strength and stiffness degradation due to flange and web local buckling of the portal joints are neglected). The lumped mass at the top of the rigid portal beam is defined based on the mass of the modeled crane. Coupled with the natural frequency of the modeled container crane, this defines the bending stiffness of the flexible portal legs. In this way, cranes can be easily modeled representing a wide range of those in use at various ports. Here, the crane mass M_C is 125.2 metric-tons, the natural period of the crane is 1.5 sec, L is 30.5 m, H_1 is 36.6 m, H_2 is 19.5 m, and L_s is 11.3 m.

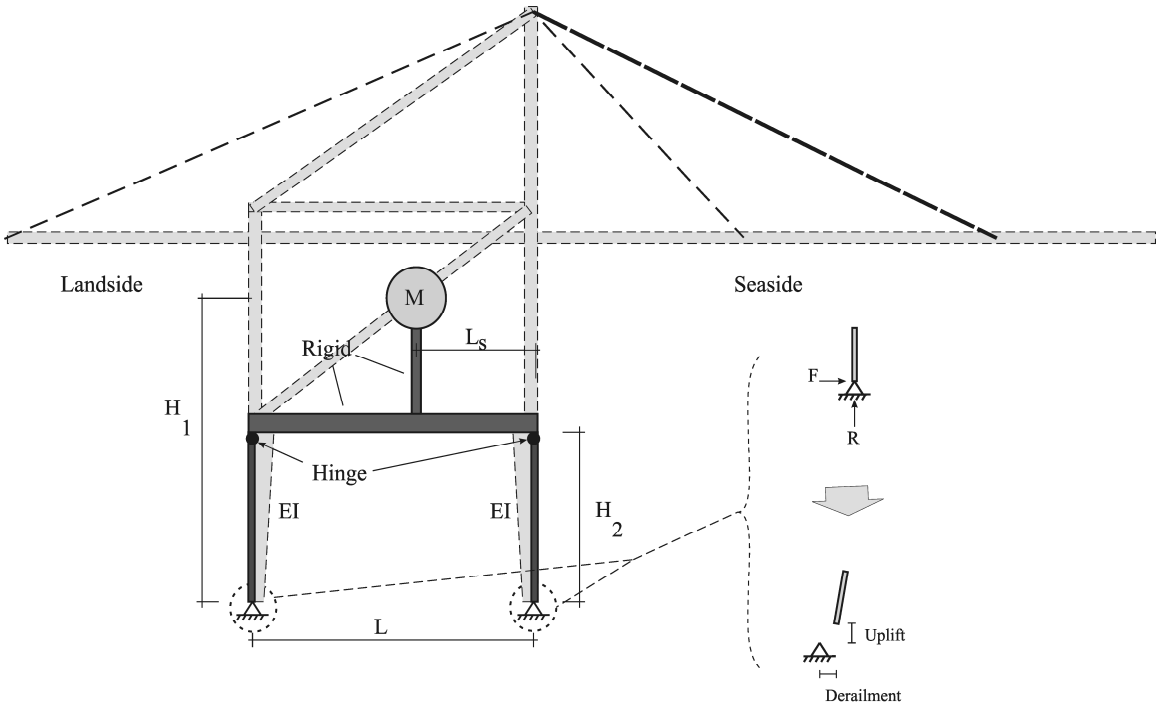

Figure 4.4: Idealized portal frame crane model, illustrating removal of constraint during uplift achieved by use of frictional contact elements

The configuration of the wharf with the surrounding embankment soils are explained in detail in chapter III. As seen in Figure 3.1, the seaside leg of the crane rests on the wharf deck on top of the batter piles and the landside leg rests on a structurally separated crane rail supported by two rows of batter piles. The distance

between the seaside and landside crane rails is 30.5 m. The FE model of the wharf and crane are developed in OpenSEES (McKenna et al. 2010).

4.3 Simplified Crane Models

The crane model with contact base conditions explained above is a numerically expensive model. A number of simplified models for cranes are considered as follows to evaluate their appropriateness to capture the effect of the crane on the wharf response.

4.3.1 Pinned Based Portal Frame Crane Models

In this approach, the portal frame is modeled the same way as the sliding/uplift model of the crane but the base condition is pinned, meaning that the crane will not uplift or slide. Considering the initial state of the sliding/uplift crane model, it can be observed that as long as the horizontal force in the base is less than the sliding resisting force and the vertical base force is in compression, the pinned frame will behave the same way as the sliding/uplift crane model.

4.3.2 Wharf without Crane and Wharf with 5% Additional Mass

Several former studies have concluded that due to the large ratio of the natural periods of the crane to the natural period of the wharf, it is the second mode of the combined wharf-crane system that is typically critical to wharf design in a given response direction (POLA 2007). It is suggested that in the second mode, the crane mass reduces the response forces in the piles, and it is thus conservative to ignore the crane mass, and consider the wharf as a single mass system. However, it is specified that the above recommendation can be followed if the following two

criteria are satisfied: 1) the period of the crane mode with maximum participating crane mass exceeds 200% of the initial elastic fundamental period of the wharf based on cracked-section properties, and 2) the crane mass (including ballast), at or close to wharf deck level, is less than 5% of the wharf mass (POLA 2007). Reducing the moment of inertia of the pile sections to $0.7I_g$ according to ACI318-05 (2005), the initial elastic fundamental period of the wharf based on cracked section properties is found to be 0.31 sec. Considering the natural period of the crane, 1.5 sec, it is clear that the first condition is satisfied. However, the definition of the closeness to the wharf deck level in the second criterion is not clear. As a consequence, a wharf without a crane and a wharf with additional 5% wharf mass rigidly attached to the deck are considered as two alternatives of the recommendations by POLA (2007) which are modeled in this study.

4.3.3 Wharf with Constant Gravity Loads of the Crane

In this simplified representation of the wharf-crane system, the model of the crane is replaced by a pair of constant downward loads with magnitudes equal to the vertical reactions of the crane under gravity. As a consequence, this model investigates the effect of the gravity force of the crane on the response of the wharf and neglects the effect of the vertical inertial and lateral interactions of the wharf and crane on the response of the wharf.

4.4 Time-History Analysis

Results of the nonlinear dynamic analysis of the wharf with different representations of the crane are presented in this section. Figure 4.5 shows the full crane model connected to the wharf with sliding/uplift capable boundary conditions.

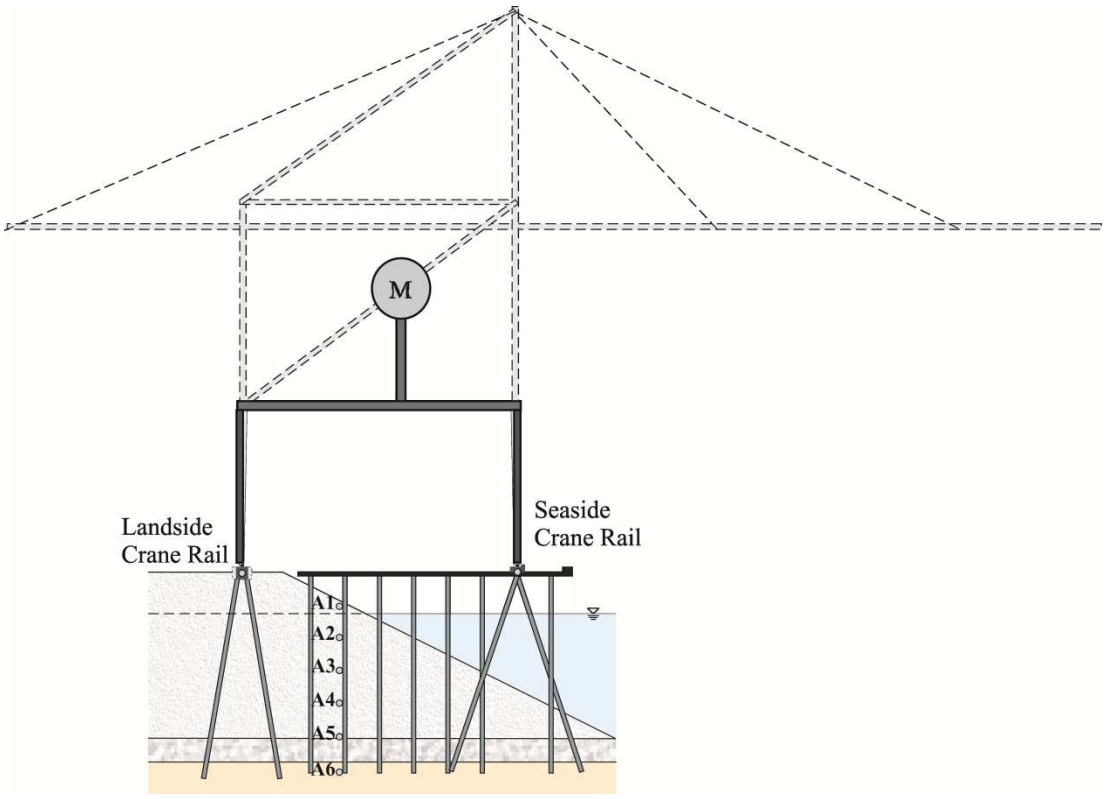

Figure 4.5 Combined model of the wharf and container crane.

4.4.1 Ground Deformation History

In this chapter, ten empirical two component ground motion time-histories which represent a broad range of possible earthquake scenarios in terms of peak ground acceleration (PGA) are selected to study different characteristics of the coupled response of the wharf and different crane models. The earthquake records are selected from the database used to develop the Next-Generation Attenuation of Ground Motion (NGA) project (Chiou et al. 2008). The characteristics of these ground motions are presented in Table 4.1.

Table 4.1 Characteristics of the selected ground motions

Record Number	Earthquake Name	Station Name	Earthquake Magnitude (Mw)	Closest Distance to Rupture (km)	PGA (g)	PGV (m/s)	PGD (m)
448	Morgan Hill,1984	Anderson Dam (Downstream)	6.19	3.30	0.423	0.253	0.046
451	Morgan Hill,1984	Coyote Lake Dam	6.19	0.50	0.711	0.516	0.12
669	Whittier Narrows-01,1987	Orange Co. Reservoir	5.99	22.8	0.185	0.102	0.01
753	Loma Prieta,1989	Corralitos	6.93	3.90	0.644	0.551	0.108
810	Loma Prieta,1989	UCSC Lick Observatory	6.93	18.4	0.45	0.187	0.038
1008	Northridge-01,1994	LA - W 15th St	6.69	29.7	0.104	0.116	0.088
1085	Northridge-01,1994	Sylmar - Converter Sta	6.69	5.20	0.828	1.175	0.345
1086	Northridge-01,1994	Sylmar - Olive View Med FF	6.69	5.30	0.604	0.781	0.241
1642	Sierra Madre,1991	Cogswell Dam - Right Abut	6.69	22.0	0.302	0.149	0.241
3469	Chi-Chi,1999	TCU068	6.3	35.7	0.045	0.087	0.025

As explained in chapter III, the nonlinear coupled ground deformation and transient pore pressure response of the wharf embankment to input ground shakings are numerically evaluated by Vytiniotis et al. (2011). Soil deformations and excess pore water pressure ratios in sand layers in the horizontal direction are applied to the far-field end of the macroelement, while for other soil springs only soil deformations are input to the model.

4.4.2 Detailed Time-History Response Study of the Wharf with Crane and without Crane

The horizontal displacement response of the wharf at the location of structurally separated landside and seaside crane rails for wharf without crane and wharf with full crane model subjected to NGA1642 and NGA1086 are presented in Figure 4.6. The large level of ground shaking during NGA1086 induces liquefaction in the embankment soil which combined with the simultaneous effect of the gravity load results in large lateral movements of the slope toward the sea. Due to the kinematic constraints between the piles and surrounding soils, large embankment soil deformations induce large pressures at the face of the piles, which consequently results in the almost monotonic movement of the wharf toward the sea. Compared to 65.3 cm of lateral displacement of the seaside crane rail during NGA1086 in the case where the crane model is included, the lateral deck displacement during NGA1642 is small and limited to 11.4 cm (Figure 4.6). A similar pattern is observed for the lateral displacement of the landside crane rail. Also, noticeable in these figures is the effect of the crane on the lateral displacement of the seaside crane rail during NGA1642 and NGA1086 in which the presence of the crane increased the horizontal seaside crane rail displacement by 39% and 16% respectively. However, the effect of the crane on the lateral response of the landside crane rail is seen to be negligible for both earthquakes. This contradicts the conclusion from former studies that based on simplified wharf and crane models concluded that container cranes may act as tuned mass dampers for the underlying wharf structure. The other noticeable phenomenon is the fact that the maximum lateral response of the wharf occurs at the end of the ground shakings which

together with the almost monotonic seaward deformations of the wharf implies that, especially during large earthquake events, kinematic loads have the major contribution to the wharf response compared to inertial induced loads in the wharf deck.

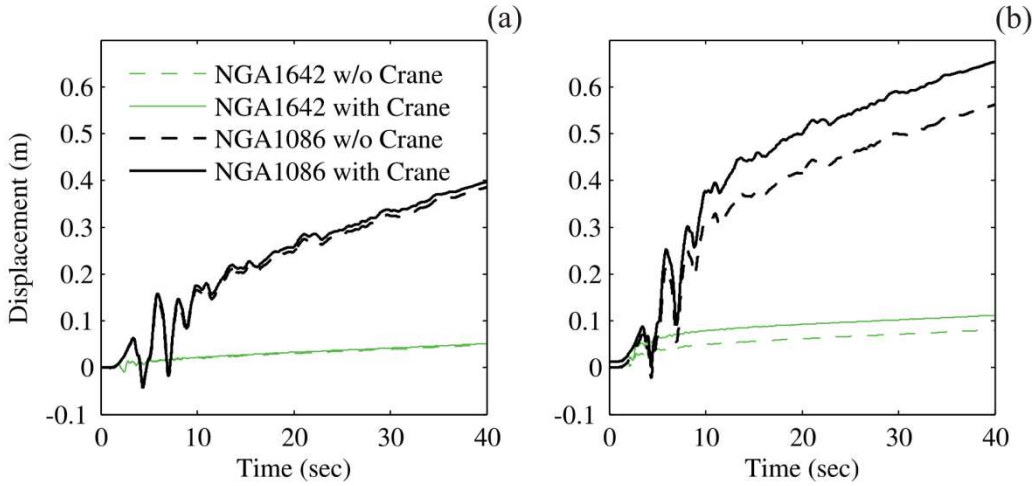

Figure 4.6 Lateral displacement of the wharf with and without crane for a) landside crane rail and b) seaside crane rail

The other response measure of the wharf that is important to the response of the crane is the vertical displacement of the crane rails. Because of the short embedment length of seaside piles as well as the large depth of seismically displaced soils in the seaside end of the embankment, the vertical resistance provided at the face and end of the piles is smaller for the seaside piles compared to the landside piles. This results in larger settlements at the location of the seaside crane rail with respect to the landside crane rail under the simultaneous effect of the gravity load and vertical ground shakings. The resulting differential displacement at the location of crane rails can lead to excessive deformation of cranes. This response measure is presented in Figure 4.7 for NGA1642 and NGA1086 in which the negative sign indicates the larger settlement of the seaside rail with respect to

the landside rail. Consistent with the level of ground shaking, the vertical differential displacement of the crane rails in the case where the crane model is included is 51.3 cm during NGA1086 and 23.2 cm during NGA1642. Furthermore, it is observed that the presence of the crane considerably increases the vertical differential displacement of the crane rails. This can be attributed to the fact that the axial loads induced by crane weight is larger at the seaside leg due to the closeness of the center of mass of the crane to this leg ($\alpha<0.5$, Figure 4.4) which accompanied with smaller resisting forces provided by seaside piles further push the surrounding soil of the seaside piles into the nonlinear range. The differential settlement of crane rails is increased by 45.2 cm and 20.4 cm for NGA1086 and NGA1642 respectively when the crane model is included.

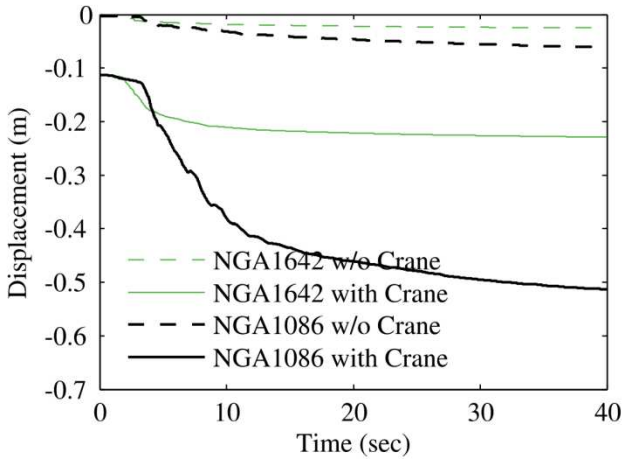

Figure 4.7 Differential settlement of the crane rails

Relative vertical displacements of landside and seaside crane legs with respect to the corresponding crane rails are presented in Figure 4.8. The lateral inertial loads in the crane during NGA1642 are quite small to counteract the upward reactions at the crane legs induced by gravity loads. As a consequence, the crane does not exhibit any uplift during NGA1642. Although the magnitude of the lateral wharf

displacement response during NGA1086 is quite large compared to the wharf response during NGA1642, the induced overturning moment is not sufficient to overcome the restoring moment induced by the gravity load of the crane. This can be observed in Figure 4.8 in which the differential vertical displacement at the crane base is almost zero for both earthquakes. The small zero-mean fluctuations are due to numerical errors induced by the highly nonlinear nature of the frictional contact element.

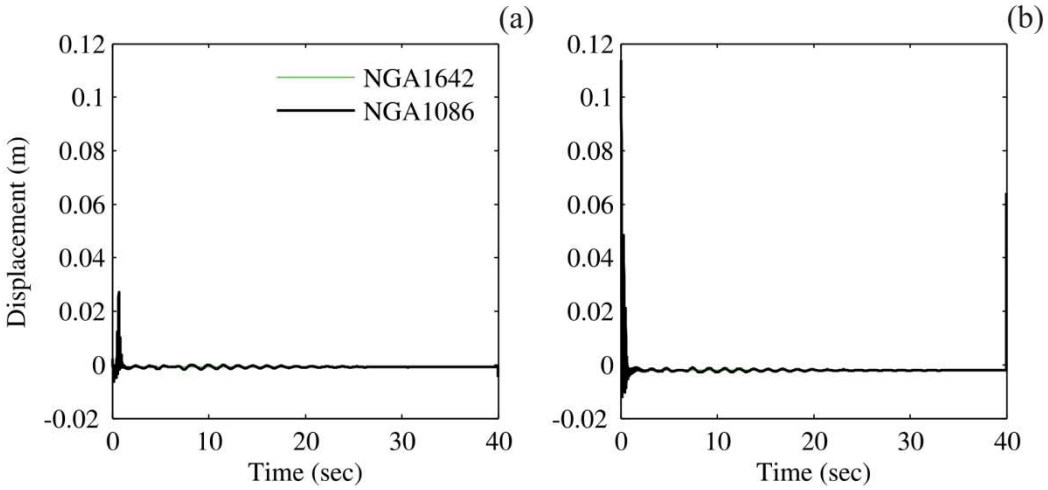

Figure 4.8 The uplift response of a) landside crane leg and b) seaside crane leg

The differential horizontal displacement of the crane legs and associated rails, referred to as sliding response of the crane, is shown in Figure 4.9 for NGA1642 and NGA1086. Both of the crane legs remain in place during NGA1642 which together with the zero vertical differential response implies that during small to moderate earthquakes, the inertial loads on the crane as a result of the lateral response of the wharf are too small to overcome gravity and friction-induced resisting forces at the base of the crane rails and as a consequence cranes behave as if they are simply supported. However during NGA1086, the landside crane rail

slides 26.1 cm inward toward the portal frame while the seaside leg remains still. The smaller gravity induced loads on the landside leg compared to the seaside leg results in proportionally smaller shear friction resisting forces at the base of the landside leg. This fact together with the almost monotonic differential settlement of the wharf deck increases the susceptibility of the landside leg to slide compared to the seaside leg.

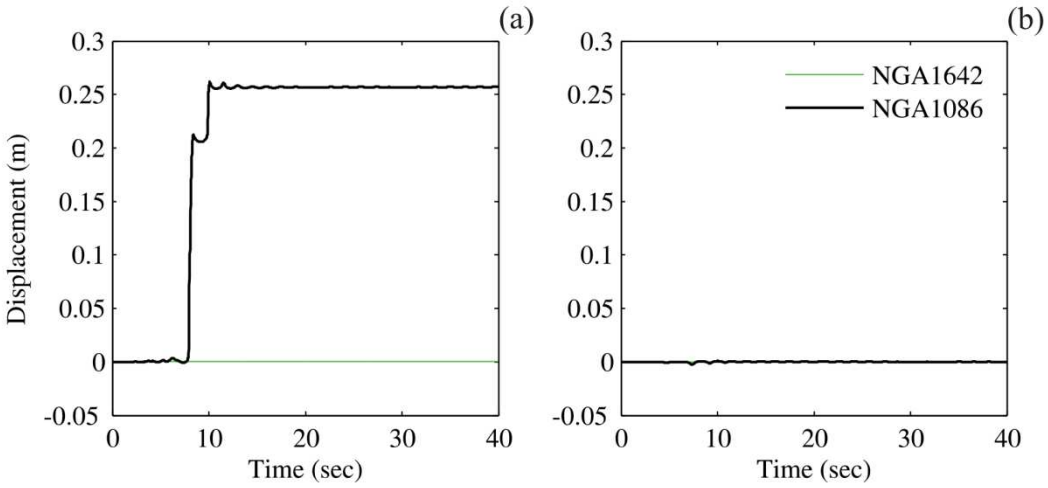

Figure 4.9 Sliding response of a) landside crane leg and b) seaside crane leg

The other important response measure of cranes is the lateral drift response of the portal frame by which the extent of the nonlinearity of the portal frame can be measured. Figure 4.10 shows the lateral portal drift of the crane for NGA1642 and NGA1086 for the landside and seaside legs. The lateral drift response of the crane during NGA1086 reaches 1% which is five times larger than the maximum drift response of 0.2% during NGA1642. However, the maximum crane drifts during these earthquakes do not exceed the 2% yield drift ratio of the portal frame and therefore the crane remains elastic. Also noticeable in these figures is the fact that the peak response of the seaside leg during NGA1086 occurs at about 8 sec,

however due to the sliding of the landside leg at the same time (Figure 4.10a), the landside leg does not sustain drifts as large as the seaside leg.

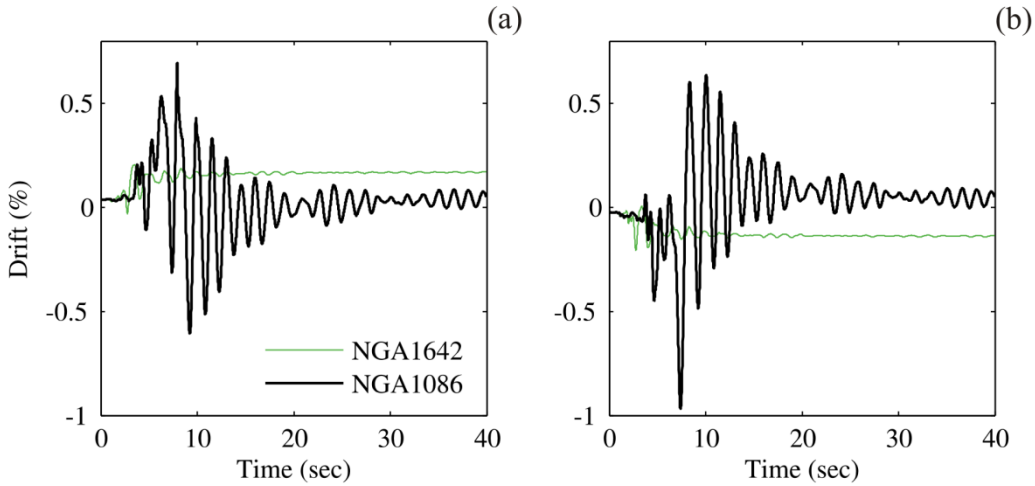

Figure 4.10 The lateral drift response of a) landside crane leg and b) seaside crane leg

4.4.3 Simplified Analytical Study of the Foundation-Wharf-Crane Interaction

Idealizing the foundation–wharf system as a single degree of freedom (SDF) oscillator with the natural period equal to the fundamental period of the wharf in the lateral direction and simplifying the crane as a SDF model to represent the initial elastic dominant lateral mode of the crane, the foundation-wharf-crane system can be represented by a 2 degree of freedom model shown in Figure 4.11. In this figure, M_{WF}, C_{WF}, and K_{WF} represent the effective mass, damping, and stiffness of the wharf and M_C, C_C, and K_C denote the effective mass, damping, and stiffness of the crane.

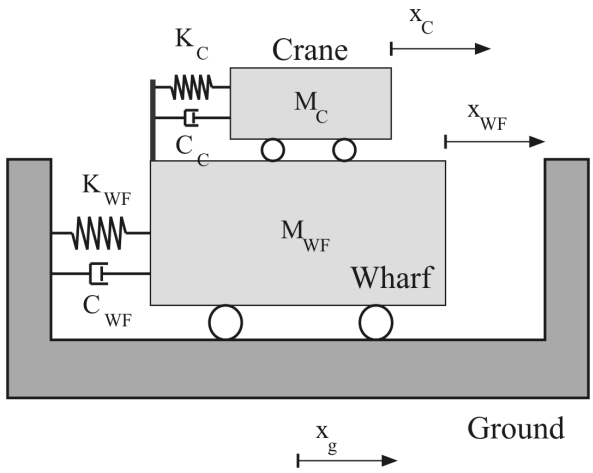

Figure 4.11 Simplified lumped mass representation of foundation-wharf-crane system.

Dynamic equilibrium equations of motions of the system shown in Figure 4.11 in response to the ground motion time-history $x_g(t)$ are as follows.

$$\begin{cases} M_{WF}\ddot{x}_{WF}(t)+C_{WF}\dot{x}_{WF}(t)+K_{WF}\left(x_{WF}(t)-x_g(t)\right)-C_C\left(\dot{x}_C(t)-\dot{x}_{WF}(t)\right) \\ \qquad -K_C\left(x_C(t)-x_{WF}(t)\right)=0 \qquad (4.1a) \\ M_C\ddot{x}_C(t)+C_C\left(\dot{x}_C(t)-\dot{x}_{WF}(t)\right)+K_C\left(x_C(t)-x_{WF}(t)\right)=0 \qquad (4.1b) \end{cases}$$

in which $x_{WF}(t)$ and $x_C(t)$ are the absolute displacement of the wharf and crane respectively. In order to simplify the above equations, the following dimensionless parameters are defined.

$$\mu=\frac{M_C}{M_{WF}}\text{: mass ratio} \qquad (4.2a)$$

$$\alpha=\frac{\omega_C}{\omega_{WF}}\text{: natural frequency ratio} \qquad (4.2b)$$

$$\zeta_{WF} = \frac{C_{WF}}{2M_{WF}\omega_{WF}} : \text{damping ratio of the foundation-wharf system} \quad (4.2c)$$

$$\zeta_{C} = \frac{C_{C}}{2M_{C}\omega_{C}} : \text{damping ratio of the crane} \quad (4.2d)$$

Assuming that the ground displacement is a harmonic function of time with amplitude x_{g0} and frequency ω_{exc}, the ground frequency ratio β is defined as

$$\beta = \frac{\omega_{exc}}{\omega_{WF}} \quad (4.3)$$

Using the above dimensionless parameters, the ratio of the displacement response amplitude of the wharf to the amplitude of the ground deformation called dynamic amplification factor R_{d1} is found to be

$$R_{d1} = \sqrt{\frac{A_1^{\,2} + A_2^{\,2}}{A_3^{\,2} + A_4^{\,2}}} \quad (4.4a)$$

in which

$$A_1 = \alpha^2 - \beta^2 \quad (4.4b)$$

$$A_2 = 2\zeta_C \alpha\beta \quad (4.4c)$$

$$A_3 = \left(\alpha^2 - \beta^2\right)\left(1 - \beta^2\right) - \alpha^2\beta^2\mu - 4\zeta_{WF}\zeta_C\alpha\beta^2 \quad (4.4d)$$

$$A_4 = 2\zeta_C\alpha\beta\left(1 - \beta^2 - \beta^2\mu\right) - 2\zeta_{WF}\beta\left(\alpha^2 - \beta^2\right). \quad (4.4e)$$

On the other hand if there is no crane operating on top of the wharf, the dynamic amplification factor R_{d2} will be simplified to

$$R_{d2} = \frac{1}{\sqrt{\left(1-\beta^2\right)^2 + \left(2\zeta_{WF}\beta\right)^2}} \tag{4.5}$$

The extent of the contribution of the wharf-crane interaction on the total response of the wharf can be characterized by defining the parameter γ as the ratio of R_{d1} to R_{d2}.

$$\gamma = \frac{R_{d1}}{R_{d2}} \tag{4.6}$$

Using the result of the complex eigenvalue analysis of chapter III, the natural period of the dominant lateral mode of the wharf-foundation configuration of this study is found to be 0.26 sec and the associated damping ratio to be 36%. Substituting the natural period of the crane, 1.5 sec, the damping ratio of the crane, 2%, and the mass ratio, μ=0.7, in Equation 4.4a, the variation of the parameter γ with respect to the ratios α and β is shown in Figure 4.4.

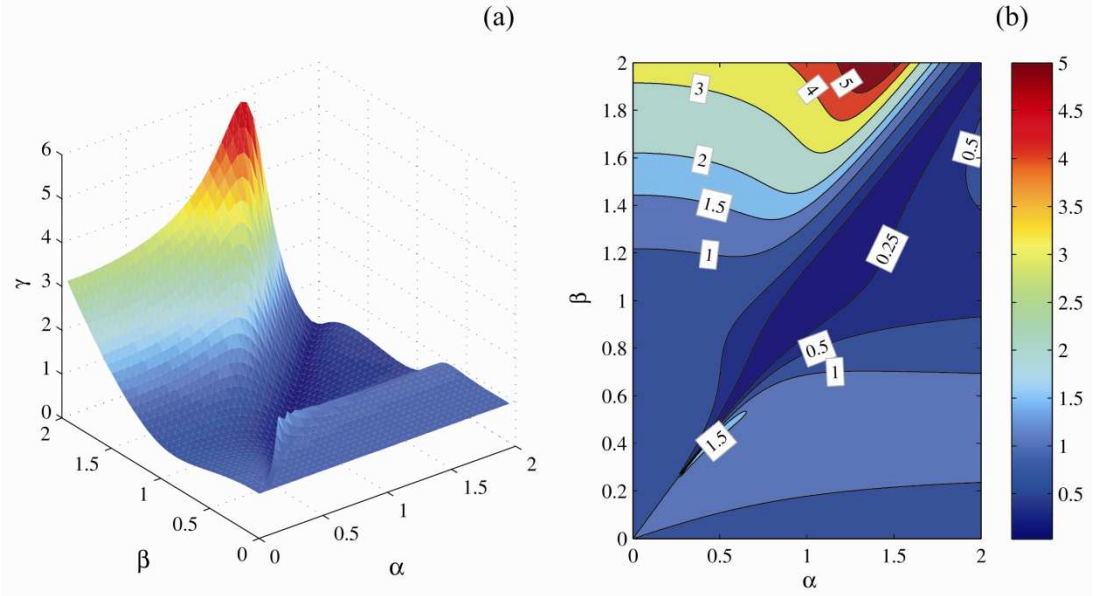

Figure 4.12 The ratio of dynamic amplification factors γ as a function of α (natural frequency ratio) and β (ground frequency ratio) a) three dimensional view and b) two dimensional contour view

It is seen that the ratio of the dynamic amplification factor γ takes a wide range of values depending on α and β in which values of γ less than one implies reduction in the steady-state response amplitude of the wharf as a consequence of the interaction of the wharf with crane while values of γ larger than 1 implies an increase in the wharf response due to the wharf-crane interaction. Based on the structural properties of the wharf and crane in this study, the value of α is 0.17 while the parameter β is dependent on the dominant ground excitation frequency.

The horizontal displacement response of the embankment soil at the location of nodes A_1 to A_6 in different depths along the length of pile G (Figure 4.5) is shown in Figure 4.13a for NGA1086. The permanent lateral drift response of the embankment at the location of the nodes is found as the moving average response of the lateral soil displacement at the corresponding locations. The permanent lateral drift response of the embankment does not contribute to the inertial response

of the wharf. The oscillating response of the soil is extracted by subtracting the permanent drift response from the total response of the soil as shown in Figure 4.13b-g. Using the Fourier transform, the power spectral density of the oscillating displacement of the nodes are found and presented in Figure 4.13h. It is observed that the dominant frequencies of the oscillating responses of the embankment at different depths of the embankment coincide. However, the amplitude of the frequency responses decreases as the depth increases (Figure 4.13h). The dominant natural frequency of the oscillating response of the soil is 0.86 Hz from which the parameter β in Equation 4.3 is found to be 0.22. Substituting the values of α and β in Equation 4.4a, the ratio γ is found to be 0.91, which implies that the presence of the crane decreases the response amplitude of the wharf by 9% in response to a harmonic ground displacement with the excitation frequency equal to the dominant frequency of the embankment soil deformation.

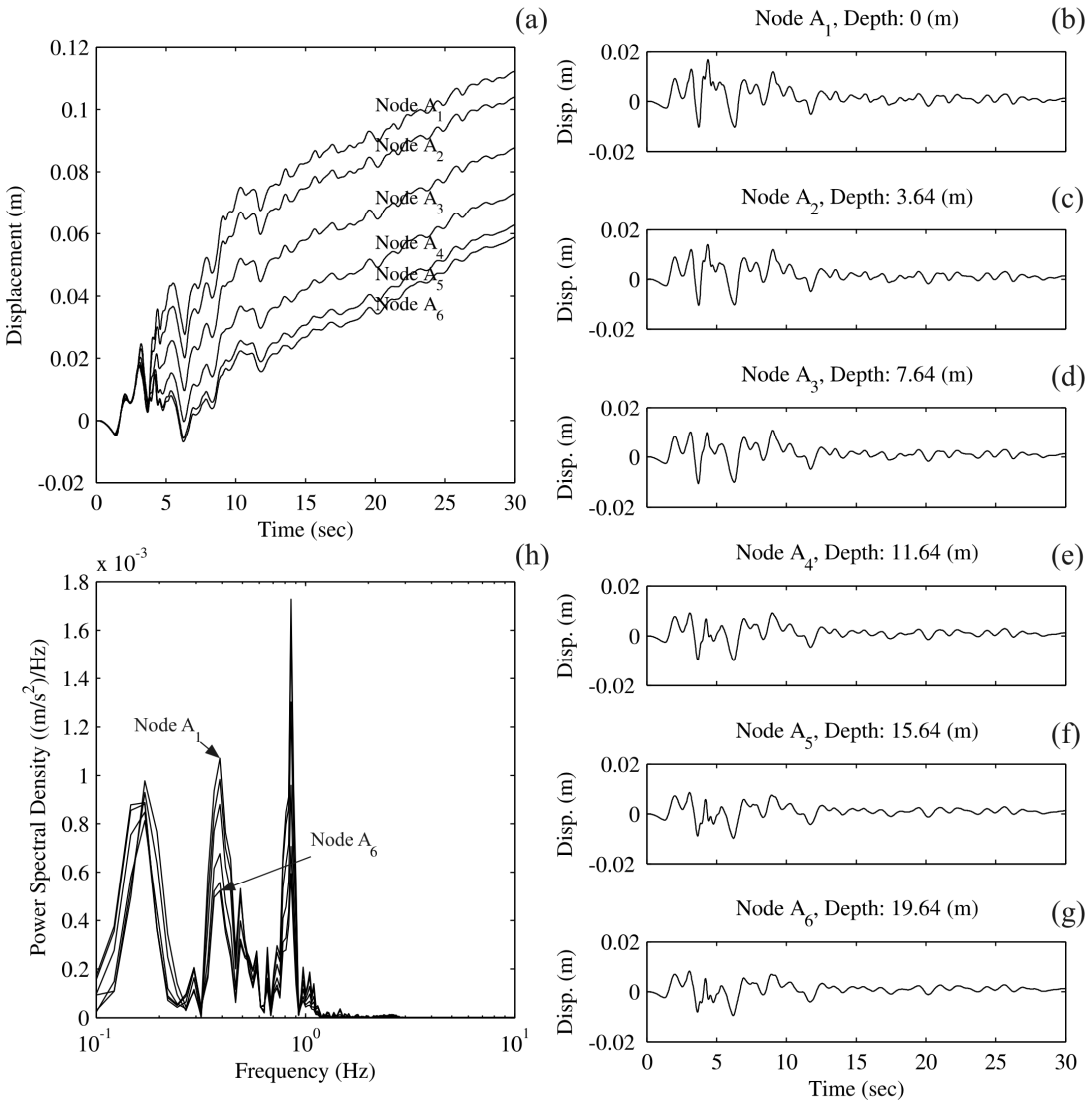

Figure 4.13 Response of the soil along pile G for NGA1086, a) the lateral displacement response of the nodes, b-g) the oscillating component of the horizontal displacement of the nodes, and h) the frequency content of the oscillating displacement response of the nodes.

4.4.4 Detailed Numerical Evaluation of the Effect of Crane's Gravity and lateral Wharf-Crane Interaction on the Lateral Response of the Wharf

The response of the foundation-wharf-crane system in the plane strain two dimensional model is contributed from the lateral and vertical response of the system to the simultaneous effect of gravity loads and the horizontal and vertical components of the ground deformation of the embankment. The distinct nature of

the cause of the dynamic response of the system in the horizontal and vertical directions suggests investigating the wharf-crane interaction in the two orthogonal directions separately. In this case, two alternative representations of the wharf-crane model are investigated numerically. The first model only includes the interaction of the wharf and crane in the lateral direction. To achieve this, crane legs are connected to an imaginary pair of crane rails through frictional contact elements using the same approach followed for the sliding/uplift crane model. The horizontal degrees of freedom of the imaginary crane rails are connected to the corresponding DOFs of the real crane rails on the deck of the wharf, while the vertical and rotational DOFs of the imaginary crane rails are fixed in the two dimensional domain. As a consequence of these boundary conditions, the wharf and crane only interact in the horizontal direction and vertical forces from the crane response will not be transferred to the wharf. In the second model, it is assumed that the vertical reaction force of the crane legs on top of the crane rails is governed by the gravity induced load of the crane. Therefore, the crane model is replaced by a pair of constant downward vertical loads at the location of the crane rails on the deck representing the effect of the gravity of the crane on top of the wharf. A nonlinear time-history analysis is performed for each of these wharf-crane representations for NGA1086 and their dynamic response in a number of response measures are compared in the following.

Figure 4.14 shows the vertical displacement of the crane rails in three wharf-crane system representations. As expected, the vertical displacement of the wharf deck in the wharf model with lateral interaction with the crane is considerably smaller than

the corresponding response of the wharf deck in the wharf model with sliding/uplift crane on top. However, only including the crane gravity induced loads on the wharf deck is seen to capture the vertical interaction of the wharf and crane properly. Small differences in the vertical responses of the crane rails in the wharf with crane gravity and wharf-sliding/uplift crane is due to the contribution of the inertial interaction of the wharf and crane in the vertical direction which is observed to be negligible with respect to the effect of the gravity of the crane.

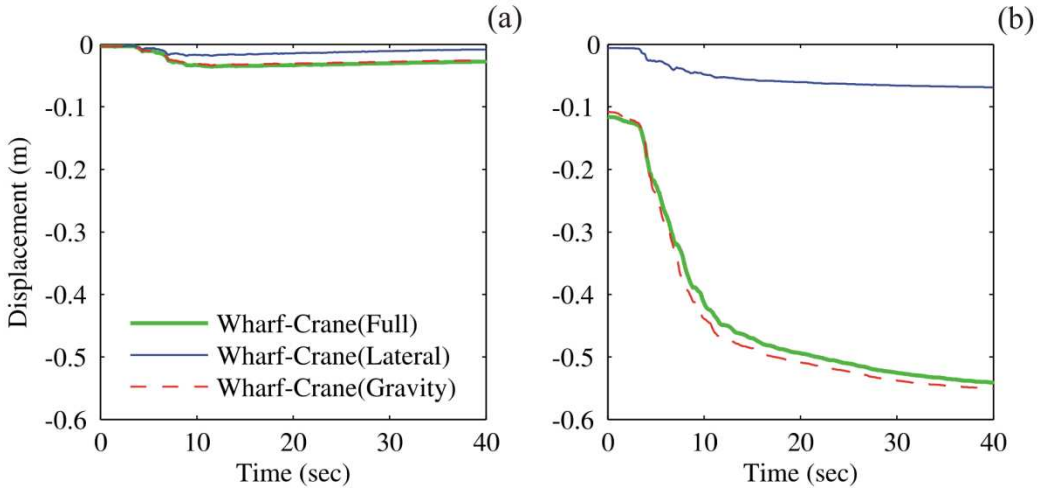

Figure 4.14 Vertical displacement response of different wharf-crane representations at (a) landside crane rail and (b) seaside crane rail

The lateral displacement response of the crane rails are presented in Figure 4.15a,b. It is observed, particularly in the seaside rail, that the response of the wharf when only the lateral interaction with the crane is included is smaller than the lateral response of the deck with sliding/uplift crane model on top. However, including crane gravity loads on the wharf deck appears to be a good representation of the effects of the crane on the lateral response of the wharf. This can be largely attributed to the relative settlement of the deck and crane rails in which case the deck is no longer horizontal and as a consequence, the projection of the vertical

gravity loads of the crane on the plane of the deck is no longer zero. It is expected that the contribution of the vertical gravity load of the crane in the lateral displacement of the deck increases with time as the relative settlement of the deck increases. This pattern is in agreement with observations from Figure 4.15a,b.

In order to identify the mechanisms of the contribution of the lateral component of the wharf-crane interaction and the vertical gravity induced loads of the crane on the lateral wharf response, the horizontal displacement of the crane rails are decomposed into two constitutive components: the monotonically increasing response of the wharf to the seaward permanent deformation of the embankment soil and the oscillating response of the wharf. Due to the kinematic interactions of the wharf with the embankment soils, the increasing seaward movement of the embankment imposes consistent lateral deformation demands on the wharf which consequently results in the movement of the wharf toward sea. This response component of the wharf is determined by finding the moving average of the lateral displacement of the crane rails and is shown in Figure 4.15c,d for landside and seaside rails, respectively. Similar to the lateral displacement response of the crane rails in Figure 4.15a,b, the average response of the crane rails in the wharf model with the gravity of the crane included on the deck is seen to be close to the corresponding response of the wharf with the sliding/uplift crane model. Subtracting the response of the rails from the corresponding average response results in a response measure called oscillating response in this study and is shown in Figure 4.15e,f for the landside and seaside rails respectively. The first noticeable phenomenon is that the presence of the crane's gravity does not affect the lateral

oscillating response of the crane rails. Since contributions from the permanent lateral deformation of the embankment and crane's gravity loads on the lateral response of the wharf is excluded in the oscillation response of the wharf, this response measure represents the response of the wharf in the analytical two DOF model in the previous section (Figure 4.11). From the analytical relation in Equation 4.4a, it was found that the ratio of the dynamic amplification factors of the wharf response to input ground deformations γ decreases by at most 9%. However, oscillating responses of the wharf deck in different wharf-crane models are close and the differences are less than 1%. The difference between analytical and numerical results is due to the limits and assumptions associated with the simplified analytical approach among which neglecting the transient response of the wharf and crane and assuming the input ground motion to be harmonic with a fixed excitation frequency are of major importance.

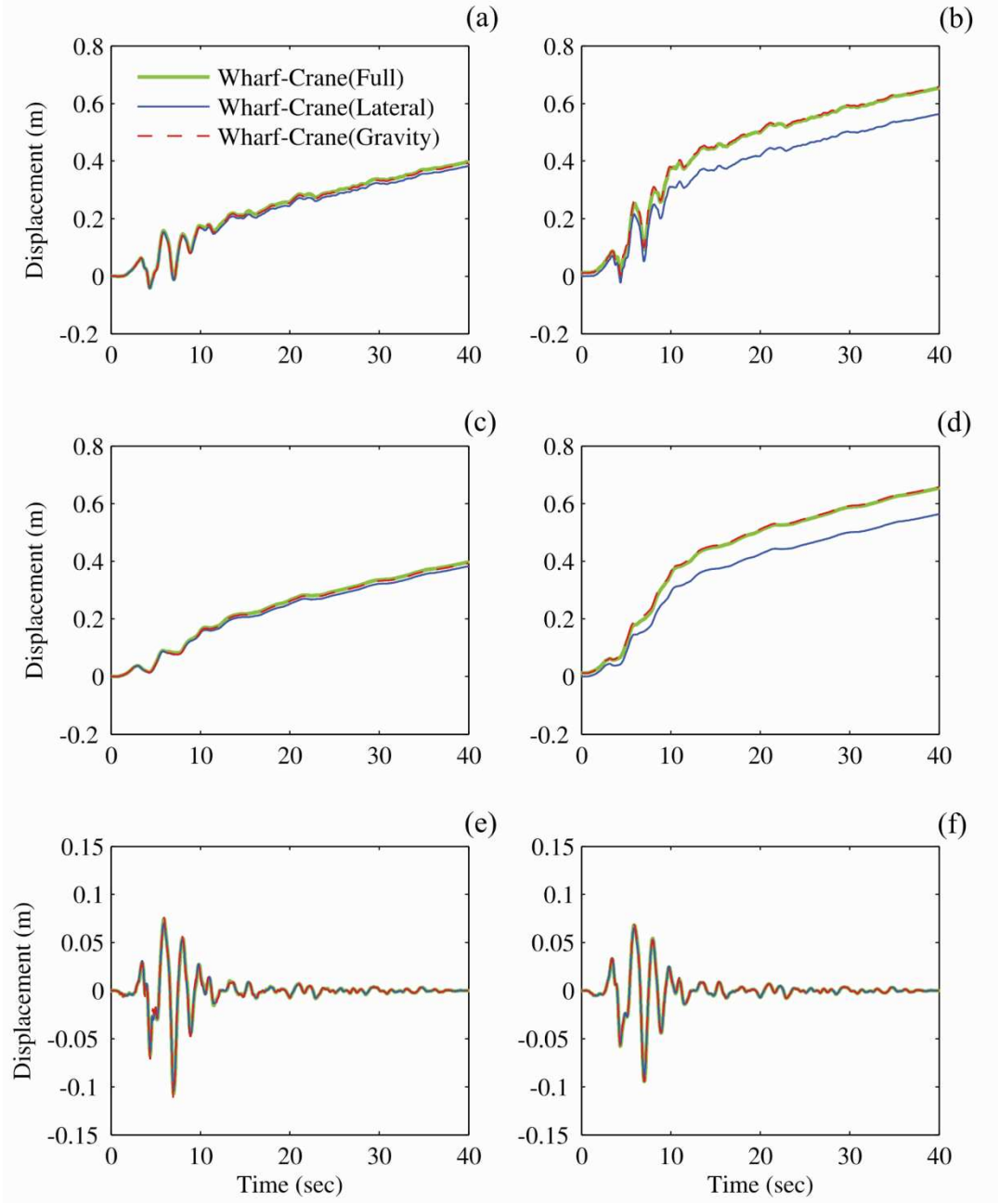

Figure 4.15 Lateral displacement response of different wharf-crane representations (a) total displacement response at landside crane rail, (b) total displacement response at seaside crane rail, (c) average displacement response at landside crane rail, (d) average displacement response at seaside crane rail, (e) oscillating displacement response at landside crane rail, (f) oscillating displacement response at seaside crane rail

4.4.5 Response of Wharf-Crane Models to the Bin of Ground Motions

In this section, the maximum response of the wharf and crane in a number of response measures is investigated for different wharf-crane representations. The results are presented as the ratio of the response measure of interest of a particular model to the corresponding response of the wharf-sliding/uplift crane model.

The maximum horizontal displacement ratio of the seaside rail together with the ratio of the relative movement of the crane rails in the horizontal direction are shown in Figure 4.16a,b respectively for different wharf-crane representations. The maximum lateral deck displacement of the wharf with a pinned crane model is almost the same as the maximum deck displacement response of the wharf with a sliding/uplift crane model for all ground motions implying that the sliding/uplift behavior of the crane has a negligible effect on the lateral response of the wharf deck. Similarly, the maximum relative displacement of crane rails in the horizontal direction of the wharf model with the pinned crane is very close to the corresponding response of the wharf with the sliding/uplift crane model for small to medium intensity earthquakes; however replacing the sliding/uplift crane with the pinned crane model results in underestimation of the relative displacement of crane rails for large intensity ground motions by at most 10%. On the other hand, the increase of the wharf mass by 5% results in almost the same response as the wharf without crane model in both horizontal response measures. Furthermore, it is observed that peak lateral responses of the wharf without crane and wharf with 5% additional mass are smaller than the corresponding responses of the wharf with sliding/uplift crane. However, the ratio of the peak responses decreases with increasing ground motion intensity. Furthermore, simplifying the wharf-crane

interaction to include only the effect of the crane's gravity load is seen to result in lateral seaside displacement responses close to the corresponding response of the wharf-sliding/uplift crane. However, the wharf-crane gravity model overestimates the relative horizontal displacement of the crane rails by at most 18%.

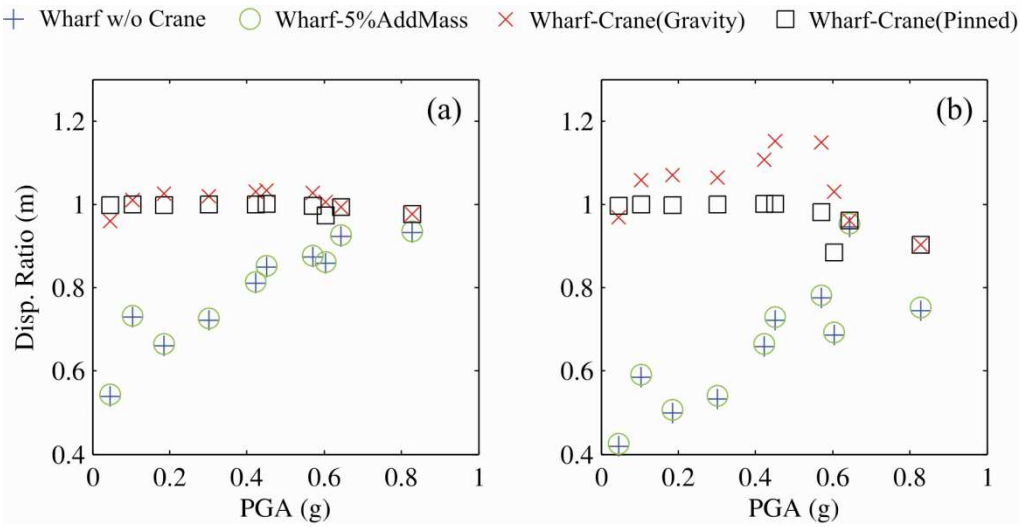

Figure 4.16 The ratio of the maximum horizontal displacement of the wharf with simplified crane models to the maximum horizontal displacement of the wharf with full crane model for a) horizontal displacement of the seaside rail and b) relative horizontal displacement of the crane rails

The ratio of the maximum vertical displacement of the seaside rail and the ratio of the maximum relative settlement of the crane rails for the wharf with different crane representations are presented in Figure 4.17. Similar to the lateral response of the wharf, the maximum vertical response of the wharf and crane rails with pinned crane is very close to the corresponding response of the wharf with sliding/uplift crane model. Furthermore, the wharf with 5% added mass behaves quite the same as the wharf without crane on top for all earthquakes. However the response of the wharf model with the sliding/uplift crane is much larger than the response of the wharf without the crane in the vertical direction. The large level of difference

between the vertical responses of the wharf model with sliding/uplift crane and wharf models without the crane and with 5% additional mass is due to the vertical interaction of the wharf with the crane. The vertical loads induced by the weight of the crane and the inertial response of the crane added to the total vertical loads from the weight of the wharf and the vertical seismically induced loads which consequently further push the surrounding soil of the piles into the nonlinear range in the vertical direction. Based on this argument, including the gravity induced loads of the crane on the wharf is expected to improve the response estimation of the wharf in the vertical direction. This expectation is in agreement with the result of time-history analysis shown in Figure 4.17a,b. The satisfactory estimation of the vertical wharf response by inclusion of the gravity of the crane implies the dominance of the contribution of the crane gravity in the vertical component of the wharf-crane interaction.

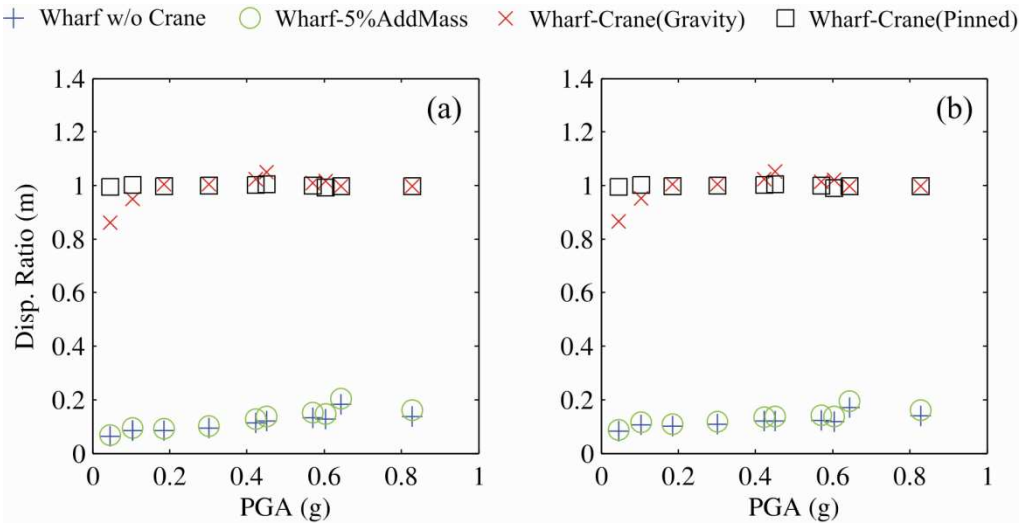

Figure 4.17 The ratio of the maximum vertical displacement of the wharf with simplified crane models to the maximum vertical displacement of the wharf with full crane model for a) vertical displacement of the seaside rail and b) relative vertical displacement of the crane rails

The behavior of the wharf with different crane representations is also investigated at the component level in the wharf. Figures 4.18a,b show the maximum curvature of the pile sections and pile-deck connections for different earthquake events respectively. From Figure 4.18a, it is observed that the maximum curvature response of pile sections in different simplified wharf-crane models is close to the corresponding response of the wharf with sliding/uplift crane for all ground motions. On the other hand, it can be seen that the wharf models without crane and with 5% additional mass underestimate the maximum curvature response while the wharf model with crane gravity overestimates the maximum curvature response of the pile-deck connections (Figure 4.18b). This phenomenon can be attributed to a number of factors. The vertical component of the dynamic wharf-crane interaction induces larger axial loads in piles compared to the case where no crane model is included which consequently results in larger stiffness degradation of the piles due to the secondary P-δ effects. On the other hand, the lateral projection component of the vertical crane reaction in the plane of the deck increases the lateral seaward deformation of the deck and consequently pile-deck connections. In the wharf model with crane gravity, the vertical component of the crane reaction is large and constant which amplifies the wharf deformation.

The smaller influence of the wharf-crane interaction on the maximum curvature response of the piles compared to the pile-deck connections is due to the fact that the maximum deformation of the pile sections occurs at the boundary of the loose and dense sand layers. The large relative deformations of the soil at the interface of loose and dense sand layers of the embankment (Figure 4.5) enforce consistently

large deformations on the pile sections in a short length of the piles close to the interface of the soil layers. For pile sections in this zone, the effect of axial loads is reduced due to the friction resistance at the face of the piles above the interface. Furthermore, the lateral confinement of piles provided by the surrounding soils decreases the effect of the wharf deck response on the response of the piles deep in the embankment. As a consequence, it is expected that the presence of the crane does not affect the response of the embedded portion of the piles close to the interface of dense and loose sand layers which agrees well with the numerical results in Figure 4.18a.

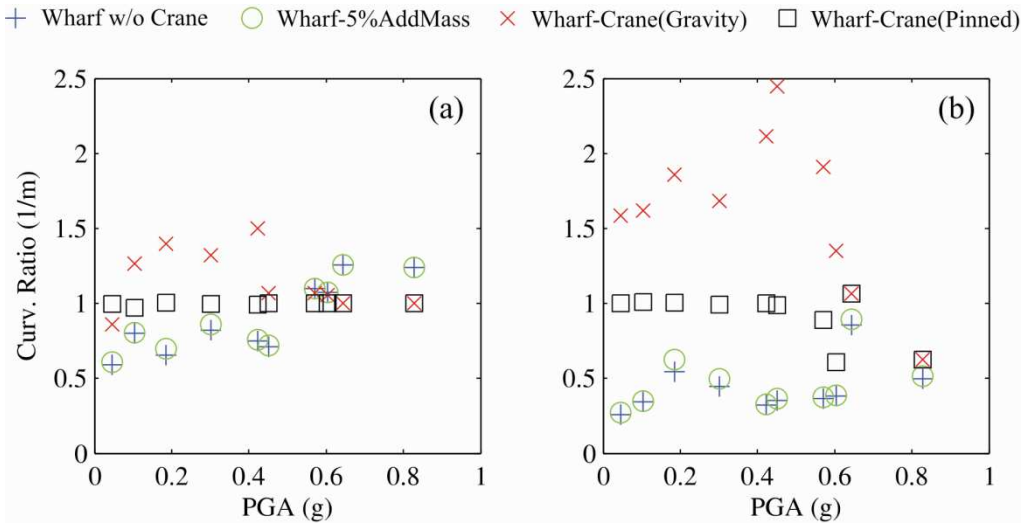

Figure 4.18 The ratio of the maximum curvature response of the wharf with simplified crane models to the maximum curvature response of the wharf with full crane model for a) pile sections and b) pile-deck connections.

The maximum drift response of the landside and seaside crane legs for pinned and sliding/uplift crane models are shown in Figure 4.19. Comparing the maximum drift in two legs, it is noticed that the maximum drift response of the pinned crane model is close to the corresponding response of the sliding/uplift crane model for small intensity earthquakes. However the pinned crane model is observed to over predict

the drift of the portal frame for large earthquakes. During small earthquakes, the inertial load on the crane induced by the lateral response of the crane rails as well as the differential horizontal response of crane rails are not large enough to cause sliding or uplift of the landside crane leg and as a consequence, the crane behaves similar to the pinned model. However in large earthquakes, the differential horizontal displacement of structurally separated crane rails is large which induce consistently large drifts in the portal frame of the pinned model. While in the sliding/uplift crane model, the sliding of the landside crane leg reduces the drift demand of the portal frame.

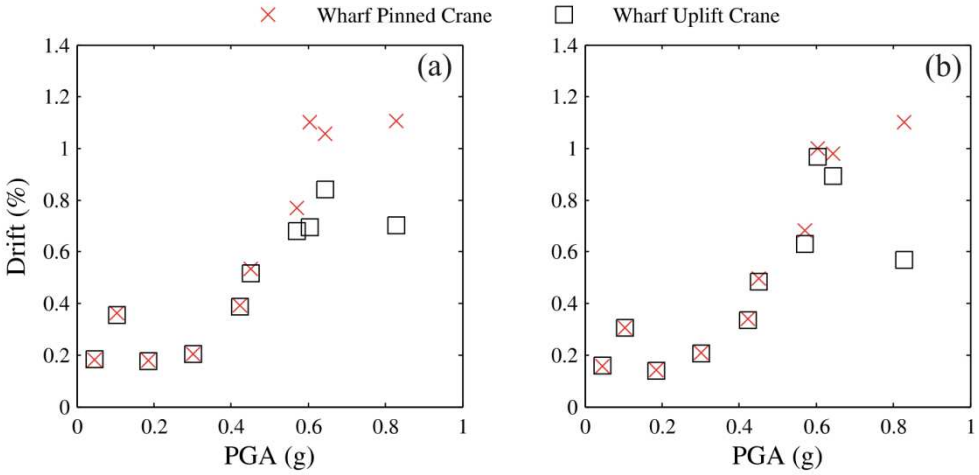

Figure 4.19 The maximum drift response of a) landside crane rail and b) seaside crane rail

4.5. Simplified Relations for Prediction of Cranes' Behavior

The complexity of the response behavior of container cranes especially during large earthquake events necessitates the use of sophisticated numerical models for seismic performance evaluation of these structures. Meanwhile, it is quite beneficial to characterize major response characteristics of container cranes using analytical relations. In the following, such relations are derived to predict the occurrence of

yielding of the portal frame, and sliding and uplift of the crane legs. Inherited in these relations is the assumption that the aforementioned nonlinear phenomena are independent from each other.

4.5.1 Yielding of the Portal Frame

In the absence of sliding and uplift of crane legs at the boundaries with crane rails, the portal frame behaves as if it is a simply supported frame with the maximum moment occurring at the connection of the crane legs to the beam in the portal frame. The beam of the portal frame is comparatively rigid with respect to the crane legs. Denoting the yield drift ratio of the crane legs by θ_y and the rigidity of the crane legs by *EI*, it is straight forward to show that based on the geometric configuration of the modeled crane in Figure 4.4, the yield moment at the top end of the crane legs – the most susceptible zone in the portal frame to yield– is

$$M_y = \frac{3EI}{H_2}\theta_y \tag{4.7}$$

On the other hand, the rigidity of the crane legs *EI* can be found as a function of H_2, the fundamental natural period of the crane T_n, and the mass of the crane *M* as follows

$$EI = \frac{M}{6}\left(\frac{2\pi}{T_n}\right)^2 H_2^3 \tag{4.8}$$

Combining Equations 4.7 and 4.8, the lateral acceleration at the center of mass of the crane required to push the portal frame into the nonlinear range a_{yield} is

$$a_{yield} = \gamma_{yield} g \,,\ \gamma_{yield} = \left(\frac{2\pi}{T_n}\right)^2 \frac{H_2}{g} \theta_y \tag{4.9}$$

4.5.2 Uplift

The uplift of the crane legs occurs when the overturning moment induced by the inertial response of the crane exceeds the restoring moment by gravity loads. The landside crane rail carries a smaller portion of the crane's gravity loads compared to the seaside leg and as a consequence it is more likely that the uplift occurs at the landside leg. Considering Figure 4.4, one can use a simple tipping analysis to find the horizontal threshold acceleration at the center of mass of the crane required for the uplift of the landside crane leg.

$$a_{uplift} = \gamma_{uplift} g \,,\ \gamma_{uplift} = \frac{\alpha L}{H_1} \tag{4.10}$$

4.5.3 Sliding

As mentioned before, the lateral resistance of the crane legs to slide with respect to the crane rails is modeled by equivalent coulomb friction which is calibrated in former studies (Jacobs, 2010). Since the crane rails are structurally separated, the horizontal differential displacement of the crane rails tends to widen the portal frame. Due to the symmetry of the portal frame, each of the crane legs deforms half of the horizontal differential displacement which results in equal inward forces F_{diff} at the base of the crane legs. Assuming linear elastic behavior for the portal frame, F_{diff} is related to the horizontal differential displacement of the crane rails Δ_{diff} at the moment of sliding as follows

$$F_{diff} = \frac{3EI\,\Delta_{diff}/2}{H_2^3} \tag{4.11}$$

In addition to the kinematic response of the crane to the relative displacement of the crane rails, the inertial response of the crane also contributes to the horizontal loads at the base of the crane legs. Due to the smaller vertical compression reaction in the landside leg compared to the seaside leg of the crane, the landside leg is more susceptible to slide during an earthquake event. The worst case scenario for the landside leg to slide occurs when the threshold acceleration a_{slide} is seaward. Formulating the equilibrium equation in the horizontal direction, the minimum acceleration required for the sliding of the landside crane leg a_{slide} is

$$a_{slide} = \gamma_{slide} g\ ,\ \gamma_{slide} = \left(\frac{1}{1/2 + \mu H_1/L}\right)\left(\mu\alpha - \frac{1}{4g}\left(\frac{2\pi}{T_n}\right)^2 \Delta_{diff}\right) \tag{4.12}$$

From the formulation in Equation 4.12, it is evident that if Δ_{diff} is larger than the following limit, the sliding of the landside crane leg will occur even if the inertial loads on the crane are negligible.

$$\Delta_{diff} \geq 4\mu\alpha g\left(\frac{T_n}{2\pi}\right)^2, \tag{4.13}$$

4.5.4 Evaluating Analytical Relations against Numerical Results

The performance of the derived analytical bounds in response prediction of the container cranes is evaluated by performing a series of nonlinear time-history analyses of the wharf with the nonlinear sliding/uplift crane models for the ground motions presented in Table 4.1. The spectral acceleration of the wharf response at

the landside and seaside crane rails for four of the largest earthquake events of Table 4.1 is presented in Figure 4.20. Although the spectral acceleration of the seaside crane rail is seen to be larger than the corresponding spectral acceleration of the landside crane rail, the spectral acceleration of the two components is similar for periods larger than 1.0 sec in which the period of the crane lays.

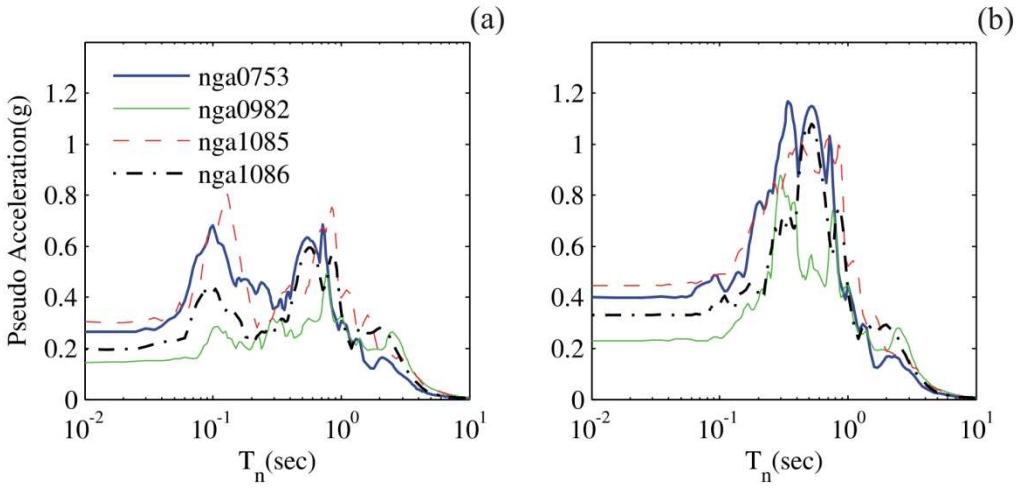

Figure 4.20 The spectral acceleration response of the motion at a) landside and b) seaside crane rails

Figure 4.21a,b shows the portal drift response of the crane versus the spectral acceleration response of the landside and seaside crane rails respectively. Considering that the horizontal differential displacement of the crane rails is very small when sliding occurs, one can neglect the term for Δ_{diff} in Equation 4.12. Substituting the geometric dimensions and dynamic specifications of the modeled crane in Equations 4.9, 4.10, and 4.12, the threshold accelerations for sliding, uplift, and yielding of the portal frame are found to be 0.195g, 0.291g, and 0.698g respectively. In order to better assess the accuracy of the spectral acceleration limits, the ground deformations of a number of presented earthquake events in Table 4.1 are amplified and the drift response of the crane in the foundation-wharf-crane

system to these ground motions are found and presented in Figure 4.21. The spectral acceleration limit of 0.698g for yielding of the portal frame is very large compared to the spectral acceleration limits for sliding and uplift and therefore is less likely to undergo yielding before substantial sliding and uplift occur. Furthermore, the sliding limit is seen to predict the occurrence of the horizontal relative movement of the landside crane leg very well. However for a few ground motions, the sliding happened while their spectral accelerations are less than the derived limit for sliding. This can be attributed to the neglected term of the horizontal differential displacement of the crane rails in Equation 4.12. Due to the smaller spectral acceleration limit for sliding compared to uplift, it is expected that the crane undergoes sliding before uplift occurs. Although this phenomenon slightly changes the dominant natural period of the crane, it is seen that the uplift limit is still an appropriate lower bound for the spectral acceleration of the landside and seaside crane rails which implies that sliding and uplift are nearly independent phenomena.

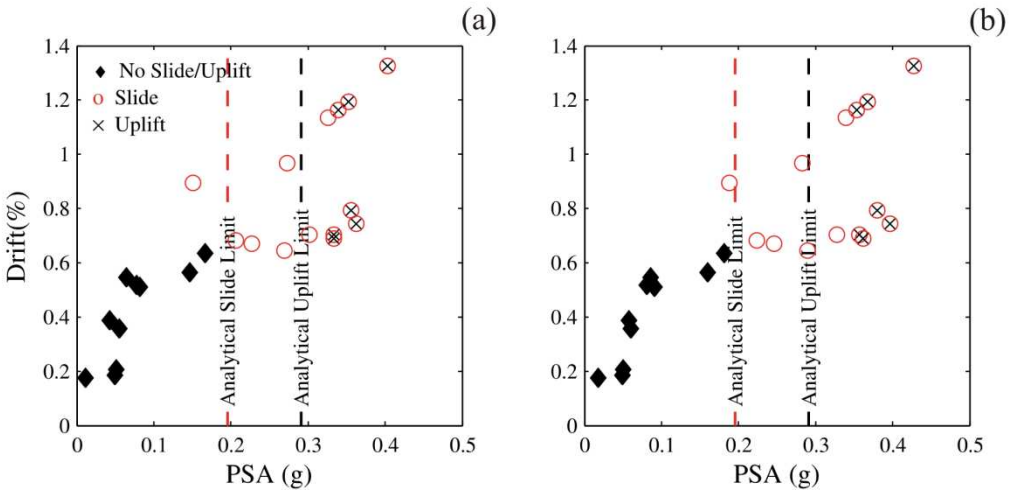

Figure 4.21 The drift response of the portal frame versus a) PSA of the landside rail and b) PSA of seaside rail

4.6 Closure

This chapter studied the dynamic response of the foundation-wharf-crane system for time-histories of the ground motions and pore water pressures of the embankment soil using nonlinear time-history analyses. Furthermore, the dynamic interaction of the wharf and crane was studied using simplified analytical models. Based on the result of the above numerical and analytical studies, the following conclusions are drawn.

1. The simplified analytical study of the wharf-crane interaction showed that the role of the crane in increasing/decreasing the lateral response of the wharf depends on a number of parameters associated with the structural properties of the wharf and crane and the input ground excitation.

2. Unlike the result of the simplified analysis which is the basis for the common assumption in former studies, the nonlinear dynamic FE analysis of the wharf and crane showed that the presence of the crane considerably

increases deformation demands on the wharf. The maximum response in different response measures of the wharf including the curvature response of pile sections and pile-deck connections as well as the horizontal and vertical response of crane rails is increased considerably when a detailed crane model is included. This behavior is a consequence of the large contribution of the crane gravity loads on the response of the wharf, the factor lacking in the formulation of the simplified approach.

In addition, a number of common simplified crane models were also analyzed with the nonlinear wharf model and their performance in response prediction of the wharf with sliding/uplift crane model was evaluated. The main conclusions of these set of analyses are:

1. Increasing the mass of the wharf deck by 5% cannot appropriately capture the effect of wharf-crane interaction on the response of the wharf.

2. The pinned crane model well represents the sliding/uplift crane model especially for small earthquakes where the intensity of the ground shaking is not large enough for sliding or uplift to occur.

3. The wharf with crane gravity captures the effect of the wharf-crane interaction on the response of the wharf properly for low and high intensity earthquakes. However, it does not adequately capture the deformation response of pile-deck connections.

Furthermore, simple analytical limits on the spectral acceleration response of the crane rails were derived to predict the occurrence of sliding, uplift, and yielding of

the portal frame. The results of the numerical simulation showed that the derived limits perform well in predicting the response of the crane. Also, for the configuration of the crane model studied in this research, sliding of the landside crane leg was found to be the most susceptible nonlinear phenomenon in the crane followed by the uplift of the landside crane leg and yielding of the portal frame.

CHAPTER 5

THREE DIMENSIONAL MODELING AND ANALYSIS OF THE PILE SUPPORTED CONTAINER WHARF

5.1 Introduction

As described in previous chapters, the three-dimensional model of wharves consists of repeating rows of piles called strips in the longitudinal direction, which together form a wharf segment. Chapter III studied the response of a wharf segment in the seaside-landside direction by performing a series of two-dimensional dynamic analyses of one strip model. This procedure is very common in seismic analysis of wharves since it requires less computational time compared to analyzing three-dimensional models. However, by reducing the size of the problem from three-dimensions to two-dimensional plain strain, some important features of the wharf response pertinent to wharf characteristics in three-dimensions will be lost. These features include: the response of the wharf in the longitudinal direction as the direct consequence of longitudinal component of the incident earthquake motion; the torsional response of the wharf due to the difference between the center of mass and the center of rigidity; and the boundary effects from adjacent segments including pounding and shear key effects. Very few studies investigated three-dimensional response of wharf segments and considered the boundary effect of adjacent segments. This chapter intends to respond to the question of the importance of incorporating three-dimensional features of wharves compared to corresponding plain strain models. First, modeling of the wharf in three dimensions is described and its modal properties are studied. The procedure of generating ground

deformations in the out-of-plane (longitudinal direction) from the result of plain strain free-field analysis is explained. Next, the three-dimensional response of the wharf is studied for a number of earthquakes in detail. Later, the chapter presents a simplified modeling procedure for three-dimensional analysis of wharves. The procedure is validated by comparing the modal properties as well as dynamic response characteristics of the simplified model with corresponding responses of the full three-dimensional nonlinear model of the wharf. Finally, the chapter presents modeling of boundary conditions of a wharf segment.

5.2 Analytical Modeling

The Finite Element model of the wharf in two dimensions is used to generate the three-dimensional wharf model. This is done by generating a strip of one wharf segment and repeating the identical strip model in the longitudinal direction. The adjacent strips are then connected together at the deck level by means of rigid beam elements to enforce the diaphragm action in the horizontal plane of the deck. Connecting the identical strips in this way, a wharf segment is generated in which the piles work together in all directions.

The transformation of the two-dimensional plain strain model of the wharf of Chapter III to three-dimensional model of a single strip requires modification of the model structure as well as constitutive elements.

1. The dimension of the model in OpenSEES is changed from two to three in "*model builder*" command. Furthermore, the degrees-of-freedom per node is increased from three to six.

2. The fiber section of the piles model the axial and flexural response behavior of pile sections which is sufficient for two-dimensional plain strain modeling of the piles. For three-dimensional analysis, the torsional behavior of the piles is aggregated with the fiber section of pre-stressed piles.
3. The soil-structure interaction in the out-of-plane direction is modeled by replacing the one-dimensional model of the macroelement with the corresponding two-dimensional model. Interactions of piles and the surrounding soil in the two orthogonal horizontal directions are uncoupled, however the near-field pore pressure build up is the result of the total amount of shear works in the two directions. For the clay layer, the same p-y elements used in the transverse direction are modeled for the out-of-plane direction.

The procedure for generating the three-dimensional model of the wharf segment from the two-dimensional plain strain model is illustrated in Figure 5.1.

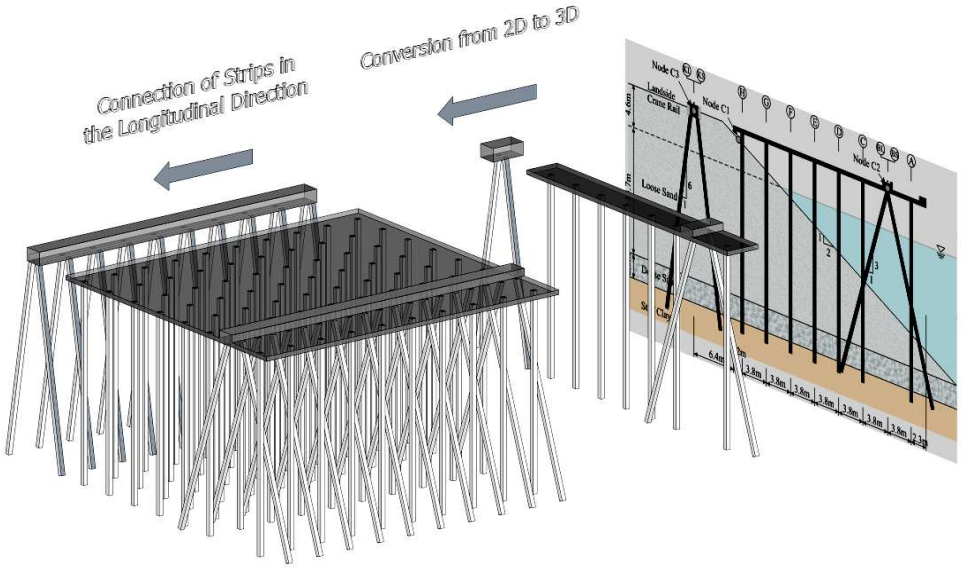

Figure 5.1 The process of generating the three-dimensional model of the wharf segment from the two-dimensional model of the wharf.

5.2.1 Modal Analysis

In order to have an understanding of the three-dimensional response characteristics of the wharf segment, a modal analysis is performed on the foundation-wharf system in the initial rest condition under gravity loads and the mode shapes and mass participating factors are derived. Figures 5.2 and 5.3 show mode shapes of the significant modes of the wharf segment and the associated natural periods and mass participation factors are presented in Table 5.1.

The first mode of the wharf is torsional in the plane of the deck (Figure 5.2a) with a natural period of 0.504 sec. This mode primarily contributes to the longitudinal deformation response of the wharf with a mass participation factor of 0.55 in the longitudinal direction.. As seen in Figure 5.2b, the second mode of the wharf is purely translational in which the wharf segment moves toward the sea, with a natural period of 0.273 sec.

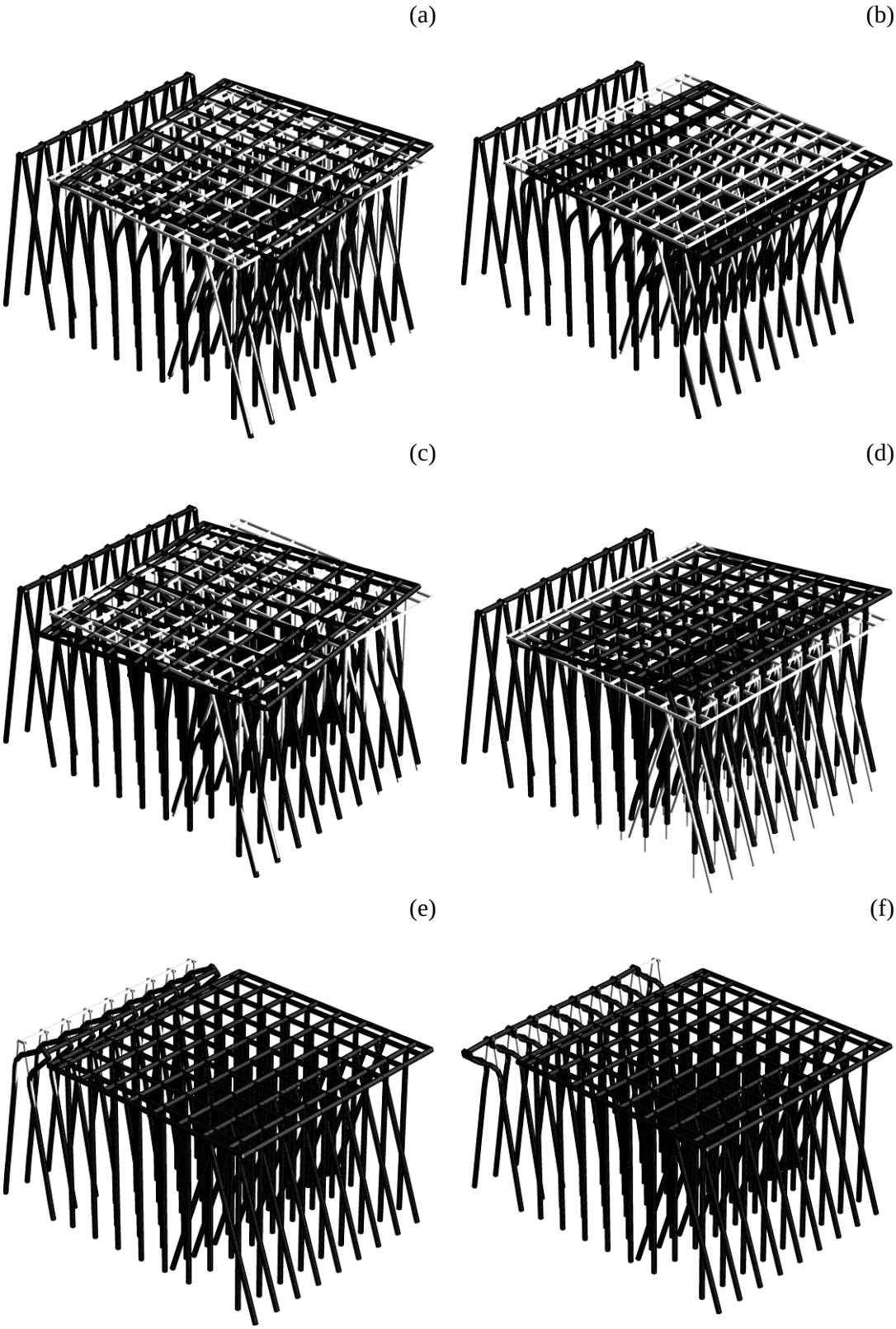

Figure 5.2 Mode shapes of the three-dimensional wharf model for a) first, b) second, c) third, d) forth, e) fifth, and f) sixth mode.

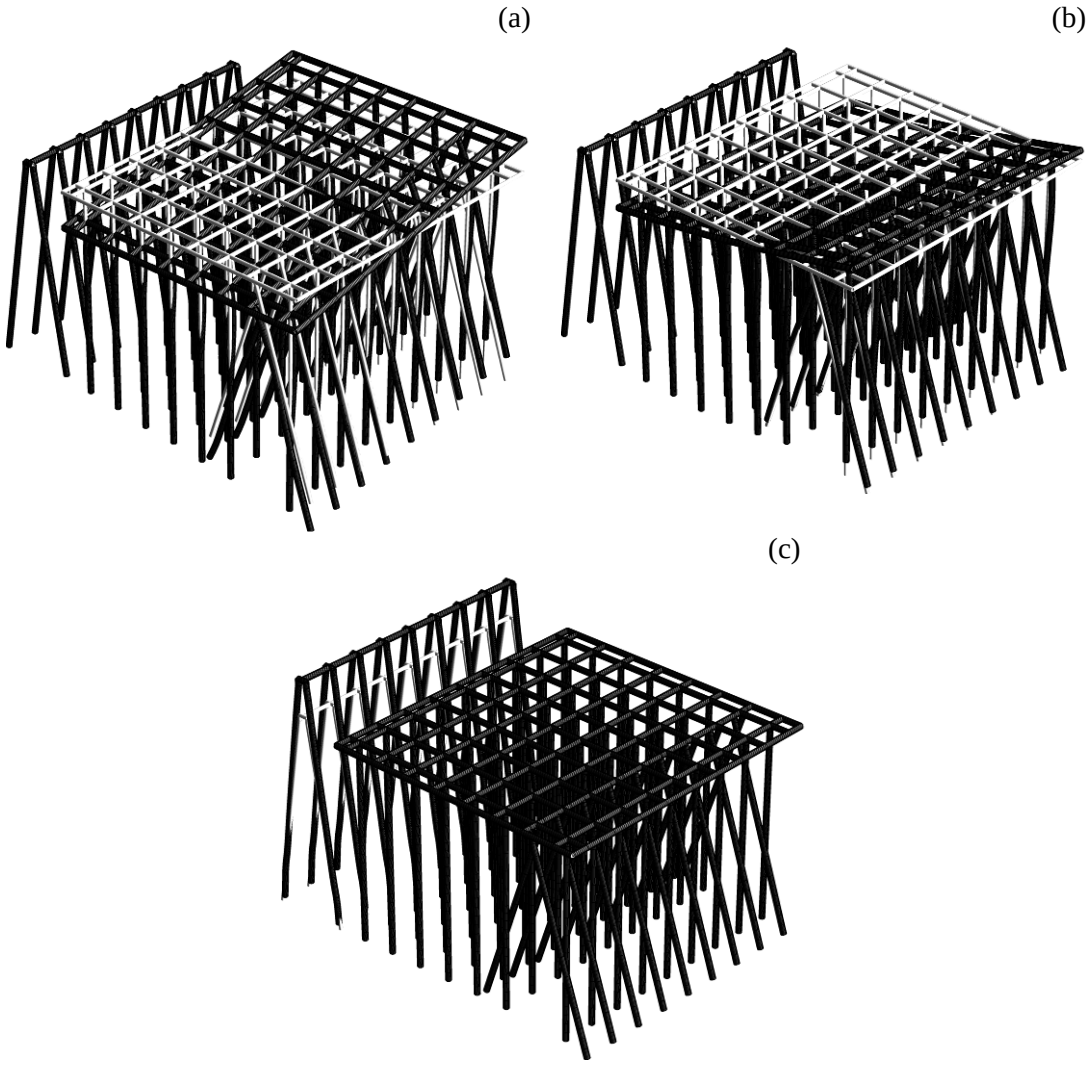

Figure 5.3 Mode shapes of the three-dimensional wharf model for a) ninth, b) eleventh and c) thirteenth mode.

Table 5.1 Natural periods of the first eighteen modes of the wharf and corresponding mass participation factors.

Mode No	Natural Period (sec)	r_{mx}	r_{my}	r_{mz}
1	0.504	0.0003	0	0.5501
2	0.273	0.9062	0.0058	0.0004
3	0.166	0.0002	0.0008	0.3933
4	0.156	0.01	0.5535	0.0005
5	0.097	0.0833	0	0
6	0.095	0	0	0.0832
9	0.078	0	0.0098	0.0005
11	0.051	0	0.3457	0
13	0.033	0	0.0833	0

r_m^* is the mass participation factor

5.2.2 Out-of-Plane Ground Motion Generation

Ground deformations as the result of incident earthquakes can be represented by their projections in Cartesian coordinate system with arbitrarily oriented three orthogonal directions. This study adapts one of the possible coordinate systems in which the axes of the coordinate are parallel to transverse, vertical, and longitudinal directions defined in Chapter III. Two dimensional plain strain free-filed analysis of the soil embankment to horizontal component of the earthquakes under gravity effects yields the transverse and vertical ground deformation response of the soil embankment. However, the response of the embankment in the longitudinal direction is required for three-dimensional response evaluation of the wharf and landside crane rail. In order to generate the out-of-plane ground deformations, a procedure is developed (Rix and Ivey) that incorporates the spectral matching

technique. Assuming that there exists a linear model to relate the two orthogonal horizontal components of earthquake accelerograms in the frequency domain, the transfer function that maps the transverse accelerogram to the out-of-plane accelerogram is derived and applied to the response spectrum of the transverse embankment deformation at the location of soil springs found from free-field analysis. The out-of-plane motion is then found by matching the spectrum of transverse deformations of the embankment to the target spectrum derived in the previous step. This procedure is outlined and explained in detail below for NGA0810 (Table 4.1). Transverse and longitudinal acceleration time-history of the earthquake are shown in Figure 5.4a,b.

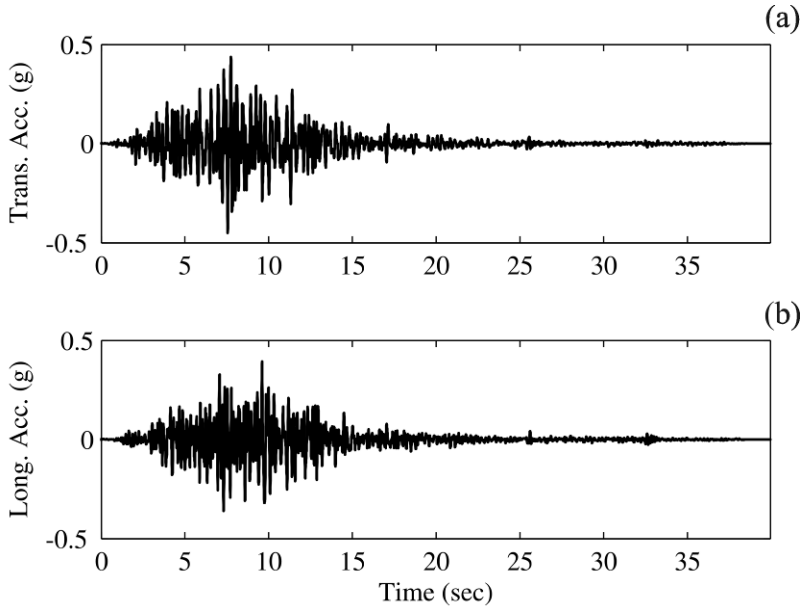

Figure 5.4 The acceleration time-history of NGA0810 in a) transverse and b) longitudinal directions.

Step 1. Spectral acceleration of the incident earthquake is found for a wide range of periods for transverse (X) and longitudinal (out-of-plane, Z) directions and are shown in Figure 5.5a,b respectively. The transfer function from X to Z is found by

$$T_{ZX}=S_{eq\,Z}/\,S_{eq\,X} \tag{5.1}$$

where $S_{eq\,Z}$ and $S_{eq\,X}$ are the acceleration response spectrum of ground acceleration in Z and X directions respectively. Figure 5.6 presents the transfer function T_{ZX} for NGA0810 found using Equation 5.1.

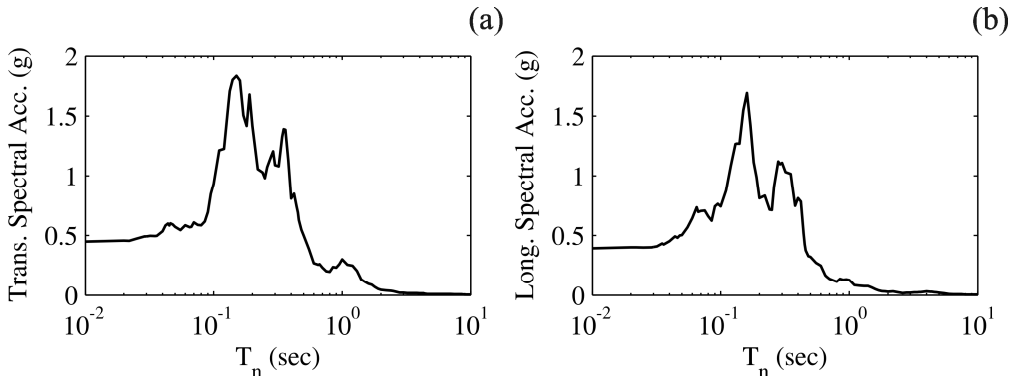

Figure 5.5 Acceleration response spectrum of NGA0810 in a) transverse and b) longitudinal directions.

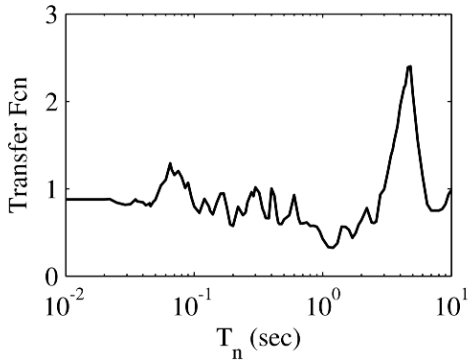

Figure 5.6 Transfer function from X to Z.

For each of the displacement records of the embankment soil, the following steps are done.

Step 2. It is assumed that the transverse displacement response of the embankment found from free-field analysis, X_{emb}, is composed of two distinct components: a) the permanent deformation of the embankment $X_{emb,\ permanent}$ as the result of the monotonic movement of the soil toward sea and b) the oscillating response $X_{emb,\ osc}$.

The moving average of the displacement records of the embankment is derived and regarded as the permanent deformation of the embankment. This component does not contribute directly to the inertial response of the soil and is subtracted from the transverse motion to find the oscillating soil response.

$$X_{emb,osc}=X_{emb}-X_{emb,permanent} \quad (5.2)$$

The transverse displacement time-history of the soil embankment at the top of pile K (Figure 3.1) during NGA0810 with the corresponding moving average response are shown in Figure 5.7a. The oscillating response of the soil is found using Equation 5.2 and is shown in Figure 5.7b. Figure 5.7c compares the frequency content of the permanent and oscillating components of the soil deformation presented in parts a and b of Figure 5.7. It is observed that except at very low frequencies, the power spectral density (PSD) of the oscillating response of the embankment is larger than the PSD of the permanent deformation by several orders of magnitude.

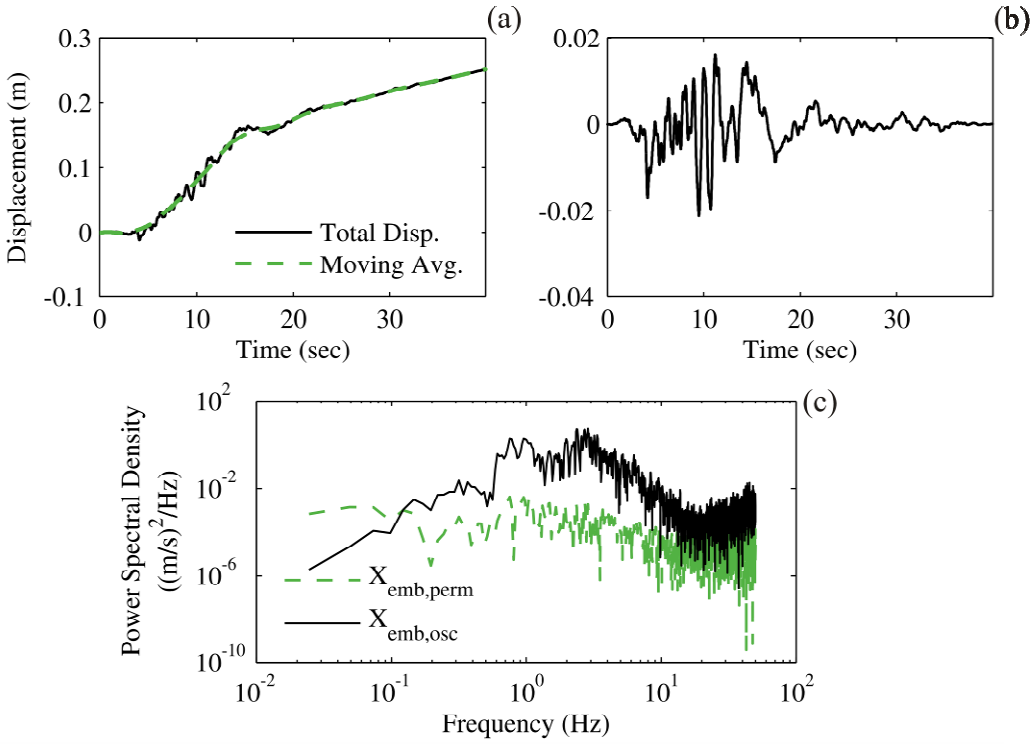

Figure 5.7 Components of the transverse soil response on top of pile K: a) total and permanent displacements, b) oscillating displacement, and c) PSD of permanent and oscillating responses.

Step 3. The response spectrum of the inertial component of the embankment deformation in the transverse direction $X_{emb,osc}$ is calculated. The target spectrum for the out-of-plane motion is derived as

$$U=S_{X\ emb,iner}\,T_{ZX} \tag{5.3}$$

The transverse spectral acceleration of the oscillating component of the soil response during NGA0810 at the top of pile K and the corresponding target spectrum for the longitudinal response are shown in Figure 5.8a,b.

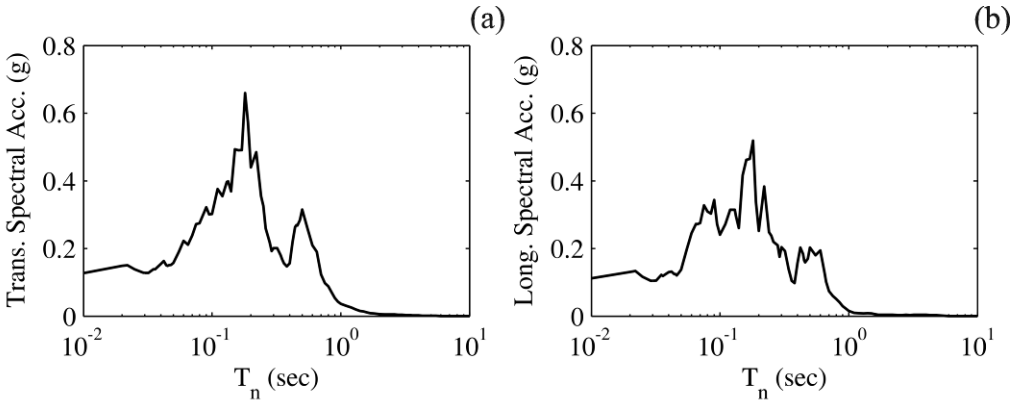

Figure 5.8 Spectral acceleration of a) oscillating component of the soil displacement at top of pile K during NGA0810 and b) the corresponding response in the longitudinal direction.

Step 4. Finally, $X_{emb,osc}$ is spectrally matched to U to derive the longitudinal deformation of the embankment Z_{emb}. Matching to the target spectrum is performed by using the program RSPMATCH (Abrahamson 1993). The resulting longitudinal displacement time-history of the embankment at top of pile K during NGA0810 is shown in Figure 5.9.

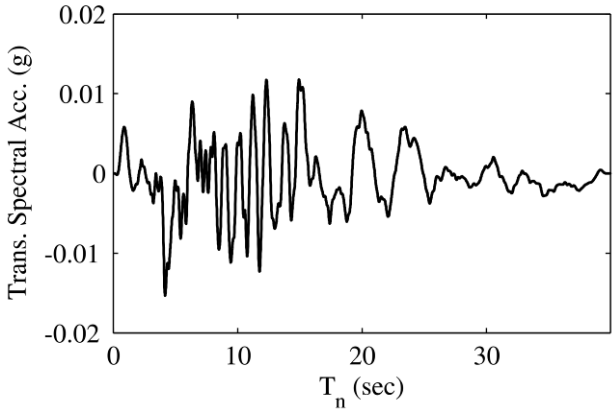

Figure 5.9 The longitudinal displacement of the embankment soil at top of pile K during NGA0810.

The program implements the algorithm proposed by Abrahamson (1993) which is a time-domain spectral matching method. This approach uses the algorithm developed by Tseng and Lilanand (1988) to match the spectrum of the original

signal to the target spectrum by adding wavelets in the time domain. In case the response spectrum of the record is below the target spectrum at long periods, the algorithm removes one of the velocity pulse lobes or decreases its amplitude to lower the spectrum at long periods. If during this process, the record is brought below the target spectrum at high frequencies, the program adds the high-frequency content back to the record. For cases where the response spectrum of the original record is above the target spectrum at long periods, the algorithm amplifies the entire spectrum to enforce the long period content of the signal to reach the desired amplitude levels. If during this process, the high-frequency content of the record is considerably amplified, then the high frequency contents are removed from the signal.

5.2.3 Three-Dimensional Response of the Wharf

The derived out-of-plane ground displacement time-histories together with the transverse and vertical ground deformations from free-filed analysis are applied to the free end of the soil springs in loose and dense sand layers and the bottom clay layer. Furthermore, the pore pressure time-histories are imported to macroelements in sand layers by adding an additional degree-of-freedom to the free end of the element. This section studies the three-dimensional response of the wharf through nonlinear time-history analysis of the wharf to the applied ground deformations for NGA0810. The three-dimensional configuration of the wharf and the nodes at which the response of the wharf will be studied are shown in Figure 5.10.

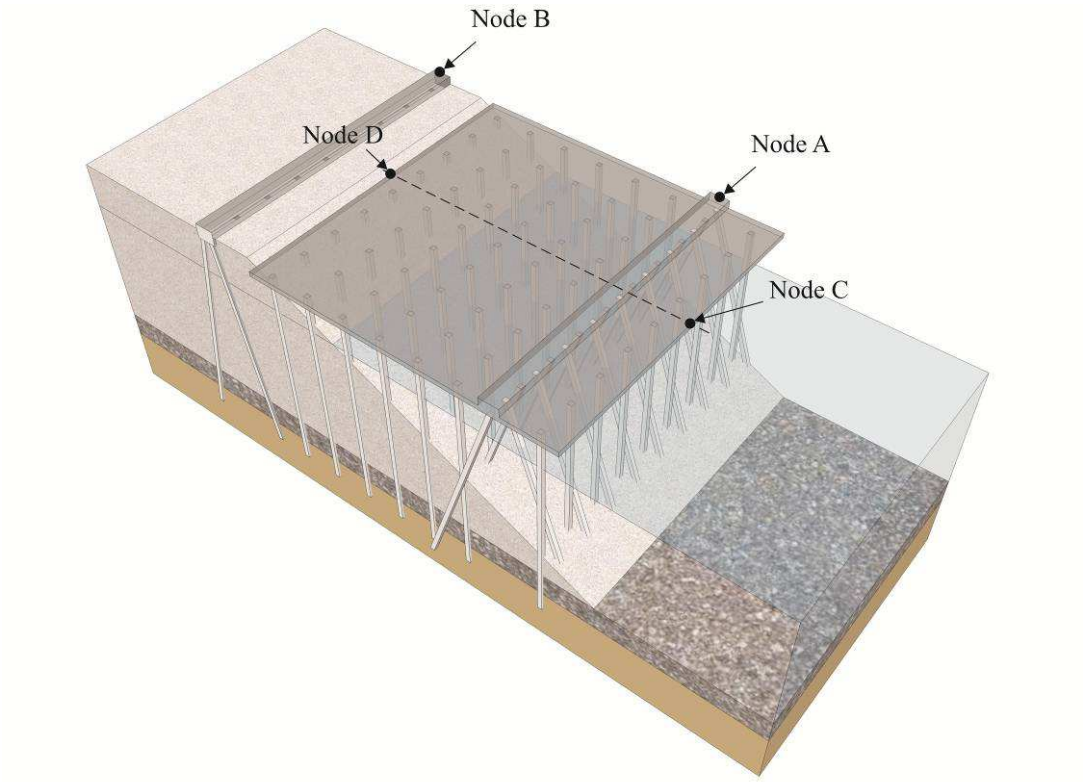

Figure 5.10 Schematic view of the wharf

Figure 5.11 presents the response of the wharf in the transverse and vertical directions at the location of seaside and landside rails and compares theses responses with the corresponding responses found from the two-dimensional analysis of the plain strain model of the wharf. Figures 5.11a,b show the transverse displacement response of the seaside and landside crane rails, respectively. It is observed that both of the crane rails almost monotonically move toward the sea, which is the consequence of the seaward movement of the embankment soil under lateral ground shakings and gravity. The permanent deformations of the seaside and landside rails are 26.6 cm and 16.2 cm respectively. The vertical displacement response of the wharf at the location of the seaside and landside crane rails are shown in Figure 5.11c,d. The permanent settlement in the seaside rail is 4.8 cm while the corresponding quantity in the landside rail is limited to 0.60 cm.

Noticeable in these figures is the fact that the transverse and vertical response of the crane rails from a three-dimensional model of the wharf closely follow the response of the wharf from the two-dimensional model. This is in agreement with the conclusion from modal analysis results which showed that the out-of-plane response of the wharf is almost uncoupled from the response of the wharf in transverse and vertical directions.

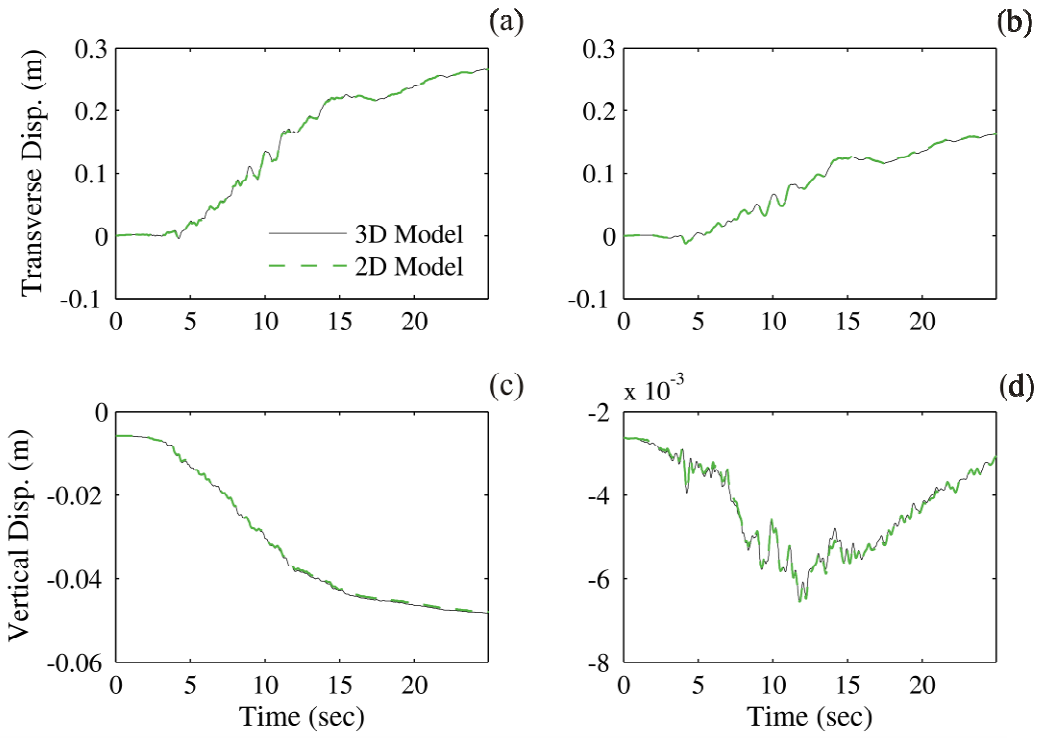

Figure 5.11 Displacement responses of the three-dimensional and two-dimensional wharf models: a) transverse displacement at the seaside rail, b) transverse displacement at the landside rail, c) longitudinal displacement at the seaside rail, and d) longitudinal displacement at the landside rail.

The longitudinal displacement response of the landside and seaside sections of the wharf are shown in Figure 5.12. As expected, the longitudinal displacement of the seaside rail, 1.4 cm, is larger than the corresponding displacement of the landside rail, 1.2 cm.

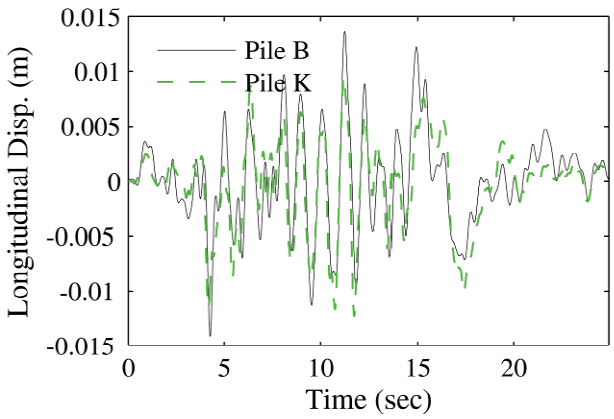

Figure 5.12 Longitudinal displacement response of the landside and seaside rails.

Figure 5.13 presents the acceleration response of the wharf at the location of the rails. The transverse acceleration of the wharf at the seaside and landside rails are shown in Figure 5.13a,b from which the maximum acceleration responses are found to be 0.19 g and 0.11 g respectively for the seaside and landside rails. Similarly, the vertical acceleration response of the rails are shown in Figure 5.13c,d. The maximum vertical acceleration of the seaside rail is 0.06 g while the corresponding response of the landside rail is limited to 0.01 g.

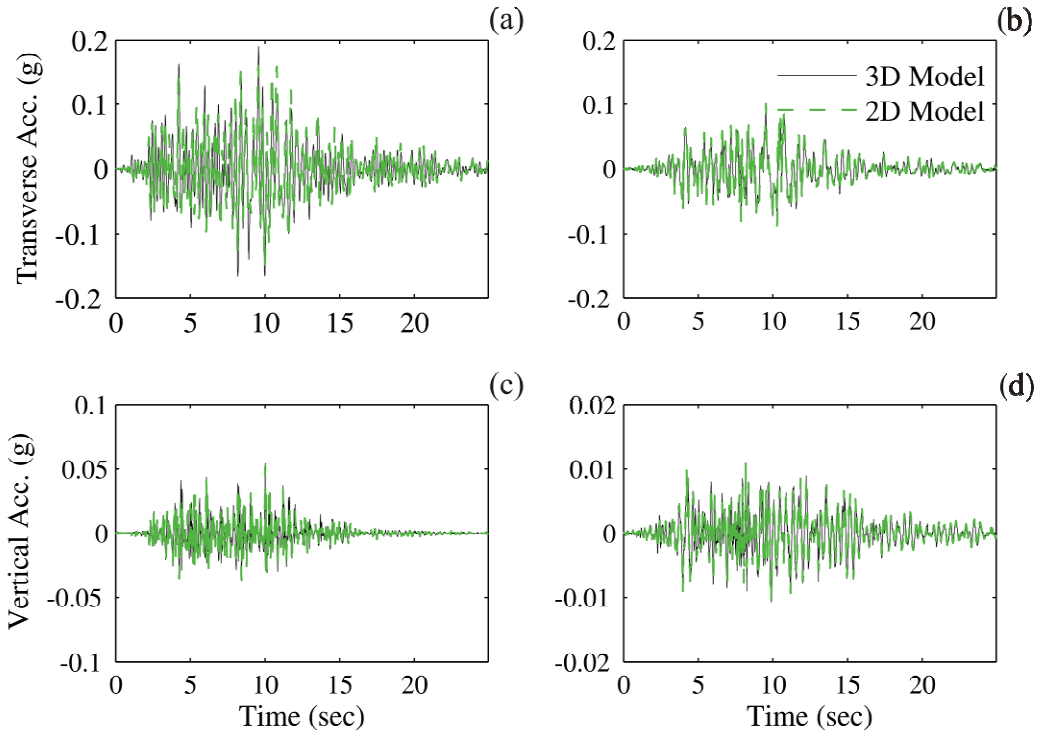

Figure 5.13 Acceleration responses of the three-dimensional and two-dimensional wharf models: a) transverse acceleration at the seaside rail, b) transverse acceleration at the landside rail, c) longitudinal acceleration at the seaside rail, and d) longitudinal acceleration at the landside rail.

The longitudinal acceleration of the seaside and landside rails are shown in Figure 5.14 in which the longitudinal acceleration of the seaside rail, 0.1 g, is found to be smaller than the longitudinal acceleration of the landside rail, 0.12 g.

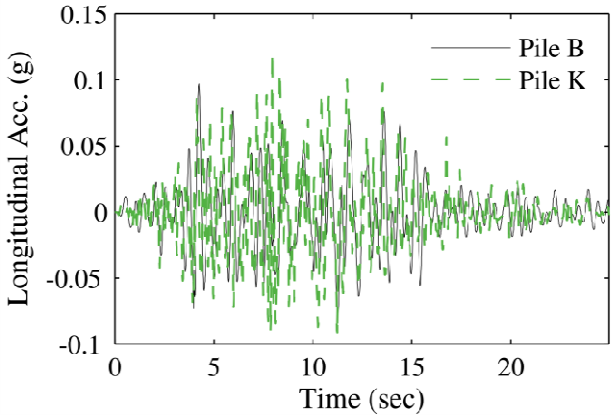

Figure 5.14 Longitudinal acceleration response of the landside and seaside rails.

The response of the pile-deck connection at the location of pile H is shown in Figure 5.15a-c. Figure 5.15a presents the time-history of the rotation response of the connection around the longitudinal axis. The almost monotonic increase in the rotation response is due to the seaward movement of the deck as a result of the pressure from the embankment soil. Very good agreement is observed in this response measure between two-dimensional and three-dimensional wharf models. The time-history of the connection moment as the result of the rotation response is shown in Figure 5.15b. The smaller rate of increase in the connection moment after 10 sec while the rotation of the connection is increasing indicates that the connection has reached its moment capacity. The resulting moment-rotation behavior of the connection is shown in Figure 5.15c. Although the rotation of the connection in the three-dimensional model closely follows the corresponding response in the three-dimensional model, the moment response of the connection in the two models are slightly different.

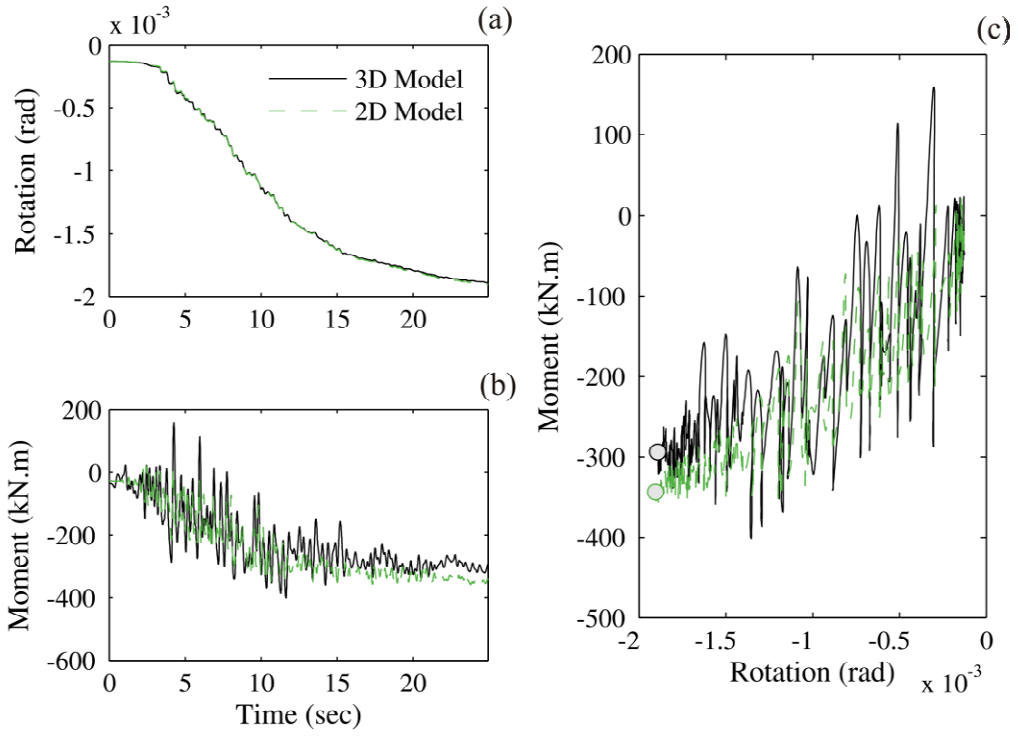

Figure 5.15 Pile H connection response to NGA0810 in the transverse direction: (a) time-history of connection rotation, (b) time-history of connection moment, and (c) moment-rotation behavior of the connection.

Similarly, the rotation and moment response of the connection of pile H to the deck around the transverse direction are shown in Figure 5.16a-b. As seen in Figure 5.16a, the rotation of the connection around the transverse direction is smaller by two orders of magnitude than the rotation response around the longitudinal axis. These small rotations are not large enough to push the connection into the nonlinear range and as a result the moment remains in the linear range and there is a small residual moment at the end of the simulation.

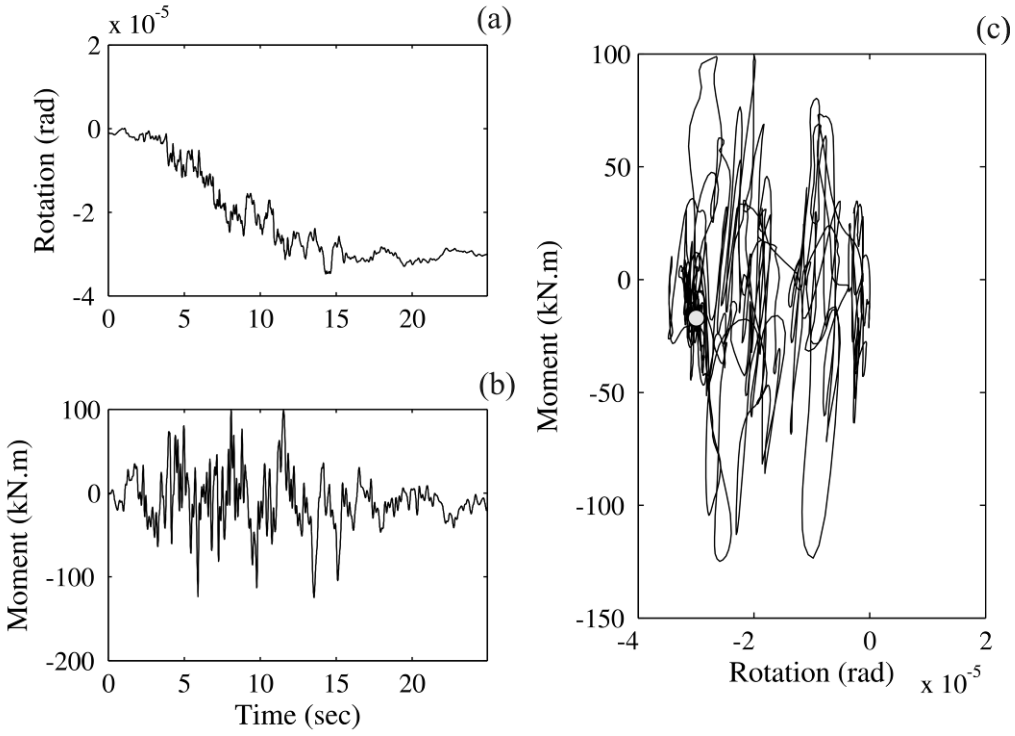

Figure 5.16 Pile H connection response to NGA0810 in the longitudinal direction: (a) time-history of connection rotation, (b) time-history of connection moment, and (c) moment-rotation behavior of the connection.

The profile of the curvature ductility of the pile sections for the transverse and longitudinal directions is shown in Figure 5.17. The ductility ratios are found by dividing the maximum curvature in the pile's sections by the corresponding yield curvature. It is seen that the maximum transverse curvature (red line) in the piles are occurring at the interface of dense and loose sand layers where the large relative deformations of the sand layers impose large curvature demands on the piles. The second zone of large transverse curvature is at the pile sections within the soil embankment close to the soil surface. These curvature demands are the consequence of the pile's resistance against seaward displacement of the wharf deck. Pile sections close to the pile-deck connections also face large curvature demands as a result of large transverse movement of the wharf deck. Also presented in Figure 5.17 is the profile of the curvature ductility in the longitudinal direction (blue line).

In general, the longitudinal curvature ductility demand is smaller than the corresponding transverse ductility demand due to the fact that the transverse deformations of the wharf under the seaward movement of the embankment are larger than the longitudinal movement of the wharf. However, in piles that are fully embedded in soil – piles supporting the landside crane rail and the row of piles at the landside end of the wharf deck, even a small longitudinal deformation of the soil imposes large curvature demands as a result of the rotational fixity at the piles head. This results in landside piles that experience large curvature demands in the longitudinal direction.

The location of the yielded sections of the piles is indicated in Figure 5.17 by black circles which coincide with the location of maximum curvatures in the transverse and/or longitudinal directions.

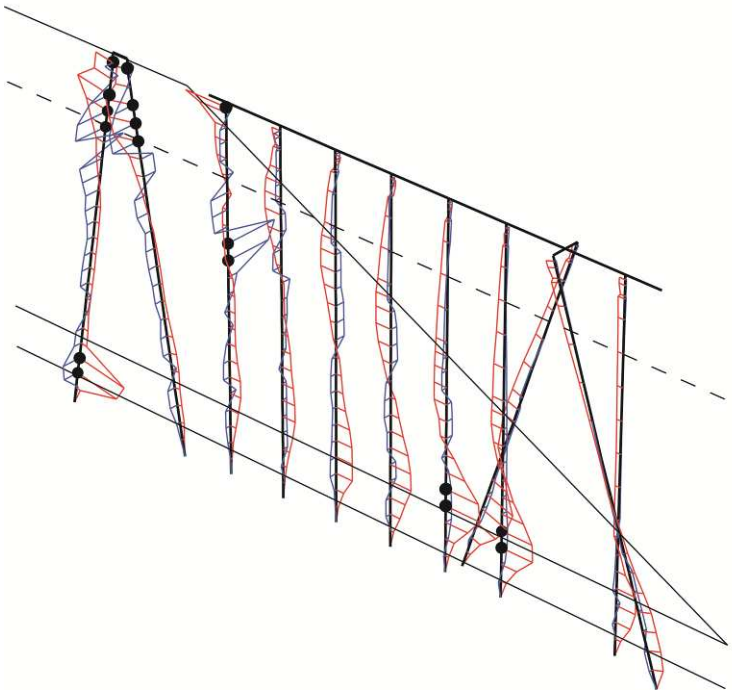

Figure 5.17 Profile of the maximum curvature ductility demand of the wharf and landside crane rail during NGA0810.

The final deformed shape of the wharf under NGA0810 is shown in Figure 5.18. The displacements are magnified 3.5 times in this figure. It is seen that the final deformation of the wharf is seaward which is the consequence of the permanent lateral movement of the soil embankment toward sea. Furthermore, the final longitudinal deformation of the wharf is seen to be negligibly small compared to the transverse deformations. This can be attributed to the fact that the longitudinal deformation of the embankment is almost symmetric and smaller than the transverse deformation of the embankment soil and consequently the permanent deformation of the soil in the longitudinal direction is small.

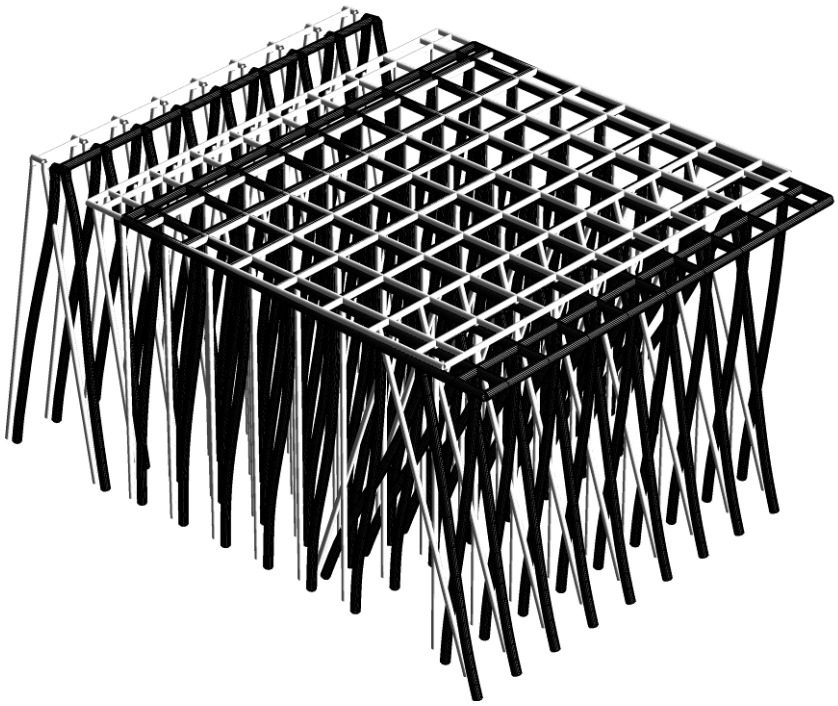

Figure 5.18 Final deformed shape of the wharf and landside crane rail during NGA0810.

5.3 Simplified Wharf Model

Few researchers have studied ways of simplifying wharf structures and calibrating them with either experimental results or numerical simulations of detailed FE models. Benzoni and Priestley (2003) considered the seismic response of wharf systems based on simple analytical models. The study presents a wharf segment modeled by a rigid deck with eight nonlinear springs at four corner nodes. The interaction of adjacent wharf segments was considered by using shear keys. Yamamoto et al. (2000) used a single degree of freedom (SDoF) model to represent the wharf dynamic behavior. Although the frequency response of the model had good agreement with test results, the time-history response did not match well with experimental results. A different modeling approach is proposed in this research in order to simplify the wharf model.

As mentioned earlier, a wharf segment is composed of a number of strips which are connected together in the longitudinal direction. The strips are identical and their number in a wharf segment is directly related to the length of the wharf. The computational time required for nonlinear dynamic analysis of a wharf segment depends on the number of degrees-of-freedom in the FE model which is a function of the number of repeating strips. A wharf segment consisting of a large number of strips requires a considerably large computational resources for nonlinear time-history analysis for a given embankment soil deformation history. Running such analysis for a large number of times, as is required for probabilistic seismic demand analysis, requires a considerably large amount of time. To overcome this problem, a simplified model is proposed that lumps the dynamic characteristics of wharf segments into a representative segment with only one strip. As such, the simulation

time of a wharf with an arbitrary number of strips would be equal to the computational time of a three-dimensional analysis of one strip of the wharf.

5.3.1 Simplifying One Wharf Segment

The proposed simplified model of the wharf is a modified single strip that represents the wharf segment by lumping the dynamical properties of the wharf to the representative strip. The procedure takes the advantage of the fact that the strips are identical and repeating in the longitudinal direction, which consequently implies that the strips are working in parallel. Therefore, the transverse behavior of the wharf segment can be captured by a single strip with modified material properties of constitutive elements including piles, pile-deck connections, and soil springs. The torsional resistance of the wharf in the horizontal plane of the deck is modeled by zero-length nonlinear rotational springs whose properties are found by performing a series of nonlinear static pushover analyses of the piles. Furthermore, the effects of inertial forces of mass are lumped into point translational and rotational nodal masses at the top of the piles in the single strip of the representative wharf model. The configuration of the simplified model is shown in Figure 5.19. The details of the procedure to generate the simplified model is explained in the following sections.

Figure 5.19 The configuration of the simplified model

5.3.2 Modeling Lateral Resistance

Lateral resistance of wharf segments against embankment soil deformations is provided by soil resistance modeled by nonlinear soil springs and structural resistance of the piles, pile-deck connections, and the deck. In particular, the transverse resistance of a wharf segment is the result of the transverse resistance of single strips that are attached in the longitudinal direction and therefore are working in parallel. The effect of these parallel strips in the transverse direction can be captured by a single strip model by assigning paralleled material properties to each of the constitutive elements. This relies on the fact that the total force-deformation behavior of a number of same elements say for example *n* elements working together in parallel is theoretically equivalent to the force-deformation behavior of one of those elements but with a material stress-strain curve in which at each point

on the curve the stress is *n* times the corresponding stress of the stress-strain curve assigned to any of the *n* elements. By changing the material properties of core concrete, cover concrete, steel rebars, and pre-stress tendons for pile sections and pile-deck connections and the material properties of the macroelements and p-y, t-z, and q-z soil springs, the lateral force-deformation behavior of a wharf segment can be fully represented by a single strip model.

5.3.3 Modeling Torsional Resistance

Although shrinking the model of a wharf segment into a single strip can capture the transverse behavior of the wharf, the torsional resistance of the wharf in the plane of the deck will not be simply captured by the geometry of one single strip. The piles contribute to the torsional resistance of the wharf in two ways: 1) the longitudinal resistance of piles times the projected transverse lever arm from the center of rotation and 2) the transverse resistance of the piles times the projected longitudinal lever arm from the center of rotation. The concept of using parallel materials for constitutive elements of a strip to lump the properties of a segment into one strip model can only capture the torsional resistance from the first source. The second source of torsional resistance is incorporated into the simplified one strip model by adding nonlinear rotational springs whose moment rotation behavior are found from the result of pushover analyses on each of the piles in a single strip. The overall nonlinear force-deformation behavior of the piles is derived by performing two-dimensional nonlinear static pushover analyses on the piles with their top nodes rotationally fixed. The results of these analyses for piles A to K are presented in Figure 5.20.

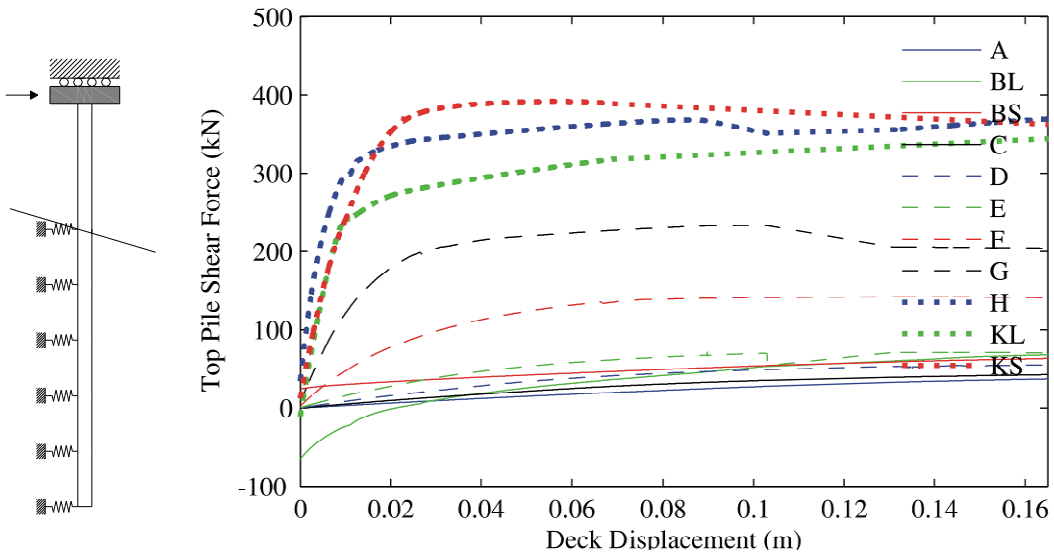

Figure 5.20 Pushover model configuration (left) and pushover results for different piles

Linear, bilinear, or trilinear curves are fitted to each of the force-deformation curves of the piles depending on the number of response regions observed in the force-deformation response. Having the type of the fitting curve fixed, the properties of the multi-linear fitted curves i.e. the intercept of the consecutive linear lines are found based on the energy method which simply minimizes the difference between the areas under the real force-deformation curve with the area under the approximate multi-linear curves. In the next step, the piles with connected soil springs in the model of the wharf are replaced by nonlinear springs to which the corresponding multi-linear force-deformation curves are assigned. Substituting all of the piles and soil springs in this way, the entire wharf model will be simplified to the wharf shown in Figure 5.21.

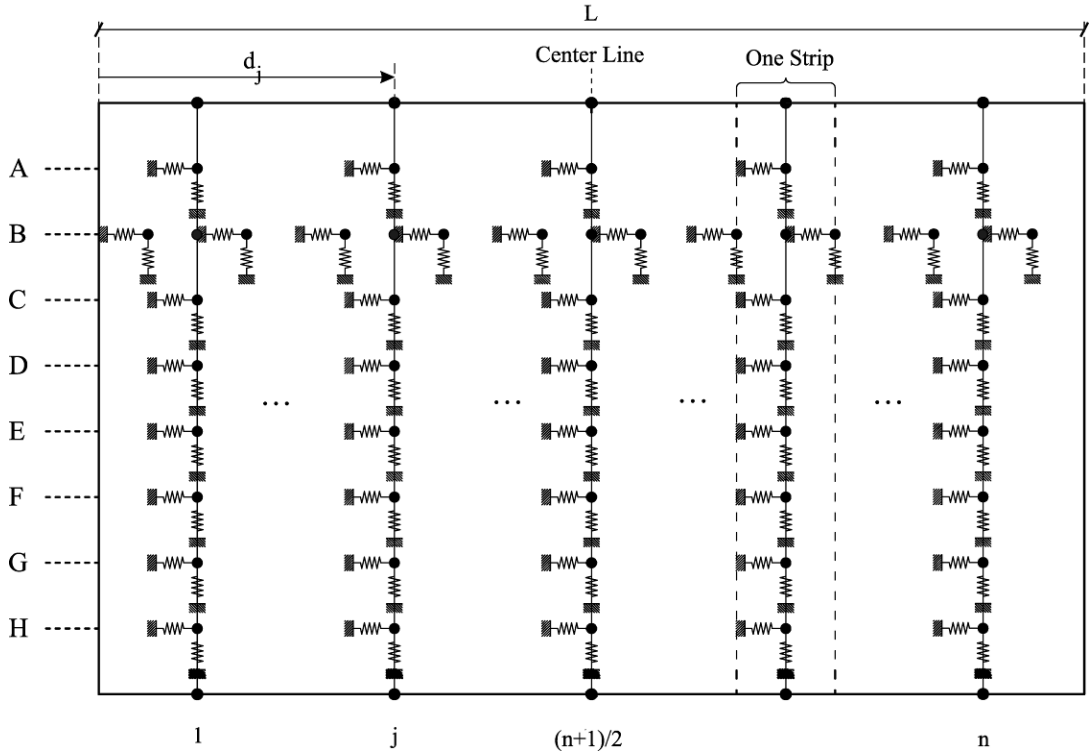

Figure 5.21 The plan view of a typical wharf segment with piles replaced with nonlinear springs (assuming that *n* in an odd number)

The moment-rotation behavior of the rotational springs in Figure 5.19 is set equal to the moment-rotation behavior of the set of nonlinear springs in the corresponding longitudinal row (Figure 5.21) about the location of the rotational spring on the center line in Figure 5.21. The derivation of equivalent rotational spring properties is explained here for a case where the force-deformation response of the pile is approximated by a bilinear curve. It is assumed that the bilinear curve shown in Figure 5.22 represents the force-deformation behavior of a typical pile in the wharf where the properties, yield displacement Δ_y, yield force F_y, initial stiffness k_c, and the ratio of post-yield to initial stiffness α are found from curve fitting using the concept of energy equivalence explained before.

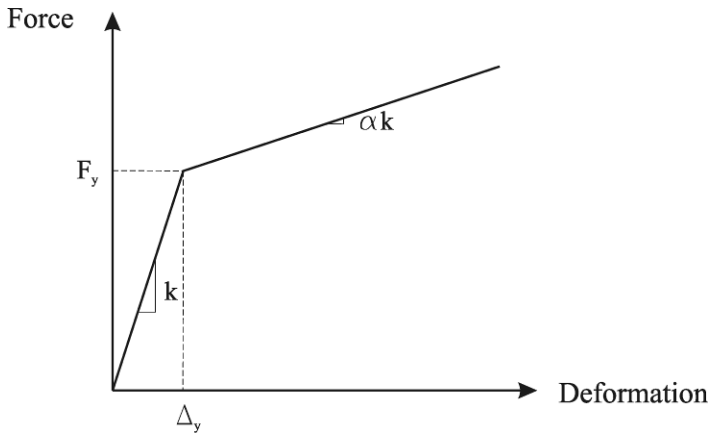

Figure 5.22 Fitted lateral force-deformation curve for piles in row C (Figure 5.21)

The contribution of the transverse resistance of the piles in a longitudinal row in the torsional resistance depends on the distance of the pile from the middle of the wharf d_i (Figure 5.21). In this case, not only the yield moment M_y but also the yield rotation θ_y will depend on how far the pile is from the middle of the segment. In the equivalent moment-rotation curve for a row of *n* piles with bilinear force-deformation characteristics, the slope of the curve changes at [*n*/2] different rotations called θ_{yi} (*i*=1,2,..,[*n*/2]). Assuming that Figure 5.22 represents the fitted force-deformation curve of the pile, we have

$$\theta_{yi} = \frac{\Delta_y}{L/2 - d_i} \tag{5.4}$$

$$k_i = \frac{2F_y\left(L/2 - d_i\right)^2}{\Delta_y} \tag{5.5}$$

$$M_{Tyi} = \sum_{j=1}^{i-1} k_{\theta j}\left[(1-\alpha)\theta_{yj} + \alpha\theta_{yi}\right] + \sum_{j=i}^{\left[\frac{n}{2}\right]} k_{\theta j}\theta_{yi}, \qquad i = 1,\cdots,\left[\frac{n}{2}\right] \tag{5.6}$$

where Δ_y and F_y are shown in Figure 5.22, n is the number of strips and d_i is the distance of strip j from the left edge of the segment shown in Figure 5.21. The moment-rotation behavior of each of the piles in the assumed row of piles about the center line of the segment and the resulting equivalent moment-rotation of the row of piles are shown in the Figure 5.23a,b respectively.

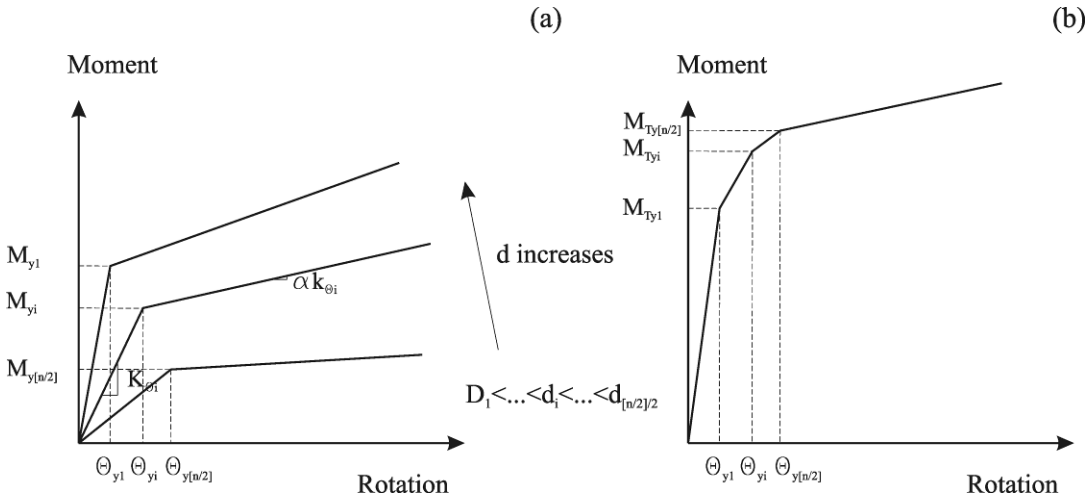

Figure 5.23 (a) Individual moment-rotation curves of the piles in row C and (b) equivalent rotational spring moment-rotation curve for the corresponding row of piles.

5.3.4 Equivalent Mass

The movement of the wharf deck in the horizontal plane can be decomposed into three components: transverse movement, longitudinal movement, and rotation in the plane of the deck. As a consequence, the equivalent mass of the wharf in one row can be calculated for each of the directions and lumped to the deck at the corresponding direction and location. Denoting the tributary mass and inertia of the wharf assigned to each pile location (Figure 5.21) by m_j and I_j, the lumped mass in two lateral and the rotational directions can be derived using

$$M_{transverse} = M_{longitudinal} = \sum_{j=1}^{n} m_j \tag{5.7}$$

$$I = \sum_{j=1}^{n} \left[I_j + m_j \left(d_j - L/2 \right)^2 \right] \tag{5.8}$$

5.3.5 Equivalent Damping

Damping in the FE model of a wharf segment is from three distinct sources: the mass and stiffness proportional (Rayleigh) damping, the nonlinear force-deformation of the elements, including piles and soil springs, and the radial damping in the soil springs. Taking the first source of damping into account in the simplified model of the wharf is rather a simple task. However including the second source is quite difficult, since the dynamic hysteretic behavior of pile structural elements and soil springs may not follow the same pattern as the simplified nonlinear springs do. More importantly, the radial damping effect in the formulation of soil springs is ignored in the process of lumping torsional resistance of the wharf into zero-length rotational springs. Therefore, a number of time-history analyses are conducted for the original wharf model with 5% Rayleigh damping and for the simplified structure with a range of Rayleigh damping from 5% to 10% to see what damping ratio better describes the amount of damping in the system. Based on the results, 7% damping was found to be a good estimate.

5.3.6 Validation of the Simplified Model

The model of the simplified wharf is validated against the full wharf model using a number of analyses including modal analysis and nonlinear time-history analysis. These results are discussed in the following sections.

5.3.6.1 Modal Analysis

Dynamic characteristics of the simplified model in the initial rest conditions are found using a modal analysis. The first five mode shapes of the simplified model are shown in Figure 5.24a-e. It is observed that the first, second, third, and forth mode shapes of the simplified wharf model coincide with the corresponding mode shapes of the full wharf model. The natural periods of these modes for the simplified model are 0.50s, 0.27s, 0.16s, and 0.158s respectively, which are in good agreement with the corresponding natural periods of 0.504s, 0.273s, 0.166s, and 0.156s from the full model of the wharf. Since the simplified model does not consider the landside crane rail and the supporting piles, the fifth mode of the simplified model corresponds to the eleventh mode of the full wharf model. This is due to the fact that modes of the full wharf between the fourth and eleventh modes are the modes that correspond to dynamic characteristics of the landside crane rail and the supporting piles which are not included in the model of the simplified wharf. The natural period of the fifth mode of the simplified model is 0.02 sec while the corresponding natural period of the full wharf model is 0.05 sec.

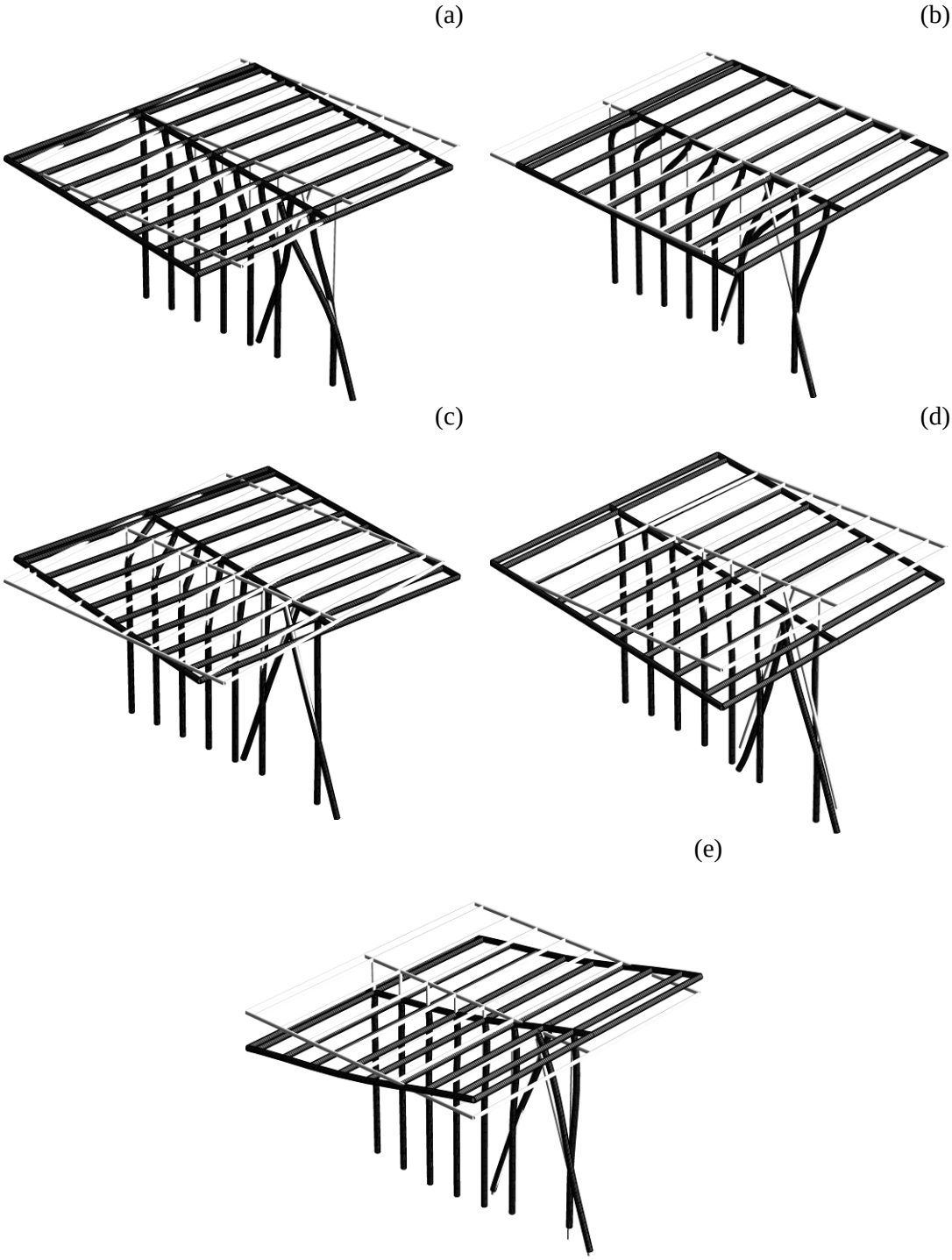

Figure 5.24 Mode shapes of the three-dimensional simplified wharf model for a) first, b) second, c) third, d) forth, and e) fifth mode.

5.3.6.2 Nonlinear Time-History Analysis

The simplified model of the wharf is also validated against the full wharf model using nonlinear time-history analysis of the two wharf models to embankment soil deformations in the three orthogonal directions. For validation purposes, ground deformation time-histories of NGA0810 and NGA0451 are chosen which represent moderate and large earthquake scenarios, respectively. The results of the analyses are presented in Figure 5.25 for the node at the seaside edge of the wharf deck on the center line of the wharf models called Node C (Figure 5.10) during NGA0451 and NGA0810. Figure 5.25a-c compares the displacement response of Node C of the two wharf models in the transverse, vertical and longitudinal directions. As expected the transverse and vertical displacement responses of the simplified model closely follow the corresponding responses of the full wharf model. The longitudinal displacement response of the simplified wharf model is also in good agreement with the corresponding response of the full wharf model. The same quantities are presented in Figure 5.25d-f for NGA0810 in which the same level of agreement is observed between three orthogonal displacement responses of the simplified and full wharf models at the location of Node C.

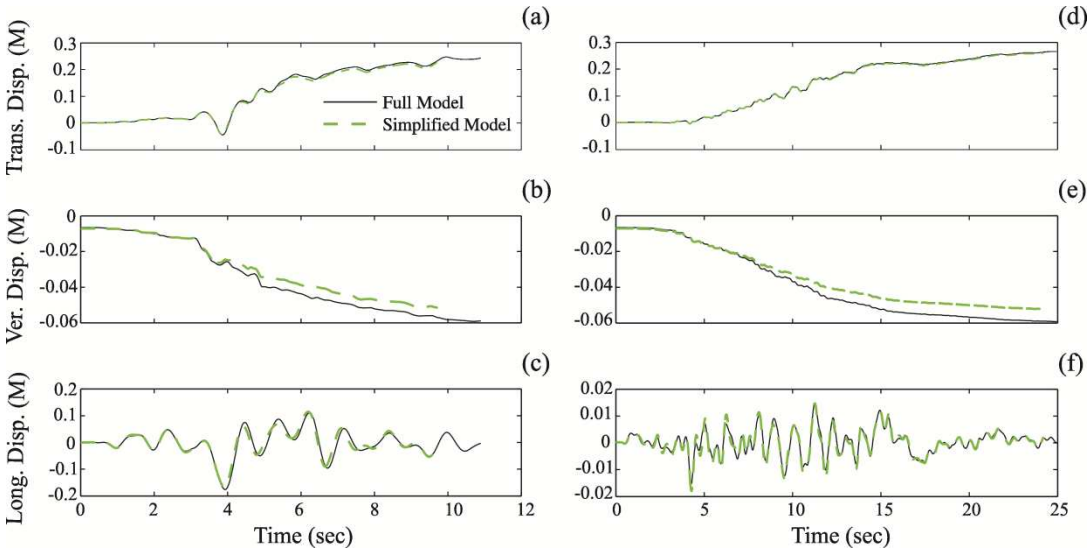

Figure 5.25 Displacement response of the full and simplified wharf models at Node C in a) transverse, b) vertical, and c) longitudinal directions during NGA0451 and the displacement response of the full and simplified wharf models at Node C in d) transverse, e) vertical, and f) longitudinal directions during NGA0810.

Displacement responses of the simplified and full wharf models at the node located on the center line of the wharf at the landside edge of the deck called Node D (Figure 5.10) for NGA0451 and NGA0810 are shown in Figures 5.26 in which good agreements are observed between the responses of the full and simplified wharf models.

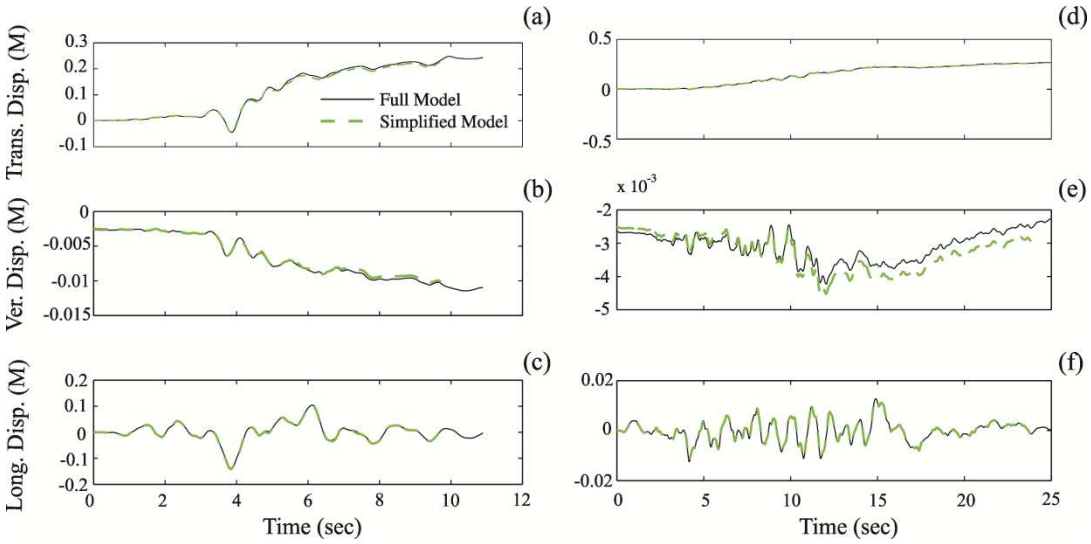

Figure 5.26 Displacement response of the full and simplified wharf models at Node D in a) transverse, b) vertical, and c) longitudinal directions during NGA0451 and the displacement response of the full and simplified wharf models at Node D in d) transverse, e) vertical, and f) longitudinal directions during NGA0810.

The good agreement observed between the results of the modal analysis as well as time-history simulations of the two wharf models helps to serve as validation of the model of the simplified wharf model.

5.4 Boundary Conditions of Wharf Segments

In order for loading and/or unloading of multiple container ships simultaneously, seaports usually consist of a number of wharf segments that are aligned along the shoreline – in this study longitudinal direction. A wharf segment interacts with the neighboring segments in the longitudinal and transverse directions. In the longitudinal direction, the torsional as well as out-of-phase longitudinal response of adjacent wharf segments may result in pounding of the segments at the deck level. On the other hand to enable the cranes on top of wharves to move in the longitudinal direction from one segment to another segment, the relative movement of the segments in the transverse direction is constrained by adding shear keys

between adjacent wharf segments. These boundary effects influence the dynamic characteristics and response of wharf segments. To account for the effect of neighboring wharves, it is necessary to model the boundary conditions at the ends of wharf segments. This is illustrated in Figure 5.27 where three adjacent segments are shown.

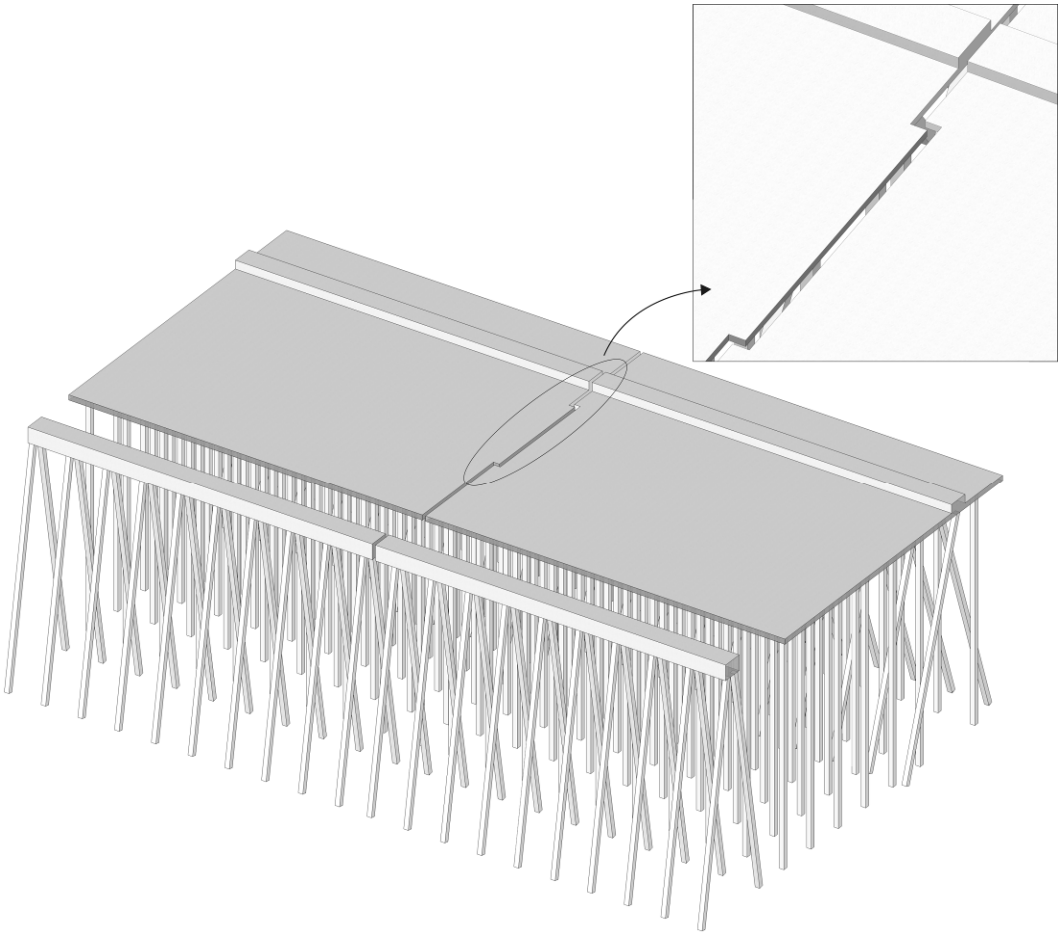

Figure 5.27 Schematic view of two wharf segments and the boundary conditions between the segments.

5.4.1 Pounding Elements

The pounding interaction between adjacent wharf segments is modeled by adding pounding elements to the FE model of the wharves. These elements connect the two adjacent vertical faces of neighboring wharf decks. When the gap distance between

the segments is zero, pounding of adjacent wharf segments occurs during which equal magnitude opposite direction axial compression forces are applied to the segments at the point of contact at which damage to wharf deck occurs. In the rest of the time when the gap distance is larger than zero, segments are uncoupled in the longitudinal direction. The phenomenological model of the pounding element needs to account for a) force-deformation behavior of the deck in the longitudinal direction, b) the effect of the local damage at the point of contact on the response of adjacent segments, and c) the gap between the segments. Figure 5.28 presents the constitutive components of the pounding element which address the above three criteria.

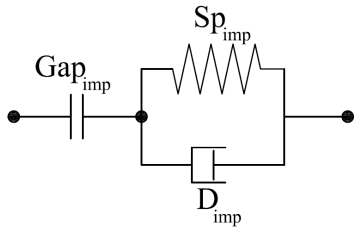

Figure 5.28 Model of the impact element

As seen in Figure 5.28, the impact element consists of a spring Sp_{imp} and a damper D_{imp} in parallel, together act in series with a gap element Gap_{imp}. The stiffness of the impact element K is the axial stiffness of the deck in the specified row and the damping of the impact element is found from

$$c = 2\xi\sqrt{\frac{KM}{2}} \tag{5.9}$$

where M is the tributary mass of the specified row and ξ is the damping ratio calculated using (Jankowski et al. 1998)

$$\xi = \frac{-\ln(e)}{\sqrt{\pi^2 + (\ln(e))^2}} \tag{5.10}$$

in which *e* is the coefficient of restitution defining the energy dissipation during impact of the adjacent segments. For concrete structures, Jankowski et al. (1998) suggest the value of 0.65 for *e*.

5.4.2. Shear Key

Shear keys, as previously mentioned, are used to constrain the relative transverse movement of wharf decks to enable the cranes to move from one wharf segment to another. The schematic configuration of the sear key in Figure 5.27 is shown in Figure 5.29. The length of the shear key L_{sk} is at least three times its height, H_{sk}, that is subjected to a horizontal demand force from seismic excitations F_{EQ}.

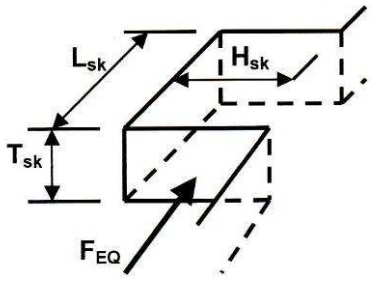

Figure 5.29 Schematic configuration of a shear key

Under the applied seismic demand force $F_{EQ,}$ the shear key may fail through four different mechanisms: shear friction, flexure, shear, or bearing failure. With reference to Figure 5.29, these limit state forces are computed as specified below.

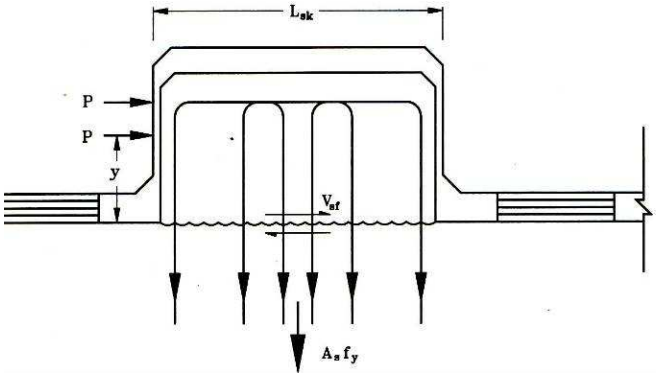

Figure 5.30 Applied and resisting force mechanism in a typical shear key (Priestley et al., 1996)

5.4.2.1 Shear Friction

As shown in Figure 5.30, the shear key may fail from the base when the applied force P is larger than the capacity V_{sf} found from (Priestly et al., 1996)

$$V_{sf} = \mu A_s f_y \tag{5.11}$$

where f_y and A_s are the yield strength and the area of the steel crossing the critical interface, and μ is the coefficient of friction along the shear crack, which is assumed to be 1.4 as it is suggested by Priestly et al. (1996).

Caltrans bridge design specifications state that the above nominal capacity should not exceed

$$V_n < 800 A_c \, (psi) \tag{5.12}$$

and

$$V_n < 0.2 A_c f_c' \tag{5.13}$$

5.4.2.2 Flexure

Considering the shear key to behave as a squat cantilever beam, the force leading to the onset of failure in this mode, P_{flex}, is computed as (Priestly et al., 1996):

$$P_{flex} = \frac{0.9}{y}(A_s f_y \frac{L_{sk}}{2}) \tag{5.14}$$

where L_{sk} is defined in Figure 5.29. It appears that Equation 5.14 was developed by taking moments about a corner of the base of the shear key. The quantity *y* in this equation corresponds to the location of the resultant lateral force from the deck along the height of the shear key. Estimation of this quantity is uncertain, and depends on the end rotation of the decks at the expansion joint. A conservative estimate of P_{flex} would result if *y* is assumed to be equal to the height of the shear key H_{sk}.

5.4.2.3 Shear

Treating the shear key as a squat cantilever beam, the beam's shear capacity can also be estimated. A first order estimate of this shear capacity, P_{shr} is provided by the following expression (ACI 318-151):

$$P_{shr} = 2\sqrt{f_c'}b_w d \tag{5.15}$$

where f_c' is the compressive strength of the concrete, b_w is the width of the beam (T_{sk} in Figure 5.29), and d is the distance from the extreme compression fiber to the centroid of the longitudinal tension reinforcement.

5.4.2.4 Bearing Strength

According to Section 10.17.1 of ACI 318-145 (ACI, 2006), the ultimate bearing force along the side of the shear key where it comes in contact with the adjacent deck segment, P_b, is:

$$P_b = 0.85 f'_c A_1 \tag{5.16}$$

where f'_c is the ultimate compressive strength of the concrete, and A_1 (bearing area) = H_{sk} T_{sk} as defined in Figure 5.29.

A nonlinear spring is used at the location of the shear key to model the constraint on the relative transverse movement of the wharf segments. The nonlinear model of the spring is shown in Figure 5.31. In this figure, P_{cap} denotes the capacity of the shear key found as the minimum of the capacities calculated from Equations 5.11 to 5.16. Megally et al. (2002) conducted a series of experiments on shear keys and found that Δ_{Max}- Δ_{gap} (Figure 5.33) equal to 9 cm is a deformation at which the capacity of the shear keys degrades to essentially zero irrespective of the investigated parameters of the shear keys. This value is used in this study to construct the nonlinear model of the shear key.

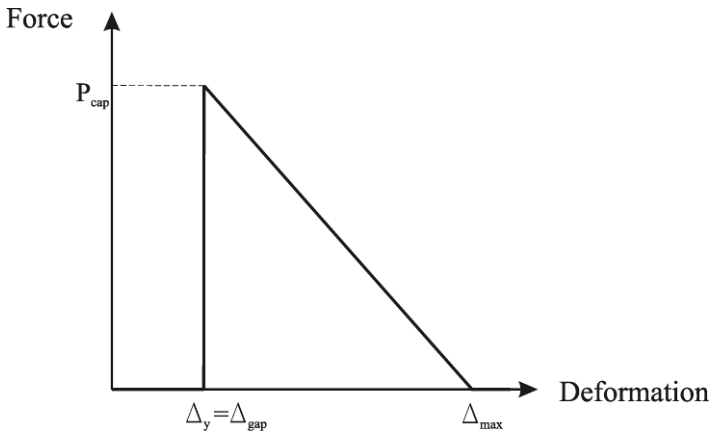

Figure 5.31 Nonlinear model of the shear key.

5.5 Response Evaluation of the Full Wharf Model Using Simplified Model of the Wharf

In section 5.3, the simplified model of the wharf consisting of a representative one strip model is presented and validated against the full wharf model using modal analysis as well as nonlinear time-history analyses. It was observed that the simplified model can accurately capture the response of the wharf at the seaside and landside edge of the deck on the centerline of the wharf. Since the wharf deck is rigid, the agreement between the responses of the simplified and full wharf models at two points on the deck implies that the simplified model of the wharf can accurately capture the deck response of the full wharf model. However, due to the specific geometry of the simplified model in which the properties of the full wharf, composed of several strips, are lumped into the single representative strip model, the simplified model cannot predict or estimate the response of substructure components of the full wharf model including pile-deck connections, pile sections, and soil springs. These responses are required for probabilistic seismic demand analysis of critical wharf components and evaluation of down time and cost in the aftermath of seismic events. This section proposes a procedure to evaluate

maximum response of the full wharf model at the component level using the simplified model of the wharf.

The response of the wharf in general can be decomposed into two components of distinct natures: inertial response and kinematic response. The inertial response of the wharf is the result of the vibrations of the superstructure (i.e. deck) where the mass of the wharf is concentrated due to the transfer of soil vibrations through piles and pile-deck connections. On the other hand, the kinematic response of the wharf is the consequence of the interaction of the piles with surrounding deforming soils. The simplified model of the wharf can capture both these responses but for the lumped strip model. However using nonlinear time-history analysis of the simplified wharf model, the time when maximum response in substructure wharf components including pile sections and pile-deck connections occurs can be captured. The time of the maximum component's response in the simplified wharf model is expected to be close to the corresponding time in the full wharf model. In the next step, embankment soil deformations at the specified time of maximum response are imposed to the soil springs and the deformation of the deck of the simplified model at the time of the maximum response are applied to the deck of the full wharf model. The state of the wharf at the time of maximum component response can be found by performing a nonlinear static analysis of the wharf for the imposed deformations. In this way, both the kinematic response of the wharf due to the surrounding soil and the inertial response of the wharf from the deck response are captured. Figure 5.32 illustrates the simplified response evaluation of the wharf

described above. This procedure is tested for earthquakes NGA0451 and NGA0810 and the results are presented below.

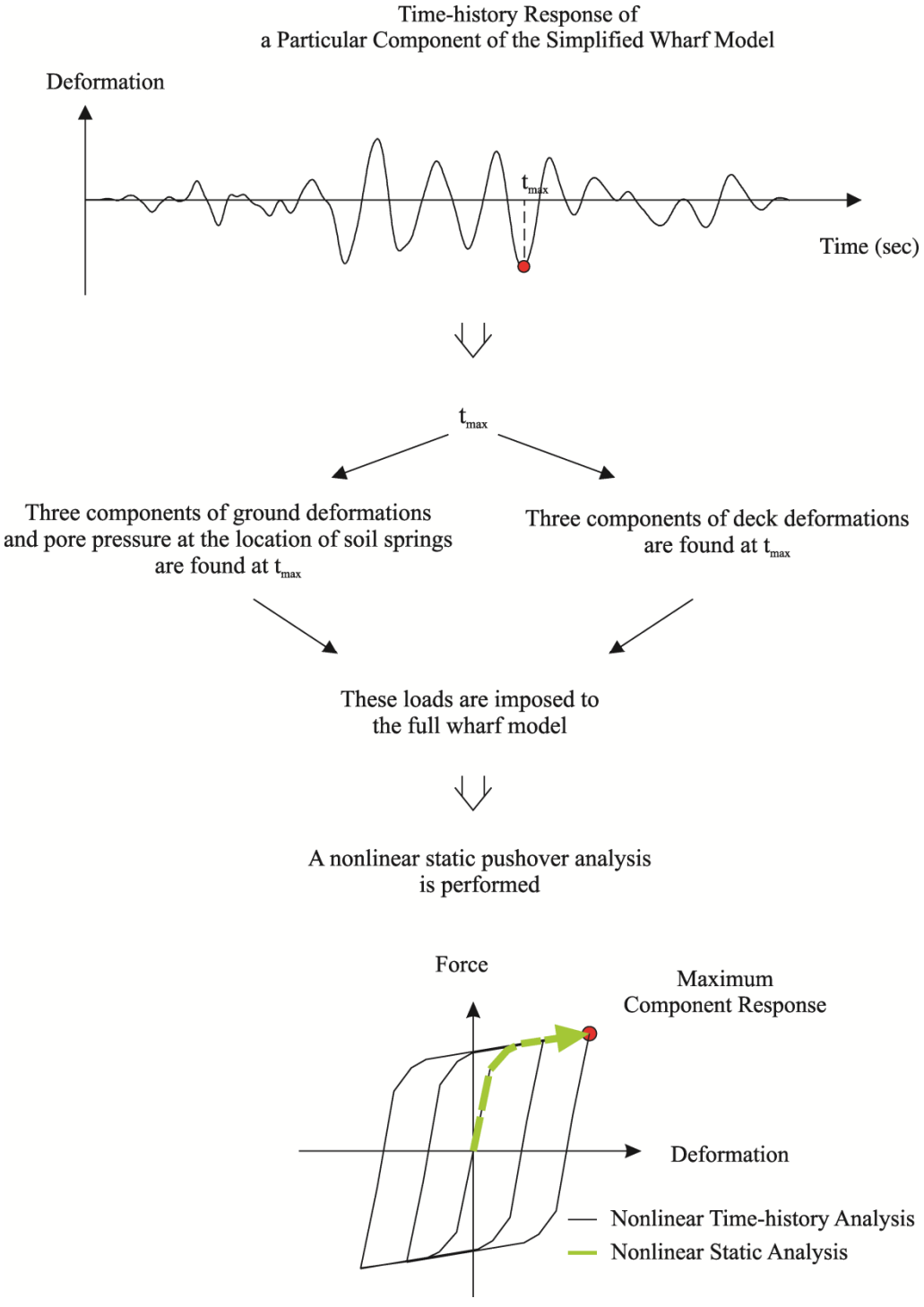

Figure 5.32 Simplified response evaluation procedure.

The first assumption in the proposed procedure is that the time of maximum components response in the simplified wharf model is equal to the corresponding time in the full wharf model. The time-history of the curvature response of pile sections with the largest maximum curvature in full and simplified wharf models are shown in Figure 5.33 and 5.34 for NGA0451 and NGA0810, respectively. It is found that the maximum curvature response of all piles sections in the simplified model occurs at 6.91 sec during NGA0451 and at 11.62 sec during NGA0810. From the simulation results of the full wharf model, the times when the maximum response of the pile sections occur are found to be 6.78 sec and 11.63 sec during NGA0451 and NGA0810, respectively. Looking at the time of the maximum response, it is observed that for the medium level earthquake, NGA0810, the simplified model well predicts the time of maximum response while the level of estimation is not as good for the large earthquake event, NGA0451. However from Figure 5.33a, the difference between the curvature response of the section at 6.78 and 6.91 is small due to the large vibration period of response of the pile section compared to the small vibration period of the corresponding response during NGA0810 (Figure 5.33b). The other noticeable phenomenon is that the time when the significant increase in pile section curvature occurs is different in the full and simplified wharf models during NGA0451. This is attributed to larger capacities of piles of the simplified model compared to piles capacities of the full wharf model which delays the occurrence of large curvature response of piles sections until the time when induced section moments as the result of the applied soil pressure are larger than the moment capacity of the piles sections in the simplified model.

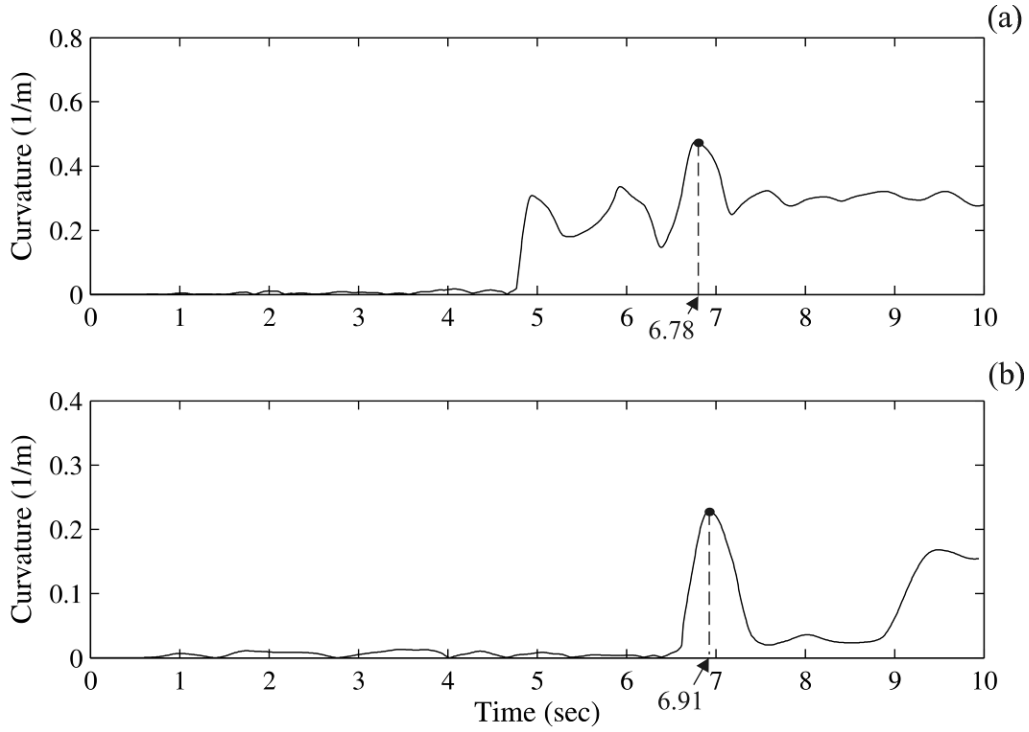

Figure 5.33 Curvature response of the pile section with the largest maximum curvature in a) full wharf mode and b) simplified model of the wharf during NGA0451.

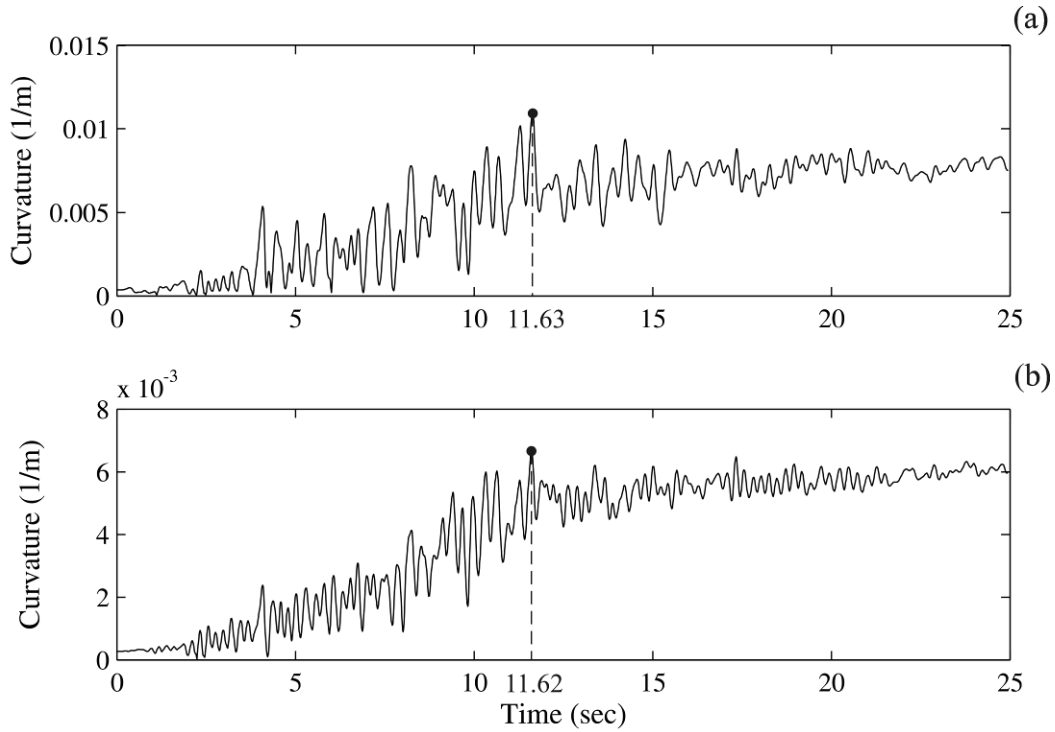

Figure 5.34 Curvature response of the pile section with the largest maximum curvature in a) full wharf mode and b) simplified model of the wharf during NGA0810.

Applying soil deformations at the point of maximum curvature response to soil springs and imposing wharf deck displacement at the corresponding time from the simplified model to the full model of the wharf and performing a nonlinear static analysis, the maximum curvatures during NGA0451 and NGA0810 are found to be 0.4254 (1/m) and 0.0103 (1/m) respectively. Comparing to the maximum curvatures of 0.4581 (1/m) and 0.0109 (1/m) from the nonlinear time-history analysis of the full wharf model, the simplified procedure yields a reasonable estimate of the maximum component response of the full wharf model.

For probabilistic seismic demand modeling of critical wharf components in the next chapter, three wharf segments are aligned in the longitudinal direction which represents a more realistic setting of wharf segments in seaports. The simplified procedure outlined above is followed with the exception that in the stage of nonlinear time-history analysis of the simplified wharf model, three simplified wharf segments that are connected through the boundary conditions explained in section 5.4 are analyzed and the time of the largest maximum components response of the middle segment is used as t_{max} in Figure 5.32.

5.6 Closure

Three-dimensional numerical modeling of the typical pile supported wharf was presented in this chapter. Performing a modal analysis, the natural periods and associated mode shapes of the wharf system were found. The main conclusions of the modal analysis are:

1. The first and third modes of the wharf are torsional in the plane of the deck, while the second mode is transverse coinciding the first mode of the two-dimensional model. This shows the contribution of the three-dimensional effects in the overall inertial response of the wharf.

2. The two-dimensional model of the wharf can capture all of the modes corresponding to the transverse motion of the wharf which consequently implies that the transverse response of the wharf is uncoupled from the longitudinal and torsional response.

A procedure to generate longitudinal ground deformation histories at the location of soil springs from the time-histories of the ground deformation in the transverse direction and the earthquake records in the two orthogonal horizontal directions were presented in this chapter. Performing nonlinear time-history analyses for three-dimensional ground deformations, it was found that:

1. The transverse response of the three-dimensional wharf model in different response measures including wharf displacement and force-deformation response of pile-deck connections closely follows the corresponding transverse responses of the two-dimensional model of the wharf.

2. Longitudinal ground deformations impose large longitudinal curvature demands on the near surface sections of the landside piles.

3. Due to the symmetry of the embankment soil as well as the wharf model in the longitudinal direction, residual deformations of the embankment soil and the wharf in the longitudinal direction are almost zero.

In order to reduce the amount of computational time for nonlinear dynamic analysis of the wharf to embankment soil deformations, a simplified model of the three-dimensional wharf model was developed. The simplified model was then validated against the full model of the three-dimensional wharf using both modal and nonlinear time-history analyses. Furthermore, a simplified analysis technique is proposed which can capture the maximum response of the wharf from nonlinear dynamic analysis using nonlinear static pushover techniques. Comparing the results of the simplified analysis method with the full nonlinear dynamic response of the wharf, it was found that the proposed method can estimate the maximum response of the wharf well.

CHAPTER 6

PROBABILISTIC SEISMIC DEMAND MODELING AND FRAGILITY ANALYSIS OF THE PILE SUPPORTED CONTAINER WHARF

6.1 Introduction

The essential role of seaports mainly as a member of supply chains in regional, national, and international scales stems from their unique functionality as intermodal transfer points in transportation networks. The activities of ports including loading and unloading of cargo and raw materials, temporary storage, and intra-port operations are concentrated in a small geographic area and therefore, any disruption in the normal performance of structural and geotechnical components of ports may lead to partial or even full disruption of the commercial activities of the port. Historical cases of earthquakes in seaports have shown that these infrastructures are very vulnerable to seismic damage and that any disruption in the activities of port infrastructures may lead to significant direct, indirect, and induced losses. Particularly poignant examples are the 1995 Kobe earthquake and the 2010 Haiti earthquake in which liquefaction and lateral spreading of embankments imposed severe damage to both structural and non-structural components of ports (Werner and Dickenson 1996, Eberhard et al. 2010). The significant economic loss on one hand and the inability of ports in transferring aid to affected zones as a consequence of port damage in the historic seismic events raised public as well as professional awareness of the port sector and its strategic role in the transport chain. This served as motivation for investigating the seismic response of wharves using numerical simulations (Roth et al. 2003; Dodds et al. 2004; Na et al. 2009; Donahue

et al. 2004) as well as centrifuge tests (Takahashi et al. 1998; Iai and Sugano 1999; McCullough et al. 2001).

Despite the importance of ports and their vulnerability to seismic damage, a limited number of researchers have studied the fragility of wharves to seismic events (Na et al. 2009, Chiou et al. 2011). Fragility analysis of geo-structural components of seaports in the framework of risk analysis provides the probability of occurrence of various prescribed damage states as a function of the firm-site ground motion by incorporating the available information on structure details and soil conditions. This chapter focuses on developing fragility curves for the pile supported wharf model studied in previous chapters. This is accomplished by developing probabilistic seismic demand models (PSDMs) of the wharf components using two and three-dimensional detailed models of the wharf structure. Based on expert opinion, numerical simulations, and experimental results, a set of limit states are considered for a number of components of the wharf structure for which their damage induces a disruption in the normal operation of ports. Using the nonlinear model and the limit states, a set of fragility curves are developed for critical wharf components for a suit of ground deformations of the soil embankment and pore water pressure generated for this study through free-field analysis. Each fragility curve is accompanied with a confidence interval derived to characterize the effect of epistemic uncertainties based on the assumption of the demand being lognormally distributed at a given intensity measure (IM).

6.2 Fragility Analysis Framework

A key component in predicting the damage of a structural system when subjected to an earthquake with expected characteristics is the fragility of the system. A fragility curve describes the probability that the structure (or a component of the structure) fails to satisfy a prescribed performance criterion conditioned on a seismic intensity measure (IM) representative of the seismic loading. Following the common notation in structural reliability, the event of a structure failing to meet a performance requirement (damage state) is defined by the case where demand (D) exceeds capacity (C); i.e. C<D. Assuming that both capacity and demand can be described by lognormal distributions, the probability of the structure exceeding a particular damage state for a given IM in closed form is (Wen et al. 2004)

$$P(C < D \mid IM) = 1 - \Phi\left(\frac{\lambda_C - \lambda_{D|IM}}{\sqrt{\beta_{D|IM}^2 + \beta_M^2 + \beta_C^2}}\right) \tag{6.1}$$

in which $\Phi(.)$ is the cumulative distribution function of the standard normal distribution; λ_C and $\lambda_{D|IM}$ are the natural logarithm of the median response capacity and the corresponding median demand for a given IM; β_C and $\beta_{D|IM}$ are the uncertainty associated with capacity and demand representative models; and β_M is the uncertainty in modeling the system.

According to Equation (6.1), evaluation of the seismic fragilities of structures requires developing PSDMs for structural components for which this study uses nonlinear time-history analysis of the wharf-foundation system as well as capacity models for the critical wharf components.

6.3 Ground Motion Selection

Generating PSDMs for critical response measures of the wharf requires selection of representative ground motions as the inputs for nonlinear time-history analysis. However the term “representative” is quite challenging to characterize. In general, the selection procedure should reflect the soil conditions at the site and include anticipated earthquake scenarios in terms of relevant earthquake characterizing parameters. Among various selection procedures of ground motions, the bin approach proposed by Shome and Cornell (1999) is commonly used and is the method adopted in this study. The bin approach defines a set of mutually exclusive and collectively exhaustive domains of anticipated earthquakes in terms of moment magnitude (Mw) and distance of the rupture zone from the site of interest (R). One of the main advantages of the bin approach for ground motion selection is that it provides a measure of representativeness for the ground motions of a bin by comparing the representative intensity measure of the selected ground motions in a bin with the corresponding measure from standard attenuation relationships.

Following Shome and Cornell (1999), the two-dimensional domain of Mw and R is subdivided into four zones representing different scenarios of possible earthquakes.

Bin I: small Mw and small R (SMSR), $M_w \in [5.5,6.5], R \in [15,35)$

Bin II: small Mw and large R (SMLR), $M_w \in [5.5,6.5], R \in [35,60)$

Bin III: large Mw and small R (LMSR), $M_w \in [6.5,8], R \in [15,35)$

Bin IV: large Mw and large R (LMLR), $M_w \in [6.5,8], R \in [35,60)$

Each bin consists of approximately 12 ground motions selected randomly from the database used to develop the Next Generation Attenuation of Ground Motions (NGA) project (Chiou et al. 2008). All of the selected ground motions are earthquakes within the United States, except for the 1995 Kobe, Japan and 1999 Chi-Chi, Taiwan earthquakes. Furthermore, seven simulated ground motions are added to the bin to represent large magnitude California earthquakes which are not present in the NGA database. In addition to non-near field bins, a fifth bin is added to include the effect of near field motions such as directivity, fling, and pulse response. The fifth bin includes 15 randomly selected ground motions from the NGA database with the distance to rupture less than 15 km. The resulting group of 63 empirical and simulated ground motions covers a broad range of earthquake scenarios in terms of minimum moment magnitude and the closest distance to rupture.

In order to check the representativeness of the ground motions in each bin for the scenario earthquake they are corresponding to, the median spectral acceleration of the ground motions in each bin are compared to the corresponding measure from the attenuation law proposed by Abrahamson and Silva (1999) for the central values of the definitive range of Mw and R of the bin. Figure 6.1a,b shows the median spectral acceleration of the horizontal component of the ground motions from the bin and the attenuation law respectively. Similarly, Figure 6.2a,b shows the same quantities for the vertical component of the ground motions from the bin and the attenuation law. The similarity of spectral acceleration of the bins of ground motions to the corresponding spectral accelerations found from the attenuation law

by Abrahamson and Silva (1999) for both horizontal and vertical components suggests that the sampled earthquakes in each bin from the NGA database are representative of their corresponding Mw-R scenario.

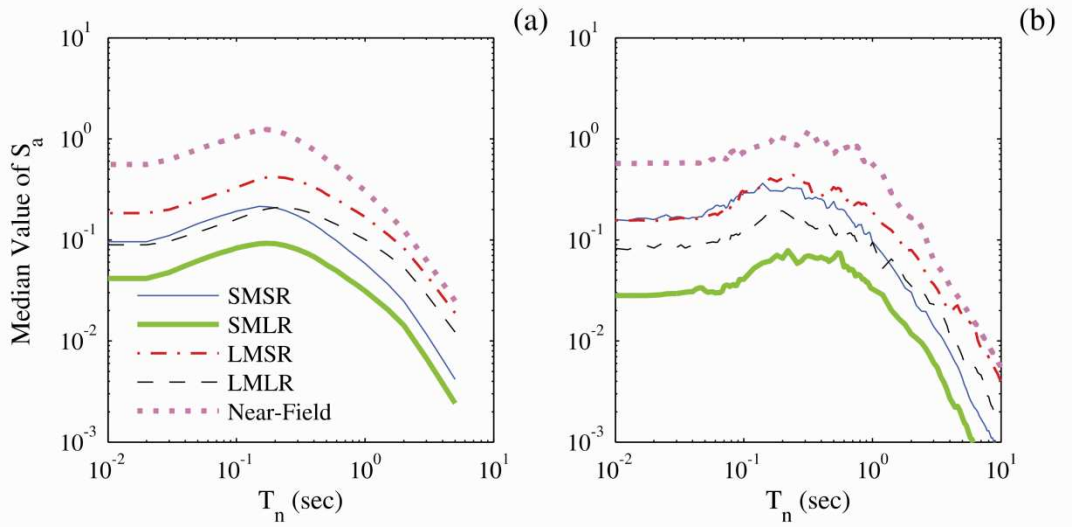

Figure 6.1 Median spectral acceleration response of the bins in the horizontal direction from a) earthquake records and b) attenuation law.

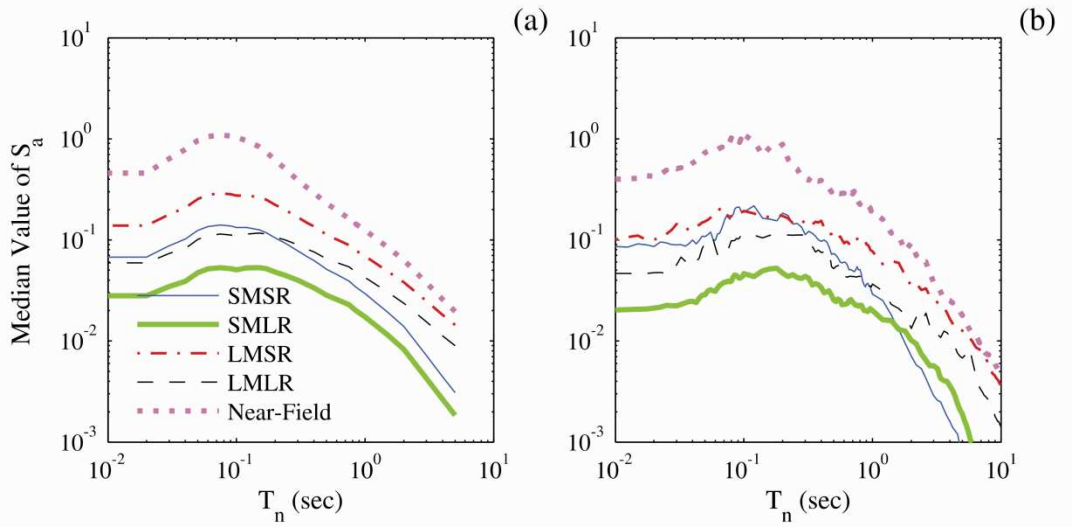

Figure 6.2 Median spectral acceleration response of the bins in the vertical direction from a) earthquake records and b) attenuation law.

The selected ground motions are used as input for numerical models of the soil embankments supporting the wharf-foundation system. The nonlinear coupled ground deformation and transient pore pressure response of the wharf embankment

to input ground shakings are numerically evaluated by Vytiniotis et al. (2011). As mentioned in chapter III, the analysis uses the advanced elasto-plastic effective stress soil model proposed by Dafalias and Manzari (2004). This model is able to realistically capture the stress-strain behavior of sand during cyclic mobility events. Soil deformations and excess pore water pressure ratios in sand layers in the horizontal direction are applied to the far-field end of the macroelement, while for other soil springs only soil deformations are input to the model. The dynamic response of the foundation-wharf-crane system is found for time-histories of ground deformation and pore pressures within the surrounding soil medium.

6.4 Probabilistic Seismic Demand Models

One of the constitutive components of the conditional probability of failure in Equation (6.1) is the demand model for which a probabilistic analysis is required to determine the parameters $\lambda_{D|IM}$ and $\beta_{D|IM}$. Based on Cornell et al. (2002), a candidate seismic demand model for the response measures of interest of individual components of the system is a power function of the following form.

$$D(IM) = a.IM^{b}.\varepsilon \tag{6.2}$$

where ε is a unit-median lognormal random variable with logarithmic standard deviation of $\beta_{D|IM}$ describing the uncertainty in the relationship; and a and b are constants estimated using regression analysis for the seismic demand model in the transformed logarithmic space in the following form.

$$\ln(D(IM)) = \ln(a) + b\ln(IM) + \ln(\varepsilon) \tag{6.3}$$

The estimates of a and b from the transformed demand model in Equation (6.3), denoted by $\hat{a}$ and $\hat{b}$, are unbiased estimators due to the assumption that ln(ε) is normally distributed. The other assumption in the demand model of Equation (6.3) is the homoskedasticity property (Gardoni et al. 2002) which implies that the model variance $\beta_{D|IM}^2$ is independent of IM or equivalently, the coefficient of variation of the error term in Equation (6.2) is uniform. From Equation (6.3), the natural logarithm of median demand for a given IM, $\lambda_{D|IM}$, is found as

$$\lambda_{D|IM} = \ln(\hat{a}) + \hat{b}\ln(IM) \tag{6.4}$$

The assumption of demand following a lognormal distribution with respect to the IM is applied to all demand measures associated with critical wharf components including the curvature of piles and pile-deck connections and the relative displacement of the structurally separated landside crane rail with respect to the wharf. Assuming that the dispersion of seismic demand parameters is independent from the IM in the logarithmic scale, the uncertainty in the seismic demand $\beta_{D|IM}$ in Equation (6.1) is determined as the logarithmic standard deviation of errors in fitting the demand models as follows.

$$\beta_{D|IM} = \left[\sum_{i=1}^{n}\left(\ln(D_i) - \lambda_{D|IM}\right)^2 \Big/ (n-2)\right]^{1/2} \tag{6.5}$$

in which n is the total number of samples.

There are particular cases where the demand in the transformed logarithmic space follows a bilinear trend with respect to the chosen IM. For such cases, the demand model in Equation (6.3) will be in the form of

$$\ln(D(IM)) = \begin{cases} \ln(a_1) + b_1 \ln(IM) + \ln(\varepsilon_1) & , IM \le IM_0 \\ \ln(a_1) + b_1 \ln(IM_0) + b_2 (\ln(IM) - \ln(IM_0)) + \ln(\varepsilon_2) & , IM > IM_0 \end{cases} \quad (6.6)$$

where ε_1 and ε_2 are unit-median lognormal random variables with logarithmic standard deviation of $\beta_{D|IM1}$ and $\beta_{D|IM2}$ respectively. The parameters a_1, b_1, b_2, and IM_0 are illustrated in Figure 6.3.

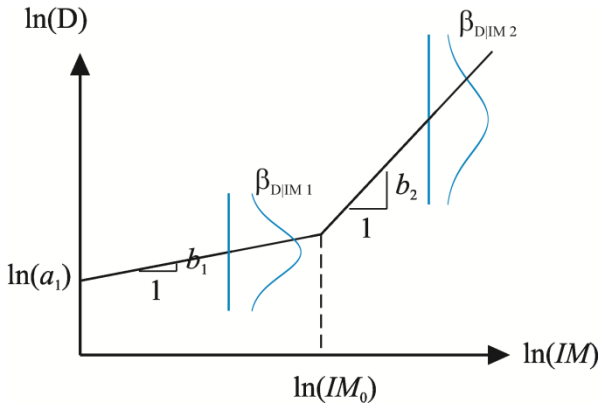

Figure 6.3 Bilinear model for PSDA.

The natural logarithm of median demand for a given IM is then found to be

$$\lambda_{D|IM} = \begin{cases} \ln(\hat{a}_1) + \hat{b}_1 \ln(IM) & , IM \le \hat{IM}_0 \\ \ln(\hat{a}_1) + \hat{b}_1 \ln\left(\hat{IM}_0\right) + \hat{b}_2 \left(\ln(IM) - \ln\left(\hat{IM}_0\right)\right) & , IM > \hat{IM}_0 \end{cases} \quad (6.7)$$

Finding the parameters of the demand estimator model in Equation (6.7) requires performing a nonlinear regression analysis for which MATLAB ToolBox commands are used.

This study does not consider the contribution of the uncertainty in material properties as it is found to be negligible compared to the effect of seismic demand on the overall response variability (Kwon and Elnashai 2006, Ellingwood et al. 2007). Therefore all material properties of the system are set equal to their corresponding mean values. Subjecting the wharf-foundation to time-histories of ground deformation and pore water pressures of the embankment soil, the dynamic response of the wharf is found using nonlinear time-history analysis and the maximum response in critical response measures are recorded.

PSDMs are developed by considering the demand on various wharf components including pile sections, pile-deck connections, the relative movement of the wharf with respect to the landside pile, shear keys, and collector trenches. Table 6.1 details the demand parameters used to assess component demands for various wharf components considered in this study.

Table 6.1 Wharf component demand measures

Demand measure	Abbreviation	Units
Pile section curvature	φ_{pile}	1/m
Pile-deck connection curvature	φ_{con}	1/m
Relative movement of the wharf deck with respect to the landside crane rail	Δ_{rail}	m
Transverse deformation of shear key	Δ_{SK}	m
Relative transverse displacement of collector trench at expansion joints	Δ_{CT}	m

6.5 Optimal Intensity Measures

This section studies the performance of different IMs in estimating various wharf demand parameters based on a number of optimality criteria. The simulation results

of the two-dimensional wharf model are used and the linear regression model of Equation (6.3) is implemented for all demand parameters. Data points out of 95% bounds around the median demand are treated as outliers and are discarded for the regression analysis.

6.5.1 Criteria for Optimality of Intensity Measures

The characterization of the median demand using a power-law formulation and constant dispersion are assumptions that are sometimes made and are not necessarily the only possible models to express seismic demand as a function of an IM. However, these representations have been used widely and have been shown to perform very well. Based on the formulations presented in Equations (6.2) through (6.7), it is evident that the selection of an optimal IM can play a predominant role on the accuracy of the model in estimating seismic demand. Their optimal selection is instrumental to obtain reasonable estimates of the vulnerability of various components as the uncertainty associated with the demand is dependent on the variable chosen as an IM to some extent, although this is not the only source of the uncertainty.

The natural question that arises following this development is "What properties make an IM optimal?" Giovenale et al. (2004) pointed out that *sufficiency*, *efficiency*, and *hazard computability* are the essential properties of a good IM. In addition, *practicality* (Luco and Cornell, 2002) and *proficiency* (Padgett et al., 2008) are properties that need to be considered, the latter one being a composite measure of efficiency and practicality. The satisfaction of these fore mentioned

properties further validates the strength and accuracy of the power law assumption of the PSDM for a given IM, among other conclusions.

Padgett et al. (2008) provides a detailed discussion of each of these characteristics of optimal IMs, including how to quantify and interpret each property. Efficiency is commonly used to establish the superiority of an IM. An efficient IM reduces the amount of variation in the estimated demand for a given IM value and at the same time maintains it constant over the entire range of the chosen IM. A lower value of the logarithmic standard deviation of the seismic demand, commonly referred to as the dispersion, $\beta_{D|IM}$, indicates an efficient IM.

Another property to measure the validity of an IM is sufficiency. An IM needs to be sufficient in order to justify the usage of total probability theorem in probabilistic seismic demand analysis (PSDA). Sufficiency refers to the property where an IM is independent of ground motion characteristics such as magnitude (M) and epicentral distance (R). This is quantified by the *p*-value which is a measure of the probability that the randomly distributed points from the analysis would result in a regression line as flat as possible (tending towards zero slope) than that actually observed. Statistically, it is the probability of getting a value of the test statistic as extreme as or more extreme than that observed by chance alone, if the null hypothesis is true. This is achieved by a linear regression of the residuals from the PSDM with respect to M and R.

Practicality is a measure of the dependence of the demand upon the IM level and the slope, *b*, is a good indicator of this dependence. When the slope, *b*, approaches

zero, there is a negligible dependence of the demand upon the IM, thereby indicating an impractical IM. A higher value of *b* indicates that the IM is more practical.

Proficiency is a composite measure of efficiency and practicality. This property is derived by rearranging the terms in the formulation presented in Equation (6.1) after substitution by Equation (6.4). The term in the denominator in the formulation given in Equation (6.8) is defined as modified dispersion, ζ, and is a measure of proficiency. A lower value of ζ indicates a more proficient IM thereby indicating a lower uncertainty in the demand model by the choice of the IM.

$$P(C < D \mid IM) = \Phi\left(\frac{\ln(IM) - \frac{\ln(\lambda_C) - \ln(\hat{a})}{\hat{b}}}{\frac{\sqrt{\beta_{D|IM}^2 + \beta_M^2 + \beta_C^2}}{\hat{b}}}\right) \tag{6.8}$$

$$\zeta = \frac{\sqrt{\beta_{D|IM}^2 + \beta_M^2 + \beta_C^2}}{\hat{b}} \tag{6.9}$$

In addition to these properties, this study also considers the coefficient of determination, R^2, as an important characteristic. A higher value of R^2 (closer to unity) suggests the goodness of the linear fit in the lognormal space thereby strongly validating the fundamental power law assumption of the IM-demand measure (DM) pairs. A higher R^2 value also indicates reduced dispersion among the data set, thereby quantifying the efficiency and proficiency measures. These properties are used to quantify the validity of IMs presented in the subsequent section.

6.5.2 Considered Intensity Measures

This section presents the results of PSDA of the two-dimensional wharf model along with a comparison of the different IMs that are commonly used in structural and geotechnical engineering. Table 6.2 summarizes the intensity measures used in this study along with the respective abbreviations. PSDMs are derived for demand measures described in Table 6.1 and the properties presented in the previous section are investigated to evaluate the applicability of different IMs.

The simplest IMs are the peak quantities of ground response i.e. peak ground acceleration (PGA), peak ground velocity (PGV), and peak ground displacement (PGD). On the other hand, spectral acceleration quantities, S_a, are the most commonly used IMs in seismic design and selection of ground motion records for seismic response evaluation of structures. S_a describes the maximum response of a single-degree-of-freedom system to a particular input motion as a function of the natural period and damping ratio of the system. Spectrum values reflect ground motion characteristics including amplitude, frequency content, and damping. In this study, spectral accelerations are computed at periods of 0.2 sec, 1.0 sec, and T_n (natural period of the wharf) for a damping ratio of 5%.

The other IM that has been used for evaluation of liquefaction potential (Kayen and Mitchell, 1997) is Arias Intensity, expressed as

$$I_h = I_x + I_y = \frac{\pi}{2g}\int_0^{t_0} a_x^2(t)dt + \frac{\pi}{2g}\int_0^{t_0} a_y^2(t)dt \qquad (6.10)$$

where a_x and a_y are the orthogonal components of the ground acceleration in the horizontal plane and t_0 is the duration of the earthquake. Arias Intensity is "the sum of the two component energy per unit weight stored in a population of undamped linear oscillators evenly distributed in frequency, at the end of earthquake shaking" (Arias, 1970). Since Arias Intensity integrates a function of acceleration over time, it reflects the amplitude variation, frequency content, and duration of the earthquake motion.

The other integral based IM is cumulative absolute velocity (CAV) which is defined by

$$CAV = \int_0^{t_0} |a(t)| dt \tag{6.11}$$

where a(t) is the ground acceleration. It is observed that CAV accounts for intensity and duration, while Arias intensity accounts for frequency content of ground motions in addition to amplitude and duration. CAV is proposed by Electrical Power Research Institute (EPRI, 1988) in order to predict the onset of structural damage and since then it has been evolved for specific engineering applications. Recently, Kramer and Mitchell (2006) showed that a variant of CAV that excludes pulses of acceleration time-history with amplitudes less than 5 cm/sec^2 have close relationship to pore pressure generation and thus reduces record-to-record variability of excess pore pressure. This IM is called CAV_5 and is defined by

$$CAV = \int_0^{t_0} \langle \chi \rangle |a(t)| dt, \quad where \quad \langle \chi \rangle = \begin{cases} 1 & , |a(t)| \le 5 cm/\sec^2 \\ 0 & , |a(t)| > 5 cm/\sec^2 \end{cases} \tag{6.12}$$

Table 6.2 Intensity measures used in the study

Intensity Measure	Definition
PGA	Peak ground acceleration
PGV	Peak ground velocity
PGD	Peak ground displacement
$S_{a\text{-}02}$	Spectral acceleration at 0.2 sec
$S_{a\text{-}1}$	Spectral acceleration at 1.0 sec
$S_{a\text{-}Tn}$	Spectral acceleration at the natural period of the wharf, T_n
I_x	One component Arias Intensity
CAV	Cumulative absolute velocity
CAV_5	Modified cumulative absolute velocity

6.5.3 Efficiency, Proficiency and Practicality Comparisons

The dispersion, $\beta_{D|IM}$, is a measure of efficiency while the slope, b, of the PSDM is a measure of practicality. Proficiency is quantified by the modified dispersion value, ζ. Further the coefficient of determination, R^2 value is considered to test regression and thereby substantiate the power law assumption and further strength of efficiency and proficiency characteristics of the IM. An optimal IM would be characterized by smaller values of $\beta_{D|IM}$ and ζ and larger values of b and R^2. Figure 6.4 shows values of these measures for conventionally used IMs and different component demand parameters.

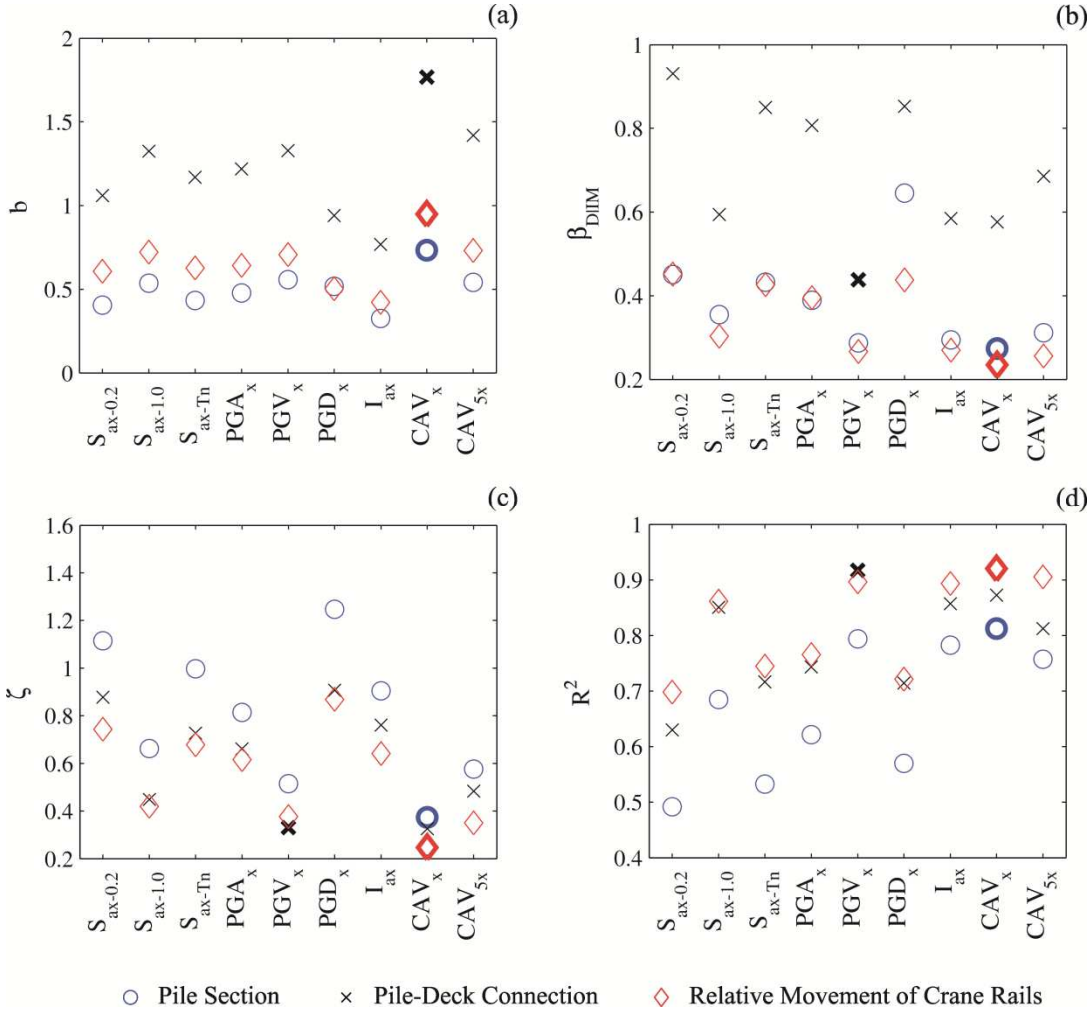

Figure 6.4 Appropriateness of different IMs in terms of a) practicality, b) efficiency, c) proficiency, and d) R^2.

It is observed that using CAV as the IM results in the largest slopes, *b*, in PSDMs for all three critical response measures of the wharf. It can also be noted that CAV is the ideal intensity measure for pile section deformation and relative movement of crane rails in terms of dispersion, $\beta_{D|IM}$, modified dispersion, ζ, and R^2. PGV and CAV_5 are the next most preferred IMs. The reason as to why velocity related IMs such as PGV and CAV perform well in predicting different demand parameters of the wharf is the fact that the soil embankment of the wharf may undergo liquefaction as a consequence of excess pore pressure built up during moderate to

large seismic events. This leads to excessive deformations of the embankment and consequently the kinematically constrained foundation-wharf system. Therefore an appropriate intensity measure to represent the severity of earthquake shaking should provide reasonable estimation of the occurrence of the liquefaction phenomenon. Numerous investigations have shown that velocity related intensity measures are well correlated with occurrence of liquefaction (Midorikawa and Wakamatsu 1988, Kostadinov and Yamazaki 2001).

Among spectral acceleration IMs, $S_{a\text{-}1.0}$ can be termed to be the best IM. This can be attributed to the fact that the period of the wharf-foundation elongates during earthquake due to the nonlinear response of the wharf-foundation structure and nonlinear interaction of the wharf with surrounding soil. The maximum response of wharf components occurs during elongated periods and as a result IMs that reflect the characteristics of input earthquakes at larger periods are more appropriate IMs.

6.5.4 Sufficiency Comparisons

Sufficiency investigates the statistical independence of the IM with respect to ground motion characteristics. A sufficient IM ensures the accuracy of results obtained using the probabilistic structural assessment framework used commonly today (Luco and Cornell 2007, Mackie and Stojadinovic 2001):

$$v(LS) = \int_{DM} \int_{IM} G(LS \mid DM) dG(DM \mid IM) d\lambda(IM) \tag{6.13}$$

In the above equation, G(LS|DM) denotes the probability of exceeding a limit state (LS) given the value of structural demand, G(DM|IM) denotes the probability of exceeding a demand measure given the value of ground motion IM, and λ(IM)

denotes the mean annual frequency of exceeding each value of the IM. Using the theorem of total probability yields the mean annual frequency of exceeding a limit state, ν(LS), as shown in Equation 6.13. Sufficiency of the IM ensures that the estimate of G(DM|IM) is independent of ground motion parameters (or other hazard parameters), and enables this straightforward application of the theorem of total probability without introducing model bias or the need to consider joint probability density functions of multiple hazard parameters.

Sufficiency of an IM has been traditionally tested using ground motion characteristics such as M and R. As mentioned earlier the sufficiency property is quantified by the *p*-value which is estimated by performing a linear regression upon the residuals, $\varepsilon_d|IM$ from the PSDM with respect to characteristics including M and R. By definition, *p*-value is the probability of rejecting the null hypothesis (Hines et al., 2003), which in this case is the independence of IM from ground motion characteristics such as M and R. Higher *p*-value therefore gives weaker evidence for rejecting the null hypothesis, meaning lower statistical significance and therefore a sufficient IM. Therefore, it is customary to reject the null hypothesis if the *p*-value is less than a particular significance level. Popular levels of significance are 0.1% (0.001), 1% (0.01) and 5% (0.05). This study uses a 5% significance level to determine the sufficiency of the proposed IMs. Figure 6.5 shows the *p*-values for all of the component demands and IMs with respect to M and R. Based on the significance level PGV, I_a, $S_{a\text{-}Tn}$, and CAV are all sufficient. It is evident that no single IM is consistently the most sufficient across the domain of component demands. For instance, considering the relative movement of the crane rails demand,

I_a is seen to be the most sufficient with respect to M, while CAV_5 is the most sufficient with respect to R.

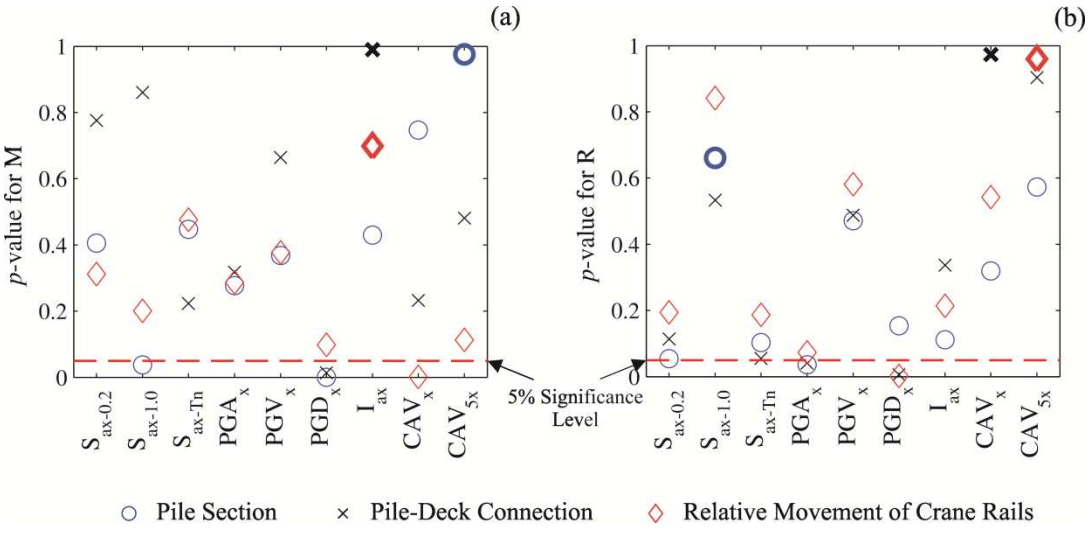

Figure 6.5 Sufficiency of different IMs with respect to a) moment magnitude and b) closest distance to rupture.

Figure 6.6 shows a comparison of the linear regression on the residuals for all critical response measure with respect to M and Figure 6.7 shows the same quantities with respect to R using PGV as the IM. In Section 6.5.1, the *p*-value was defined as the measure of the probability that the randomly distributed points from the analysis would result in a regression line as far horizontal (zero slope) than that observed actually. This is demonstrated in the plots shown in Figure 6.6 and 6.7. The study of sufficiency reveals that PGV is the optimal IM that passes the test of sufficiency with respect to M and R and is the IM used in this study for fragility analysis of wharf components.

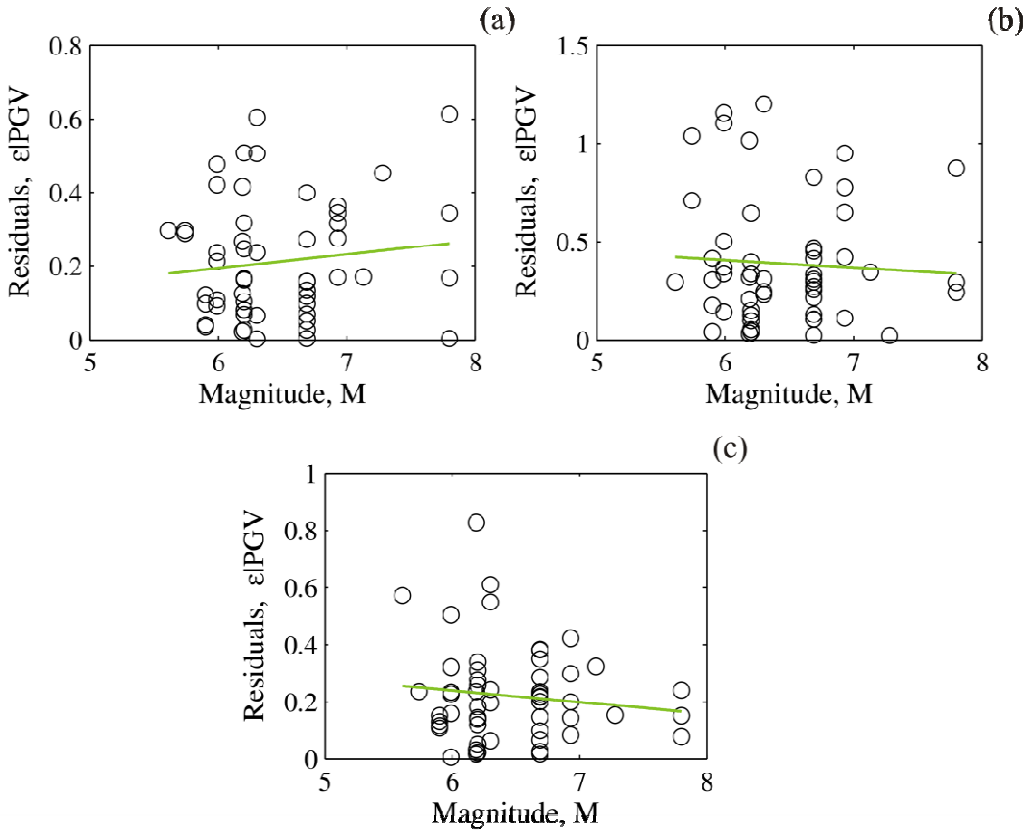

Figure 6.6 Sufficiency of PGV with respect to M for a) pile sections, b) pile-deck connections, and c) relative movement of the wharf with respect to the landside crane rail.

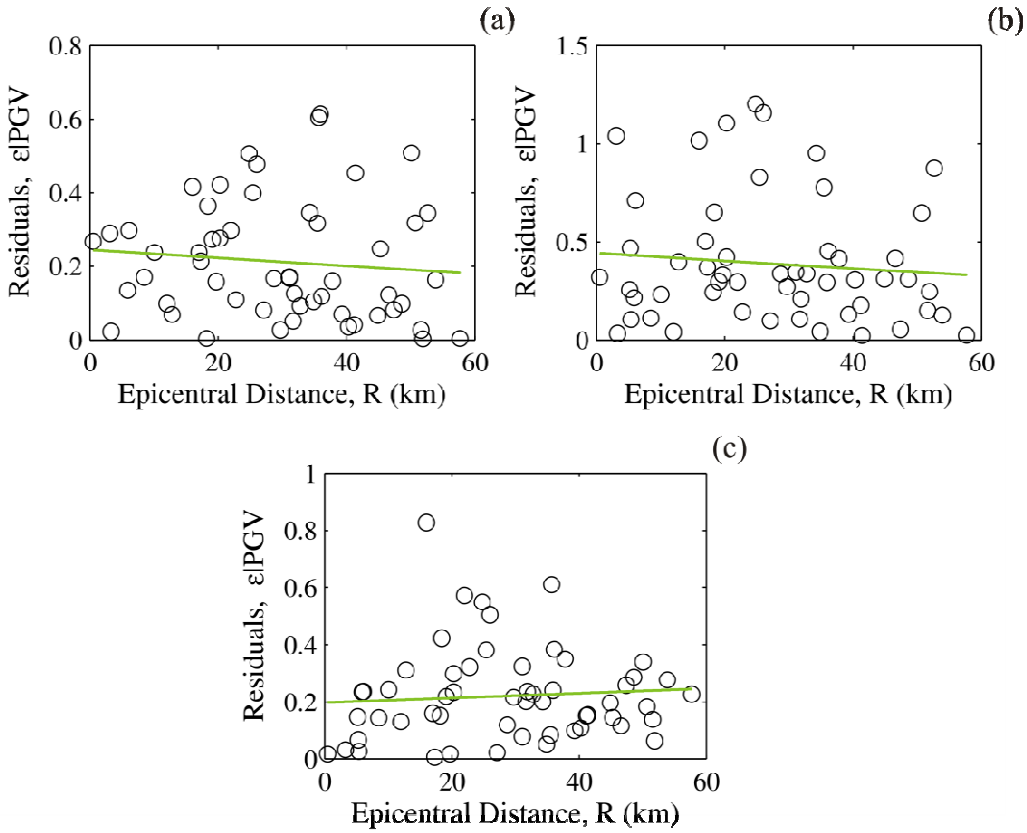

Figure 6.7 Sufficiency of PGV with respect to R for a) pile sections, b) pile-deck connections, and c) relative movement of the wharf with respect to the landside crane rail.

6.6 PSDMs of Wharf Components Using PGV as IM

6.6.1 PSDMs from Two-Dimensional Wharf Model

This section presents the result of probabilistic seismic demand analysis of the two-dimensional plain strain model of the wharf of chapter III. Based on the discussion in the previous section, it is concluded that PGV is the most appropriate IM to model demand parameters of the wharf system. Figure 6.8 shows the seismic demand of the piles and pile-deck connections in terms of curvature and the displacement of the landside crane rail relative to the wharf in the transverse direction as a function of PGV. As noted before, linear and nonlinear regression analyses are used to find the parameters of the fitted lognormal distribution of the

demand models in Equations (6.3) and (6.6). The mean and standard deviation of the estimated parameters are presented in Table 6.3 for pile sections, pile-deck connections, and relative displacement of the wharf with respect to the crane rail. These statistics are illustrated in Figure 6.8 in which the solid lines are the means of the probability models and the dashed lines in each figure represents the upper and lower bound corresponding to one standard deviation from the mean. It is observed that the assumption of independence of the demand from intensity measure in the logarithmic scale is almost valid for all demand parameters. Furthermore, all of the demand parameters are seen to be reasonably well described by linear or bilinear models in the logarithmic scale.

Table 6.3 Statistics of the estimated parameters of demand models.

Response Measure	Parameter	Mean	Standard deviation
Pile-deck connection curvature: φ_{Con} (1/m)	a	0.143	0.162
	b	1.361	0.067
	$\beta_{D\|IM}$	0.559	-
Pile section curvature: φ_{Pile} (1/m)	a_1	0.016	0.320
	b_1	0.550	0.119
	$\beta_{D\|IM\ 1}$	0.269	-
	PGV_0	0.451	0.093
	b_2	5.115	0.818
	$\beta_{D\|IM\ 2}$	0.613	-
Relative displacement of the wharf with respect to the landside crane rail: Δ_{Rail} (m)	a	0.189	0.093
	b	0.696	0.038
	$\beta_{D\|IM}$	0.321	-

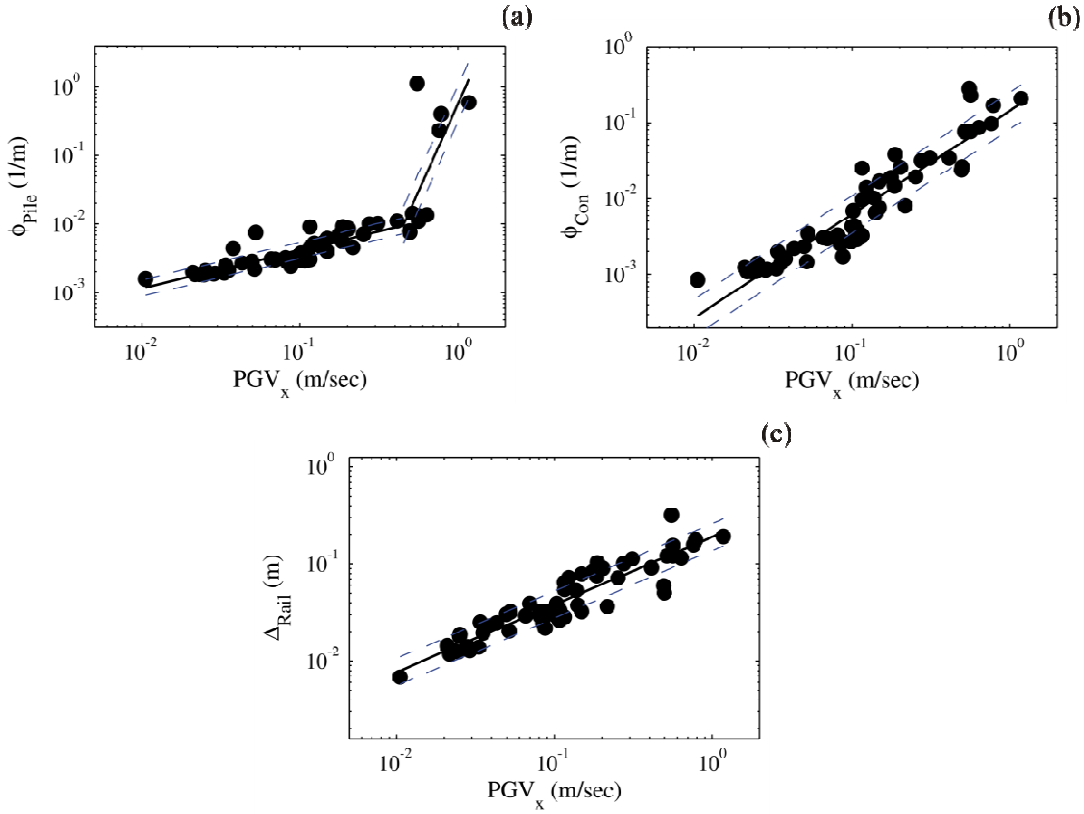

Figure 6.8 Probabilistic seismic demand models for (a) pile-deck connections, (b) pile sections, and (c) relative movement of the wharf with respect to the landside crane rail.

The assumption that the errors in the demand models are lognormally distributed is checked for the horizontal displacement of the wharf relative to the landside crane rail by dividing the range of intensity measures into 4 equal zones in the logarithmic scale and comparing the numerically evaluated distribution of ln(ε) in each zone with the lognormal distribution with unit median and logarithmic standard deviation of $\beta_{D|IM}$ given in Table 6.3 as shown in Figure 6.9a. It is seen that in all zones, the relative frequency of errors follows lognormal distribution to a reasonable degree. Figure 6.9b compares the distribution of the numerically evaluated error in the demand model for relative crane rail displacement when considering the entire range of IM (i.e. only one zone for IM). As expected, the assumption of lognormality of errors tends to be more realistic as the number of samples increases.

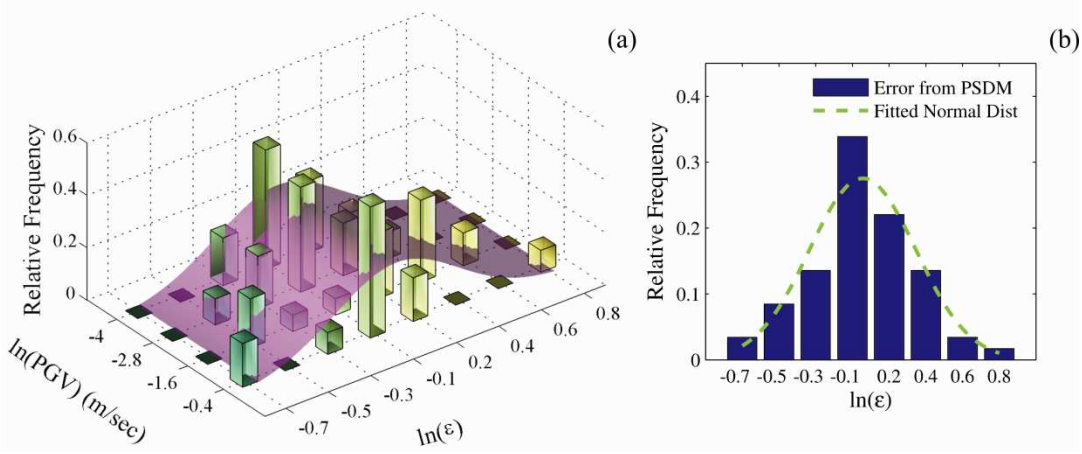

Figure 6.9. Distribution of the error ln(ε) for (a) individual zones of IM and (b) the entire range of IM.

6.6.2 PSDMs from Three-Dimensional Wharf Model

Three-dimensional modeling and analysis of wharves incorporates three-dimensional response features of the structure including longitudinal and torsional response and the boundary conditions of shear keys and pounding of wharf decks. Consequently, three-dimensional modeling of the wharf enables more realistic seismic performance assessment of the structure compared to the corresponding two-dimensional model. The demand measures pertaining to three-dimensional response of the wharf include shear key's responses at the longitudinal ends of wharf segments, and the relative transverse movement of adjacent decks at expansion joints which controls the damage to crane rails and collector trench.

Since the nonlinear time-history analysis of the wharf with two adjacent wharf segments as boundary conditions is computationally expensive for probabilistic seismic demand analysis, the simplified static procedure developed for seismic response assessment of wharves in chapter V is used to determine the response of piles sections and pile-deck connections. In this procedure, the dynamic response of

three identical simplified one strip wharf segments that are connected in the longitudinal direction is determined for a scenario earthquake and the time of maximum response t_{max} in the component of interest is found. In the next step, linearly increasing soil and wharf deformations with maximum deformations equal to the corresponding soil and wharf response at t_{max} are applied to the full model of the wharf. A pushover analysis is performed for the imposed deformations and the response of the wharf in the component of interest is recorded as the maximum component response of the wharf. Since the relative movement of the wharf with respect to the landside crane rail, the response of shear keys, and the relative transverse movement of the decks at expansion joints correspond to the global behavior of the wharf whose response is closely captured by simplified one strip model, these responses are determined directly from the response of the three simplified one strip models of the wharf connected in the longitudinal direction.

Figure 6.10 presents the response of wharf components with respect to the geometric mean of the two orthogonal horizontal PGVs of the corresponding earthquakes. It must be noted that direct comparison between the PSDMs of the two and three-dimensional wharf models is not feasible as their IMs are different. Similar to the PSDM for the two-dimensional wharf model, curvature demand of pile sections is represented well by a bilinear model. Since the longitudinal response of the wharf contributes to the total curvature response of piles sections, it is expected that the maximum piles sections curvature is increased over all ranges of the IM. This is observed to be true especially for the PGV range of 0.05 m/s to 0.2 m/s which consequently pushes the point of intersection of the two linear regression

lines to the left in the PSDM of the three-dimensional model compared to the PSDM of the two dimensional wharf model. The statistics of parameters of the models are presented in Table 6.4.

Table 6.4 Statistics of the estimated parameters of demand models.

Response Measure	Parameter	Mean	Standard deviation
Pile-deck connection curvature: φ_{Con} (1/m)	a	0.204	0.162
	b	1.257	0.067
	$\beta_{D\|IM}$	0.821	-
Pile section curvature: φ_{Pile} (1/m)	a_1	0.047	0.32
	b_1	0.723	0.119
	$\beta_{D\|IM\ 1}$	0.510	-
	PGV_0	0.181	0.093
	b_2	2.274	0.818
	$\beta_{D\|IM\ 2}$	0.459	-
Relative displacement of the wharf with respect to the landside crane rail: Δ_{Rail} (m)	a	0.165	0.093
	b	0.646	0.038
	$\beta_{D\|IM}$	0.411	-
Transverse deformation of shear key : Δ_{SK} (m)	a	0.034	0.093
	b	0.451	0.038
	$\beta_{D\|IM}$	0.368	-
Relative transverse displacement of collector trench at expansion joints: Δ_{CT} (m)	a	0.034	0.093
	b	0.451	0.038
	$\beta_{D\|IM}$	0.368	-

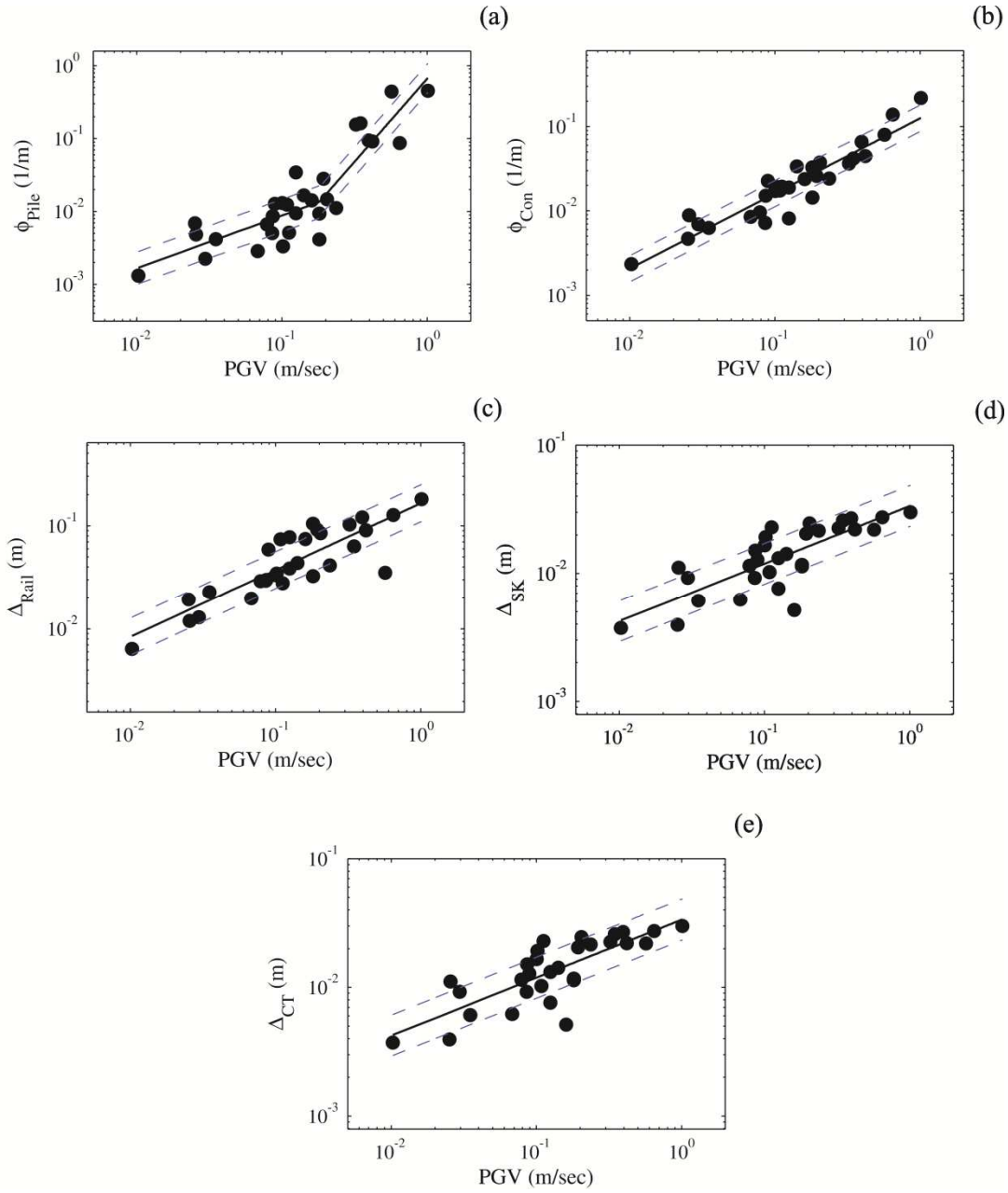

Figure 6.10 Probabilistic seismic demand models for (a) pile-deck connections, (b) pile sections, (c) relative movement of the wharf with respect to the landside crane rail, (d) shear keys, and (e) collector trenches.

6.7 Component Limit States

The capacities of the structural components of the wharf in Equation (6.1) are defined in terms of limit state models. Similar to the fragility analysis of buildings and bridges, the limit states for wharf components are defined by qualitative

damage states such as slight, moderate, and extensive; the first two states are adopted from PIANC (2001). The slight damage state has a high probability of occurrence during the life time of the wharf in which no structural damage is permitted. On the other hand, the moderate damage state has a lower probability of occurrence compared to the slight damage state in which only reparable damages and limited residual deformations are allowed. Since damage states are mutually exclusive, all other damages that are more severe and consequently less probable than the ones associated with slight and moderate damage states falls into the extensive damage state category.

A number of response measures that are critical in the overall structural response of the wharf and the performance of associated components such as cranes are considered in this study. As mentioned before, these critical response measures are the curvature of piles and pile-deck connections, the relative displacement of the wharf with respect to the landside rail, the transverse deformation of shear keys, and the relative transverse displacement of collector trench at expansion joints. The limit states associated with these responses are assumed to be lognormally distributed.

6.7.1 Pile-Deck Connections

Deformation limit states of pile-deck connections are obtained from the experimental tests conducted by Lehman et al. (2009). The results of the experiment are shown in Figure 6.11. The slight damage state of the connection is limited to the case of minimally spalled concrete without any loss of vertical load carrying capacity (Figure 6.11a). The moderate damage state corresponds to the case where horizontal and diagonal cracking of the concrete cover of the piles appear due to

extensive bending and shear demands (Figure 6.11b). The damage to pile-deck connections in this state is repairable. In the extensive damage state, the connection undergoes severe unrepairable damage mainly caused by the rupture and displacement along the diagonal crack (Figure 6.11c). The drift limits provided in the study by Lehman et al. (2009) are converted to curvature limits at the connection using numerical simulation of the test specimen which are presented in Table 6.6.

(a) (b) (c)

Figure 6.11 Damage to pile-deck connections at a) slight, b) moderate, and c) severe damage states (Lehman et al., 2009)

6.7.2 Pile Sections

The curvature limit states for different sections of pre-stressed piles are found using moment-curvature analyses. Typically the cross-section of a pile contains all or a number of the following discretized sub-regions: the cover layer of unconfined concrete, the inner core region of confined concrete, the circular layer of longitudinal reinforcing steel, and the circular layer of pre-stressing strands. In order to determine the deformation capacity of the piles, the strain limits of the constitutive section materials are used to determine the corresponding section

curvature. PIANC (2001) has provided a set of strain limits for constitutive materials of pile sections for the first two damage states. It is assumed that the extensive damage in a pile section occurs when constitutive materials of the section reach the strain limit of 2/3 of their corresponding ultimate strain. The strain limits for each of the constitutive materials are presented in Table 6.5.

Table 6.5 Strain limits associated with defined limit states for constitutive materials of pre-stress pile sections

	Limit State		
Material Response	Slight	Moderate	Severe
Concrete extreme fiber compression strain	0.004	0.008	–
Core concrete extreme fiber compression strain	–	–	2/3 ε_{cu}
Reinforcing Steel tension strain	0.01	0.01	2/3 ε_{su}
Prestressing strand incremental strain	0.005	0.015	2/3 ε_{pu}

Performing moment-curvature analyses for different sections of the pre-stressed piles in the wharf configuration, the curvature limits are determined as the minimum of the curvatures corresponding to the strain limits of different constitutive section materials for each limit state. The derived curvature limits for all sections in the wharf are presented in Figure 6.12. The median of the curvature limit of different pile sections in each limit state is considered as the curvature limit of the corresponding capacity limit state.

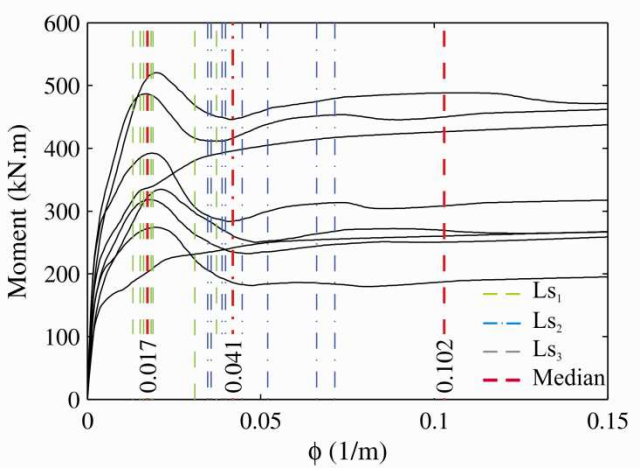

Figure 6.12 Moment curvature curves of different sections of the piles and the median limit states.

6.7.3 Relative Displacement of the Wharf with Respect to the Landside Rail

The displacement thresholds for each of the three limit states for the relative movement of the landside crane rail with respect to the wharf is provided by Werner and Cook (2010) based on expert opinion. Relative displacement of 0.3 cm to 2.5 cm is considered as the slight damage state in which the girder supporting the crane rail is unlikely to suffer physical damage. The second limit state corresponds to the case of cracks occurring in the girder of the crane rail with no derailment in the crane. Relative displacements of 2.5 cm to 15.2 cm are considered to be the definitive range for the moderate damage. If the relative displacement of the rails is beyond the limit of moderate damage, the crane is expected to suffer significant damage either due to the derailment or yielding and local buckling of the sections in the crane legs in addition to severe damage in the rails.

6.7.4 Shear Keys

According to the force-deformation behavior of shear keys discussed in section 5.4.2 of chapter V, the initial stiffness of shear keys is large and once the applied

load on the lateral face of a shear key exceeds the initial capacity of the component P_{cap}, the load carrying capacity of the shear key rapidly decreases and the shear key fails. Therefore, only the severe damage state is defined for the shear key response and the associated limit state is chosen to be equal to the transverse gap between the faces of shear keys (i.e. 2.5 cm).

6.7.5 Collector Trench

The power required for the operation of heavy duty cranes is distributed on the wharf deck through a collector trench. As seen in Figure 6.13, the trench is made into the wharf deck in the longitudinal direction and is continuous over the wharf segments. Consequently during earthquakes, the relative transverse movement of the adjacent decks at the location of collector trench may cause the loss of contact of the crane with the collector trench and damage to the structure of the collector trench. Based on the details of collector trenches and engineering judgment, Werner and Cook (2010) identified three damage states and provided corresponding relative transverse deformation bounds. The slight damage corresponds to the minor loss of alignment of crane rails and loss of contact between crane and trench conductor bars. Moderate damage of the trench is referred to as the case where the crane rail is damaged moderately and loss of contact between crane and trench conductor bars occurs. The severe damage corresponds to major crane rail damage, misalignment of crane and trench conductor bars, and damage to collector trench structure. The associated deformation limits for each of the damage states are presented in Table 6.6.

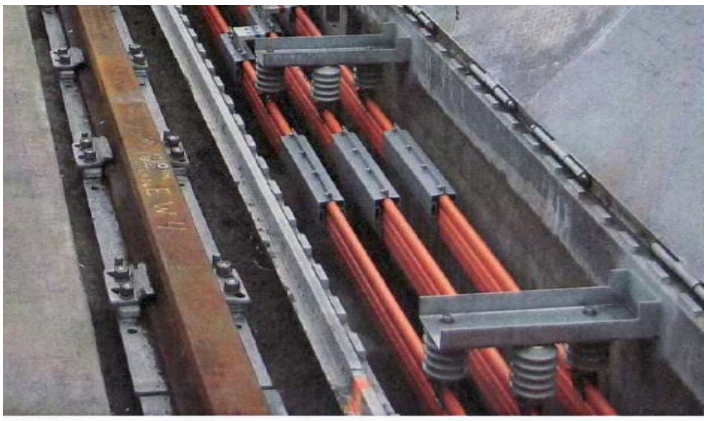

Figure 6.13 Crane Rail and Collector Trench (Photographs courtesy of Bill Cooke of Manson Construction Co., Richmond CA.)

The summary of deformation limits of different wharf components associated with three limit states chosen for this study are presented in Table 6.6.

Table 6.6 The deformation limits of critical wharf components corresponding to the chosen limit states.

	Limit State		
Component	Slight	Moderate	Severe
Pile-deck connection rotation (1/m)	0.007	0.035	0.080
Pile section curvature (1/m)	0.017	0.041	0.102
Relative displacement of the landside rail with respect to wharf deck (cm)	0.3	2.50	15.2
Transverse deformation of shear key (cm)			2.54
Relative transverse displacement of collector trench at expansion joints (cm)	0.95	1.91	3.81

6.8. Component Fragility Curves

After developing the probabilistic seismic demand models and determining the corresponding limit states of the wharf damage for the critical components, component fragility curves are constructed using the closed form given in Equation

(6.1). Following Wen et al. (2004), the dispersion in the capacity β_C and modeling β_M are assumed to be equal to 0.30 while the dispersion in the demand $\beta_{D|IM}$ is found from Equation (6.5).

From discussion of the PSDA in section 6.6, it was found that the maximum curvature of the piles sections is well described by a bilinear model as shown in Figure 6.8a and Figure 6.10a. Substituting the bilinear demand model of Equation (6.7) into Equation (6.1), the fragility function is derived for IMs larger than IM_0 as

$$P(C < D \mid IM) = \Phi\left(\frac{\ln(IM) - \frac{1}{\hat{b}_2}\left[\ln(\lambda_C) - \ln(\hat{a}_1) + (\hat{b}_2 - \hat{b}_1)\ln(IM_0)\right]}{\frac{\sqrt{\beta_{D|IM}^2 + \beta_M^2 + \beta_C^2}}{\hat{b}_2}} \right) \tag{6.13}$$

The development of fragility curves as denoted in previous sections involves characterization of the contributing sources of uncertainties and their quantifications. Two distinct classes of uncertainties are aleatoric referring to inherent randomness of the nature of the problem and epistemic uncertainties which includes uncertainties stemming from the lack of knowledge. Confidence bounds on the developed fragility estimates are a measure to reflect the effect of reducible uncertainties (i.e. epistemic uncertainty in the predicted values of fragility curves). A two-sided confidence interval of confidence level 100(1-α) % is an interval having a probability of (1-α) of containing the parameter of interest. The lower and upper $\alpha/2$ quantile of the logarithmic mean of the demand model given the intensity measure $<\lambda_{D|IM}>_{1-\alpha}$ is found according to Ang and Tang (2006) as

$$\left\langle \lambda_{D|IM} \right\rangle_{1-\alpha} = \lambda_{D|IM} \pm t_{n-2,1-\frac{\alpha}{2}} \beta_{D|IM} \sqrt{\frac{1}{n} + \frac{\left(IM - \overline{IM}\right)^2}{\sum\left(IM_i - \overline{IM}\right)^2}} \tag{6.14}$$

in which n is the number of samples, $t_{n,\alpha}$ is the αth percentile of the Student's t distribution with degree of freedom n, IM_i (i=1,…,n) is the value of the IM for the ith data point, and $\overline{IM}$ is the mean of IM_is.

The resulting fragility curves for pile sections, pile-deck connections and the relative displacement of the landside crane rails with respect to the wharf for slight, moderate, and extensive damage states for the two-dimensional model of the wharf are shown in Figure 14a-c respectively. Using Equation (6.14), the 90% confidence bounds on $\lambda_{D|IM}$ are calculated for various damage states and response measures of the wharf and the results are presented in Figure 6.11 using dash lines.

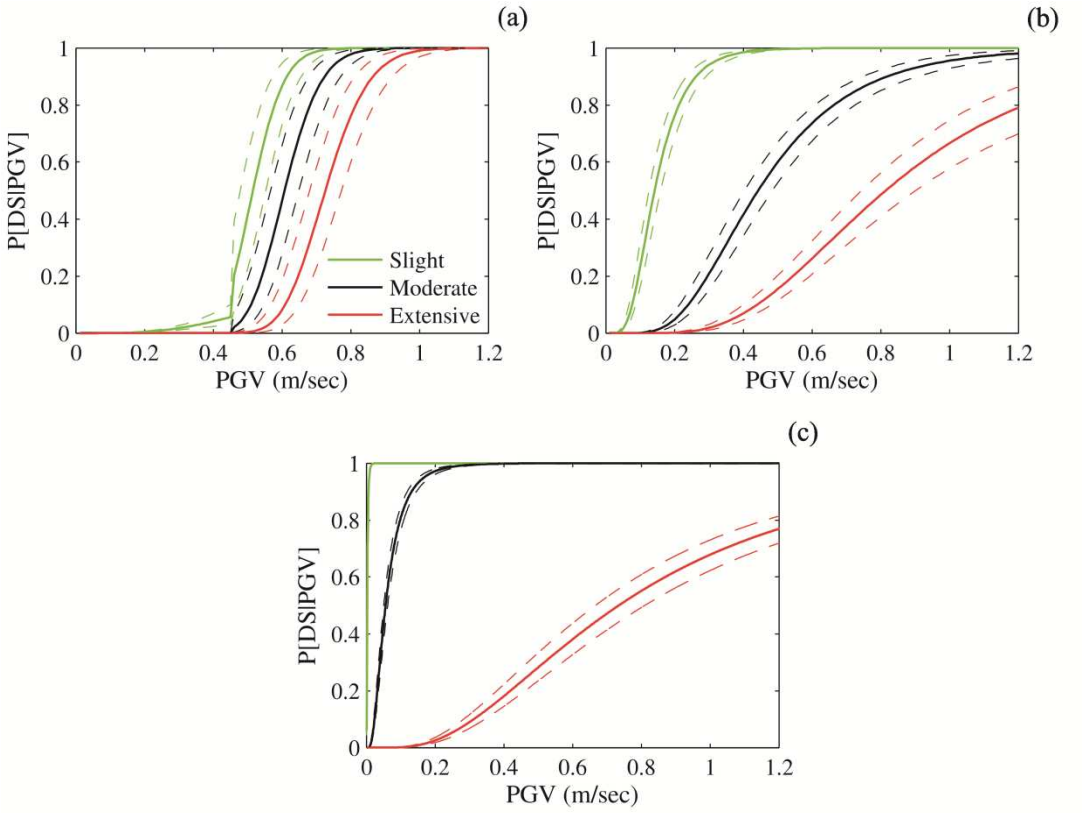

Figure 6.14 Seismic fragility curves for (a) pile sections, (b) pile-deck connections, and (c) relative movement of the wharf with respect to the landside crane rail (solid lines are the fragility estimates and the dashed lines are the corresponding 90% confidence bounds).

From the set of fragility curves in Figure 6.14, the pile-deck connections appear to be more susceptible to slight damage compared to pile sections over the entire range of PGV. However, moderate and extensive damage of pile-deck connections is more probable than the occurrence of the same damage states in the pile sections for PGVs less than 0.7 m/sec. Furthermore, the wharf damage as a result of excessive relative displacement of the wharf with respect to the structurally separated landside crane rail is seen to be highly probable especially for slight and moderate damage levels. This response measure of the wharf has a large impact on the operation of the container cranes, and therefore requires more attention. A possible retrofit

measure for the excessive relative displacement of the wharf can be connecting the separate landside rail and wharf using reinforced concrete.

Seismic fragility curves of critical response measures of the three-dimensional wharf model are shown in Figure 6.15. Compared to the fragility curves of the two dimensional wharf model, probabilities of slight, moderate, and extensive damage of pile sections are increased significantly. The same observation is made for the fragility curves for slight and moderate damage levels for pile-deck connections. However the fragility curves for extensive damage of pile-deck connections and all damage states of the relative movement of wharf with respect to the landside rail remains almost unchanged. Figure 6.15d,e shows the fragility curves of shear keys and collector trenches – the components whose response could not be captured by two-dimensional model of the wharf.

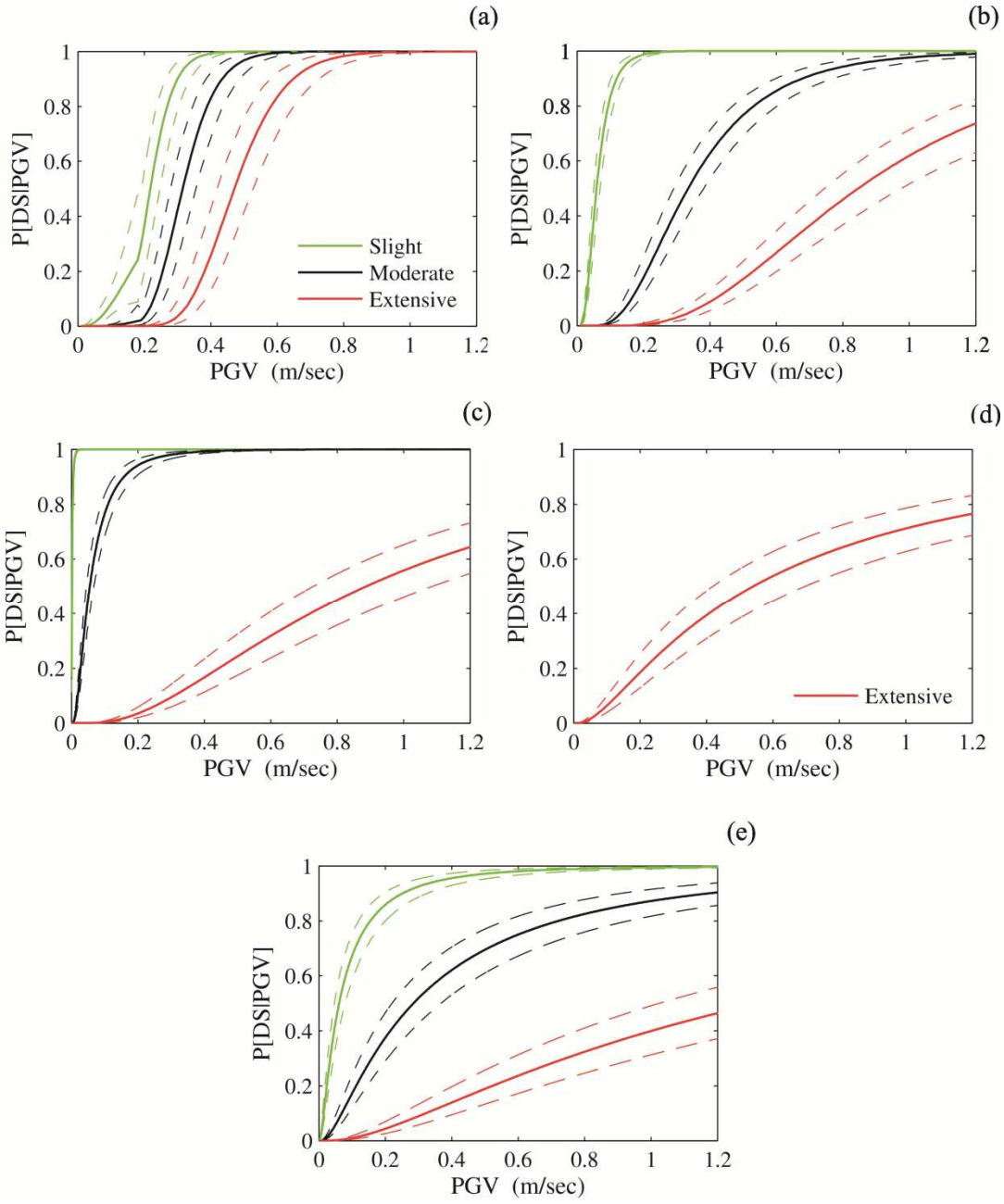

Figure 6.15 Seismic fragility curves for (a) pile sections, (b) pile-deck connections, (c) relative movement of the wharf with respect to the landside crane rail, (d) shear keys, and (e) collector trenches (solid lines are the fragility estimates and the dashed lines are the corresponding 90% confidence bounds).

6.9 Closure

Two and three-dimensional models of the wharf in liquefiable embankment soils were analyzed using soil deformation time-histories generated for an ensemble of

synthetic and recorded ground motions for the west coast of the United States. Theses ground motions represent a broad range of earthquake scenarios in terms of moment magnitude and the closest distance to rupture. Various intensity measures (IMs) for probabilistic seismic demand analysis (PSDA) were considered and their performance in estimating wharf demand parameters was assessed for different optimality criteria. The main conclusions of the analysis of IMs are:

1. Cumulative absolute velocity (CAV) is the most efficient, practical, and proficient IM and provides the best fit with demand parameters of the wharf in the logarithmic scale. However, CAV is not a sufficient IM with respect to moment magnitude, M.

2. PGV and CAV_5 are the next optimal IMs in terms of efficiency, practicality, and proficiency. Furthermore, both PGV and CAV_5 satisfy the sufficiency criteria for moment magnitude and closest distance to rupture.

Using PGV as the IM, the results of PSDA for critical wharf component demand measures for two and three-dimensional wharf models were presented. These response measures included the curvature of piles and pile-deck connections, the relative displacement of the wharf with respect to the landside rail, the transverse deformation of shear keys, and the relative transverse displacement of collector trench at expansion joints. PSDA of wharf components showed the following results:

1. Pile section curvature demand from both two and three-dimensional models of the wharf are well described by bilinear regression models, while other demand measures are appropriately represented by linear models.

2. The demand on pile sections and pile-deck connections in the three-dimensional model of the wharf are notably larger than the corresponding demands in the two-dimensional wharf model.

Three damage states were considered and the corresponding limits were found using numerical simulations, experimental results, and expert opinion. A set of fragility curves were generated for the wharf response measures using the PSDMs of the two and three-dimensional wharf models. It was found that

1. The relative movement of the wharf with respect to the landside rail is the most susceptible component to slight and moderate damage.

2. Pile sections are more vulnerable than pile-deck connections over the entire range of PGV.

3. Probabilities of exceeding slight, moderate, and extensive damage limits of pile sections are considerably larger in the fragility curves of the three-dimensional wharf model compared to the same quantities of the two-dimensional wharf models. In general, fragility curves of the three-dimensional wharf model exhibit larger probabilities of failure compared to the corresponding quantities from the two-dimensional wharf model.

CHAPTER 7

SUMMARY AND CONCLUSIONS, IMPACT, AND FUTURE WORK

7.1 Summary and Conclusions

Historical cases of seismic events in port areas have shown that port facilities are vulnerable and the damage to these facilities often results in a reduction in capacity and significant economic losses to the local and regional economy. Noticing that a number of major US seaports including the port of Los Angeles, Long Beach, Oakland, Seattle, Charleston, and Savannah are located in seismically prone areas, assessment of the vulnerability of seaport systems to seismic events is important. The main objective of this thesis was to develop a detailed understanding of the seismic behavior of wharf systems using probabilistic methods and subsequently develop a set of fragility curves to be used in risk assessment of seaports. As the first step, a typical pile-supported wharf on the west coast of the United States representing the class of wharf construction in the late 1960s and early 1970s was considered. Seismic design procedures used for these types of wharves are much less robust than currently available procedures. However this vintage of wharf is still in use in major seaports and therefore understanding their seismic response behavior is of great importance. A two-dimensional plane strain model of a marginal wharf of this vintage in potentially liquefiable soils is generated by incorporating advanced structural and soil-structure interaction modeling procedures which include advanced models of pre-stressed piles, pile-deck connections, and interaction of piles with potentially liquefiable soils. The results of

complex modal analysis of the wharf indicated large levels of damping ratios of the system ranging from 36.1% to 81.5%. The modal damping ratios found in this study are very large compared to the modal damping ratios typically assumed in prior studies which did not assess the nonlinear soil behavior. This can affect the procedures for simplification of the wharf models using equivalent linear elastic models. Furthermore, nonlinear dynamic analysis of the wharf subjected to strong levels of ground shaking showed that liquefaction and seaward movement of the embankment are detrimental in the response of wharves; factors that were not considered or well represented in former studies. Analyses results also showed large liquefaction-induced values of relative horizontal displacement between the structurally separate landside crane rail and the wharf deck (which supports the seaside crane rail). This is particularly important since even small relative displacements between the landside and seaside crane rails can cause crane derailment and damage. Furthermore, the zones of damage detected by this study coincided with damage patterns observed in historic cases of wharf damage in past earthquakes.

Seismic performance of wharf-crane systems is one of the key factors in the functionality of ports in the aftermath of earthquake events. The specific effect of wharf-crane interaction is studied for the first time in this research using a sliding/uplift capable model of a container crane. Subjecting the wharf to time histories of ground displacement and excess pore water pressures within the underlying soil embankment and performing nonlinear time-history analyses, it was found that unlike the conclusion of former studies, the dynamic interaction between

the wharf and crane may amplify the response of the wharf. These results suggest that wharf–crane interaction should be given more careful consideration than is currently required when evaluating the seismic response of a wharf system. Furthermore, simple analytical limits on the spectral acceleration response of the crane rails were derived to predict the occurrence of sliding, uplift, and yielding of the portal frame. The results of the numerical simulation showed that the derived limits perform well in predicting the response of the crane.

Due to the complexity of the numerical modeling and analysis of wharf systems, very few studies investigated three-dimensional seismic response of wharves. This study presented a procedure for three-dimensional modeling of wharves in liquefiable soils. The framework included modeling structural elements and soil springs, and generating out-of-plane ground deformations. Modal analysis results of the wharf showed that torsional modes have a predominant role in the inertial response of the wharf. However, the transverse seaward deformation of the wharf due to the transverse deformation of the liquefied top loose sand layer was found to govern the overall wharf response.

Large computational times required for nonlinear dynamic analysis of the wharf system is a major drawback for this method of analysis to be applicable for probabilistic seismic demand analysis in which a large number of simulations are required. A simplified model of the three-dimensional wharf was introduced in this study by lumping the properties of wharf segments into a single strip representative model. The simplified model was shown to closely capture linear and nonlinear dynamic behavior of wharves found by modal and time-history analyses.

Furthermore, a simplified analysis technique was proposed to estimate the maximum response of the full wharf using nonlinear dynamic analysis results of a simplified wharf model combined with a nonlinear static pushover analysis of the wharf.

Probabilistic seismic demand models of critical response measures of the wharf were developed using either linear or bilinear regression models. The choice of intensity measure was made based upon a rigorous probabilistic analysis of various IMs and different demand parameters of the wharf. The IMs included peak ground acceleration (PGA), peak ground velocity (PGV), peak ground displacement (PGD), spectral acceleration at 0.2 seconds ($S_{a\text{-}0.2}$), spectral acceleration at 1.0 seconds ($S_{a\text{-}1.0}$), spectral acceleration at the fundamental period of the two-dimensional wharf model ($S_{a\text{-}Tn}$), arias intensity (I_a), cumulative absolute velocity (CAV), and modified cumulative absolute velocity (CAV_5). It was found that PGV is the most appropriate IM for demand modeling of wharf systems in liquefiable soils, based on xxxxx.

Convolving the probabilistic demand models with component capacities, a series of fragility functions were developed for critical wharf components using the PSDMs of the two and three-dimensional wharf models. The capacities or limit states used to develop fragility curves were derived from numerical simulations, experimental results, and expert judgment. Fragility analysis of wharf components showed that the relative movement of the wharf with respect to the landside rail is the most susceptible component to slight and moderate damage. However, pile sections are the most vulnerable components of the wharf to extensive damage primarily due to the large deformation demands on the piles at the interface of loose and dense sand

layers. Furthermore, fragility curves of the three-dimensional wharf model were found to exhibit larger probabilities of failure compared to the corresponding quantities from the two-dimensional wharf model. This finding is not particularly surprising since longitudinal and torsional responses of the wharf in the three-dimensional wharf model contribute to component responses.

7.2 Impact

This research provides a detailed rigorous approach to evaluating the seismic behavior of pile-supported wharves in liquefiable embankment soils. One primary contribution of the research is a framework for generating seismic fragility curves that would permit seismic risk assessment of seaport systems. Additional benefits and contributions of the research include the following:

- The current understanding regarding the seismic behavior of wharves is primarily based on simplified and sometimes unrealistic models of wharf components. This study on the other hand provides an enhanced understanding of the seismic behavior of pile-supported container wharves in liquefiable soils using a realistic representation of constitutive structural and geotechnical wharf components. The three-dimensional analytical modeling and response evaluation of the wharf is the first study in this class that considers both kinematic and inertial response behavior of wharves simultaneously in liquefiable embankment soils.
- A simplified modeling procedure for wharves is presented in this study which decreases the computational time required for time-history analysis of the structure while capturing the nonlinear dynamic behavior of the wharves

accurately. While specifically applied to pile-supported wharf structures, the simplified method can be applied to any geo-structure which is symmetric in at least one dimension.

- This study provides the first systematic and comprehensive assessment of the dynamic interaction of wharves and container cranes. The results of this study showed that the common assumption of cranes acting as tuned mass dampers for underlying wharves during seismic events is not appropriate. Also provided in this research are analytical relations to predict the occurrence of sliding and uplifting phenomena as well as yielding of the crane's portal frame. These relations provide a simple tool for the performance assessment of container cranes that can be integrated in performance based design procedures.
- The development of seismic fragility curves of pile supported wharves has been very limited; consequently this research offers a significant contribution in this aspect. These fragility curves indicate the most vulnerable components of wharves and therefore provide decision makers with essential tools for maximizing investment in wharf retrofit. The fragility curves developed as a part of this research will fill a major gap in existing seismic risk assessment software, and offer a means to assess the regional impact of the condition of wharves following a natural hazard event.

7.3 Future Work

The insights provided by this work suggest additional research in the following areas:

- The wharf system considered in this study is a typical configuration of wharves in the late 1960s and early 1970s. Future studies could consider newer wharves designed based on recent seismic codes. Such studies will provide valuable insights about the efficiency of the new seismic provisions in reducing seismic damage of wharf structures.
- Embankment soil profile has a predominant role in the seismic behavior of wharf structures. Modeling and dynamic response assessment of wharves in different embankment soils will be a valuable contribution to seismic fragility assessment of classes of pile supported wharves.
- Assessment of the impact of various retrofit strategies from geotechnical considerations to structural measures coupled with the performance requirement of seaport systems enables port owners to wisely invest in the most efficient methods of seismic risk reduction of the ports.

REFERENCES

Abramhamson, N. A., and Silva, W. J., 1997. "Empirical response spectral attenuation relations for shallow crustal earthquakes." Seismological Research Letters, 68(1), 94–127.

ACI Committee 318, 2005. "Building Code Requirements for Structural Concrete (ACI 318-05) and Commentary (318R-05)." American Concrete Institute, Farmington Hills, Mich., 430 pp.

Ang, A.H.-S., and Tang W.H., 2007. "Probability concepts in engineering: emphasis on applications to civil and environmental engineering (2nd ed.)." John Wiley and Sons, New York.

Aki, K., and Richards, P. G, 1980. "Quantitative Seismology: Theory and Methods (2nd ed.).", University Science Books, Sausalito, CA.

Badoni, D., and Makris, N., 1996. "Nonlinear response of single piles under lateral inertial and seismic loads." Soil Dynamics and Earthquake Engineering, 15, 29–43.

BEA, 2008. "Gross Domestic Product by Metropolitan Area for 2006." U.S. Department of Commerce, Bureau of Economic Analysis, Washington, D.C.

Benzoni, G., and Priestley, M. J. N., 2003. "Seismic Response of Linked Marginal Wharf Segments." Journal of Earthquake Engineering, 7, 513–539.

Boulanger, R. W., Curras, C. J., Kutter, B. L., Wilson, D. W., 1999. "Seismic soil-pile-structure interaction experiments and analyses." Journal of Geotechnical and Geoenvironmental Engineering, 125, 750–759.

Boulanger, R. W., Kutter, B. L., Brandenberg, S. J., Singh, P., Chang, D., 2003. "Pile foundations in liquefied and laterally spreading ground during earthquakes: centrifuge experiments & analyses." Report No. UCD/CGM-03/01, University of California, Davis, CA.

Brackmann, E., 2009. "Performance tools for piles and pile-to-wharf connections." M.S. Thesis, Department of Civil and Environmental Engineering, University of Washington.

Chang, S.E., 2000. "Disasters and transport systems: loss, recovery and competition at the Port of Kobe after the 1995 earthquake." Journal of Transport Geography, 8, 53–65.

Chaudhuri1, S. R., Karmakar, D., Na, U. J., Shinozuka, M., 2009. "Seismic Performance Evaluation of Container Cranes." Proceedings of the ATC & SEI Conference on Improving the Seismic Performance of Existing Buildings and Other Structures.

Chiou, B., Darragh, R., Gregor, N., Silva, W., 2008. "NGA project strong-motion database." Earthquake Spectra, 24, 23-44.

Cornell, C. A., Jalayer, F., Hamburger, R. O., Foutch, D. A., 2002. “Probabilistic basis for the 2000 SAC Federal Emergency Management Agency steel moment frame guidelines.” Journal of Structural Engineering, 128(4), 526–533.

Dafalias, Y. F., and Manzari, M. T., 2004. “Simple plasticity sand model accounting for fabric change effects.” Journal of Engineering Mechanics, 130, 622-634.

De Sousa, R. M., 2000. “Force-based finite element for large displacement inelastic analysis of frames.” Ph.D. Thesis, Department of Civil Engineering, University of California, Berkeley, CA.

Dodds, A. M., Martin , G. R., Arulmoli, K., Bauleka, W., Toan, D. V., 2004. “Lifeline Upgrade for a Wharf in Soft Ground.” in Proceedings of Geotechnical Engineering for Transportation Projects, Los Angeles, pp. 1739-1746

Donahue, M. J., Dickenson, E. S., Miller, T. H., and Yim, S. C., 2005. “Implications of the Observed Seismic Performance of a Pile-Supported Wharf for Numerical Modeling.” Earthquake Spectra, 21, 617–634.

Eberhard, M., Baldridge, S., Marshall, J., Mooney, W., Rix, G. J., 2010. “The Mw 7.0 Haiti Earthquake of Jauary 12, 2010.” V. 1.0, USGS/EERI Advance Reconnaissance Team Report, 2010.

Ellingwood, B. R., Celik, O. C., Kinali, K., 2007. “Fragility assessment of building structural systems in Mid-America.” Earthquake Engineering and Structural Dynamics, 36, 1935-1952.

Federal Emergency Management Agency (FEMA), 2000. “Recommended Seismic Design Criteria for New Steel Moment-Frame Buildings.” Report No. FEMA-350 SAC Joint Venture, Washington D.C., NY.

Fenves, G. L., and DesRoches, R., 1995. “Evaluation of the Response of 1-10/215 Interchange Bridge near San Bernardino in the 1992 Landers and Big Bear Earthquakes.” Report No. CSMIP/95-02, University of California, Berkeley, CA.

Gardoni, P., Der Kiureghian, A., Mosalam, K. M., 2002. “Probabilistic capacity models and fragility estimates for reinforced concrete columns based on experimental observations.” Journal of Engineering Mechanics, 128(10), 1024–1038.

Gaythwaite, J. W., 2004. “Design Of Marine Facilities For The Berthing, Mooring, And Repair of Vessels.”, AASHTO Pres.

Gazetas, G., Makris, N., 1991. “Dynamic pile-soil-pile interaction. Part I: Analysis of axial vibration.” Earthquake Engineering and Structural Dynamics, 20, 115–132.

Giovenale, P., Cornell, A. C., Esteva, L., 2004. “Comparing the adequacy of alternate ground motion intensity measures for the estimation of structural responses.” Earthquake Engineering and Structural Dynamics, 33(8), 951-979.

González, L., Abdoun, T., Dobry, R., 2009. “Effect of soil permeability on centrifuge modeling of pile response to lateral spreading.” Journal of Geotechnical and Geoenvironmental Engineering, 135, 62–73.

Iai, S., and Sugano, T., 1999. “Soil–structure interaction studies through shaking table tests.” Theme Lecture for the Second International Conference on Earthquake Geotechnical Engineering, Balkema, pp. 927–940.

Ishihara, K., 1996. “Soil Behavior in Earthquake Geotechnics.” Oxford University Press Inc., New York, NY.

Jacobs, L., Kosbab, B., Leon, R. T., DesRoches, R., 2010. “Seismic Behavior of Jumbo Container Crane,” Earthquake Spectra, In Press ,January, 2010.

Chiou, J. S., Chiang, C. H., Yang, H. H., Hsu, S. Y., 2011. “Developing fragility curves for a pile-supported wharf.” Soil Dynamics and Earthquake Engineering, 31(5-6), 830-840.

Kanayama, T., and Kashiwazaki, A., 1998. “Study on the dynamic behavior of container cranes under strong earthquakes.” Pressure Vessels and Piping Conference, Fairfield, NJ, USA.

Kanayama, T., Kashiwazaki, A., Shimizu, N., Nakamura, I., Kobayashi, N., 1998. “Large shaking table test of a container crane by strong ground excitation.” Pressure Vessels and Piping Conference, Fairfield, NJ, USA.

Kobayashi, N., Kuribara, H., Honda, T., Watanabe, M., 2004, “Nonlinear seismic responses of container cranes including the contact problem between wheels and rails.” Journal of Pressure Vessel Technology, Transactions of the ASME, 126, 59-65.

Kosbab, B., DesRoches, R., Leon, R. T., 2009. “Seismic Behavior of Modern Jumbo Container Cranes,” Proceedings of the Behavior of Steel Structures in Seismic Areas Conference (STESSA 2009), Philadelphia, PA, USA.

Kostadinov, M. V., and Yamazaki, F., 2001. “Detection of soil liquefaction from strong motion records.” Earthquake Engineering and Structural Dynamics, 30, 173–193.

Kruse, J., 2009. “Communicating the importance of seaports: Bringin’ it home.” American Association of Port Authorities (AAPA) Annual Convention, Galveston, TX.

Kwon, O. S., Elnashai A., 2006. “The effect of material and ground motion uncertainty on the seismic vulnerability curves of RC structure.” Engineering Structures, 28(2),289–303.

Lai, C. G., and Rix, G. J., 1998. “Simultaneous Inversion of Rayleigh Phase Velocity and Attenuation for Near-Surface Site Characterization.” Georgia Institute of Technology, School of Civil and Environmental Engineering, Report No. GIT-CEE/GEO-98-2.

Lancaster, P., 2002. “Lambda-Matrices and Vibrating Systems.” Dover Publications Inc., Mineola, NY.

Land, C. E., 1972. “An evaluation of approximate confidence interval estimation methods for lognormal means.” Technometrics, 14, 145-158.

Lehman, D. E., Brackmann, E., Jellin, A., Roeder, C. W., 2009. “Seismic performance of pile-wharf connections.” in Proceedings of TCLEE 2009: Lifeline Earthquake Engineering in a Multihazard Environment, Oakland, pp. 865–877.

Luco, N., Cornell, A. C., 2007. “Structure-specific scalar intensity measures for near-source and ordinary earthquake ground motions.” Earthquake Spectra, 23(2),357-392.

Makris, N., and Gazetas, G., 1992. “Dynamic pile-soil-pile interaction. part II: lateral and seismic response.” Earthquake Engineering and Structural Dynamics, 21, 145–162.

Matsui, T., and Oda, K., 1996. “Foundation damage of structures, Soils and foundations.” Special issue on geotechnical aspects of the January 17, 1995 Hyogoken-Nambu earthquake, 189–200.

McCarthy, P., Soderberg, E., Dix, A., 2009. “Wind damage to dockside cranes: Recent failures and recommendations.” Oakland, CA.

McCullough, N. J., Dickenson, S. E., Schelchter, S. M., 2004. “The seismic performance of piles in waterfront applications.” In Proceedings of Ports’01:America’s Ports-Gateway to the Global Economy, Norfolk.

McKenna, F., Scott, M. H., Fenves, G. L., 2010. “Nonlinear finite-element analysis software architecture using object composition.” Journal of Computing in Civil Engineering, 24, 95–107.

Menegotto, M., and Pinto, P., 1973. “Method of analysis for cyclically loaded reinforced concrete plane frames including changes in geometry and nonelastic behavior of elements under combined normal force and bending.” in Proceedings of IABSE Symposium on Resistance and Ultimate Deformability of Structures Acted on by Well-Defined Repeated Loads, International Association for Bridge and Structural Engineering, Zurich, 112–123.

Midorikawa, S., and Wakamatsu, K., 1988. “Intensity of earthquake motion at liquefied sites.” Soils and Foundations, 28(2), 73-84.

Na, U. J., Chaudhuri, S. R., Shinozuka, M., 2009. “Performance evaluation of pile-supported wharf under seismic loading.” in Proceedings of TCLEE 2009: Lifeline Earthquake Engineering in a Multihazard Environment, Oakland, 1032–1041.

Na, U. J., and Shinozuka, M., 2009. “Simulation-based seismic loss estimation of seaport transportation system.” Reliability Engineering and System Safety, 94(3), 722-731.

Nagle, K., 2009a. “Healthy, vibrant seaports support economic resurgence.” Trade and Industry Development, Nov/Dec 2009, 14-16.

Nagle, K., 2009b. “Healthy seaports deliver more than goods.” The Propeller Club Quarterly, Fall 2009, 10.

National Research Council, 1985. “Liquefaction of Soils During Earthquakes.” National Academy Press, Washington D.C., NY.

OCDI, 2002. “Technical standards and commentaries for port and harbor facilities in Japan.” The Overseas Coastal Area Development Institute of Japan.

Pachakis, D., Kiremidjian A. S., 2004. “Estimation of downtime-related revenue losses in seaports following scenario earthquakes.” Earthquake Spectra, 20(2),427–449.

Padgett, J. E., Nielson, B. G., DesRoches, R., 2008. “Selection of optimal intensity measures in probabilistic seismic demand models of highway bridge portfolios.” Earthquake Engineering and Structural Dynamics, 37(5), 711-725.

PIANC, 2001. “Seismic Design Guidelines for Port Structures.” Permanent International Navigation Association, A.A. Balkema Publishers, Rotterdam, Netherlands.

POLA, 2007. “Code for Seismic Design, Upgrade and Repair of Container Wharves and Commentary.” The Port of Los Angeles, San Pedro, California.

Priestley, M. J. N., Seible, F., Calvi, G. M., 1996. “Seismic Design and Retrofit of Bridges (1st ed).” Wiley-Interscience, New York, NY.

Rix, G. J., Werner, S. D., Ivey, L. M., 2009. “Seismic Risk Analyses for Container Ports.” in Proceedings of TCLEE 2009: Lifeline Earthquake Engineering in a Multihazard Environment, Oakland, 888–899.

Roeder, C. W., Graff, R., Soderstorm, J., Yoo, J. H., 2005. “Seismic performance of pile-wharf connections.” Journal of Structural Engineering, 131, 428–437.

Roth, W. H., and Dawson, E. M., 2003. “Analyzing the seismic performance of wharves, part 2: SSI analysis with non-Linear, effective-stress soil models.” in Proceedings: the Sixth U.S. Conference and Workshop on Lifeline Earthquake Engineering, Long Beach, 395–404.

Roth, W. H., Dawson, E. M., Mehrain, M., Sayegh, A., 2003. “Analyzing the Seismic Performance of Wharves, Part 1: Structural-Engineering Approach.” in Proceedings: the Sixth U.S. Conference and Workshop on Lifeline Earthquake Engineering, J. E. Beavers (editor), Long Beach, 385–394.

Shome, N., and Cornell, C. A. 1999. “Probabilistic seismic demand analysis of nonlinear structures.” Reliability of Marine Structures Rep. No. RMS-35, Dept. of Civil and Environmental Engineering, Stanford Univ., Stanford, CA.

Smith, D., Naesgaard, E., Kullmann, H., 2004. “Seismic design of a new pile and deck structure adjacent to existing caissons founded on potentially liquefiable ground in Vancouver, BC.” in Proceedings: 13th World Conference on Earthquake Engineering, Vancouver, Paper No. 2138.

Soderberg, E., Hsieh, J., Dix, A., 2009. “Seismic Guidelines for Container Cranes.” in TCLEE 2009. Oakland, CA: ASCE, 2009.

Spacone, E., Filippou, F. C., Taucer, F. F., 1996. “Fiber beam-column model for non-linear analysis of R/C frames: part I. Formulation.” Earthquake Engineering and Structural Dynamics, 25, 711–725.

Stopford, M., 2009. “Maritime economics.” London, Routledge.

Takahashi, A., Takemura, J., Kawaguchi, Y., Kusakabe, O., Kawabata, N., 1998. “Stability of piled pier subjected to lateral flow of soils during earthquake.” in Proceedings of the International Conference Centrifuge 98 (IS-Tokyo 98), 1, 365–370.

Teraoka, M. and Fujii, S., 2000. “Seismic damage and performance evaluation of R/C beam-column joints.” The Second US-Japan Workshop on Performance-Based Engineering for Reinforced Concrete Building Structures, Hokkaido, Japan, 379–390.

Thach, P. N., Yang, S., 2009. “A Simplified Method for Estimating Target Displacement of Pile-Supported Wharf under Response Spectrum Seismic Loading.” Proceedings of the International Symposium on Computational Structural Engineering, China.

Tokimatsu, K. and Asaka Y., 1998. “Effects of liquefaction-induced ground displacements on pile performance in the 1995 Hyogoken-Nambu earthquake.” Soils and Foundations, Special Issue No. 2, 163–178.

Towhata, K. Ishihara, 1985. “Modeling soil behavior under principal axes rotation.” Fifth International Conference on Numerical Methods in Geomechanics, 523-530.

U.S. Maritime Administration, 2009. “U.S. Water Transportation Statistical Snapshot.” U.S. Department of Transportation, Maritime Administration, Washington, D.C.

Varun, 2010. “A nonlinear dynamic macroelement for soil-structure interaction analyses in liquefiable sites.” Ph.D. Thesis, School of Civil and Environmental Engineering, Georgia Institute of Technology.

Varun, Assimaki, D., 2010. “A nonlinear dynamic macroelement for soil-structure interaction analyses of pile-supported waterfront structures.” International Journal for Numerical and Analytical Methods in Geomechanics, In Press.

Vytiniotis, A., Whittle, A.J., Kausel, E., 2011. “Effects of seismic motion characteristics on cyclic mobility and liquefaction.” Fifth International Conference on Earthquake Geotechnical Engineering, Santiago, Chile.

Wen, Y. K., Ellingwood, B. R., and Bracci, J. M. 2004. “Vulnerability functions.” Mid-America Earthquake Center, Univ. of Illinois, Technical Rep. No. DS-4, Champaign, Ill.

Werner, S. D., 1998. “Seismic Guidelines for Ports.” American Society of Civil Engineers, New York, NY.

Werner, S. D., Cook, W.C., 2009. “Wharf repair estimates for use in demonstration seismic risk analysis of port systems.” Prepared for NEES-GC Project: Seismic Risk Mitigation of Port Systems.

Werner, S. D., Dickenson, S. E., 1996. “Hyogo-Ken Nanbu earthquake of January 17, 1995: a post-earthquake reconnaissance of port facilities.” American Society of Civil Engineers, New York, NY.

Wilson, D. W., Boulanger, R. W., Kutter, B. L., 2000. “Observed seismic lateral resistance of liquefying sand.” Journal of Geotechnical and Geoenvironmental Engineering, 126, 898–906.

Yassin, M., 1994. “Nonlinear analysis of prestressed concrete structures under monotonic and cyclic loads.” Ph.D. Thesis, Department of Civil Engineering, University of California, Berkeley.